SISSA
Scuola Internazionale Superiore di Studi Avanzati

Neuroscience Area –
PhD course in Molecular Neurobiology

Sensory Neuron Rewiring in Pancreatic Ductal Adenocarcinoma: from Single-Cell RNA Profiling to Extracellular Vesicles-based strategies

Candidate:
Michele Montrone

Supervisor:
Prof. Paul Alexander Heppenstall
Co-supervisors:
Elena Genova, PhD
Fernanda De Castro Reis, PhD

Academic Year 2024-2025

Thesis overview

This thesis is divided into two main sections, each reflecting one of the two core research projects I undertook during my four-year PhD program.

Chapter I focuses on the transcriptional characterization of sensory neuronal populations (dorsal root ganglia neurons, DRG neurons) that innervate the pancreas in physiological conditions versus in pancreatic ductal adenocarcinoma (PDAC). This work aimed to identify molecular signatures and cellular heterogeneity associated with cancer-related neuronal remodeling employing single cell RNA sequencing (scRNAseq) analyses. The study culminated in the submission of a manuscript to a peer-reviewed journal: the version presented here corresponds to the submitted article, currently under review.

Chapter II shifts to the field of nanomedicine and biotechnology, describing the development and optimization of extracellular vesicles (EVs) as customizable drug delivery platforms for the transport of therapeutic mRNAs. This work explores a range of bioengineering strategies to enhance EV targeting specificity and cargo loading efficiency. Although the system remains at a pre-prototype stage, the findings lay the groundwork for future translational applications.

ACKNOWLEDGMENTS

. This work would not have been possible without the crucial help and expertise of:

- Dr. Elena Genova, PhD: performed pancreatic injection and set up the whole single cell picking workflow. She assured mice health too and taught me a lot about immunostaining troubleshooting and organoids handling; she also accounts for the elegant mitotrack validation and analysis, as well as for quantification. We share the authorship of the present work as we worked out all the wet lab experiments.

- Dr. Uday Rangaswamy, PhD: Outstanding computational biologist, whose expertise and enthusiasm in the field grows stronger and comprehensively every day. I owe him the most interesting brainstorming about all the speculation and/or testable theories about the present work (especially the EVs mediated mRNA transfer from cancer to neurons). He has so far the most rigorous lateral thinking I've ever witnessed. We share the authorship of the present work as he performed all the scRNAseq data elaboration, comparison and analysis. The Suerat kid in town.

- Prof. Paul Alexander Heppenstall: more than just a mentor, a shiny example of why one should choose the academic career. A really nice fine human being, beyond academic honors.

- Fernanda De Castro Reis, PhD: Heppenstall's group Lab Manager. A professional full of patience that has always favored dialogue over fighting, even when I was acting unintentionally rude or messing up Lab's equipment due to some bachelor-graded mistakes. All that I know in the magical world of gel blotting, I owe to her.

- Prof. Remo Sanges: professor of Computational biology at SISSA, Trieste, Italy. Uday's mentor and a rigorous, constructive reviewer. He always comes clear and polite about what is wrong with your conclusions, helping you to find a reasonable and logical way out.

- Dr. Gloria Ros, PhD: A tireless researcher, a true source of inspiration for her students and for me. Rigorous, rational, and evidence-based: an exceptional problem solver in the world of RT-qPCR and Western blotting, and a fine soul.

- All the SISSA technical staff, with special mention to Federica Ferrero and Micaela Grandolfo (FACS Facility and Confocal Microscopy Facility), Beatrice Pastore (Tissue cultures and animal welfare), Massimo Righi, Christina Vlachouli and Helena Krmac (Molecular Biology Facility).

- Elettra Grdina, Lorenzo Maschietto, Angel Pascal Camerota and Alberto Petrocelli from SISSA Animal Facilities: all that I know about animal handling, rodents' welfare and regulatory I owe to them.

- Michele Coscia: one of my master thesis students, whose help has been crucial during scheduling, wet lab experiments and especially brainstorming: a fresh, passionate and relentless young scientific mind.

Table of contents

Chapter I – Sensory Neurons Rewiring in Pancreatic Ductal Adenocarcinoma

1. ABRSTRACT

2. LIST OF FIGURES

3. INTRODUCTION

3.1 Pancreatic Cancer: a still unaddressed global burden

3.1.1 Epidemiology and pathogenesis of Pancreatic Ductal Adeno Carcinoma (PDAC)

3.1.2 The rising of Cancer Neuroscience

3.1.3 General overview of the mouse sensory system

3.1.4 Pancreas-Brain sensory crosstalk in healthy pancreas

3.1.5 Pancreas-Brain sensory crosstalk in PDAC

3.1.6 Neuroimmune interactions in pancreatic cancer

3.2 Modelling PDAC in the laboratory

3.2.1 in vitro models: pancreatic organoids

3.2.2 in vivo models: the KPC mouse

3.2.3 Architecture of the pancreatic tissue: main differences between mouse and human

3.3 Single Cell RNA sequencing applied on peripheral nervous system

3.3.1 General overview of a scRNA seq experiment

3.3.2 Pros & Cons of scRNA seq dataset

3.3.3 Transcriptomic knowledge of the mouse sensory system: state of the art.

4. AIMS OF THE THESIS

5. MATERIALS AND METHODS

5.1 Animals used for scRNAseq and EVs isolation

5.2 Dorsal Root Ganglia Primary Dissociation Culture

5.3 Retrograde labelling

5.4 Immunofluorescence

5.5 Mitochondria staining in DRG neurons

5.6 Co-localization quantification

5.7 Histology

5.8 RNA Sequencing and library preparation

5.9 Nested PCR on sequenced neurons

5.10 RT-qPCR on sequenced DRG neurons and isolated EVs

5.11 Organoid-derived EVs isolation

5.12 Pancreatic slice-derived EVs isolation

5.13 Blood derived-EVs isolation

5.14 Clustering and annotations of DRG neurons identity

5.14.1 Mapping and quantification of genes in sequenced cells

5.14.2 From bulk sample processing to analysing single cells using Seurat

5.14.3 Annotation of cells using Monocle3

5.14.4 Identification of markers and differential gene expression analysis

6. RESULTS

6.1 Single-cell RNA sequencing identifies sensory neuron subtypes innervating healthy pancreatic tissue and PDAC tissue

6.2 Prevalence of the NF subpopulation amongst sensory neuron subtypes innervating pancreas

6.3 Reduced non-peptidergic fraction in DRG from KPC mice

6.4 Novel detection of Pdx1-Cre and Snca in KPC DRGs and evidence of EVs transfer

6.5 Functional enrichment analysis reveals altered mitochondrial activity in KPC DRGs

7. DISCUSSION

8. BIBLIOGRAFHY

1. ABSTRACT

Background & Aims: Neuronal innervation of the pancreas has historically been characterized using marker-based classification and physiological studies, but its transcriptomic landscape remains only partially explored. A detailed molecular profile of pancreatic sensory neurons could provide insights into their role in health and disease, particularly in pancreatic ductal adenocarcinoma (PDAC), where neural remodeling influences tumor progression and pain signaling.

Methods: Wild-type and PDAC mice were injected with the retrotracer Fast Blue into pancreatic or cancerous tissue. Dorsal root ganglia were cultured, and Fast Blue-positive sensory neurons were isolated, lysed, and analyzed using single-cell RNA sequencing. Data was validated using immunohistochemistry, organoid cultures and qPCR.

Results: We performed transcriptomic profiling of sensory neurons innervating the pancreatic head and tail under normal and cancer conditions. Our analysis identified neurofilament-containing neurons (NF) as the predominant sensory subtype in both contexts, while non-peptidergic neurons (NP) were underrepresented in tumor-associated innervation. Differential gene expression analysis revealed a unique subset of genes upregulated in sensory neurons innervating pancreatic tumors, many linked to mitochondrial activity. Further validation also revealed the presence of transcripts transferred via extracellular vesicles (including a non-coding portion of the PDX1 gene), suggesting a novel mechanism of tumor-neuron interaction.

Conclusions: Our findings provide a detailed characterization of pancreatic and pancreatic ductal adenocarcinoma sensory innervation. We identified a circulating long non-coding RNA of potential tumor origin in the PDAC mouse model, revealing new therapeutic and biomarker opportunities in pancreatic cancer.

Keywords: sensory neurons; pancreas; pancreatic ductal adenocarcinoma; single cell RNA sequencing; tumor microenvironment.

2. LIST OF FIGURES

Figure 1- Key anatomical features of the human pancreas

Figure 2- Biomorphology of human PDAC lesions

Figure 3- Progression model for pancreatic cancer

Figure 4- Type of interactions between cancer and the nervous system

Figure 5- General overview of the mouse peripheral nervous system

Figure 6- Sensory innervation from the pancreas to the brain

Figure 7- Evidences on the different neurochemical axis between nervous system and pancreas

Figure 8- Perineural invasion in PDAC

Figure 9- Crosstalk between sympathetic innervation and PDAC tumour microenvironment

Figure 10- Crosstalk between parasympathetic innervation and PDAC tumour microenvironment

Figure 11- Crosstalk between sensory innervation and PDAC tumour microenvironment

Figure 12- Proposed mechanisms for the emergence of nerves in the tumor microenvironment

Figure 13- Complexity of the cross talk between PNS and immune system around TME

Figure 14- Current PDAC organoid applications

Figure 15- Cre recombinase system in KPC mice

Figure 16- Comparison of mouse and human pancreatic anatomy

Figure 17- General workflow of single-cell RNA sequencing

Figure 18- . Workflow of Smart-seq2 protocol

Figure 19- PCA of 622 neurons resulting in four clusters (Usoskin et al., 2015)

Figure 20- Overlap of our scRNAseq dataset and the reference's one

Figure 21- Representative histology for PDAC lesion in sequenced animals

Figure 22- Seurat unsupervised clustering of our scRNAseq

Figure 23- Transcriptomic and immunofluorescence quantifications (distribution)

Figure 24- Transcriptomic and immunofluorescence quantifications

Figure 25- immunofluorescence quantifications of WT and KPC animals

Figure 26- Volcano plot for differentially expressed genes in neurons innervating PDAC

Figure 27- Percentage of WT and KPC DRG cells expressing Pdx1 5'UTR

Figure 28- IGV snapshot of neurons (rows) whose Pdx1 5'UTR count > 10

Figure 29- Barplot of RT-qPCR validation of gene of interest (Pdx1) across 3 sample types

Figure 30- Agarose gel of end-point PCR for Pdx1 5'UTR fragment across all animals

Figure 31- scRNAseq reads from sequenced KPC and WT DRG neurons innervating the pancreas

Figure 32- Agarose gel of RTqPCR for Pdx1 5'UTR-Tg Cre fragment in pooled KPC mice

Figure 33- Agarose gel of RT-q PCR for Pdx1 5'UTR and Snca in blood circulating EVs

Figure 34- GO annotations in KRAS DRG neurons and mitotracker analysis

Figure 35- Boxplot of RT-qPCR validation for selected mito genes in pooled KPC mice

Figure 36- Mitochondrial count and number of branches comparison between WT and KPC mice

Figure 37- Representative mitotracker imaging from WT and KPC mice DRG neurons

3. INTRODUCTION

3.1 Pancreatic Cancer: an unaddressed global burden

3.1.1 Epidemiology and pathogenesis of Pancreatic Ductal Adeno Carcinoma (PDAC)

Pancreatic ductal adenocarcinoma (PDAC) is the most common type of pancreatic cancer and the third leading cause of cancer-related death in the USA. Although the incidence of PDAC is relatively low, the number of cases is steadily increasing each year and PDAC is projected to become the second leading cause of cancer-related mortality by 2030 (Park et al., 2021). PDAC is a highly lethal cancer with a poor prognosis. This is mainly due to the lack of effective tools for early diagnosis. Approximately 50-60% of patients have advanced disease with distant metastasis at diagnosis. Meanwhile, only 10-15% of patients present with localized surgically resectable cancer (Kolbeinsson et al., 2023). Early diagnosis is further hindered by the lack of well-defined symptoms in the lowest stages of the disease (Wood et al., 2022). However, 80% of patients experience abdominal pain, the origin of which is not fully understood (J. Wang et al., 2021). Although the 5-year survival rate has doubled over the past 10 years, it remains very low at 12%. This is because the primary treatments for PDAC, which include chemotherapy and surgical resection, still face many challenges that prevent significant progress in patient care (Halbrook et al., 2023). The use of multiagent cytotoxic therapies has led to modest improvements in recent years, but therapeutic resistance remains a hallmark of PDAC (Park et al., 2021). This resistance is mainly due to the presence of a tumor microenvironment (TME) that strongly supports tumor progression (Sherman & Beatty, 2023). In contrast, surgical resection is limited by the fact that only 15-20% of patients are eligible for surgery due to the late diagnosis of PDAC. Moreover, complete resection does not guarantee a cure, as nearly 75% of patients develop recurrence within two years following surgery (Halbrook et al., 2023). Therefore, it is essential to develop tools for early diagnosis and new therapies that provide greater benefits to patients, along with improving the understanding of PDAC biology (Wood et al., 2022). PDAC originates from the exocrine pancreas (Halbrook et al., 2023; Aktinson MA et al., 2020). The pancreas

is a glandular organ responsible for regulating metabolism and blood glucose levels. It is divided into two compartments: the exocrine and the endocrine (Fig.1).

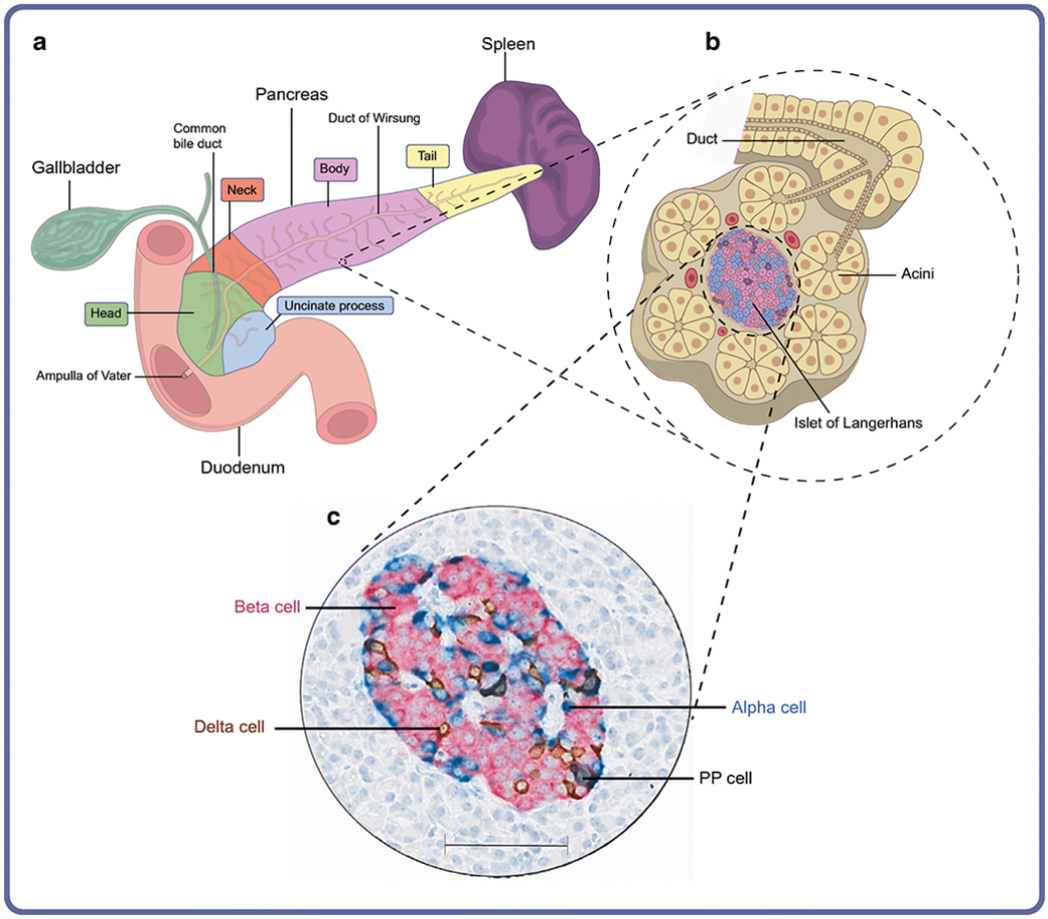


Figure 1. Key anatomical features of the human pancreas. (**a**) Diagram of the pancreas, and surrounding organs. (**b**) Schematic representation of organization of the endocrine and exocrine pancreas at the cellular level. (**c**) Human pancreatic islet shows the four endocrine cell types. Scale bar, 100 µm. (from Atkinson MA et al., 2020)

The exocrine compartment consists of acinar and ductal cells. Acinar cells produce digestive enzymes that are secreted into the pancreatic ducts and delivered to the intestine. The endocrine compartment is made up of the so-called islets of Langerhans, which are composed of five cell types (alpha, beta, delta, epsilon, and PP cells) that produce peptide hormones involved in blood glucose homeostasis. Insulin and glucagon are particularly important, as they respectively lower and raise blood glucose levels (Agerskov & Nyeng, 2024). PDAC develops through a process called acinar-to-ductal metaplasia (ADM), which is the transdifferentiation of pancreatic acinar cells into ductal-like cells.

This acinar cell plasticity serves as a protective mechanism in response to genetic damage and environmental stress. However, if cellular pressure persists, ADM can act as a precursor lesion for the development of Pancreatic Intraepithelial Neoplasia (PanINs; Marstrand-Daucé et al., 2023). PanINs are the most common precancerous lesions that precede PDAC, classified as either low-grade or high-grade lesions (Fig.2 D & E, and F respectively), based on their structural alterations. Their progression to PDAC (Fig.2 C) occurs over several years, as genetic mutations accumulate. However, the majority of PanINs do not progress to PDAC (Wood et al., 2022).

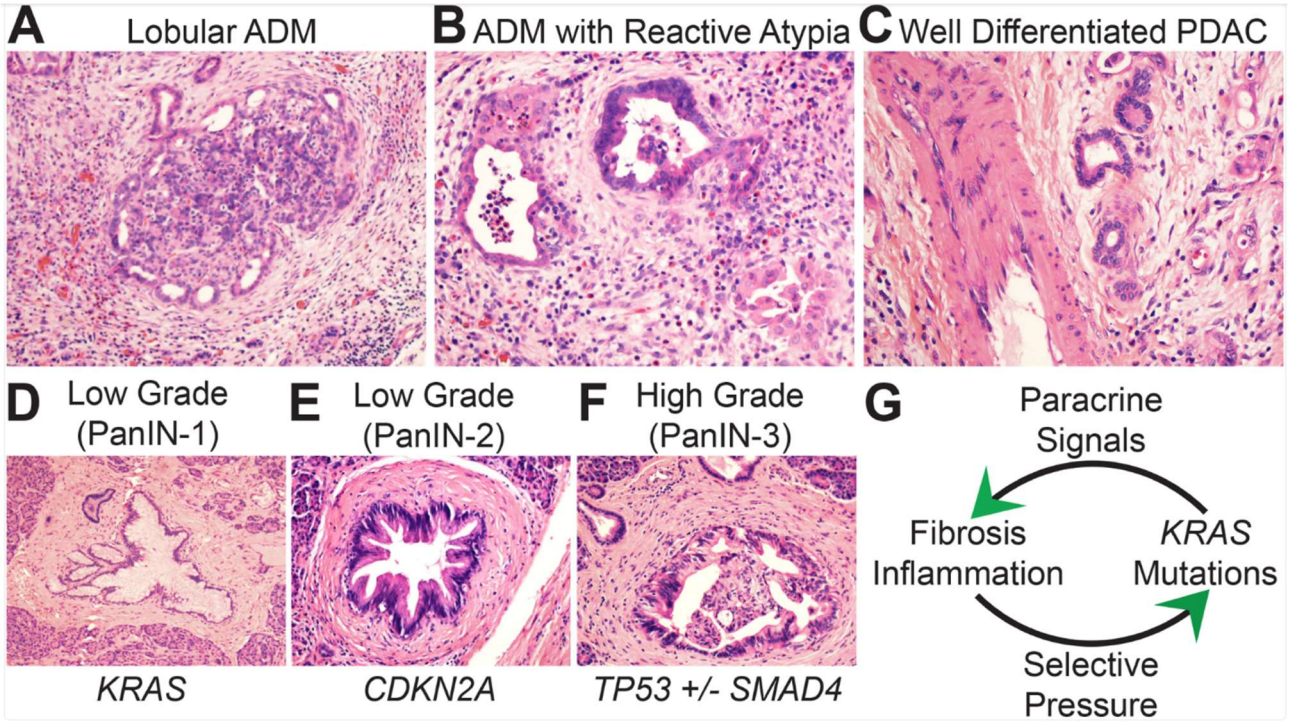


Figure 2. Biomorphology of PDAC precursor lesions. (A) At low magnification acinar to ductal metaplasia (ADM) maintains a lobular architecture surrounded by a fibroinflammatory stroma. Metaplastic ducts are seen on the periphery and residual acinar units on the interior. (B) At high magnification metaplastic ducts show morphology that overlaps with malignancy including luminal necrosis, nuclear atypia, and jagged glandular outlines. (C) The ADM ductal units in B are more atypical than this bland-appearing PDAC that is infiltrating adjacent to a large vessel. (D–F) Dysplasia increases as genetic drivers accumulate during precursor progression. (G) Gene:environment positive feedback maintains precursor lesions (from McDonald OG, 2022)

The progression of PDAC is also influenced by the presence of a stromal TME that promotes tumor growth and metastasis formation. In particular, cells with mutated KRAS shape the TME by

disrupting the activity of a variety of cells, included fibroblasts, components of the extracellular matrix (ECM), immune cells, nerves, and endothelial cells. This process strengthens a strong inflammatory response, leading to the development of invasive PDAC (Sherman & Beatty, 2023). The most important genetic driver in PDAC is the KRAS oncogene. KRAS mutations are present in 90% of PDAC patients and appear early, at the stage of low-grade lesions. The most frequent mutation is $KRAS^{G12D}$. As progression to high-grade lesions occurs, loss-of-function mutations in the tumor suppressor genes CDKN2A, TP53, and SMAD4 also emerge (Halbrook et al., 2023; Fig.3): specifically, it has been reported that KRAS is activated in 95% of PDAC patients, while the tumor suppressor genes CDKN2A, TP53, and SMAD4 are inactivated in 95%, 75% and 55% of patients, respectively (Saiki & Horii, 2014).

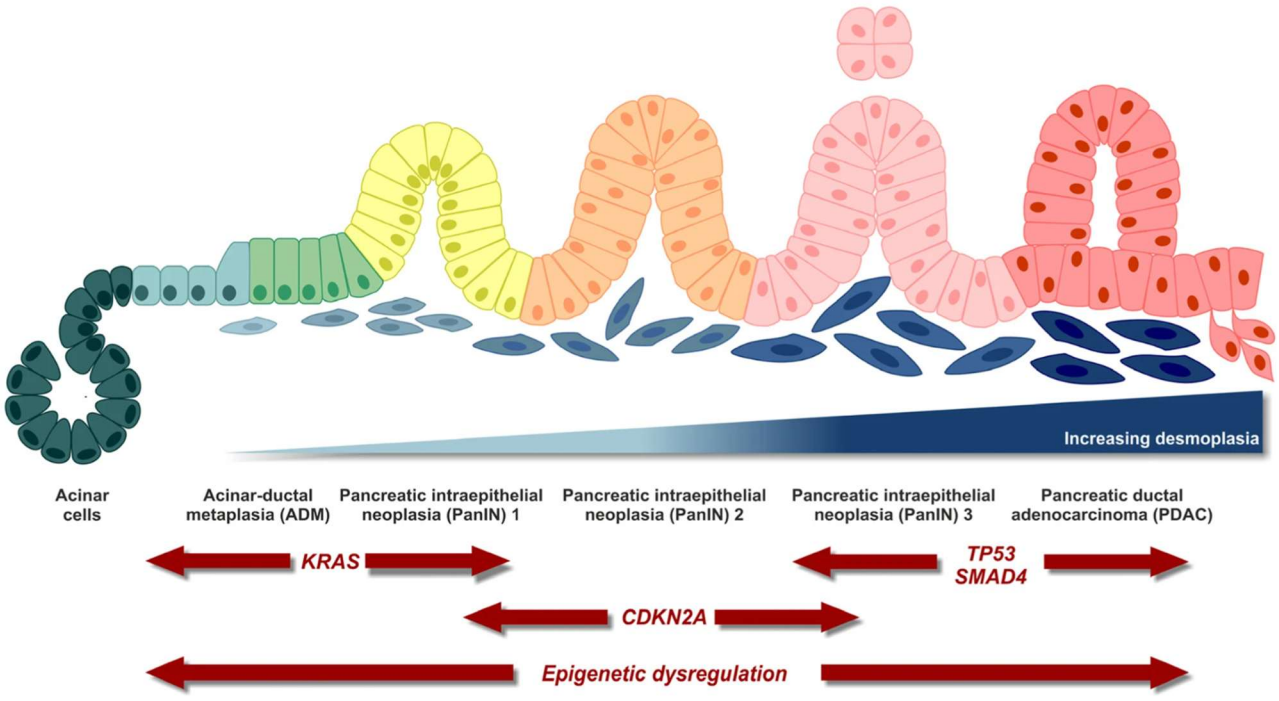


Fig.3- Progression model for pancreatic cancer. Normal duct epithelium progresses to infiltrating cancer (*left* to *right*) through a series of histologically defined precursors (PanINs). The overexpression of HER-2/*neu* and point mutations in the K-*ras* gene occur early, inactivation of the *p16* gene at an intermediate stage, and the inactivation of *p53, DPC4,* and *BRCA2* occur relatively late (from Orth M. et al., 2019)

3.1.2 The rising of Cancer Neuroscience

In recent years, it has become increasingly clear that the nervous system and cancer are closely interconnected. Beyond its "canonical" functions, the nervous system is involved in various physiological processes, such as organogenesis, homeostasis, regeneration, and plasticity throughout the body. In pathological contexts, cancer establishes interactions with the nervous system to exploit the processes it governs and remodel it to promote tumor progression and metastasis formation. These interactions between cancer and the nervous system form the basis of an emerging field called "cancer neuroscience." This new discipline is dedicated to investigating the role of the nervous system in cancer pathogenesis, with the goal of harnessing this knowledge to develop novel anti-cancer therapies (Winkler et al., 2023). The mechanisms through which the nervous system and cancer interact are diverse and bidirectional (Fig.4). In the central nervous system (CNS), synaptic contacts between neurons and tumor cells can promote tumor growth, either through the release of neurotransmitters by neurons or via electrochemical mechanisms. It remains unclear whether such synapse formation also occurs in the nerves of the peripheral nervous system (PNS). Nevertheless, throughout the nervous system, the release of paracrine factors, such as neurotransmitters or growth factors, by tumor cells can influence both neurons and cells in the tumor microenvironment (TME), enhancing the pro-tumor neural activity of the TME. For example, tumor cells have been observed to release neurotrophins that promote axonogenesis within the TME, fostering tumor innervation. Furthermore, both neurons and tumor cells can release circulating factors that exert systemic effects, influencing the immune system in either pro-tumor or anti-tumor ways (Monje et al., 2020).

The bidirectional nature of nervous system-cancer interactions is also evident in the side effects that cancer therapies have on patients. In particular, chemotherapy and radiotherapy cause severe long-term effects, including cognitive decline and peripheral neuropathy. The exact causes and mechanisms underlying this neurotoxicity are still unclear, but new studies are emerging on the subject. Nevertheless, further investigation is needed to develop new cancer treatment strategies that significantly improve patients' quality of life (Lan et al., 2023).

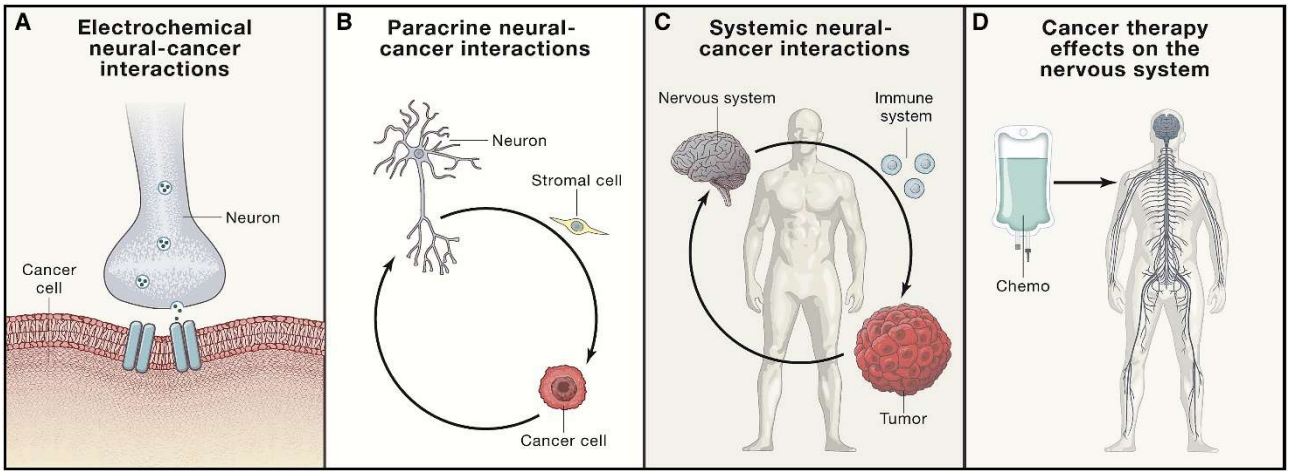
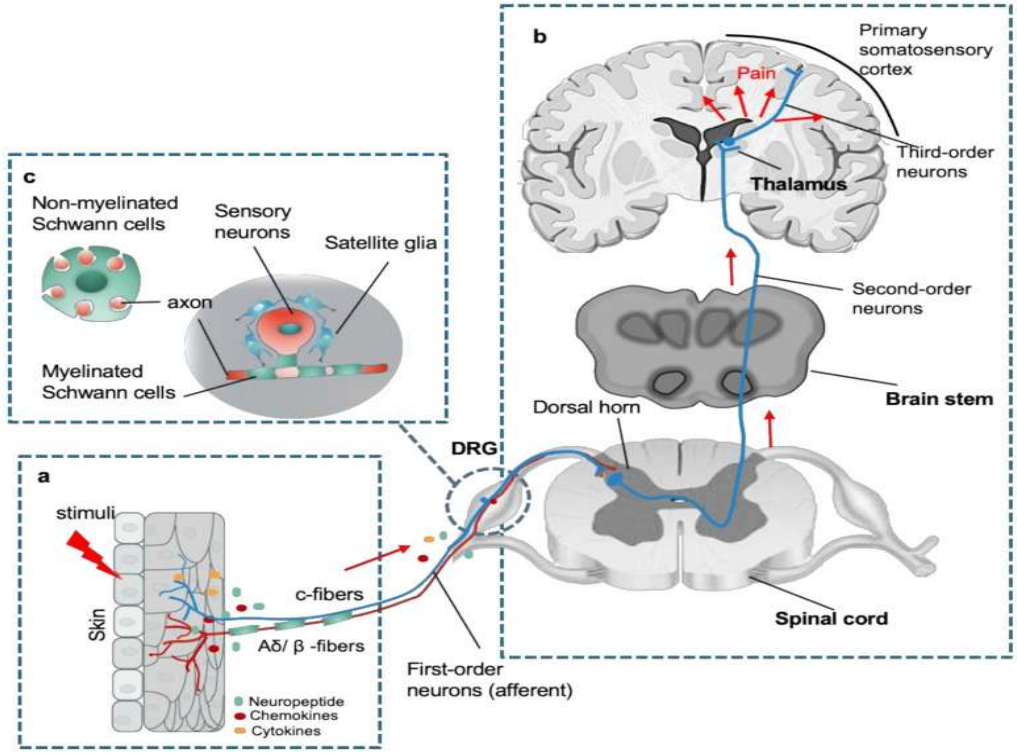


Figure 4. Type of interactions between cancer and the nervous system (from Monje et al., 2020).

All these pathological factors underscore the significance of studying the nervous system in the context of cancer to enhance and develop effective oncological therapies. Although cancer neuroscience is a nascent discipline, it is evident that targeting nervous system-cancer interactions that support tumor growth will become a crucial component of future anti-cancer therapies. Preclinical studies aimed at blocking these interactions in various tumor types are already underway; however, much remains to be done (Mancusi & Monje, 2023). In particular, the mechanisms underlying the role of the nervous system in tumor pathogenesis are not yet fully understood. Therefore, gaining this knowledge will be crucial for the advancement of cancer neuroscience and will require interdisciplinary collaboration between neuroscience, developmental biology, immunology, and cancer biology (Monje et al., 2020).

3.1.3 General overview of the mouse sensory system

A



B

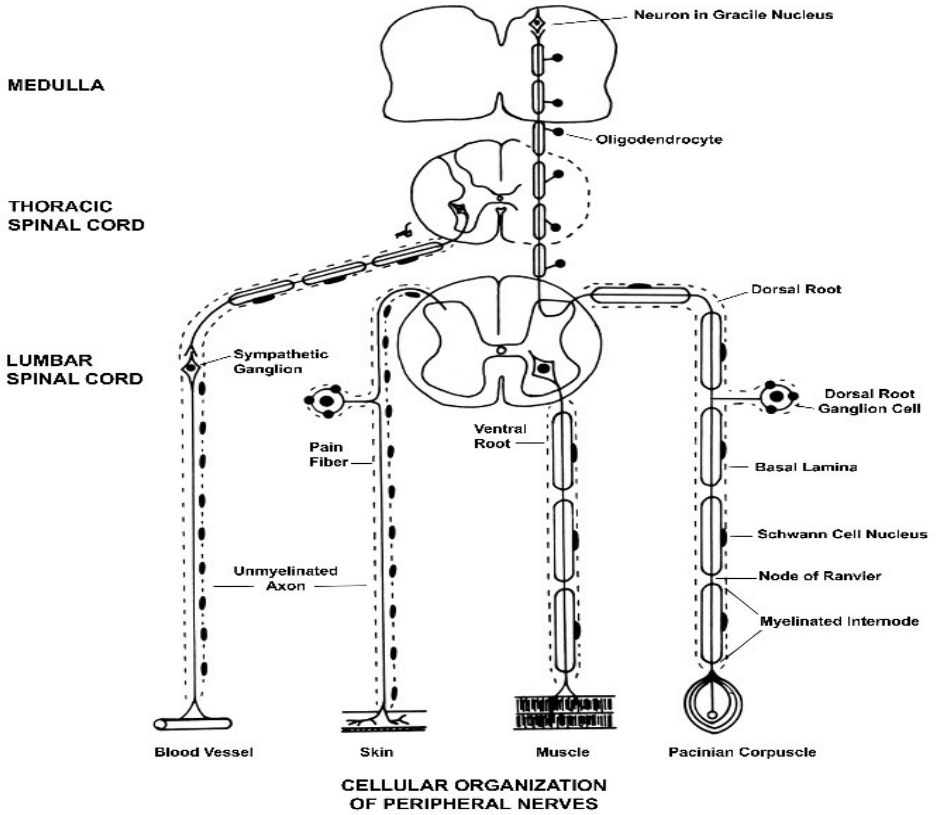


Figure 5. General overview of the mouse peripheral nervous system (A from Liu JA et al.,2021; B from Jortner BS., 2020).

The peripheral nervous system (PNS) consists of nerves and ganglia distributed throughout the body that are responsible for transmitting information between the central nervous system (CNS) and the rest of the organism. The connection to the CNS occurs through cranial and spinal nerves, which project to the brain and spinal cord (Lanigan et al., 2021). The PNS includes an afferent sensory component and an efferent motor component (Catala & Kubis, 2013).

From the periphery, afferent sensory fibers enter the dorsal roots of the spinal cord via the sensory ganglia of cranial nerves and the dorsal root ganglia (DRG; Fig.5 A & B; Lanigan et al., 2021). The dorsal root ganglia (DRG) are paired on either side of each vertebra in the spinal column and contain the cell bodies of primary sensory neurons (approximately 15,000 neurons/DRG) (Esposito et al., 2019). Typically, rodents have 30-31 pairs of DRG: 8 pairs of cervical DRGs, 13 pairs of thoracic DRG, 5 or 6 pairs of lumbar DRG, and 4 pairs of sacral DRG (Meltzer et al., 2021).

The primary sensory neurons of the PNS innervate the skin, muscles, bones, and visceral organs, allowing the detection of various types of stimuli, both innocuous and noxious, from the external environment and internal organs (Meltzer et al., 2021). DRG neurons have a pseudo-unipolar shape, featuring two branches – one peripheral and one central – that form a T-shaped junction. The diameter of their cell bodies can range from 20 μm to 150 μm (Esposito et al., 2019). Due to their heterogeneity, DRG neurons can be distinguished based on various criteria, such as cell body size, degree of myelination, axon caliber, conduction velocity, and gene expression profile. In general, nerve fibers can be classified into four different types: Aα, Aβ, Aδ, and C. Aα and Aβ fibers are myelinated, have large diameter cell bodies, and exhibit high conduction velocity. They vary according to the type of stimuli they detect: Aα fibers include proprioceptors, while Aβ fibers include low-threshold mechanoreceptors (LTMRs). Aδ fibers are lightly myelinated, have medium diameter cell bodies, exhibit intermediate conduction velocity, and include nociceptors. Finally, C fibers are unmyelinated, have small diameter cell bodies, exhibit slow conduction velocity, and include thermoreceptors, LTMRs, pruriceptors, and nociceptors (Zheng et al., 2022). The transmission of action potentials from the peripheral sensory endings of DRG neurons to the spinal cord is mediated by voltage-gated

ion channels located on the surface of the neurons (Esposito et al., 2019; Middleton et al., 2022). This enables the release of neurotransmitters such as substance P, calcitonin gene-related peptide (CGRP), vasoactive intestinal polypeptide (VIP), endothelin, histamine, and glutamate (Keskinov et al., 2016).

3.1.4 Pancreas-Brain sensory crosstalk in healthy pancreas

The pancreas is innervated by components of the autonomic nervous system (ANS; sympathetic and parasympathetic) and the sensory nervous system (Agerskov & Nyeng, 2024). All of these fibers contribute to the proper functioning of the pancreas (Ni B. et al., 2023). The ANS represents the involuntary component of the nervous system, playing a crucial role in maintaining the homeostasis of internal organs. The ANS is composed of three main parts: the sympathetic nervous system, the parasympathetic nervous system, and the enteric nervous system. The sympathetic nervous system is known as the "fight or flight" division, while the parasympathetic nervous system is referred to as the "rest and digest" division. Typically, these two systems function as antagonists; however, they can also collaborate in the same processes. They also communicate with the enteric nervous system, which provides intrinsic innervation to the gastrointestinal tract (Wehrwein et al., 2016). Pancreatic innervation can be divided into intrinsic and extrinsic (Fig.6), depending on whether the cell bodies of their neurons are located inside or outside the pancreas (Makhmutova & Caicedo, 2021).

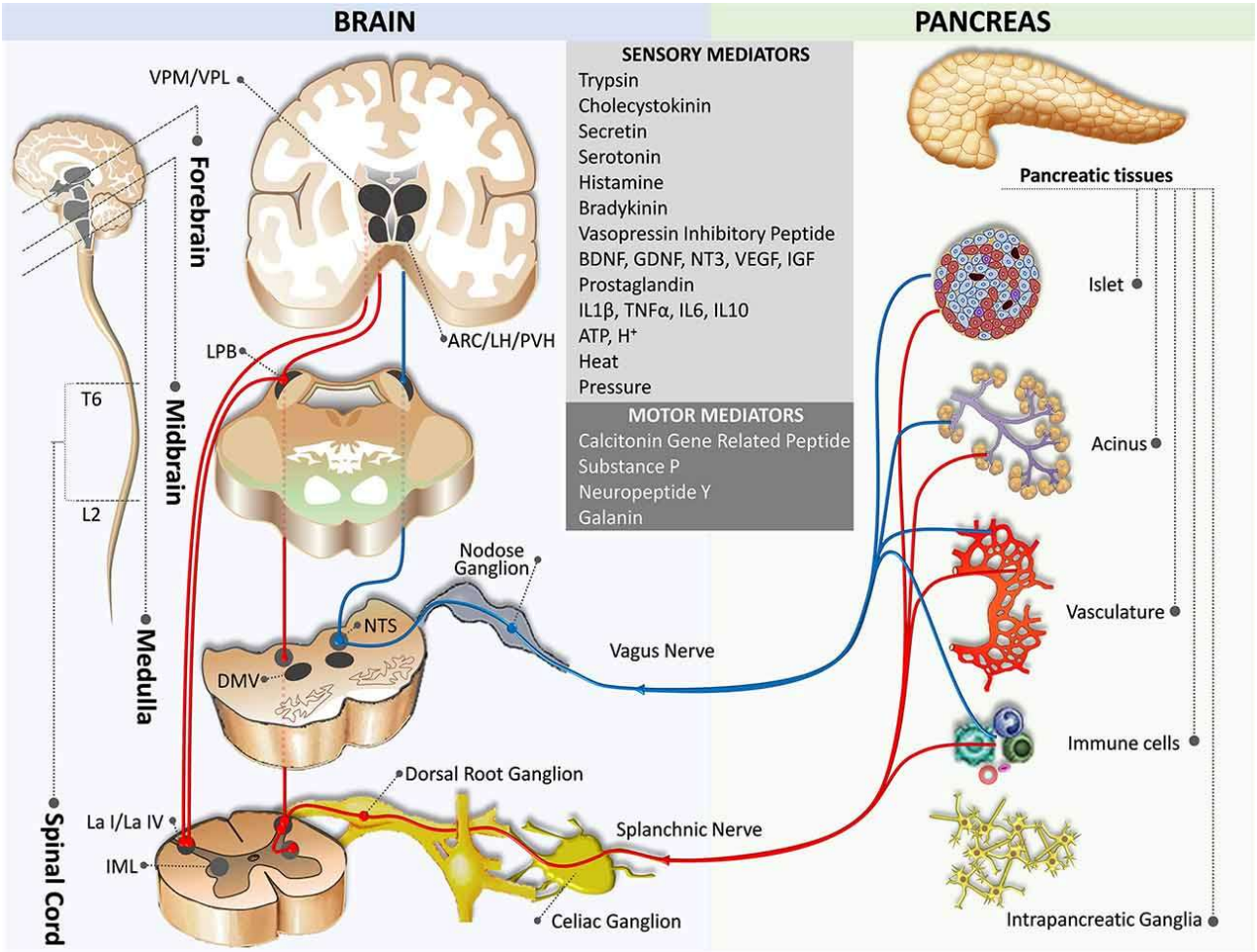


Figure 6. Sensory innervation from the pancreas to the brain. The blue pathway marks the parasympathetic afferent pathway, while the red pathway indicates the sympathetic afferent pathway. ARC,arcuate nucleus of the hypothalamus; DMV, dorsal motor nucleus of the vagus; IML, intermediolateral nucleus of the spinal cord; L2, spinal cord lumbar 2 segment; La I/La IV, lamina I and IV of the spinal cord gray matter; LH, lateral hypothalamic nucleus; PB, parabrachial nucleus; NTS, nucleus of the tractus solitaries; PVH, paraventricular hypothalamic nucleus; T6, spinal cord thoracic 6 segment; VPM/VPL, the ventral posteromedial/posterolateral nuclei of the thalamus (from Lkhagvasuren B. et al., 2021).

Intrinsic innervation comprises neurons organized in intrapancreatic ganglia, which are distributed throughout the pancreatic parenchyma. The neurons in these ganglia are predominantly cholinergic and innervate pancreatic blood vessels, islets, ducts, and acini. While their role in pancreatic function is not yet fully understood, it is believed that stimulation of the intrapancreatic ganglia by extrinsic innervation promotes the secretion of insulin and pancreatic exocrine enzymes (Makhmutova & Caicedo, 2021). Extrinsic neural input into the pancreas is composed of five autonomic branches: two

efferent pathways – parasympathetic and sympathetic; two afferent pathways - vagal and spinal; and the entero-pancreatic axis. While parasympathetic neurons project exclusively to intrinsic ganglia, the other extrinsic branches also target pancreatic structures directly (Makhmutova & Caicedo, 2021). Primary parasympathetic neurons with cell bodies in the dorsal motor nucleus of vagus (DMV) travel in the vagus nerve and synapse exclusively in the pancreatic ganglia without targeting acinar or endocrine structures directly. Both primary parasympathetic and intrinsic pancreatic neurons are cholinergic, thus primarily releasing acetylcholine (ACh), along with other neurotransmitters such as vasoactive intestinal polypeptide (VIP), gastrin, and nitric oxide (NO). Parasympathetic fibers regulate blood glucose homeostasis after food intake by promoting the secretion of digestive enzymes from acinar cells and insulin from β-cells (Agerskov & Nyeng, 2024). Sympathetic innervation comprises primary neurons residing in the intermediolateral column of the spinal cord that send projections to postsynaptic neurons of the perivertebral column and celiac ganglia via splanchnic nerves (Lkhagvasuren B. et al., 2021; Makhmutova & Caicedo, 2021). Noradrenergic projections of secondary sympathetic neurons enter the pancreas via mesenteric nerves and innervate pancreatic ganglia, vasculature, endocrine islets, ducts, and lymph nodes, releasing neurotransmitters such as norepinephrine (NE), galanin, and neuropeptide Y (NPY). In response to stress and hypoglycemia, sympathetic fibers regulate blood glucose homeostasis by inhibiting insulin secretion from pancreatic β-cells and promoting glucagon secretion from α-cells, thus increasing blood glucose levels (Agerskov & Nyeng, 2024). The pancreas receives both vagal and spinal sensory innervation. Vagal sensory neurons have cell bodies in the nodose ganglion, and their projections travel alongside parasympathetic efferent fibers in the vagus nerve. Spinal sensory neurons originating bilaterally in the T9-T13 dorsal root ganglia travel alongside sympathetic fibers in splanchnic and mesenteric nerves. Substance P- and CGRPpositive sensory fibers are found throughout exocrine tissue and in the majority of pancreatic islets. Vagal sensory fibers project preferentially to pancreatic islets, indicating that the exocrine sensory component is primarily of spinal origin. Although the role of sensory fibers in pancreatic function is not yet fully understood, they are believed to play a part in

inflammatory processes. However, it is known that DRG neurons in the afferent fibers of the spinal nerve contribute to pain sensation (Lkhagvasuren B. et al., 2021). The pancreas is also innervated by the enteric nervous system, particularly by neuronal plexuses from the stomach and duodenum. These neurons are cholinergic and serotonergic, and they primarily innervate the intrapancreatic ganglia, while a smaller portion reaches the pancreatic acini, islets, ducts, and blood vessels. Enteric serotonergic fibers exert both excitatory and inhibitory effects on pancreatic secretion (Makhmutova & Caicedo, 2021). A schematic recapping of all of the main interactions between nervous system and the pancreas is reported in Fig.7 as follows:

Table 1. Pancreatic innervation pathways

Neuronal subtype	Detected in murine pancreas	Neurotransmitters	Cell types innervated	Effect in adult pancreas
Sympathetic nervous system	E12.5 (Burris and Hebrok, 2007)	Galanin, NPY, NA (Babic and Travagli, 2016)	Intra-islet endothelial cells, acinar and ductal cells, intrapancreatic ganglia, islets (Babic and Travagli, 2016)	Increases blood glucose by lowering plasma insulin concentration (Gilliam et al., 2007; Malaisse et al., 1967). Stimulation of glucagon secretion from alpha cells (Adeghate et al., 2000). Increases vasoconstriction (Barlow et al., 1974).
Parasympathetic nervous system	E12.5 (Croizier et al., 2016.)	PACAP, gastrin, GRP, VIP, ACh, NO (Hampton et al., 2022)	Intrapancreatic ganglia, acinar cells, islets (Lkhagvasuren et al., 2021)	Decreases blood glucose by stimulation of insulin secretion from beta cells directly (Mussa et al., 2011). Increases enzyme secretion from acinar cells (Mussa and Verberne, 2008). Increases glucagon in times of hypoglycemia (Berthoud and Powley, 1990).
Sensory nervous system	E12.5 (Burris and Hebrok, 2007)	PACAP, CGRP, SP (Lkhagvasuren et al., 2021)	Intrapancreatic ganglia, islets (Lkhagvasuren et al., 2021)	Increases inflammation in diabetes and increases pain in various diseases, e.g. acute pancreatitis (Wick et al., 2006a,b).
Intrapancreatic ganglia	E10.0 (NC cells) (Plank et al., 2011)	PACAP, Galanin, GRP, NPY, VIP (Li et al., 2019) ACh (Wang et al., 1999) NA (Yi and Love, 2005) SP (Shen et al., 2016)	Intrapancreatic neurons, acinar and duct cells, islets (Li et al., 2019; Kirchgessner and Pintar, 1991).	Form the pancreatic intrinsic neuronal network (Li et al., 2019). Increase insulin secretion (Sha et al., 2001; Stagner and Samols, 1985). Decrease exocrine secretion (Jiang et al., 2011).
Enteric nervous system	N/A	ACh, GRP, Galanin, VIP, PACAP, SP, CCK, NPY (Konturek et al., 2003)	Intrapancreatic ganglia, acinar cells, islets (Kirchgessner and Gershon, 1990)	Role in nutrient-stimulated pancreatic exocrine secretion (Konturek et al., 2003).

Figure 7. Collection of evidences on the different neurochemical axis between nervous system and pancreas ACh, acetylcholine; CCK, cholecystokinin; CGRP, calcitonin gene-related peptide; GRP, gastrin-releasing peptide; MS, study in mice: N/A, not applicable; NA, noradrenaline; NC, neural crest; NO, nitric oxide; NPY, neuropeptide Y; PACAP, pituitary adenylate cyclase-activating polypeptide; SP, substance P; VIP, vasoactive intestinal polypeptide.

(Adapted from Agerskov & Nyeng, 2024)

3.1.5 Pancreas-Brain sensory crosstalk in PDAC

Several studies have shown that neurons and nerve fibers infiltrate the TME, playing a key role in the progression and metastasis of various solid tumors (W. Wang et al., 2020). In parallel, cancer cells can influence the nervous system by inducing neuronal remodeling and promoting the infiltration of neural inflammatory cells. Therefore, the communication between the nervous system and cancer is bidirectional (Capodanno & Hirth, 2023). A common feature of PDAC is perineural invasion (PNI), where cancer cells invade peripheral leading to metastasis formation (W. Wang et al., 2020). PNI occurs in 80-100% of PDAC patients and is associated with poor prognosis and reduced survival (Mardelle et al., 2024). It also contributes to high recurrence rates and causes severe pain (Li J. et al., 2021). PNI is mediated by various signaling molecules released by both cancer cells and nerves (W. Wang et al., 2020). Overexpression of the chemokine CX3CL1 and its receptor CX3CR1 is linked to PNI and post-surgical recurrence. Semaphorin 3D (SEMA3D) released by cancer cells activates Plexin D1 (PLXND1) located on dorsal root ganglion (DRG) neurons, enhancing the migration of PDAC cells in patients with PNI (Ni B. et al., 2023; Fig. 8).

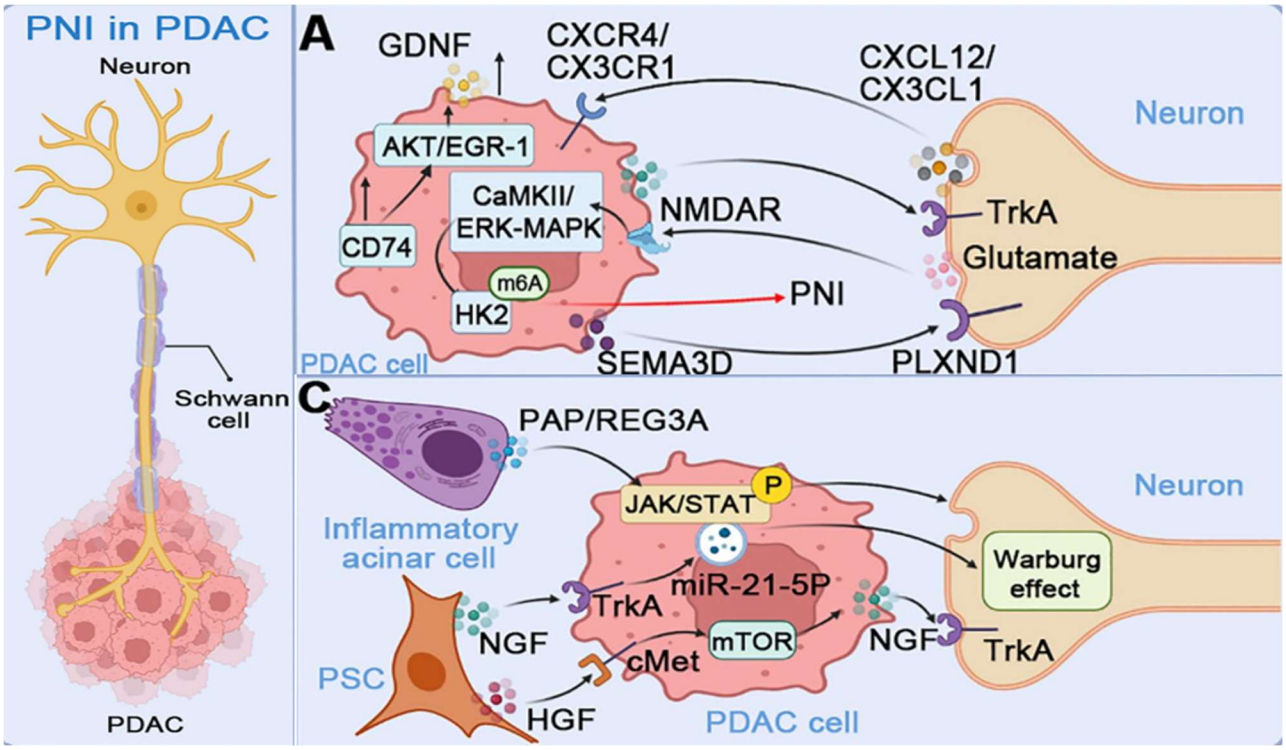


Figure 8. PNI in PDAC. **A** Direct interaction between PDAC cells and neurons in PNI. The neurogenic chemokines CXCL12 and CX3CL1 promote tumor cell invasion of nerves through their respective receptors CXCR4 and CX3CR1. Glutamate from neurons up-regulates HK2 expression through NMDAR2B and mRNA m6A modification of downstream Ca2+-dependent CaMKII/ERK-MAPK pathways, enhances glycolysis in nerve cells, and ultimately promotes PNI. Tumor cell-derived SEMA3D activates PLXND1 on DRG neurons to increase the migration and invasive activity of PDAC. The upregulation of CD74 on PDAC enhances its invasive capability and GDNF secretion *via* the AKT/EGR-1 pathway, thereby enhancing PNI. **C** Role of PSCs and acinar cells in PNI. PSCs induce PDAC cells to produce miR-21-5P exosomes through the NGF-TrkA axis, which further augments the Warburg effect of neurons and promotes PNI. HGF from PSCs activates the mTOR-NGF pathway through the c-Met receptor on PDAC cells, which boosts PNI. The pancreatitis associated protein (PAP/REG3A) produced by inflammatory acinar cells in the microenvironment around the tumor promotes PNI by activating the JAK/STAT signalling pathway in PDAC. Abbreviations: PDAC, pancreatic ductal adenocarcinoma; NGF, nerve growth factor; Trk, tropomyosin receptor kinase; HK2, hexokinase 2; NMDAR2B, N-methyl-d-aspartate receptor subunit 2B; HGF, hepatocyte growth factor; IM, inflammatory monocytes; CTSB, cathepsin B; MMP, matrix metalloproteinase; PLXND1, Plexin D1; SEMA3D, Semaphorin 3D; GDNF, glial cell line-derived neurotrophic factor; PNI, perineural invasion; TIMP1, tissue inhibitor of metalloproteinases 1; PSC, pancreatic stellate cells; PAP, pancreatitis-associated protein; REG3A, regenerating islet-derived protein 3 alpha

(Adapted from Wang W. et al., 2020).

Sympathetic nerves are associated with tumor progression mediated by stress. Stress has been shown to increase β-adrenaline levels, which activates the NGF-BDNF/Trk pathway in a β2-adrenergic receptor (ADRB2)-dependent manner, leading to acinar-to-ductal metaplasia (ADM) and, subsequently, to PDAC tumorigenesis (J. Wang et al., 2021). PNI progression is also promoted by norepinephrine (NE) through the β-AR/PKA/STAT3 pathway, which upregulates the expression of nerve growth factor (NGF) and matrix metalloproteinases (MMPs). NGF drives the axonogenesis of tumor-associated nerves by acting on tyrosine receptor kinase A (TRKA), while MMPs degrade the extracellular matrix (ECM) surrounding both tumor and nerve tissue (Wang W. et al., 2020; Fig. 9).

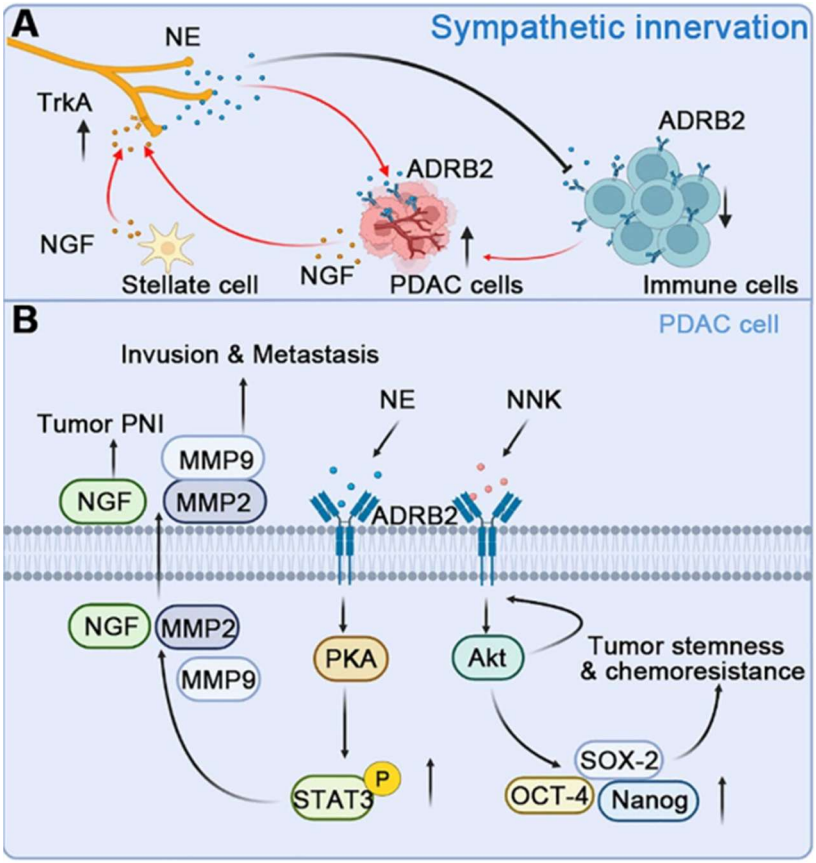


Figure 9. Sympathetic innervation and signaling pathways between NE and PDAC cells. **A** PDAC cells and pancreatic stellate cells release NGF to act on the TrkA receptors on the sympathetic nerve and promote the sympathetic innervation of the tumor. On the contrary, the neurotransmitter NE released by the sympathetic nerve promotes the proliferation of tumor cells through the ADRB2 receptors on tumor cells and endothelial cells and inhibits immune function by binding to receptors on immune cells to promote tumor progression. **B** The combination of NE and ADRB2 activates the downstream PKA-STAT3 signaling pathway, increases the phosphorylation level of STAT3, and promotes the release of

NGF, MMP2, and MMP9 from tumor cells. Activation of ADRB2 by NNK triggers the downstream Akt pathway which in turn increases the expression of ADRB2. The levels of OCT-4, SOX-2, and Nanog are also up-regulated and thus promote the tumor stemness and chemoresistance of PDAC. Abbreviations: PDAC, pancreatic ductal adenocarcinoma; NE, norepinephrine; NGF, nerve growth factor; TrkA, tropomyosin receptor kinase A; ADRB, β-adrenergic receptor; MMP, matrix metalloproteinase; NNK, 4-(methylnitrosamino)-1-(3-pyridyl)-1-butanone; OCT-4, octamerbinding transcription factor-4; SOX-2, SRY-Box transcription factor 2 (Adapted from Wang W. et al., 2020).

The role of parasympathetic nerves appears to be conflicting. Overexpression of cholinergic receptors has been found in PDAC, and high parasympathetic nerve density is correlated with early recurrence (L. Zhang, et al., Cancer Res. 2016; L. Zhang, Xiu, et al., OncoTargets and Therapy). However, different studies focused on vagotomy in tumor-bearing mice have yielded opposing results. Yang and colleagues showed a reduction in PNI and a consequent increase in survival, while Renz and colleagues showed an acceleration of PDAC tumorigenesis (Renz, Takahashi et al., 2018; Yang et al., 2020). These findings suggest that parasympathetic innervation may have distinct roles during different stages of PDAC progression (Ni B. et al., 2023; Fig.10).

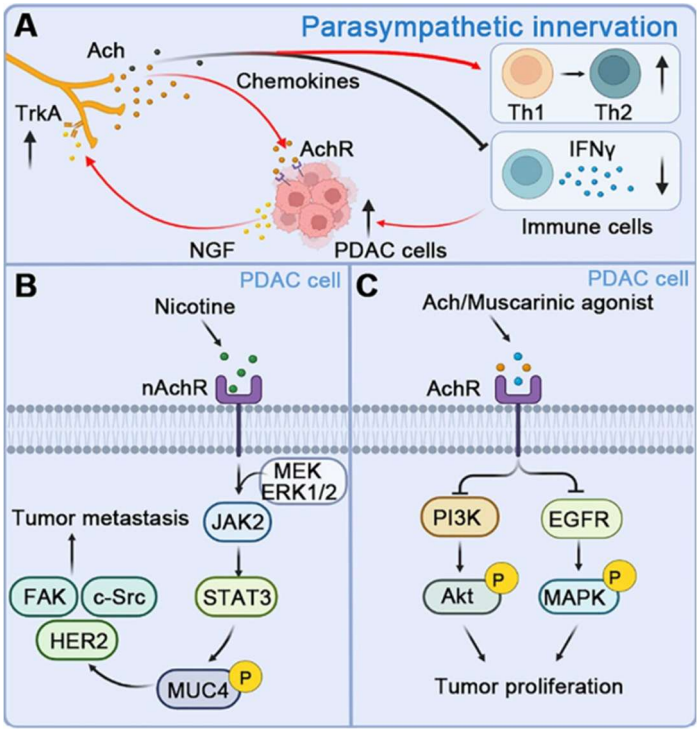


Figure 10. Parasympathetic innervation and crosstalk with PDAC cells. **A** PDAC cells release the neurotrophic factor NGF, which combines with TrkA on the parasympathetic nerve and promotes the proliferation of the parasympathetic

nerve and the innervation of PDAC, resulting in an increase in the level of acetylcholine (ACh) and promotes the growth of PDAC cells. In addition, parasympathetic nerves can also promote the transformation of Th1 to Th2 immune cells by releasing chemokines and inhibiting the release of IFNγ from CD8 + T cells, resulting in immunosuppression. **B** The activation of the α7 subunit of nAChRs by nicotine increases the expression of MUC4 through JAK2/STAT3 downstream signaling and in cooperation with the MEK/ERK1/2 pathway. MUC4 upregulation further promotes the metastasis of PDAC *via* the activation of downstream effectors, such as HER2, c-Src, and FAK. **C** Activation of ACh receptors by muscarinic agonists inhibits downstream EGFR/MAPK and PI3K/ AKT signaling pathways and inhibits the proliferation of PDAC cells. Abbreviations: PDAC, pancreatic ductal adenocarcinoma; NGF, nerve growth factor; TrkA, tropomyosin receptor kinase A; nAChR, nicotinic acetylcholine receptor; ACh, acetylcholine (Adapted from Wang W. et al., 2020).

Sensory nerves serve multiple functions in their interactions with PDAC cells, especially at the level of DRG. DRG neurons support the development of PNI by releasing various molecules such as neurotrophins, glial cell line-derived neurotrophic factors (GDNF), and chemokines. Specifically, GDNF promotes the migration of PDAC cells by recruiting the RET proto-oncogene, which activates pathways such as ERK, JNK, p38 MAPK, and PI3K/AKT (J. Wang et al., 2021). DRG neurons also influence tumor metabolism by supplying serine to the nutrient-poor TME of PDAC, thereby providing essential metabolic support (J. Li et al., 2021, Fig.11).

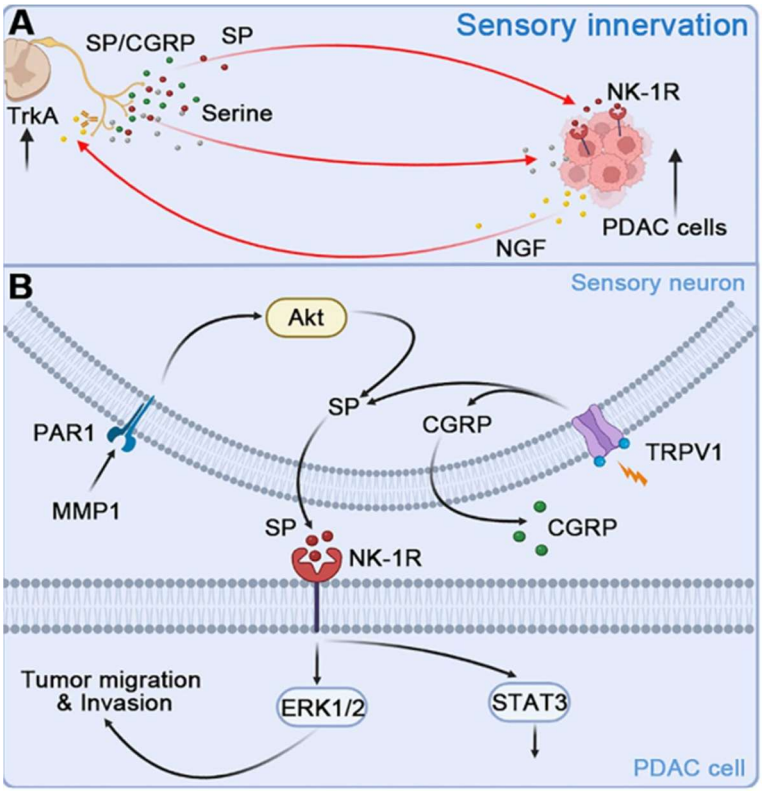


Figure 11. Molecular mechanisms by which sensory neurons promote PDAC progression. **A** PDAC cells release NGF, promote the sprouting of sensory nerves *via* TrKA, resulting in increased levels of CGRP and SP, and promote the growth of PDAC cells by binding to the SP receptors NK-1Rs on tumor cells. Sensory nerves also secret exogenous serine to maintain the survival of PDAC. **B** TRPV1 is activated by the acidic environment of TME, resulting in the increasing release of SP and CGRP from nociceptive neurons. MMP1 binding to its receptor PAR1 in DRG neurons mediates PNI of PDAC cells by activating the Akt pathway and induces the release of SP. SP promotes the migration, invasion, and PNI of PDAC cells through NK- 1Rs by the activation of downstream ERK signaling. It also fuels the progress of PanIN by activating the STAT3 signaling pathway. Abbreviations: PDAC, pancreatic ductal adenocarcinoma; NGF, nerve growth factor; TrkA, tropomyosin receptor kinase A; NK-1R, neurokinin 1 receptor; CGRP, calcitonin gene-related peptide; SP, substance P; TME**,** tumor microenvironment; TRPV1, transient receptor potential vanilla 1; PAR1, protease-activated receptor-1; MMP, matrix metalloproteinase; PanIN, pancreatic intraepithelial neoplasms. PNI, perineural invasion (Adapted from Wang W. et al., 2020).

Overall, apart from blood and lymphatic vessels, evidence indicates that neurogenesis (increased number of neurons) and axonogenesis (tumor-induced neural sprouting toward the tumor microenvironment) also play a vital role in tumorigenesis and cancer progression. Studies have reported that neurogenesis and axonogenesis are present in pre-neoplastic lesions and probably

contribute to the initiation of cancer as an early event of the pre-malignant phase (Wang W. et al., 2020; Mauffrey P. e t al., 2019; Ayala GE et al, 2008; Fig.12, Fig.7).

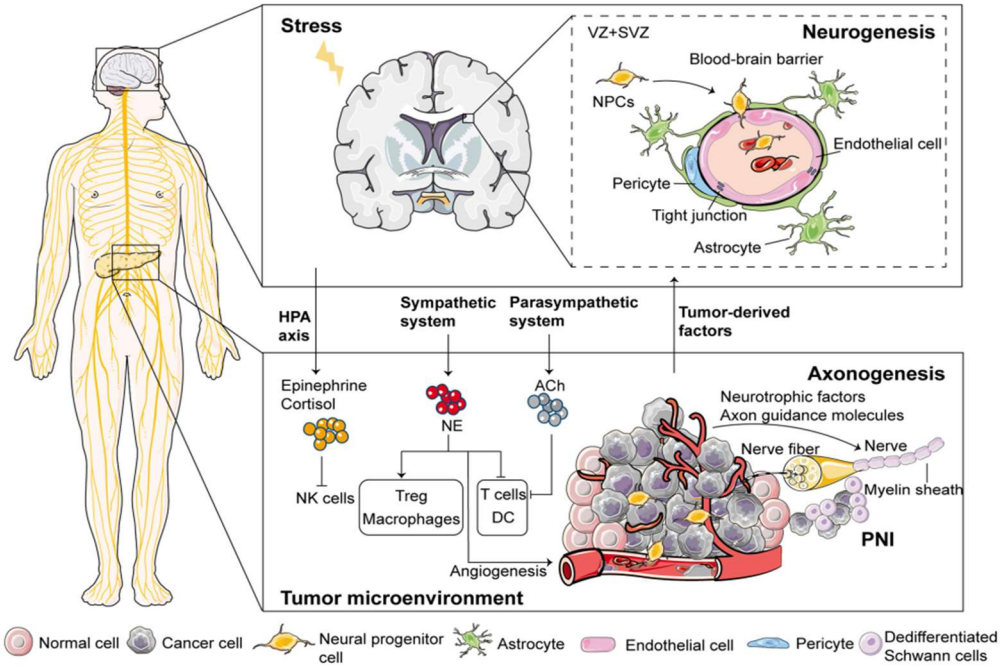


Figure 12. Proposed mechanisms involved in the emergence of nerves in the tumor microenvironment. Regarding neurogenesis (i.e., increased number of neurons), the neural progenitor cells (NPCs) leave the subventricular zone (SVZ) and egress into circulation through the disrupted blood-brain barrier during cancer development. After reaching and infiltrating the primary tumor or metastatic tissues, these NPCs differentiate into new adrenergic neurons, which regulate tumor growth and metastasis. For axonogenesis (i.e., tumor-induced neural sprouting toward the tumor microenvironment), cancer cells and some stromal cells can enhance neuronal outgrowth and initiate tumor innervation through multiple mechanisms. Sympathetic nerves release NE while parasympathetic nerves release ACh in the tumor microenvironment, and are, therefore, involved in modulating immune responses. Moreover, stress regulates immune responses through two major neural pathways; the HPA axis and the sympathetic nervous system. Schwann cells can act as leading cells that actively dissociate, recruit, and guide cancer cells to neurites through heterocellular contact, thereby, leading to PNI. VZ, ventricular zones (Adapted from Wang W. et al., 2020)

3.1.6 Neuroimmune interactions in pancreatic cancer

Neuroimmunology studies to date have tended to focus on interactions between nerves and immune systems at the local level. Peripheral neuroimmune interactions critically regulate systemic and local tissue immunity. Novel data show that the immune system and nervous system play mutual roles in

the body and are essential in immune, metabolism-related, neoplastic, and other diseases (Veiga-Fernandes et al., 2016; Veiga-Fernandes et al., 2017; Pavlov et al., 2018). With its neuroimmunological properties, the pancreas is richly supplied with neuronal connections that mediate crucial physiological activities. In addition, pancreatic draining lymph nodes have pancreatic innervation and exert some immunomodulatory effects (Guyot et al., 2019). Notably, research on pathogenesis and therapeutic options for treating pancreatic ductal adenocarcinoma (PDAC), including recently identified local forms, from the viewpoint of crosstalk of the neuroimmune network and intervention techniques is at the cutting edge. Current evidence reveals the neuroimmune crosstalk occurring in PDAC, explaining the role of interactions between different types of nerve and immune cells in PDAC in terms of tumor formation, development, and metastasis (Yang et al., 2020; Guillot et al., 2022;). Importantly, these neuroimmune interactions have significant clinical implications. Studies have shown that neural invasion and neuroimmune signalling contribute to the immunosuppressive tumor microenvironment, which may explain the poor prognosis and limited therapeutic efficacy observed in PDAC patients. These findings underscore the potential of neuroimmune research to translate into novel therapeutic approaches that address the unmet clinical needs in PDAC.

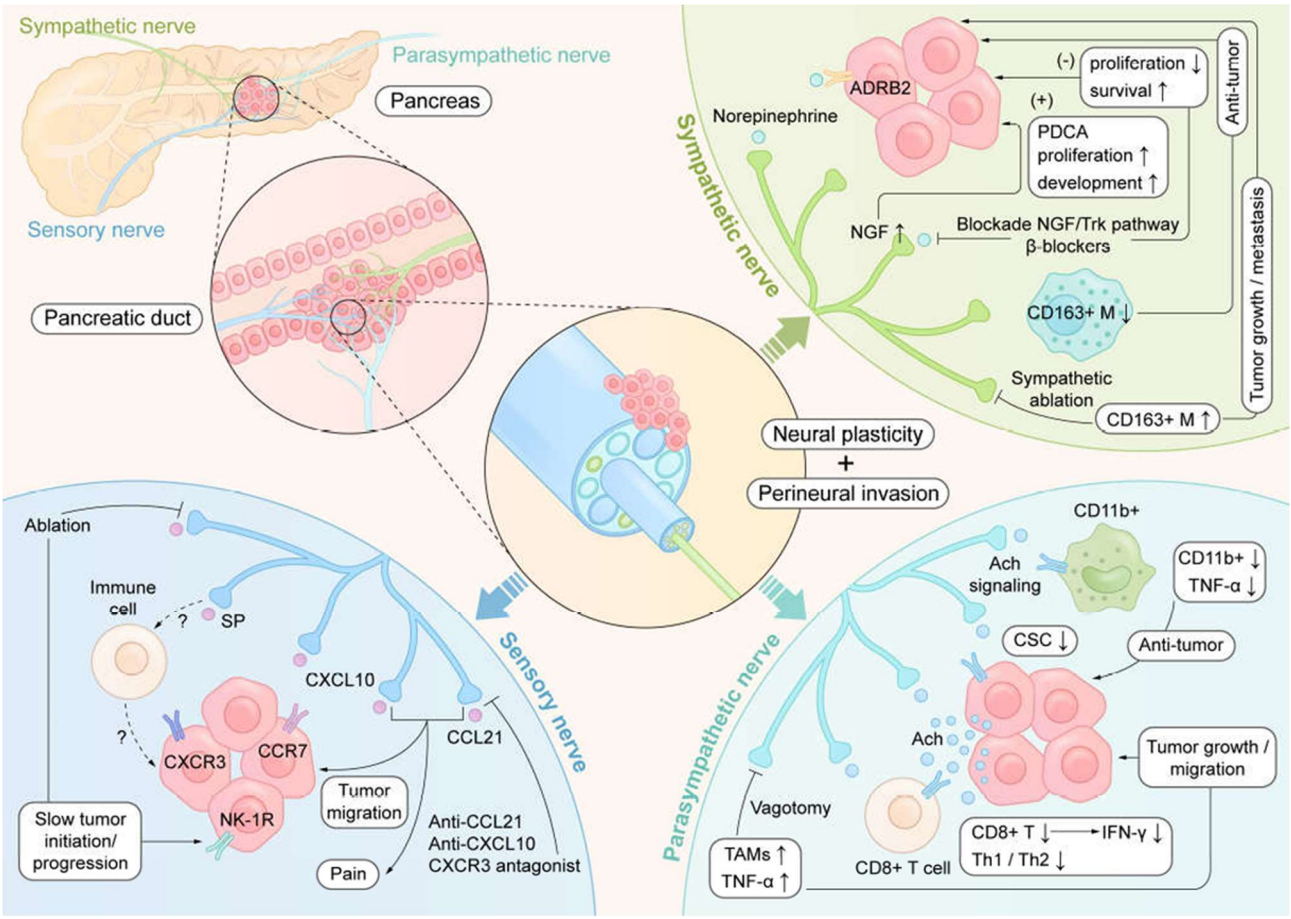


Figure 13 The schematic illustrates the complex interplay between sympathetic nerves, parasympathetic nerves, sensory nerves, and immune cells within the tumor microenvironment of pancreatic ductal adenocarcinoma (PDAC). Key interactions include: ***(1) Sympathetic nerve signalling*** via adrenoceptor beta 2 (ADRB2) and its role in tumor progression (Renz, Takahashi et al., 2018); ***(2) Parasympathetic nerve signalling*** via acetylcholine (Ach) and its impact on cancer stem cell (CSC) activity (Partecke et al., 2017); ***(3) Sensory nerve involvement*** through substance P (SP) and neurokinin-1 receptor (NK-1R) pathways, which promote tumor migration and immune modulation (Stopczynski et al., 2014). Ach, acetylcholine; IFN-γ, interferon-γ; TAMs, tumor-associated macrophages; TNF-α, tumor necrosis factor-α; NGF, nerve growth factor. Adapted from Cheng J. et al, 2025.

Neuroimmune crosstalk, which can serve as a crucial immunomodulatory hub, has been reported in both healthy and disease states. Accumulating data support the concept that neural circuits, including somatosensory and autonomic divisions, mediate host defense strategies through direct influence on immune regulation and inflammatory pathways in peripheral systems (Ordovas-Montanes et al., 2015; Guyot et al., 2019; Cheng J. et al, 2025). Neuroimmune regulation is related to neoplastic

diseases and plays a specific role in the occurrence and development of tumors. For example, in a mouse model of triple-negative breast cancer, sciatic nerve stimulation can inhibit tumor growth by activating natural killer cells in the tumor microenvironment; likewise, the sympathetic nervous system can maintain the inflammatory microenvironment and promote the occurrence of hepatocellular carcinoma by activating the a1-adrenergic receptors of Kupffer cells (Li G. et al., 2025; Huan et al., 2017). In pancreatic cancer, nerves are significantly infiltrated by cytotoxic T lymphocytes, macrophages, and mast cells, which account for 35%, 39%, and 21%, respectively, of all perineural inflammatory cells, and perineural invasion can induce neuronal damage and inflammation (Demir et al., 2013; Saloman et al., 2016). Colocalization of nerve and immune cells may affect nerve and immune functions, and this neuroimmune regulation may lead to changes in disease. The neuroimmune interactions occurring in PDAC at the peripheral nerve level, including the regulation of immune cells and sympathetic, parasympathetic, and sensory nerves, are summarized in Figure 13: neuroimmune interactions are emerging as key therapeutic targets in PDAC, yet critical gaps persist. First, mechanisms driving dynamic neuroimmune crosstalk—especially during metastatic transition—remain unclear. Second, clinical translation is hindered by unproven long-term efficacy/safety of interventions like neural ablation or neurotransmitter blockade. Key priorities include spatiotemporal mapping, patient-specific targeting, nerve-stromal reprogramming, and so on.

3.2 Modelling PDAC in laboratory

3.2.1 in vitro models: pancreatic organoids

Organoids are 3D cellular models capable of self-renewing and self-organizing into differentiated cells that recreate the corresponding organ of origin (Huch et al., 2017). They can be generated either from embryonic stem cells (ESCs), adult stem cells (ASCs), and/or induced pluripotent stem cells (iPSCs). Organoids derived from ASCs are generated from adult tissues and can be used for disease modelling using patient-derived materials. To grow, they require a cocktail of growth factors that

recreates the signaling environment of the original tissue. Organoids derived from ESCs or iPSCs are generated through a process involving multiple differentiation steps, aided by the addition of growth factors or inhibitors that mimic the signals guiding development during gastrulation and organogenesis (Corrò et al., 2020). Organoids are prepared in suspension, avoiding direct contact with the culture dish. They can be produced using scaffold or scaffold-free techniques. Scaffolds are biological or synthetic hydrogels that mimic the natural extracellular matrix (ECM), with Matrigel being the most commonly used (Orkin et al., 1977). Scaffold-free techniques include culturing cells in medium droplets that hang from a plate, and the "air-liquid interface" method, where cells are grown on a basal layer of fibroblasts or Matrigel, submerged in medium that gradually evaporates (Timmins & Nielsen, 2007; Turner et al., 2016). The applications of organoids are numerous, including development and disease modelling, precision medicine, toxicological studies, biobank creation, and regenerative medicine (Corrò et al., 2020; Fig. 14).

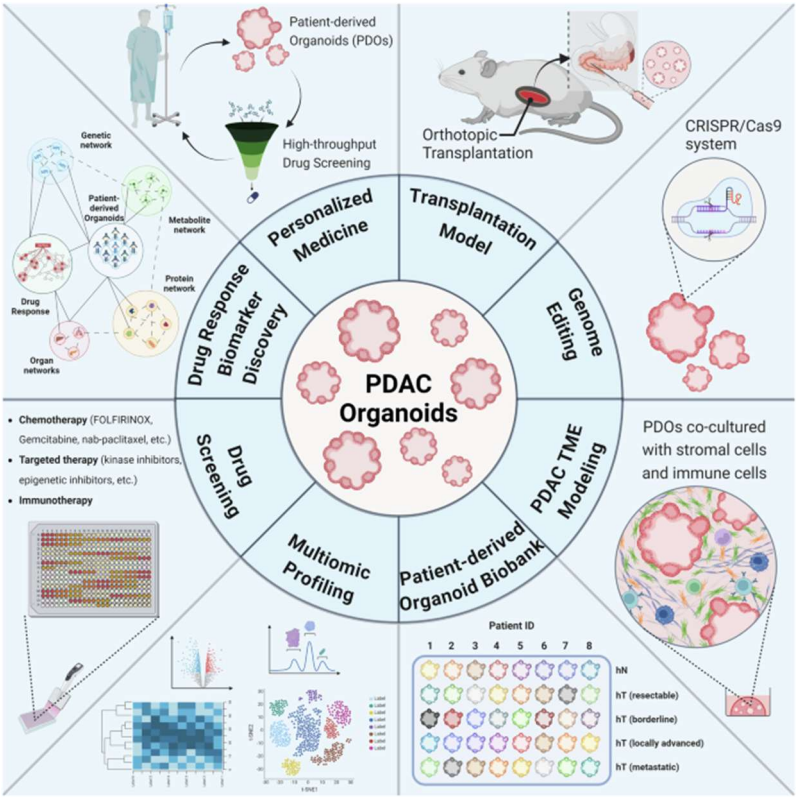


Figure 14. Current PDAC organoid applications (From Xu J. et al., 2025)

In cancer research, the development of organoids from patient-derived ASCs has allowed the generation of tumor organoids for various types of cancer, such as those of the brain, breast, prostate, pancreas, and many others (Kretzschmar, 2021).

Concerning the pancreas, organoids for PDAC can be obtained from both mice and humans using fetal progenitor cells, adult ductal cells, and PSCs. Some organoids have also been created from pancreatic islet and acinar cells (Grapin-Botton & Kim, 2022). However, it has been observed that only ductal cells are capable of forming organoids that can be maintained long-term in vitro, while acinar cells cannot (Casamitjana et al., 2022). Patient-derived organoids can be developed from all stages of PDAC progression by isolating surgically resected tumors or material obtained through biopsies (Tiriac et al., 2019). PDAC organoids can also be transplanted into immunodeficient mice, where they show the ability to develop PanINs capable of progressing into PDAC with metastasis (Yao et al., 2021). Organoids have proven to be superior models for studying PDAC and evaluating drug treatments compared to traditional models, such as 2D cultures, genetically engineered mouse models (GEMMs), and patient-derived xenografts (PDXs) (Balak et al., 2019). This is due to their ease of pharmacological testing, predictive value for early PDAC diagnosis, and stability in maintaining characteristics shared with the original tumor. However, their application to PDAC is still in its early stages, and they present several disadvantages. In particular, they are costly and time-consuming to produce, and development protocols are not standardized, resulting in a lack of reproducibility. Furthermore, PDAC organoids are unable to replicate many components of the TME, such as fibroblasts, endothelial cells, immune cells, and neural crest cells (Yao et al., 2021).

3.2.2 in vivo models: the KPC mouse

Genetically engineered mouse models (GEMMs) are important tumor models created by introducing genetic mutations that activate or silence specific oncogenes and tumor suppressor genes, which play a fundamental role in the context of certain tumors. They are particularly relevant as preclinical models for evaluating the development of new therapeutic treatments and for studying the biology of

human diseases. Additionally, they provide an excellent alternative to xenograft models, as they accurately reproduce the genetic and phenotypic complexity of tumors and possess a complete immune system (Gopinathan et al., 2015).

Among the various types of GEMMs created over the years, the Lox-Stop-Lox (LSL)- $Kras^{G12D}$; LSL-$Trp53^{R172H}$; Pdx1-Cre (KPC) model is the most commonly used for PDAC (Low et al., 2021). KPC mice are characterized by the presence of the mutant alleles $KRAS^{G12D}$ and $TP53^{R172H}$, both preceded by a Lox-Stop-Lox (LSL) cassette. The expression of both genes is controlled by a Cre recombinase driven by a pancreas-specific promoter, such as Pdx-1. In the presence of Cre, the LSL cassettes are removed, allowing for gene expression in the pancreas (Gopinathan et al., 2015; Fig. 15).

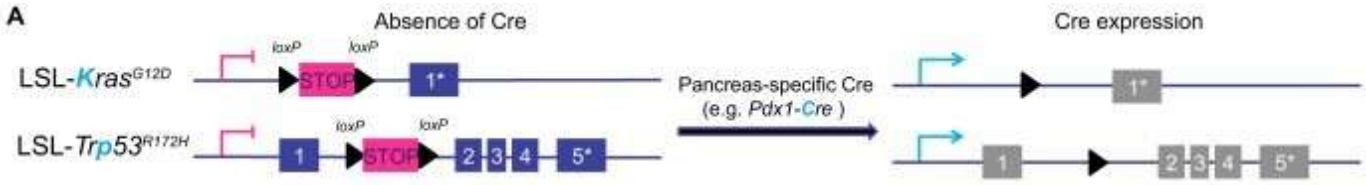


Figure 15. Cre recombinase system in KPC mice (Adapted from Gopinathan et al., 2015)

This system can be made inducible by using tamoxifen-dependent Cre recombinase. Achieving this involves the use of Cre-ER, a Cre recombinase fused to the ligand-binding domain of the estrogen receptor (ER). This allows the expression of genes controlled by Cre-ER to be induced at a desired time by administering tamoxifen to the mice. Tamoxifen is an agonist of the estrogen receptor. Once injected, it is metabolized to 4-OHT, which binds to Cre-ER, allowing it to translocate to the nucleus and remove the LSL cassette (Chen M.-Y. et al., 2023).

KPC mice develop spontaneous tumors very rapidly, with a penetrance of 90%. They are capable of developing early PanIN lesions that progress to advanced PDAC with metastasis and recapitulate the TME of human PDAC. For these reasons, they represent excellent models for studying the pathogenesis of PDAC and evaluating immunotherapies (Mallya et al., 2021).

Despite their numerous advantages, KPC mice also have limitations. In particular, their maintenance requires time and financial resources, and advanced imaging equipment is necessary to monitor tumor

progression (Chen H. et al., 2021). Additionally, in some cases the tissue-specific promoters used may lead to off-target pathologies (Gopinathan et al., 2015).

3.2.3 Architecture of the pancreatic tissue: main differences between mouse and human

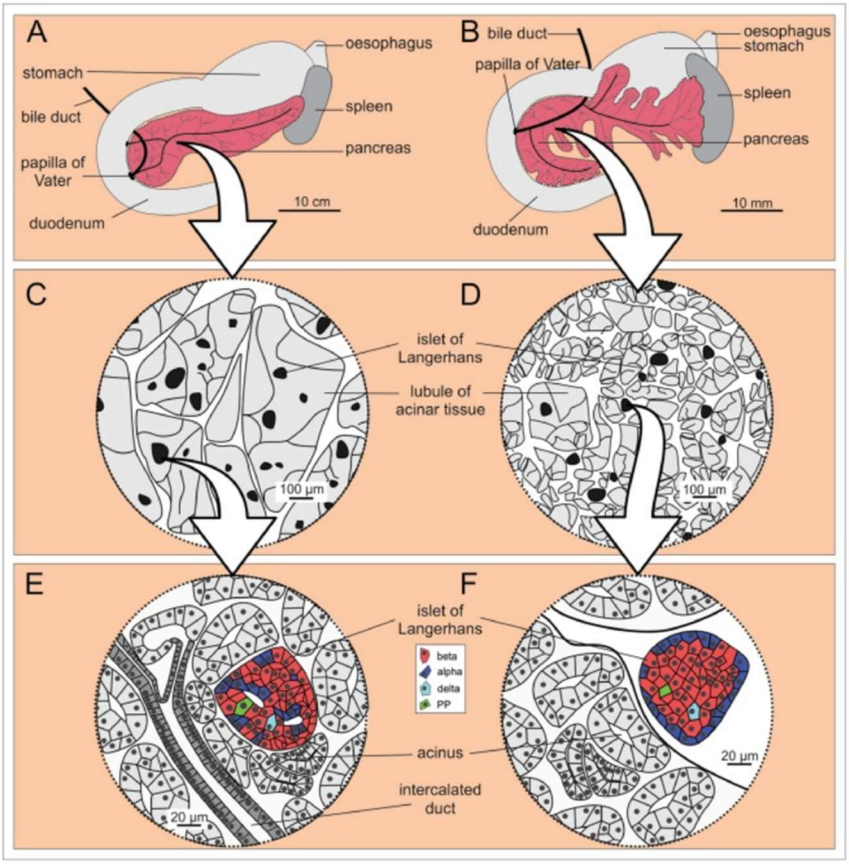


Figure 16. Microscopic anatomy of human (A,C,E) and mouse (B,D,F) pancreas. (A,B) Macroscopic anatomy of human and mouse pancreas, respectively. (C,D) Enlargement of a portion of the pancreas shows that the lobules are larger in humans than in mice, whereas the islets of Langerhans are of comparable size in humans and mice. (E,F) The cell composition and location of the islets of Langerhans within the pancreas are markedly different in the two species. Note the more diffusely distributed endocrine cells in humans (E) and the mantle-core pattern in mice (F). From Milojević M et al., 2021

When utilizing mouse models to investigate human pancreatic diseases, it is essential to consider the anatomical and histological differences between the human and murine pancreas. The human pancreas is a relatively compact organ, while the mouse pancreas presents a more diffuse architecture.

In mice, the pancreas is divided into three distinct lobes: the duodenal, splenic, and gastric lobes (Dolenšek et al., 2015). The splenic lobe, the largest of the three, is analogous to the body and tail of the human pancreas. The gastric lobe is a smaller appendage of the splenic lobe, and the duodenal lobe corresponds to the head of the human pancreas. Both the exocrine and endocrine compartments of the pancreas exhibit interspecies differences. In humans, the exocrine pancreas is organized into lobules composed of acini—clusters of acinar cells—that drain into intercalated ducts. These ducts converge into progressively larger ducts and ultimately empty into the main pancreatic duct (duct of Wirsung). This duct, in conjunction with the common bile duct, releases its contents into the duodenum via the ampulla of Vater (Horiguchi & Kamisawa, 2010). In mice, the drainage system involves a large interlobular duct that collects secretions from the three lobes. The splenic and gastric ducts merge early with the common bile duct, while the duodenal duct joins the system later, just before entering the duodenum (Higashiyama et al., 2016; Fig. 16). The endocrine pancreas also differs markedly between species. In mice, the islets of Langerhans are more heterogeneously distributed and structurally simpler than in humans (Dolenšek et al., 2015). Nerve distribution patterns further distinguish the human and murine pancreas. In the mouse, nerve trunks are primarily located around blood vessels and intrapancreatic lymph nodes; notably, interlobular septae are devoid of nerve fibers. The highest nerve density is observed in the head of the pancreas, including a greater abundance of nociceptive fibers marked by substance P, a neuropeptide involved in pain transmission (Saricaoglu et al., 2020). In humans, nerves similarly enter the pancreas following blood vessels, though detailed characterization of their relationship with lymph nodes remains limited. Functionally, sympathetic innervation in humans is closely associated with exocrine tissue and vasculature, exerting an inhibitory influence on both acinar and ductal secretion. In contrast, murine acinar cells receive only sparse sympathetic input. Conversely, sympathetic fibers minimally innervate human islets, whereas in mice, they form a neurovascular complex by directly contacting α cells and encircling adjacent arterioles (Chiu et al., 2012).

3.3 Single Cell RNA sequencing applied on peripheral nervous system

3.3.1 General overview of a scRNA seq experiment

Single-cell RNA sequencing (scRNA seq) is a recently developed technology that enables unbiased, high-resolution, and high-throughput transcriptomic analysis of individual cells. This allows for additional transcriptomic insights compared to traditional bulk RNA seq methods (Kolodziejczyk et al., 2015). In oncology, scRNA seq has led to significant advancements in studying intra-tumoral heterogeneity and therapeutic resistance (Seow et al., 2020). Its ability to analyze intra-tumoral heterogeneity at single-cell resolution has made it a popular technology in recent years, aiding in the optimization of therapeutic strategies and the identification of rare cell populations resistant to treatments (Li X. & Wang, 2021). Since the advent of the first scRNA seq in 2009, multiple scRNA seq techniques have been developed. However, all these techniques share a common workflow: preparation of single-cell suspensions, capture and lysis of individual cells, reverse transcription and amplification, library preparation, sequencing, and subsequent analysis (Lv G. et al., 2023; Fig. 17). Generally, the starting material for scRNA seq comes from biological tissue samples that are digested to obtain single-cell suspensions (Luecken & Theis, 2019). Digestion occurs through mechanical or enzymatic stress, depending on the sample type. This is followed by cell capture to isolate single cells into individual spaces where they are lysed (Van De Sande et al., 2023). Various methods can be used for this purpose. Low-throughput, time-consuming methods include micropipetting and laser capture microdissection (LCM) (Kolodziejczyk et al., 2015). High-throughput methods include plate-based techniques, in which cells are isolated in wells, and droplet-based techniques, where cells are isolated in microfluidic droplets (Lv G. et al., 2023). After cell capture and lysis, the next step involves reverse transcription of mRNA into cDNA and subsequent amplification via PCR or in vitro transcription (IVT). This is a crucial step as it ensures greater sensitivity in scRNA-seq (Zhang Y. et al., 2021). PCR is a nonlinear amplification process that depends on the amplified sequence. IVT is a linear amplification process, but it requires an additional reverse transcription step, which can lead to a 3’ coverage bias (Kolodziejczyk, 2015). Before sequencing, the resulting cDNA is fragmented to obtain

a homogeneously sized pool of transcripts, and barcode sequences are added to trace the origin of the reads (Van De Sande et al., 2023). Cell-specific barcodes are used to multiplex cells before sequencing, allowing for the identification of the cellular origin of each mRNA. Multiplex sequencing increases throughput and reduces reagent usage (Zhang Y. et al., 2021). Unique molecular identifiers (UMIs) can also be used to identify each mRNA molecule from each individual cell, allowing recognition of transcript copies resulting from reverse transcription and amplification of each mRNA (Kolodziejczyk et al., 2015).

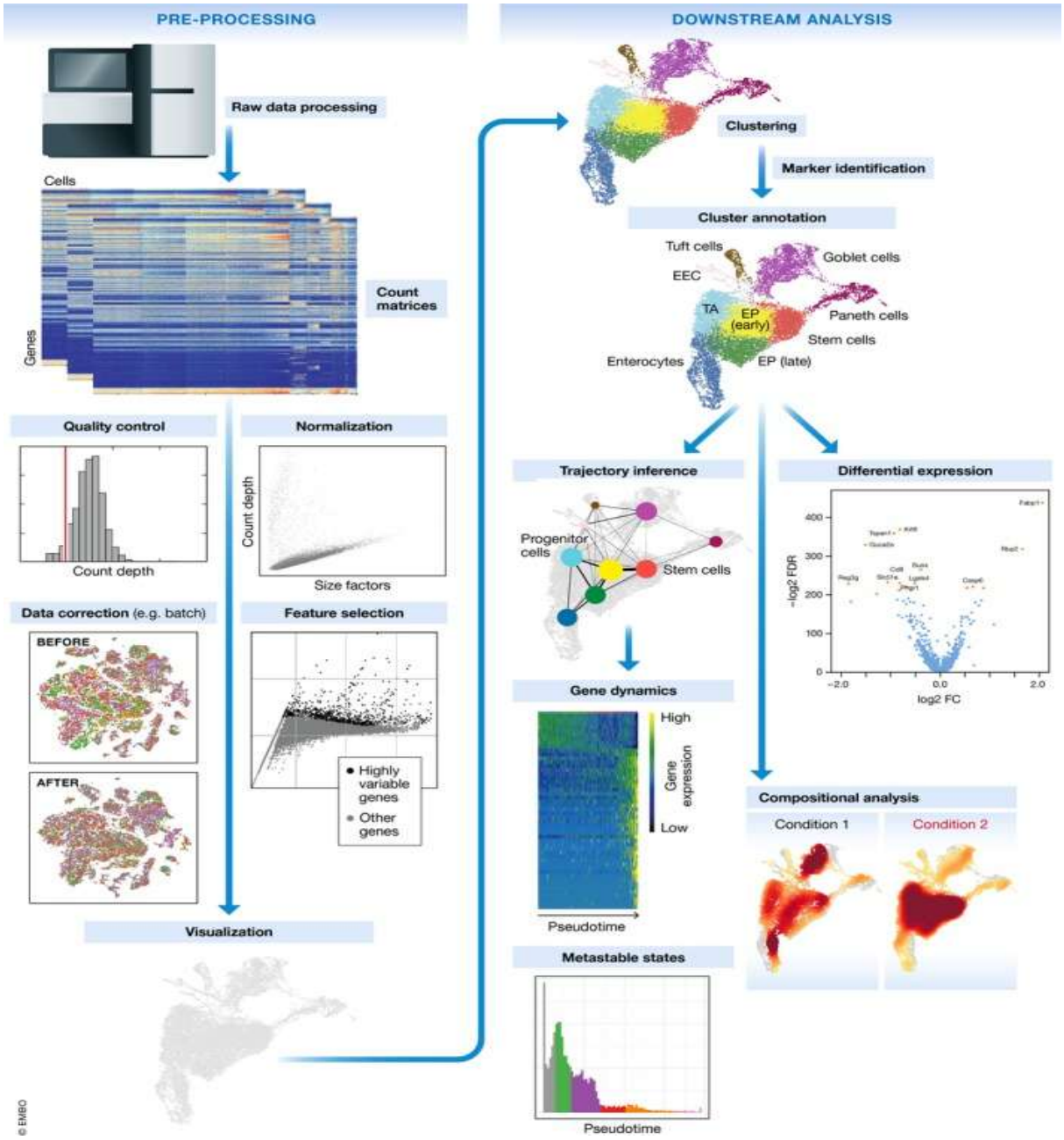


Figure 17. General workflow of single-cell RNA sequencing (from Luecken & Theis, 2019)

Sequencing can be performed using either full-length or tag-based protocols. In full-length protocols, the entire mRNA transcript is sequenced, whereas in tag-based protocols, only the 5' or 3' regions of mRNA are amplified (Lv G. et al., 2023). In this work, the Smart-seq2 method was used, a full-length protocol developed by Picelli and colleagues that employs the Moloney murine leukemia virus (M-MLV) template switching method for reverse transcription (Fig.18). To achieve this, the cell lysis solution must contain tailed oligo-dT oligonucleotides, which allow the primers in the reverse transcription reaction to anneal to polyadenylated mRNA sequences. Template switching occurs through the presence of template switch oligonucleotides (TSO) containing a locked nucleic acid (LNA) that enables the M-MLV reverse transcriptase to synthesize a complementary sequence to the TSO. cDNA amplification is performed via PCR, followed by tagmentation for library preparation and Illumina sequencing (Picelli et al., 2014).

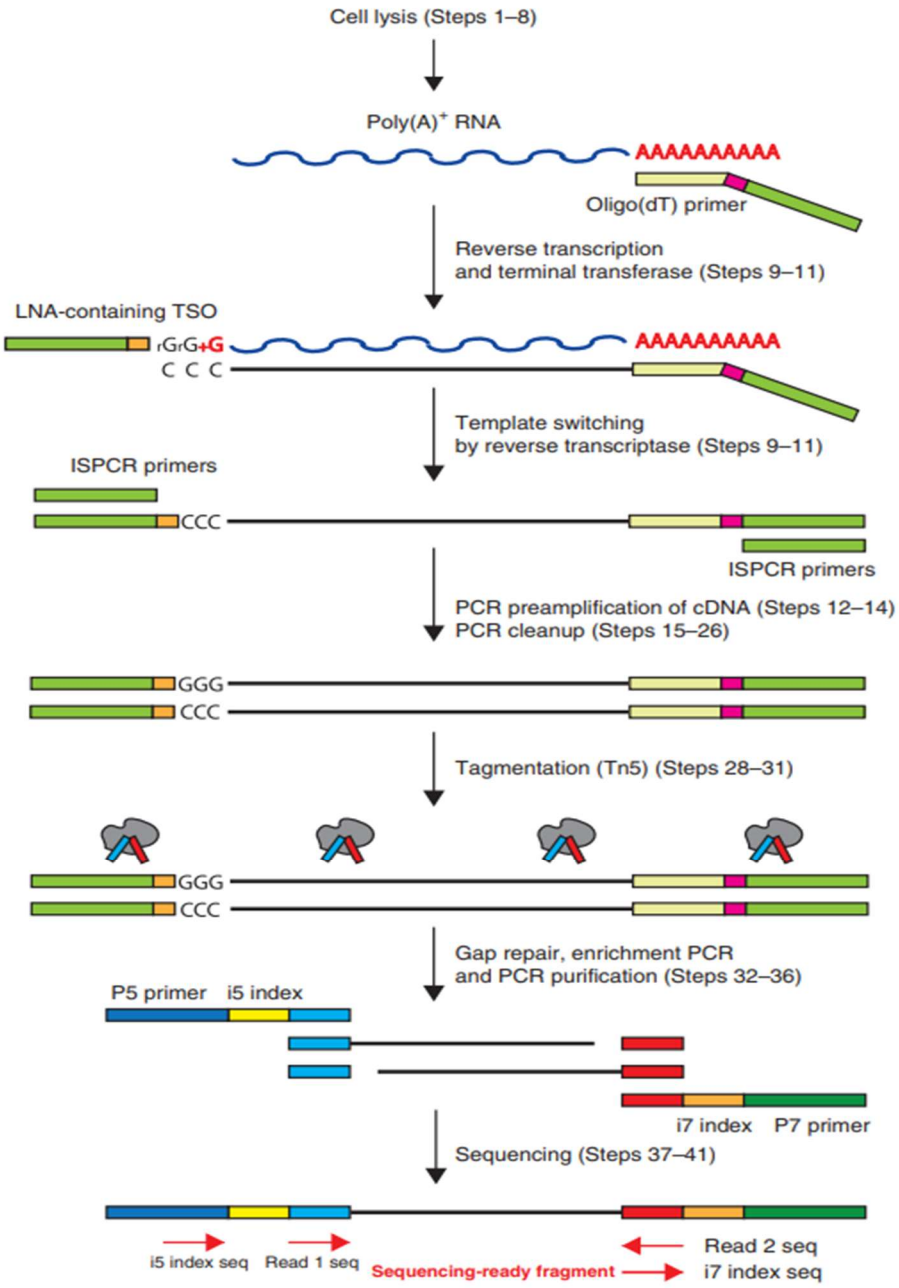


Figure 18. Workflow of Smart-seq2 protocol (Picelli et al., 2014)

Finally, the read data obtained from sequencing are subjected to various types of analysis, including quality control, barcode-based clustering (demultiplexing), and alignment in read processing pipelines (Luecken & Theis, 2019). These pre-processing analyses are used to count reads and filter the data. Once clean data is obtained, downstream analyses can be performed, such as unsupervised clustering to group cells with similar expression profiles, identification of marker genes associated with each cluster, and visualization of clusters in 2D or 3D (Van De Sande et al., 2023).

3.3.2 Pros & Cons of scRNA seq dataset

The technology of single-cell RNA sequencing (scRNA seq) has revolutionized transcriptomic studies, enabling gene expression analysis at single-cell resolution (Chen G.et al., 2019). Compared to traditional bulk RNA seq, scRNA seq is a precise and detailed technique that allows for the detection of rare cell populations, the study of cellular heterogeneity, and the tracking of distinct cellular lineage trajectories during development (Qi R. et al., 2020). Nonetheless, one of the major limitations of scRNA seq is the presence of high technical and biological noise, posing a significant bioinformatic challenge for data analysis. This variability stems from biases in transcript coverage, low capture efficiency, and sequencing coverage (Chen G. et al., 2019). Technical noise is also caused by the low amounts of starting material and biases associated with cDNA amplification (Kim B. et al., 2019). Additionally, computational analyses are limited by the large amount of data generated by scRNA seq protocols (Kolodziejczyk et al., 2015). For these reasons, pre-processing steps are essential to ensure good data quality for downstream analyses (Chen G. et al., 2019). Pre-processing analyses are performed on raw sequencing data to generate count matrices of molecular or read counts (Fig.17; Luecken & Theis, 2019). The resulting matrices are cell-by-gene, specifying the counts of each gene in each cell (Van De Sande et al., 2023). First, raw data processing pipelines perform read quality control, grouping reads based on cellular barcodes and UMIs (demultiplexing), genome alignment, and quantification. Cell quality control is also carried out, where cellular barcodes are filtered by setting threshold values to remove outliers, such as dead cells, cells with broken membranes, or doublets (Luecken & Theis, 2019). This filtering is based on variables such as UMI counts per cell, UMI counts per gene, and the proportion of expressed mitochondrial genes (Seow et al., 2020). Quality control is generally repeated multiple times with more or less stringent thresholds, as data quality can only be assessed based on downstream analysis results (Lv G. et al., 2023). Subsequent pre-processing steps include normalization, data correction, feature selection, and dimensionality reduction (Luecken & Theis, 2019; Fig.17). Normalization is useful to remove technical noise or biases in raw data, ensuring comparability between individual cells (Jovic D. et al.,

2022). Data correction addresses additional issues, such as batch effect, dropouts, and cell cycle effect (Luecken & Theis, 2019). Dropouts are a significant challenge, as scRNA seq protocols effectively measure the expression of only 10% of total genes, generating sparse matrices filled with many zeros (Kuksin et al., 2021). On the other hand, batch effect introduces technical variability due to the use of different methods for cell dissociation, library preparation, and sequencing (Chen G. et al., 2019). The choice of corrections to apply depends on the downstream analyses that will follow (Luecken & Theis, 2019). scRNA seq dataset matrices can contain up to 25,000 genes, so it is essential to reduce their size before performing downstream analyses. First, feature selection is conducted, filtering the dataset by selecting 1,000–5,000 highly variable genes (HVGs) (Luecken & Theis, 2019). HVGs are genes with high cell-to-cell variability, important in downstream analyses to obtain precise clusters (Jovic D. et al., 2022). Dimensionality reduction algorithms are then used to further reduce dataset size (summarization) and visualize data on a scatter plot (visualization) (Luecken & Theis, 2019). For summarization, principal component analysis (PCA) is typically used, followed by t-distributed stochastic neighbor embedding (t-SNE) or Uniform Manifold Approximation and Projection (UMAP) for visualization (Jovic D. et al., 2022). Pre-processing analyses must be conducted based on the type of downstream analysis to follow (Luecken & Theis, 2019). Downstream analyses can be cell- or gene-level. Cell-level analyses may include cell clustering and trajectory inference, while gene-level analyses may include differential gene expression and gene regulatory network inference (Cardona-Alberich et al., 2021). Clustering is a method of dividing cells into groups based on similarities in their gene expression profiles. The most widely used clustering algorithm is k-means. However, as datasets size continues to grow, community-detection-based algorithms, particularly the Louvain algorithm with K-nearest neighbour (KNN) graphs, are becoming popular (Seow et al., 2020). Clustering is followed by annotation, where marker genes characterizing each cluster are identified. This step helps determine the cellular identity of each cluster. Annotation is performed by comparing data-derived marker genes with marker genes from the literature or reference databases (Luecken & Theis, 2019). Marker genes are visualized using UMAP and heatmaps (Seow et al.,

2020). This type of annotation is manual and time-consuming. A faster alternative is automated cluster annotation, using methods capable of transferring annotations from references to the dataset (Luecken & Theis, 2019). However, this approach does not allow for the identification of rare or novel cell types (Jovic D. et al., 2022). Among gene-level analyses, differential expression (DE) analysis identifies significant changes in gene expression between two experimental conditions (Luecken & Theis, 2019). This analysis uses volcano plots or heatmaps to visualize genes that are significantly over- or underexpressed between cell groups (Kuksin et al., 2021).

In conclusion, scRNA seq has enabled major advancements in studying gene expression, significantly enhancing our understanding of biological systems. Nevertheless, scRNA seq analyses remain highly complex and lack standardization, posing a challenge for newcomers in the field (Luecken & Theis, 2019). More innovative algorithms are therefore needed to enhance reproducibility and facilitate researchers' work (Chen G. et al., 2019).

3.3.3 Transcriptomic knowledge of the mouse sensory system: state of the art.

Dorsal root ganglion (DRG) neurons detect peripheral stimuli that contribute to thermoception, mechanoception, proprioception, nociception, and pruriception, and transmit them to the central nervous system (CNS). Over the years, these neurons have mostly been classified from an anatomical perspective, and the lack of markers for their identification has hindered accurate functional classification (Xie et al., 2023): as a matter of fact, early classifications focused on broad distinctions between nociceptive and non-nociceptive neurons, such as differences in cell soma size, degree of myelination of their axons and their termination patterns, and thresholds of responses to defined stimuli. Recently, scRNA seq has allowed for a more in-depth study of the transcriptomic profiles of DRG neurons, enabling the identification of DRG neuron clusters in mice (C. Li et al., 2018). With advancements in transcriptomic profiling, more refined classifications emerged, with one of the early landmark studies in this area being conducted by Usoskin and colleagues (Usoskin et al., 2015), who used single-cell RNA sequencing of mouse DRG neurons to categorize sensory neurons into several

distinct subtypes. This molecularly driven nomenclature categorizes sensory neurons into four main types distinguished by gene expression and putative functional roles: NF neurons express neurofilament heavy chain and are associated with myelinated mechanoreceptors and proprioceptors, PEP neurons express neuropeptides like substance P and calcitonin gene-related peptide and were previously classified as peptidergic nociceptors, NP neurons correspond to non-peptidergic nociceptors, and TH neurons show expression of tyrosine hydroxylase and likely function as unmyelinated low threshold mechanoreceptors. More recently, similar studies with increased resolution have been conducted across various species to refine the classification further (Zeisel et al., 2018; Hockley JRF et al., 2019; Kupari et al., 2021; Yu H et al., 2024). This framework has facilitated the exploration of sensory neuron function in chronic pain, inflammation, and disease progression, including cancer.

In this thesis, we used as a reference the study from Usoskin and colleagues, who utilized comparable methodologies for single-cell profiling: we selected this as reference dataset over other available resources for several reasons. For example, another study by Zeisel et al. surveyed the entire mouse nervous system, lacking a dedicated emphasis on sensory neurons (Zeisel et al., 2018). Conversely, the dataset from Hockley et al. covered only thoracolumbar and lumbosacral DRGs rather than the full range of DRG populations (Hockley JRF et al., 2019). Meanwhile, a work by Kupari et al. was based on primate rather than mouse DRGs (Kupari et al., 2021). Notably, both Hockley and Kupari also referenced Usoskin's classification framework.

Usoskin's seminal work was based on a low-coverage scRNA-seq (3574 ± 2010 genes/neuron) of 799 cells derived from lumbar mouse DRGs innervating the hind limbs, in order to obtain an unbiased classification of sensory neuron types. Principal component analysis (PCA) revealed five main clusters, one of which was identified as non-neuronal and therefore excluded. Of the total cells, 622 were classified as neurons, 68 were ambiguous, and 109 were non-neuronal. After filtering out non-neuronal cells and outliers, the expression of known markers was examined in the four confirmed clusters, allowing their identity to be identified (Fig.19). The first identified cluster was the

neurofilament-containing (NF) cluster, which expressed neurofilament heavy chain (*Nefh*) and parvalbumin (*Pvalb*). The second was the peptidergic (PEP) cluster, which expressed substance P (*Tac1*), TRKA (*Ntrk1*), and calcitonin gene-related peptide (CGRP). The third was the non-peptidergic (NP) cluster, which expressed *Mrgprd* and *P2rx3*. Finally, the fourth was the tyrosine hydroxylase-containing (TH) cluster, which expressed tyrosine hydroxylase (*Th*) (Fig.19 B; Usoskin et al., 2015).Further neuronal subtypes were discovered by performing an iterative PCA on each of the four detected clusters, including only genes that were differentially expressed when compared against another subtype. From this analysis, a total of eleven subtypes were identified: NF1 to NF5, NP1 to NP3, PEP1 and PEP2, and TH (Fig.19A). A differential expression analysis of the 622 neurons was then performed to determine the expression patterns that characterized each cluster and verify if they matched previous knowledge regarding the functions of sensory neurons. A heatmap was generated to represent the 50 most significantly enriched genes for each population (452 genes in total, excluding redundancy). This resulted in a clear separation of the expression levels of these population-specific genes between neuronal families.

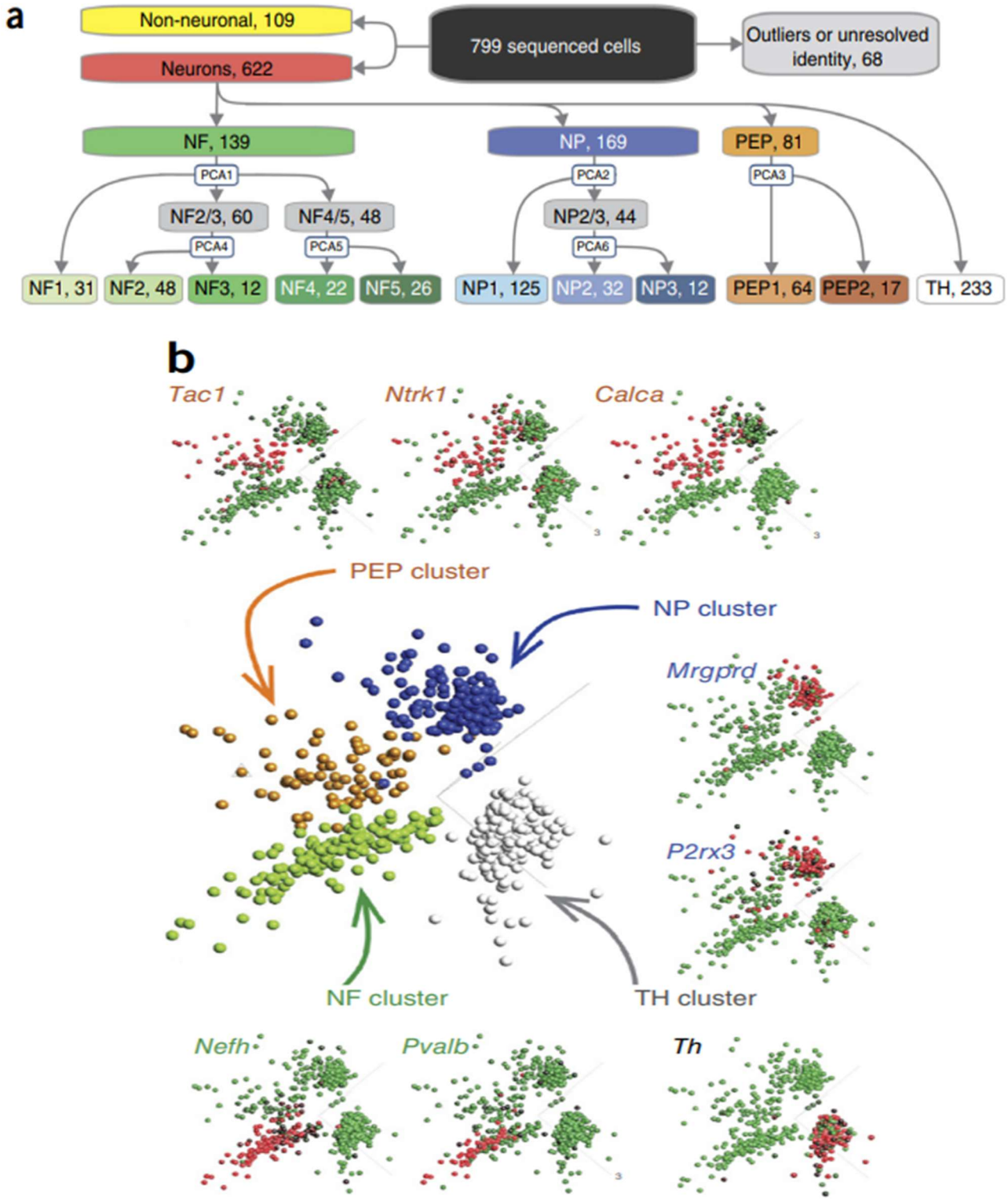


Figure 19 A: Eleven subtypes of sensory neurons identified by iterative PCA; B: PCA of 622 neurons resulting in four clusters and relative expression of representative genes (*Tac1* encodes substance P; *Ntrk1*, TRKA; *Calca*, CGRP; *Mrgprd*, MGRPRD; *P2rx3*, P2X3; *Nefh*, neurofilament heavy chain; *Pvalb*, parvalbumin; *Th*, tyrosine hydroxylase; Adapted from Usoskin et al., 2015)

4. AIMS OF THE THESIS

This thesis aims to characterize the transcriptomic identity of sensory neurons innervating the pancreas under both physiological and pathological conditions, with a particular focus on pancreatic ductal adenocarcinoma (PDAC). By combining retrograde tracing and single-cell RNA sequencing, the study seeks to uncover molecular differences in neuronal subtypes between healthy and tumor-bearing pancreatic tissues. A secondary objective is to investigate potential mechanisms of tumor–neuron communication, including the role of extracellular vesicle-mediated RNA transfer. Ultimately, this work aspires to identify novel biomarkers and therapeutic targets in the context of pancreatic cancer neurobiology.

5. MATERIALS AND METHODS

5.1 Animals used for scRNAseq and EVs isolation

All animal procedures were performed in accordance with European Union (EU) guidelines (2010/63/UE) and Italian law (decree 26/14) and the ethical committee from SISSA. All experiments performed are listed in the 22DAB16 project approved by the Italian Ministry of Health, in agreement with the EU Recommendation 2007/526/CE.

Kras$^{LSL\text{-}G12D}$; **p**53^{LoxP}; Pdx1-**C**reER (KPC) triple mutant model of tamoxifen-inducible pancreatic ductal adenocarcinoma (PDAC) was purchased from Charles River (Strain number: 032429). To induce the tumor development, a suspension of tamoxifen (Sigma-Aldrich) in corn oil (Sigma-Aldrich) was administered to pups via lactation following oral administration of the mother with 6 mg of the drug on post-natal day 0, 1, 2, and 4.

Mice were sacrificed within 8-9 weeks for analysis of acinar-to-ductal metaplasia and pancreatic intraepithelial neoplasia (mPanIN) while within 11-13 weeks for invasive pancreatic ductal adenocarcinoma. For all the scRNAseq experiments adult C57Bl/6J mice (from 8 weeks old) were used as a control, whereas for EVs isolation sibling mice among those whose genotype for **K**ras$^{LSL\text{-}G12D}$ was not showing the G12D point mutation (WT) were used as controls. Mice were maintained according to institutional guidelines on a 12/12-hour light-dark cycle in an enriched housing environment and had access to food and water ad libitum. In particular, a more nutritious food (5LJ5 - PicoLab® High Energy Mouse Diet, LabDiet) was used to guarantee the normal growth of the newborn. For all experiments only adult (age 8-15 weeks) male and female mice were used.

5.2 Dorsal Root Ganglia Primary Dissociation Culture

DRG neurons from adult KPC and C57/Bl6 mice (eight to twelve-week-old) were prepared as previously described. Briefly, adult mice (more than 6 weeks old) were euthanized in a CO_2 chamber and the spinal column rapidly removed. All DRG neurons were removed and placed in PBS. Sensory

ganglia were enzymatically digested in Collagenase type IV (10ng/µL, Sigma-Aldrich C5138) resuspended in 1 mL of DMEM-GlutaMAXTM (31966047, Life Technologies-Gibco) for 26 minutes at 37°C. Then, cells were centrifuged and incubated with 1 mL of 0.05% Trypsin EDTA (Gibco 25300-054), for 22 minutes at 37°C. Trypsin was inactivated with 500 mL of DMEM-GlutaMAXTM supplemented with 10% FBS (ECS0180L, Euroclone) and 1% pen/strep. Cell debris was removed by passing cell suspension through a 100µm filter (BD™, 340632). The cell suspension was pelleted and resuspended in DMEM-GlutaMAX™ (Gibco, 31966-047) supplemented with 10% FBS (Euroclone, ECS0180L) and 1% pen/strep (Euroclone, ECB3001D) and plated in a droplet of growth medium on a 35 mm glass coverslip (MatTek) precoated with poly-L-lysine (100µg/mL) and laminin (20µg/mL). Cells were maintained at 37 °C and 5% CO_2 in a humidified incubator. For the scRNA sequencing experiment 6 and 12 independent bio replicates were taken for tumor and healthy group, respectively.

5.3 Retrograde labeling

To identify sensory neurons innervating the healthy pancreatic tissue and the tumoral tissue, retrograde labeling with Fast Blue (FB, #17740-1, Polysciences) was performed. To this end, animals were anesthetized with 4% isoflurane in 100% O_2 at a flow rate of 1.0 L/min for 10 min. During the procedure anesthesia was maintained delivering a 2.0% Isofluran-O_2 mixture while respiratory function was monitored carefully. Adequate anesthesia was confirmed by absence of the pedal reflex (toe pinch). Briefly, the left abdominal part was shaved and disinfected with ethanol and povidone-iodine solution. The surgery was performed exposing the spleen and the pancreas. Four uL of 2% w/v Fast Blue in PBS was injected using a Hamilton syringe into the healthy pancreatic tissue or into the tumor with 4-5 injections of 1 uL each. The tissue of the abdominal cavity was sewed together with a sterile absorbable surgical suture wire (FPGLA1CN, vetsuture). After 1 week the mice were sacrificed for the DRG collection and digestion for single cell RNA sequencing analysis or immunocytochemistry.

We injected Fast Blue in mice WT and KPC 9 to 13 weeks old. We did not analyze tumor innervation after the 14th week because of technical reasons, the tumor was too big (> 1.5 cm x 1.5 cm) for the retrotracer injection.

5.4 Immunofluorescence

Thoracic and lumbar DRGs were dissected from both control and KPC mice (female and/or male) after 1 week following retrotracer intra-pancreatic injection. Single cell suspensions were obtained as described above and left to attach to glass coversplips overnight. Prior to staining cells were washed twice with PBS at room temperature. Samples were then postfixed in 4% PFA for 10 minutes at room temperature, and after 3 washes in PBS permeabilized with 0.05% Triton X-100 (Merck, X100) in PBS pH 7.4 for 10 minutes at room temperature. After two PBS washes, fixed single cell suspensions were treated with blocking solution [3% goat serum (Sigma Aldrich, G9023) in 0.01% Tween-20 (Merck, P1379) in PBS pH 7.4] for 30 minutes at room temperature, washed twice with PBS and finally incubated with primary antibodies in blocking solution over night at 4°C, motionless. The day after, samples were washed twice with ice cold PBS and then treated with secondary antibodies for two hours at 4 °C. Finally, samples were washed twice with ice cold PBS and mounted with Moviow solution. The primary antibodies used were mouse anti-NF200 (Merck, 1:500, MAB5266), rabbit anti-TH (Thermofisher, 1:500, PA5-18372), rabbit anti-SubP (1:500; ImmunoStar cat. #20064). For detection, goat 488-conjugated Alexa secondary antibody against mouse (Invitrogen, A11029) and goat 594-conjugated Alexa secondary antibody against rabbit (Invitrogen, A11032) were used at a dilution of 1:1000. For isolectin B4 staining, Isolectin GS-IB$_4$ From *Griffonia simplicifolia*, Alexa Fluor™ 647 Conjugate (Thermofisher, 1:500, I32450) was added to the secondary antibodies mix.

5.5 Mitochondria staining in DRG neurons

To validate gene ontology analyses on differentially regulated genes in DRG neurons innervating either the normal or tumor-bearing pancreas, we quantified the mitochondrial pattern and abundance

in DRG sensory neurons following retrograde tracing with Fast Blue. Briefly, single-cell suspensions of primary dissociated Fast Blue-positive DRG neurons were prepared from thoracic and lumbar dorsal root ganglia dissected from one KPC mouse with a tumor and one sibling WT mouse as a normal pancreas control. A total of four dishes were prepared for each animal. Cells were incubated at 37°C with 5% CO2 for 24 hours to allow proper attachment. The medium was then replaced with a 200 nM solution of MitoTracker™ Dye (53271, Sigma Aldrich) diluted in HBSS and incubated for 30 minutes at 37°C. Excess dye was removed by washing the cells twice with HBSS. Subsequent processing followed the protocol outlined in the "Immunofluorescence" section, with minor modifications. Specifically, this time we stained one dish for each sensory neuron cluster type individually: NF, NP, PEP, and TH. For secondary antibodies, we used Alexa Fluor 488-conjugated goat anti-mouse (Invitrogen, A11029) and Alexa Fluor 488-conjugated goat anti-rabbit (Invitrogen, A11034). For isolectin B4 staining, Isolectin GS-IB$_4$ From *Griffonia simplicifolia*, Alexa Fluor™ 647 Conjugate (Thermofisher, 1:500, I32450) was used as a secondary antibody. Images were acquired using a Nikon C2+ laser confocal microscope (Nikon, Japan) equipped with a dry 40x/0.95 NA objective. A total of 20–24 optical sections per sample were taken at a pixel resolution of 0.2 µm. The final sample size consisted of 80 cells, 40 per condition (KPC vs. WT), with 10 cells imaged per cluster type.

5.6 Co-localization quantification

Z stack images were acquired with a Nikon C2+ laser confocal microscope (Nikon, Japan) using a 10x 0.45 NA objective, consisting of 5 optical slices of 100 µm thickness taken at 20 µm intervals. Two distinct fields were acquired for each animal and further analyzed in ImageJ using the tool developed and published by Lunde & Glover (Lunde & Glover, 2020). Manual counting of two overlapping signals was then performed with the ImageJ plugin "Cell counter".

5.7 Histology

The tissue was fixed in 10% formalin for 24-48 h based on tissue dimension at room temperature. After washing with PBS, the fixed tissue was dehydrated with ethanol and xylene. The tissue was incubated in liquid paraffin (65°C) two times for 30 minutes each and then embedded in paraffin and let it harden at 4°C. 4 µm sections of mouse tissues were stained with Hematoxylin and Eosin (H&E) and scanned at 40X magnification using Aperio GT450 DX (Leica). The description of the exocrine pancreatic lesions followed criteria defined in Hruban et al (Hruban et al., 2006). Both mouse PanIN (mPanIN) and invasive carcinoma were graded using the criteria that are applied to human cancers.

5.8 RNA sequencing and library preparation

Fast Blue positive DRG neurons were manually collected using a fire polished pipette with a tip diameter of ~25 µm pulled (Flaming-Brown puller, Sutter Instruments, Novato, CA, USA) from borosilicate glass capillaries (BF150F-3, World Precision Instrument) that was filled with 1µl of PBS. Each cell was expelled into an RNAse free tube containing 20 uL of lysis buffer composed of 19 uL of 0.4% Triton + 1ul RNAse inhibitor 40 U/uL (Thermo, #10777019). Then, 2.4 uL of the lysate was mixed in another RNAse free tube with 1 uL of dNTPs 10 mM (Kappa KK1017) and 1 uL of oligo dT 5′–AAGCAGTGGTATCAACGCAGAGTACT30VN-3′ 5 uM (Sigma-Aldrich).

Samples were immediately frozen in liquid Nitrogen and thereafter, the tubes were stored at -80°C until further processing. scRNA seq on picked DRG neurons was performed at EMBL's Genomic Core Facility, Heidelberg, Germany. Briefly, a modified smart-seq2 protocol (Picelli et al., 2014) using SuperScript IV RT and tagmentation procedure previously described (Hennig et al., 2018) was used to prepare full-length cDNA sequencing libraries. The RT reaction mix was as follows: 2 µl SSRT IV 5x buffer; 0.5 µl 100 mM DTT; 2 µl 5 M betaine; 0.1 µl 1 M MgCl2; 0.25 µl 40 U/µl RNAse inhibitor; 0.25 µl SSRT IV; 0.1 µl 100 uM TSO, 1.15 µl RNase-free H2O. RT thermal conditions: 52C 15min, 80C 10min. cDNA was generated using 22 PCR cycles. The cDNA cleanup (0.6x SPRI ratio) was carried out omitting the ethanol wash steps and the elution volume was 13 µl of H2O. For

tagmentation, the sample input was normalized to 0.2ng/uL. Before the final cleanup after tagmentation and PCR, 3 µl of each sample were pooled in a single tube and the pool was cleaned up using 0.7x SPRI ratio.

5.9 Nested PCR on sequenced DRG neurons

Due to the low starting material, we employed a nested PCR approach using exon junction primers designed to target the full-length *Pdx1* mRNA. cDNA was synthesized from the lysates of 13 cells, as described below. For the first PCR reaction, 1 µL of the synthesized cDNA was added to 24 µL of a standard PCR master mix (Thermo Fisher, EP075) containing 250 nM of Primer Pair 1. The reaction was performed for 20 cycles under the following conditions: 95°C for 3 minutes, followed by 20 cycles of 95°C for 30 seconds, 60°C for 10 seconds, and 72°C for 15 seconds. Subsequently, 1 µL of the first PCR product was added to 9 µL of a qPCR master mix (SsoAdvanced, 1725270, Bio-Rad) containing 250 nM of Primer Pair 2 for a second round of amplification. This real time PCR was run for 40 cycles under the following conditions: 95°C for 30 seconds, followed by 40 cycles of 95°C for 10 seconds and 60°C for 10 seconds. The run concluded with a melting curve analysis, using a temperature increment of 0.5°C per cycle with each step lasting 15 seconds. Primer Pair 1 was designed to produce a 207 bp amplicon, while Primer Pair 2 generated a nested 93 bp amplicon within the initial product. The reference sequence used was NM_008814.4. Primers listed in Table1 in Supplementary.

5.10 RT-qPCR on sequenced DRG neurons and isolated EVs

To validate scRNA seq reads data, we performed RT-qPCR on cDNA from pooled DRG neurons to represent all the tested conditions (4 KPC and 13 WT mice). The starting material was processed in a manner consistent with the library preparation protocol described above. Cell lysates of randomly picked 20 cells per animal (4 KPC, 13 WT) were thawed on ice and then pooled together up to a total of 28.6 uL of starting material (2.2uL lysate/cell). Prior to cDNA conversion, samples were diluted

with 40 uL of TRIS HCl pH 9 10mM + KCl 50mM and 20 uL of Protease Inhibitor (COEDTAF-RO, Roche). cDNA conversion was performed using the Takara kit (Takara, RR047A) following the manufacturer's instructions with slight modification. First, genomic DNA (gDNA) was digested by incubating the sample with 4 µL of gDNA Eraser and 16 µL of 5× gDNA Eraser Buffer at 42°C for 3 minutes. cDNA synthesis was then carried out using oligo(dT) primers and random hexamers supplied with the kit. The reaction mix contained 25 µL of this solution, 2 µL of reverse transcriptase enzyme, and was supplemented with 1 M betaine, and 6 mM MgCl2. The cDNA conversion was performed at 37°C for 15 mins followed by 50°C for 2 mins, and 37°C for 2 mins, for 15 cycles (Picelli et al., 2014). The reaction was then inactivated by heating at 85°C for 10 seconds. Subsequently, 1 µL of the synthesized cDNA was added directly to 9 µL of a qPCR mastermix solution (SsoAdvanced, 1725270, Bio-Rad) containing 250nM of primers. qPCR was performed for 40 cycles with the following conditions: 95°C for 30 seconds, followed by 95°C for 10 seconds and 60°C for 10 seconds per cycle. The run concluded with a melting curve analysis, conducted at a temperature increment of 0.5°C per cycle, with each step lasting 15 seconds. Independently of the biological source, EVs were processed and tested for RT-qPCR in the same way Primers were designed based on the mapped reads for the transcript of interest (Table1):

Target	FW (5'->3')	RV (5'->3')
Snca	GGCATTTCATAAGCCTCACTGC	CCACTGGCTTTGTCAAGAAGG
mt-Tq	CTAGGACAATAGGAATTGAACC	TAGGATAAGGTGTTTAGGTAGCA
mt-ND3	TCGACCCTACAAGCTCTGC	CATGGTAGTGGAAGTAGAAGAGC
Cox17	ACTGAAGCCCTGCTGTGC	CCCTCATGCACTCCTTGTGG
Pdx1 full length (PAIR 1)	CTCCCTTTCCCGTGGATGAA	GGTCAAGTTCAACATCACTGCC
Pdx1 full length (PAIR 2)	ATGAAATCCACCAAAGCTCACG	GGCAGTACGGGTCCTCTTG
Pdx1 5' UTR	AACTGTCAAAGCGATCTGGG	CTACAAGCCAGGCCTTAGG
Pdx1 5' UTR–Tg Cre	AACTGTCAAAGCGATCTGGG	CGAACATCTTCAGGTTCTGC
m_GAPDH	ATCTTCTTGTGCAGTGCCAGCCTCGTC	GAACATGTAGACCATGTAGTTGAGGTCAATGAAGG
m_β2-microglobulin	ATGGGAAGCCGAACATACTG	CAGTCTCAGTGGGGGTGAAT
m_mt-RNR2	CTAGAAACCCCGAAACCAAA	CCAGCTATCACCAAGCTCGT

Table1- primers used in this study.

5.11 Organoid-derived EVs isolation

Normal pancreas (WT) and cancer organoids (KPC) were cultured following the TuvesonLaboratories guidelines for murine and human organoids (Huch et al., 2013; Boj et al., 2015). Once expanded and stabilized, the organoids (four standard domes/well) were cultured with 2 mL of feeding medium for three days in a 6-wells plate at 37°C with 5% CO2. After three days, the medium was collected and centrifuged at 500×g for 10 minutes at 4°C to remove cell debris. The supernatant was subsequently centrifuged at 10,000×g for 20 minutes at 4°C to eliminate apoptotic bodies and microvesicles. Finally, the supernatant underwent ultracentrifugation at 100,000×g for 70 minutes at 4°C using a swinging rotor (Optima XE-90, Swinging Rotor SW41 Ti, Beckman & Coulter) to collect

EVs. After discarding the supernatant, the resulting pellet was resuspended in 30 µL of lysis buffer (0.4% Triton X and 5.2% RNaseOut in H2O).

5.12 Pancreatic slice-derived EVs isolation

Acute slices were obtained from two male siblings KPC mice, one with a tumor and the other serving as a normal pancreas control (KPC and WT, respectively), as described by Rodríguez-Merced et al. (Rodríguez-Merced et al., 2023) with minor modifications. The pancreas was separated from the spleen and rinsed in a preservative solution consisting of 2x PBS supplemented with 10 mg/mL of soybean trypsin inhibitor (transport solution). 350-µm thick slices were prepared using a vibratome, with the blade power set to medium. The slices were then transferred to transport solution and kept on ice for the duration of the procedure. Afterward, the slices were plated on a 0.4 µm pore size PET track-etched membrane cell culture insert (Falcon, 353090) and incubated at 37°C with 5% CO_2. The following day, the medium was replaced, and after 48 hours, EVs were harvested from the conditioned medium and analyzed by PCR as described above.

5.13 Blood derived-EVs isolation

Blood was collected from two pools of animals: one male and one female 15 weeks old KPC sibling mice presenting the tumour (KPC group) and one male and one female 15 weeks old KPC mice with normal pancreas as a control (WT group). Up to 600uL of blood was obtained from each group and immediately transferred to an Na_2EDTA pre-coated 1.5mL low binding Eppendorf, added with 50uL of 0.1M Na_2EDTA pH 8. After mixing by inversion several times, plasma was separated from blood by centrifugation at 2000xg for 10 minutes at 4°C, transferred to a new collection tube then diluted with the same volume of Gibco™ PBS (pH 7.4) and mixed well. After a centrifugation step at 2000xg for 30 minutes at 4°C, supernatant was then transferred to a new collection tube and centrifuged at 12000xg for 45 minutes at 4°C. Finally, supernatant was collected and ultracentrifuged at 200,000×g

for 70 minutes at 4°C using a swinging rotor (Optima XE-90, Swinging Rotor SW41 Ti, Beckman Coulter) to collect EVs. After discarding the supernatant, the resulting pellet was resuspended in 30 µL of lysis buffer (0.4% Triton X and 5.2% RNaseOut in H_2O).

5.14 Clustering and annotations of DRG neurons identity

5.14.1 Mapping and quantification of genes in sequenced cells

Quality control was performed on all FASTQ files received from the sequencing facility using FastQC (Andrews, 2010), MultiQC (Ewels et al., 2016), and QoRTs (Hartley et al., 201. The read files were mapped to the GRCm39 version of the genome assembly using the STAR aligner (Dobin et al. 2013). *Mus_musculus.GRCm39.dna.primary_assembly. fa* and *Mus_musculus.GRCm39.108. chr.gtf* files were downloaded from Ensembl (Harrison et al., 2024) and used to generate a reference index. This was followed by aligning the reads of each cell to the reference genome one at a time. Strandedness was verified from the resulting BAM (Binary Alignment Map) files using the infer_experiment.py function of the RSeQC package (Wang L. et al., 2012), confirming the library as unstranded as expected from the Smartseq2 protocol. Since the data consisted of single-end reads, sorting them prior to counting was unnecessary. Finally, gene counts were extracted for each cell using the htseq-count (Anders et al., 2015) function, resulting in a gene-count matrix for all the sequenced cells.

5.14.2 From bulk sample processing to analyzing single cells using Seurat

Seurat (Hao et al., 2024), an R package designed for quality control, analysis, and exploration of single-cell RNA-seq data, was used for further downstream analyses. First, a seurat object was created using the CreateSeuratObject() function, by passing the gene count matrix and the quality control metrics calculated for each cell using QoRTs results as metadata. The PercentageFeatureSet() function was used to compute the percentage of counts attributed to mitochondrial and ribosomal

genes for each cell. To visualize the quality control parameters, the VlnPlot() function was used. Cells having non-zero counts for more than 1,000 genes were selected for further analysis.

5.14.3 Annotation of cells using Monocle3

Monocle3 package was used to identify the cell types present in our dataset. A cell dataset object was created for the reference (Usoskin et al., 2015) and the query (our data) data, using new_cell_data_set() function. Both datasets were subsetted to include only common genes. Size factors were re-calculated using estimate_size_factors() function. The reference dataset was transformed to low dimensional PCA and UMAP spaces using preprocess_cds() and reduce_dimension() functions. The build_nn_index parameter was set to TRUE to build a nearest neighbor index in the UMAP space, which was later used to transfer the reference annotations to the query. The transformed models and nearest-neighbor index were saved using save_transform_models() function and later loaded into the query dataset with load_transform_models() function. The query data was projected into the reference space using preprocess_transform() and reduce_dimension_transform() functions. The two data sets were combined using combine_cds() function to visualize the overlap of query cells on reference space using plot_cells() function. Finally, cell type annotations from the reference are transferred to the query dataset using the transfer_cell_labels() and fix_missing_cell_labels() functions. The transferred annotations were added to the metadata of the seurat object. Cells with unsolved, not-a-neuron and other outlier annotations were excluded from further analysis. The seurat object was normalized for each mouse, using SCTransform() function. Dimensionality reduction to PCA and UMAP spaces was done using RunPCA() and RunUMAP() functions with default parameters. Lastly, nearest-neighbor graph construction and unsupervised clustering (using the default Louvain algorithm) were performed with FindNeighbors() and FindClusters() functions. DimPlot() function was used to visualize cells and the group.by parameter was varied depending on what was to be visualized.

5.14.4 Identification of markers and differential gene expression analysis

FindAllMarkers() function was used to identify markers of the different DRG populations in the dataset. Genes that are expressed in at least 10% of the cells were tested, to return both up-regulated and down-regulated putative markers of each DRG population. Genes with adjusted p-value (p_val_adj) <= 0.05 were considered as markers. DoHeatMap() function was used to plot the heatmap of the top n marker genes of the different DRG populations. To identify differentially expressed genes between KPC and WT cells, FindMarkers() function was used, testing genes expressed in at least 10% of total cells. Wilcoxon Rank Sum test was applied as the statistical test used to identify DEGs in both the functions. Genes with p_val_adj <= 0.05 and absolute log2 fold change (abs(avg_log2FC)) >= 0.25 were considered as differentially expressed. The resulting DEGs were visualized with a volcano plot, using EnhanchedVolcano R package (Blighe et al., 2024). Gene ontology (GO) analysis was performed for up and down-regulated DEGs separately. Genes used for testing in differential expression analysis served as universe for GO analysis. biomaRt R package (Durinck et al., 2005) was used to retrieve gene information (eg. entrez ID) required for GO analysis. GOstats (Falcon et al., 2007) and GO.db (Carlson, 2019) R packages were used to identify the enriched terms for up and down-regulated genes, and the results were visualized using ggplot2 R package (Wickham, 2011).

6. RESULTS

6.1 Single-cell RNA sequencing identifies sensory neuron subtypes innervating healthy pancreatic tissue and PDAC tissue

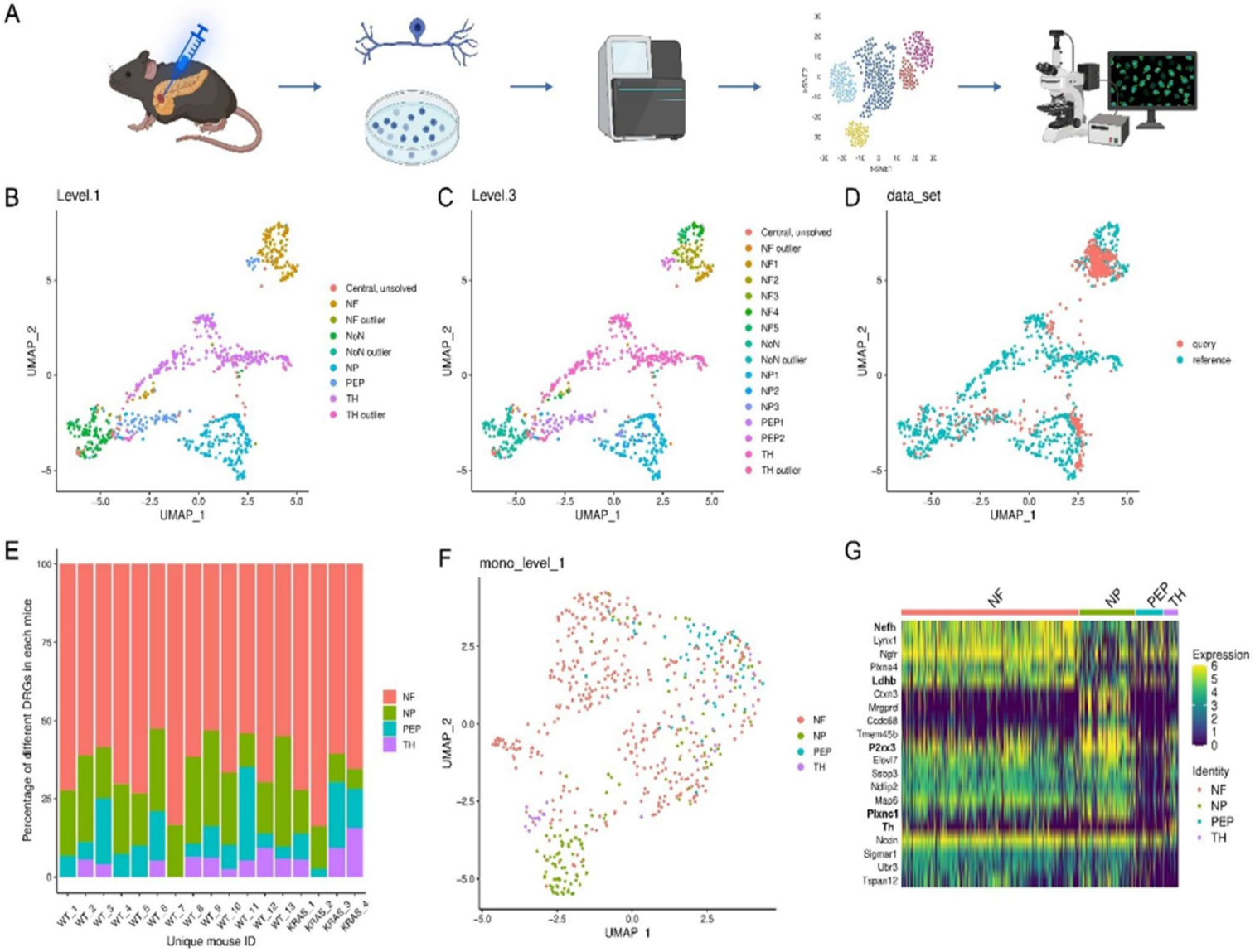


Figure 20. A: Schematic workflow of the experiment starting from Fast Blue injection into healthy or cancer pancreatic tissue, picking of single positive cells after DRG culture, scRNA sequencing and data analysis. B and C: Unsupervised clustering of the Usoskin's dataset, cells were visualized by their types and subtypes as assigned in the reference study (NF, neurofilament-containing; NoN, non-neuronal cells; NP, non-peptidergic; PEP, peptidergic; TH, tyrosine hydroxylase. D: Overlap of our database with the reference dataset. Fig 1E) Distribution of DRGs into classes in each mouse. F) UMAP obtained after Seurat based clustering; the color is based on cell assignment done using monocle 3. G: Heatmap of top 5 marker gene identified after annotation. Highlighted are known marker genes of DRG subtypes that are up/down regulated in subtype populations.

To characterize dorsal root ganglia (DRG) neurons innervating the pancreas, we injected retrograde tracer Fast Blue (FB) into the head and tail regions of the pancreas in 13 wildtype (C57BL/6j) and 4 KPC (**K**ras$^{LSL-G12D}$; **p**53^{LoxP}; Pdx1-**C**reER) mice. Lumbar and thoracic DRG were dissociated, and FB+ cells were hand-picked and processed for sequencing. A total of 715 cells were sequenced and analyzed (Fig 19A). Evaluation of pancreatic tissue sections confirmed preinvasive PanIN or PDAC lesions in KPC mice (Fig.21). Quality control parameters were calculated for each cell, including the number of genes identified, the number of RNA molecules detected, and the total ribosomal and mitochondrial content (Fig. 22A). Cells that had non-zero counts for fewer than 1,000 genes were removed from the subsequent analysis. A total of 620 cells remained for further analysis, with an average of 35 cells per animal (Fig. 22B). Unsupervised clustering using seurat with default parameters identified six discrete clusters (Fig. 22C). However, the top markers of each cluster (Fig.22D) did not capture discreet DRG subtypes. To more reliably identify DRG subtypes, we used the validated sensory neuron dataset from Usoskin et al. (GSE59739) as a reference. Upon reanalyzing the data, we observed that cells clustered according to the original annotations assigned in the study (Fig. 20B, C). The recapitulation of their classification confirmed the robustness of the dataset and its suitability as a reference for our analysis. Guided by Monocle3 pipelines (see Methods), we projected our data onto the Usoskin reference map (Fig. 20D). Most of the cells clustered within the NF (neurofilament-containing) subtype, while fewer cells mapped to NP (non-peptidergic), PEP (peptidergic), or TH (Tyrosine hydroxylase–expressing) subtypes. Cells that were annotated as outliers, non-neuronal, or lacked annotations were excluded from further analysis. By examining annotated DRG subtype proportions across individual mice, we consistently observed a dominance of NF neurons and fewer TH cells in both wild-type and KPC cohorts (Fig. 20E).

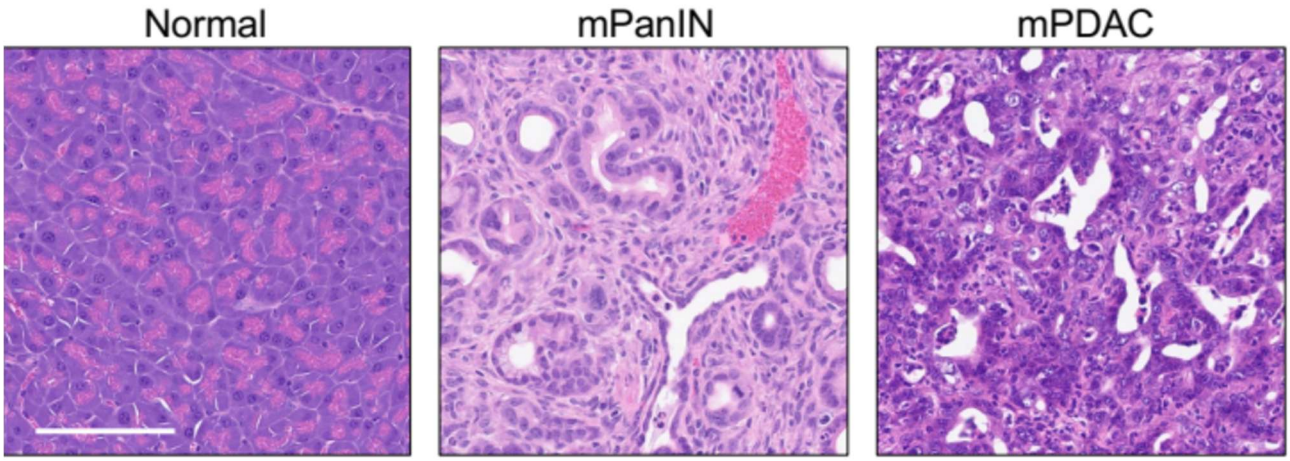


Figure 21. Hematoxylin and Eosin (H&E) staining of murine pancreatic tissue used for sequencing analysis. From left to right: normal pancreatic tissue from a wild-type C57BL/6j mouse; PanIN ductal structures from a KPC mouse; invasive ductal carcinoma from a KPC mouse. Scale bar, 100 µm.

Notably, the seurat-based clustering approach also showed concordance with these annotated subtypes, supporting the reliability of our reference-based strategy (Fig. 20F). As an additional validation, we extracted top marker genes for each annotated DRG subtype and compared them to known DRG markers (Fig. 20G). The NF population showed high expression of *Nefh* and *Ldhb*, whereas *Plxnc1* and *P2rx3* were elevated in NP neurons; notably, *Plxnc1* was downregulated in PEP cells, and *Th* was enriched in the TH neurons. These expression patterns align strongly with established DRG subtype-specific markers, confirming the robustness of the reference-based annotation.

Together, these findings confirm that the in-silico annotation using the Usoskin reference dataset is robust and well-aligned with complementary analyses. This provides a solid framework to proceed with further exploration of DRG roles in pancreatic function and the progression of PDAC.

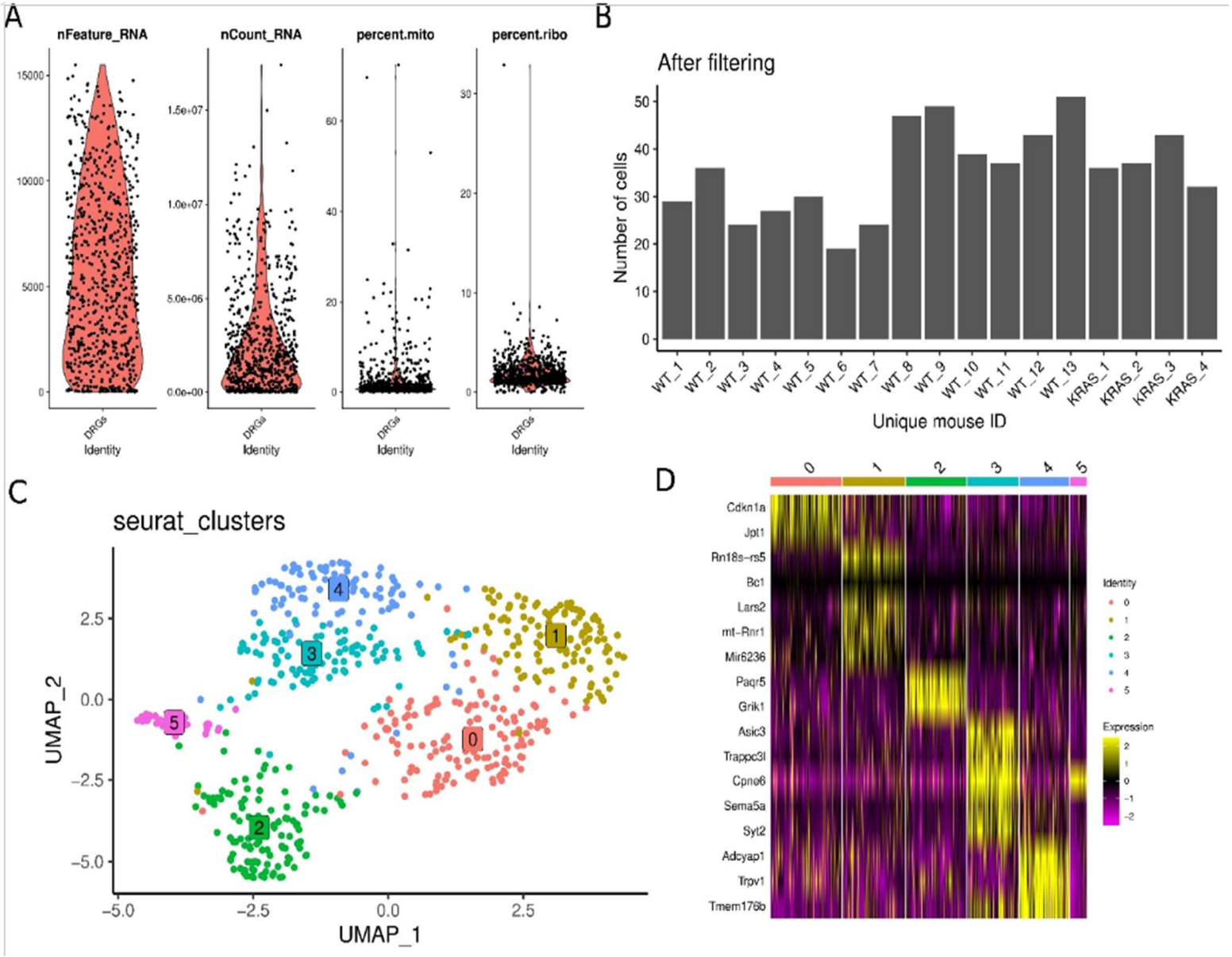


Figure 22. A: Quality control parameters analysis calculated for each cell, including the number of genes identified, RNA molecules detected, and ribosomal and mitochondrial content. B: Cells with fewer than 1,000 detected genes or high ribosomal/mitochondrial content were excluded, leaving 620 cells for further analysis. C: Identification of 6 unsupervised clusters using Seurat. D: Examination of the top markers revealed that the clustering did not capture discrete DRG types.

6.2 Prevalence of the NF subpopulation amongst sensory neuron subtypes innervating pancreas

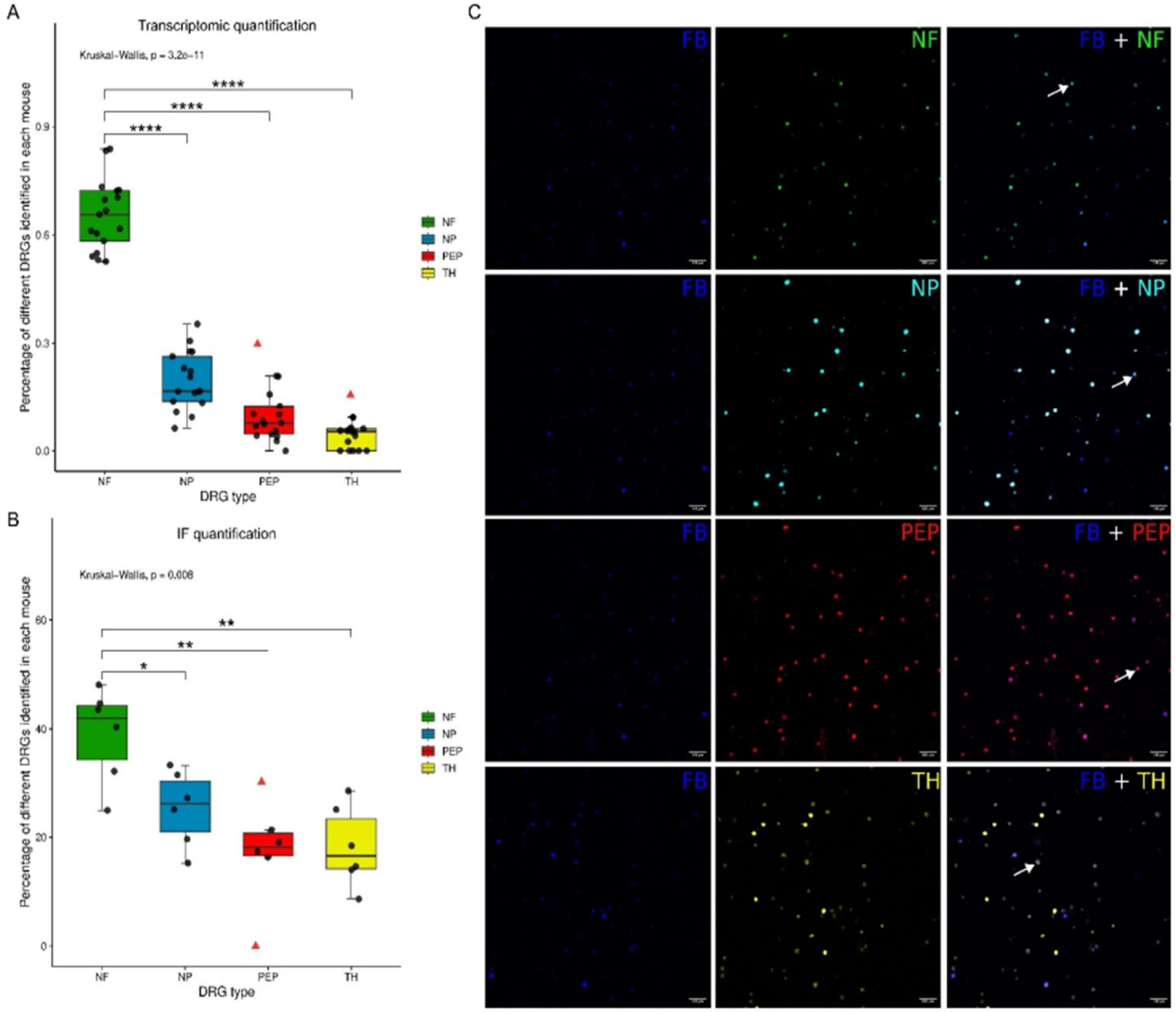


Figure 23 A:Transcriptomic quantification of Fast Blue positive DRGs across the different classes. B: Immunofluorescence (IF) quantification of Fast Blue positive DRGs across the different classes. C: Immunostaining of Fast Blue positive DRGs with antibodies against Neurofilament 200 (NF), Isolectin B4 (NP), Substance P (PEP), Tyrosine Hydroxylase (TH). Scalebar 100um.

The quantification of DRG subtypes using RNAseq across all 17 mice revealed a consistent abundance of NF neurons, comprising an average of 65% of the total DRGs identified per mouse. NP

neurons were the second most frequent subtype, with an average of 20%, followed by PEP and TH neurons, which accounted for 10% and 5%, respectively (Fig. 23A). The predominance of NF neurons was evident across both KPC and WT mice, and it was statistically significant (Kruskal-Wallis test, $p < 0.01$). To further validate and substantiate our transcriptomic findings, we performed immunofluorescence on cultured DRG from 6 mice (3 KPC and 3 WT). We used anti-NF200, anti-TH, anti-Substance P antibodies and Isolectin B4 staining to identify NF, TH, PEP and NP neurons, respectively. The IF results (Fig. 23C) corroborated our single-cell observations, revealing specific fractions of NF, NP, PEP, and TH DRGs innervating the pancreas. Again, NF neurons emerged as the most abundant DRG subtype, comprising an average of 39% of total FB+ cells, followed by NP neurons at 25%. PEP and TH neurons accounted for roughly 18% each. The enrichment of NF neurons was again statistically significant (Kruskal-Wallis test, $p < 0.01$) and remained consistently high in both KPC and WT mice in terms of relative abundance (Fig 23B).

6.3 Reduced non-peptidergic fraction in DRG from KPC mice

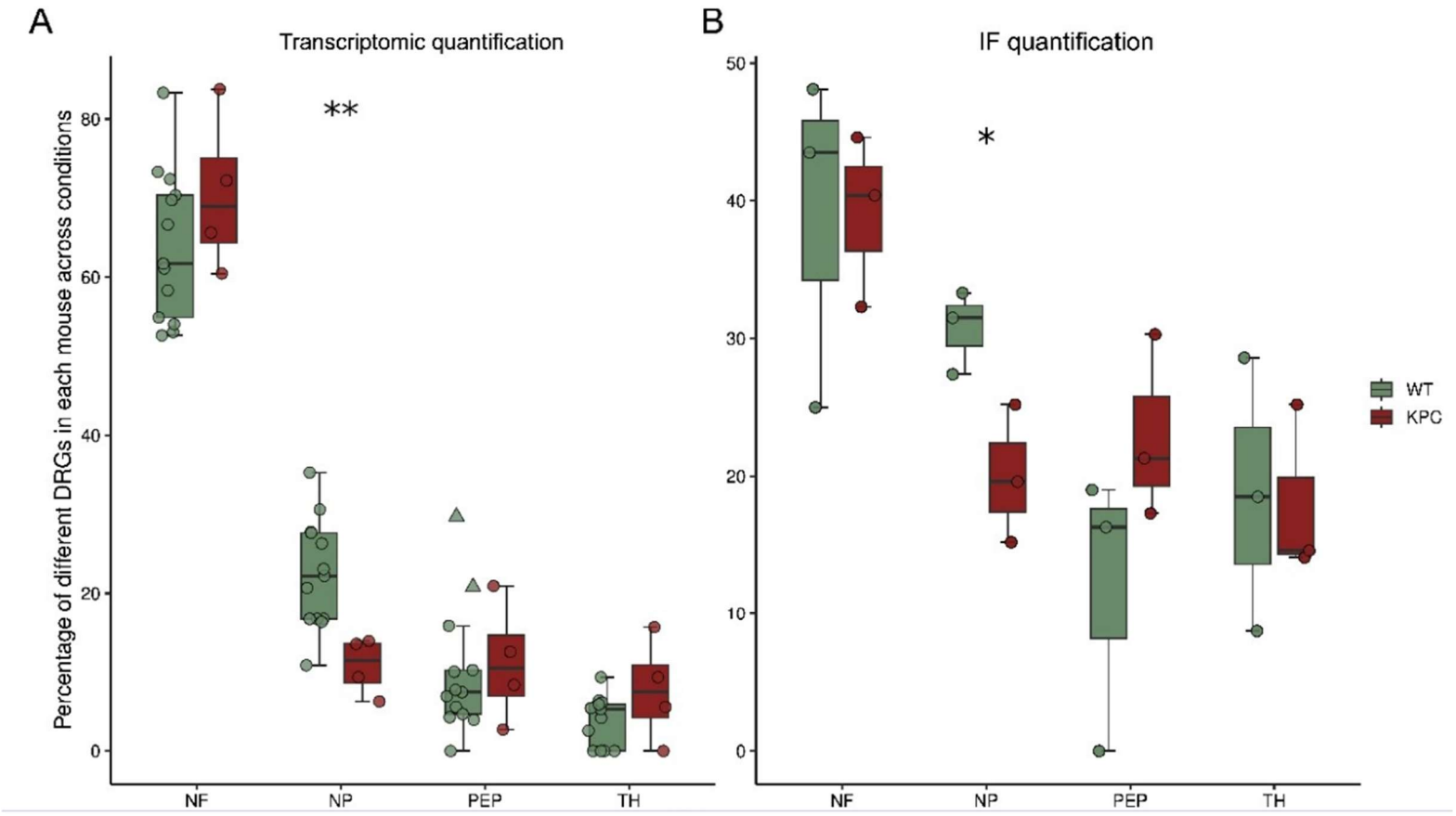


Figure 24. A: Transcriptomic quantification of Fast Blue-positive DRGs across different classes, categorized by KRAS mutant and WT mice (t-test, p-value 0.0013). B: Immunofluorescence (IF) quantification of Fast Blue positive DRGs across the different classes, categorized by KRAS mutant and WT mice (t-test, p = 0.044

The transcriptomic data revealed a significant reduction in the proportion of non-peptidergic (NP) sensory neurons in KPC mice compared to WT mice (average NP KPC 10.73% vs NP WT 22.36% t-test, p-value 0.0013) (Fig. 24A). No significant differences were found for the other DRG neurons subtypes between the conditions. The same reduction was also observed in the immunofluorescence performed on cultured DRG from 3 KPC and 3 WT mice (Fig. 25C). The IF analysis confirmed the significant reduction in the proportion of non-peptidergic neurons in KPC mice (Fig. 24B, FB+ non-peptidergic cells in KPC was 20% versus 30.7% in WT, t-test, p = 0.044). No statistically significant differences were found for the other DRG subtypes between the conditions.

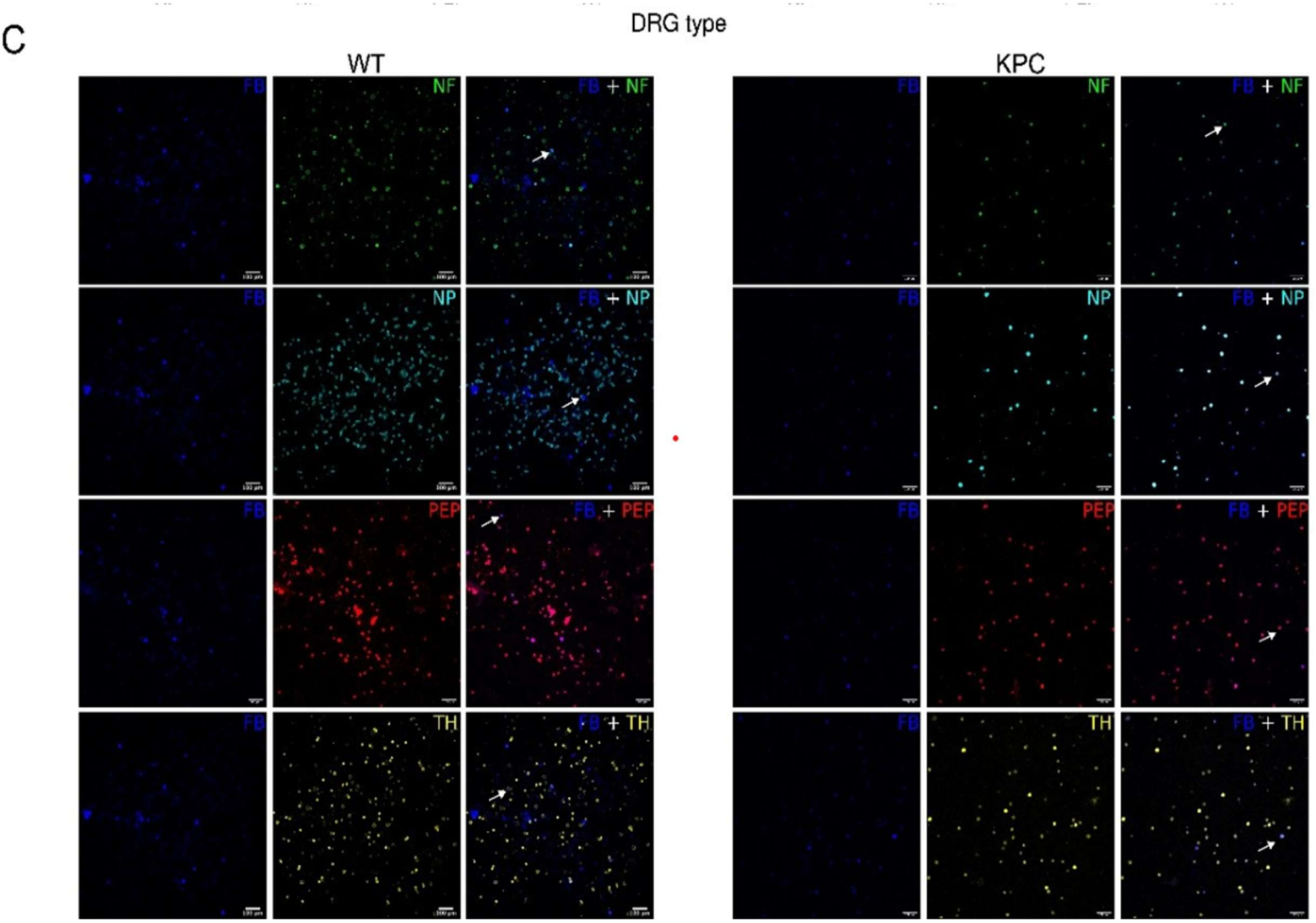


Figure 25. C: Immunostaining of Fast Blue-positive DRGs from wild-type (WT) or KPC mice using antibodies against Neurofilament 200 (NF), Isolectin B4 (IB4), Substance P (SP), and Tyrosine Hydroxylase (TH). Scalebar 100um

6.4 Novel detection of Pdx1-Cre and Snca in KPC DRGs and evidence of EVs transfer

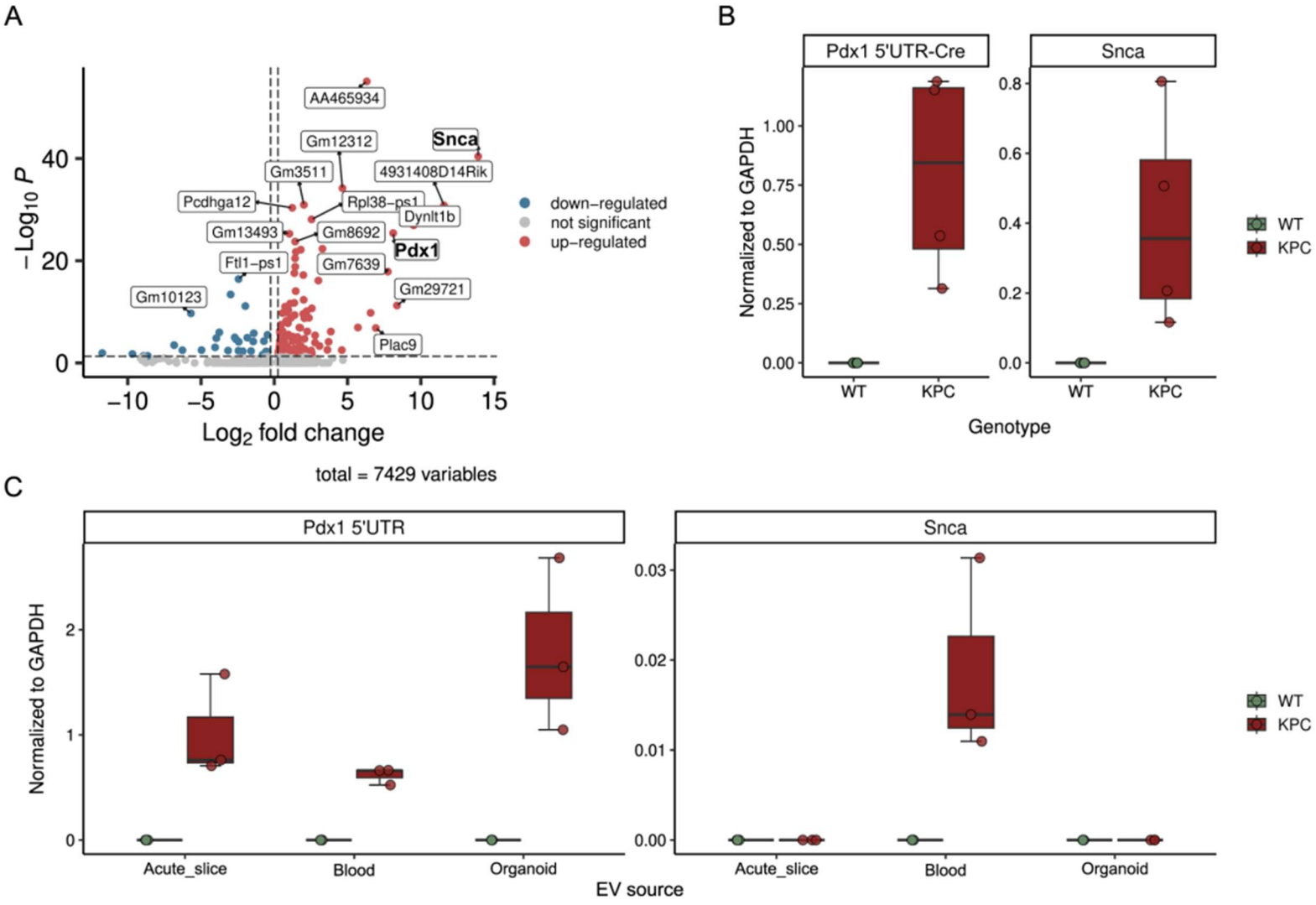


Figure 26. A: Volcano plot highlighting Pdx-1 5'UTR and Snca among the most up-regulated genes (red) and immune-system related genes among the down-regulated (blue); B: Barplot of RT-qPCR validation of genes of interest (*Pdx1 5'UTR* and *Snca*) showing differential distribution across all animals tested (4 KPC, 13 WT). Samples were treated as technical replicates, as 20 cells were pooled for each animal starting from lysates sent to scRNA seq analysis. Normalized to GAPDH; C: Barplot of RT-qPCR validation of genes of interest (*Pdx1 5'UTR* and *Snca*) across all different EVs source (organoids, acute slices and blood). N=3, normalized to *GAPDH*.

Differential expression analysis between KPC and wild-type (WT) DRGs revealed 180 significantly altered genes, including 149 upregulated and 31 downregulated in KPC DRGs (Fig. 26A). Among the upregulated genes, *Pdx1* (*adj. p* = 3.92×10^{-26}) and *Snca* (*adj. p* = 3.83×10^{-12}) were particularly striking, as they had not been previously reported in DRG neurons. Notably, both genes were detected

exclusively in KPC neurons (*Pdx1*$^{+}$ - 31%; *Snca*$^{+}$ - 40%, of all KPC DRGs) with most positive cells falling within the NF subtype (Fig.27). Further inspection showed that *Pdx1* reads were predominantly mapped to the 5′UTR region (Fig.28). Consistent with the transcriptomic findings, RT-qPCR using 5′UTR–specific primers for *Pdx1* and primers for canonical *Snca* (Methods, Table 1) confirmed the exclusive expression of these transcripts in KPC DRGs, whereas WT DRGs were devoid of these signals (Fig. 26B, Fig.29, Fig.30).

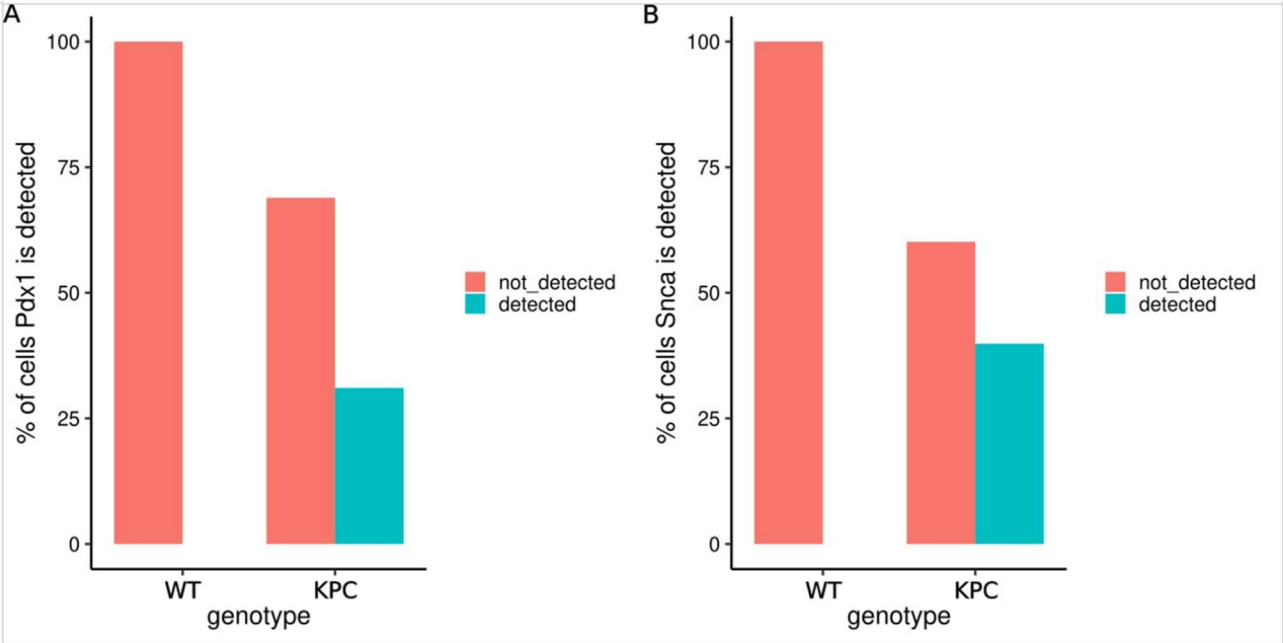


Figure 27. A: Percentage of WT and KPC DRG cells expressing Pdx1 5'UTR. Pdx1 5'UTR was detected in 31% of KPC cells, predominantly in NF DRGs, while it was not detected in WT DRGs. B: Percentage of WT and KPC DRG cells expressing Snca. Snca was detected in 40% of KPC cells, predominantly in NF DRGs, while it was not detected in WT DRGs.

Intriguingly, in these samples we were not able to detect the full length *Pdx1* transcript. We reasoned that the 5'UTR-truncated *Pdx1* transcripts in KPC DRG, may actually be derived from the exogenous CreERT2 transgene that is preceded by a portion of the *Pdx1* promoter and integrated randomly into the genome of KPC (Gu et al., 2002). We thus re-examined the sequencing data for the presence of either this transgene or endogenous *Pdx1* transcripts in those DRG which were positive for *Pdx1* 5'UTR reads. As shown in Fig.31, overlap with CreERT2 sequence was evident in all samples, while

endogenous Pdx1 reads extending beyond the 5'UTR were never detected. This was experimentally validated using qRT-PCR to generate amplicons that extended from the 5'UTR into either the CreERT2 transgene, or endogenous canonical *Pdx1*. Again, CreERT2 amplicons were detected at similar levels to the 5'UTR transcripts in DRG from KPC mice, while endogenous canonical Pdx1 transcripts were never observed (Fig.32 A, B and C).

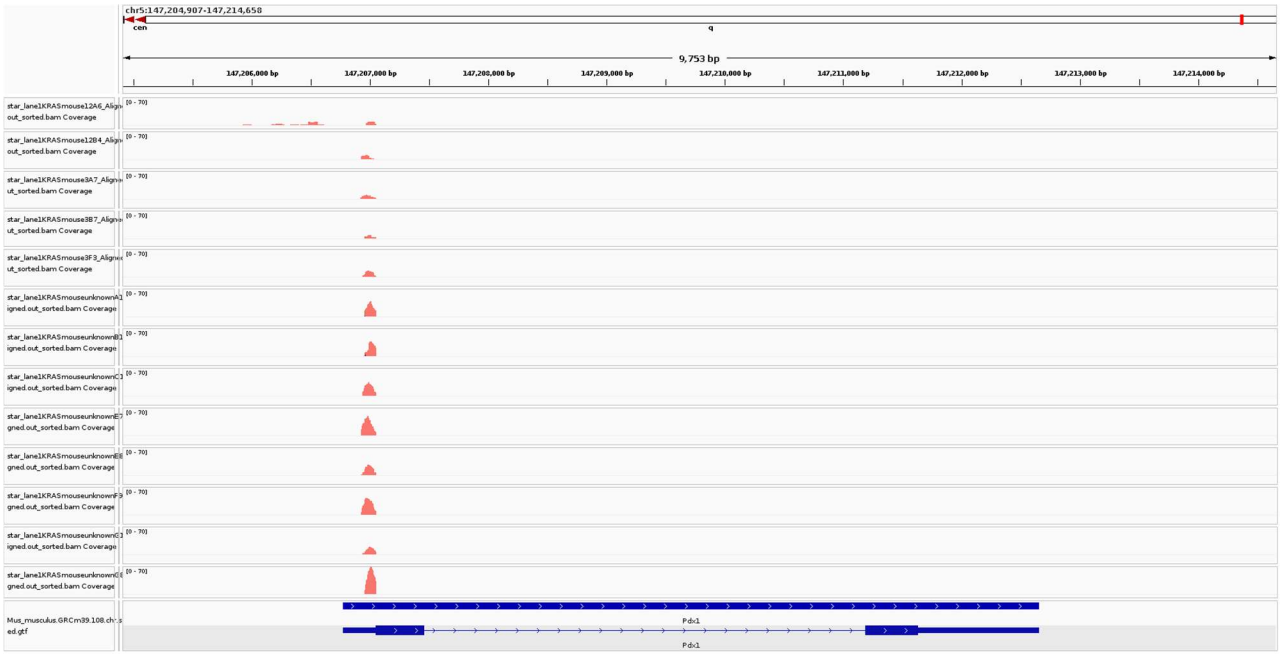


Figure 28. IGV snapshot of neurons (rows) whose Pdx1 5'UTR count > 10. Evidence of reads mapping particularly on the 5' UTR of Pdx1.

Given these unexpected findings, we hypothesized that *Pdx1-Cre* and *Snca* transcripts might be circulating via EVs. To test this, we isolated EVs from three complementary models— (1) in vitro (organoids), (2) ex vivo (acute slices), and (3) in vivo (blood) samples—and probed for 5′UTR *Pdx1-Cre* and *Snca* by RT-qPCR. Strikingly, Pdx1 5' UTR was consistently detected in vesicles from all three KPC models, including blood-derived EVs, but was absent from WT controls (Fig. 26C; Fig.33). Conversely, Snca was detected only in EVs derived from KPC blood, remaining undetectable in KPC organoid– or acute slice–derived EVs and in all WT EV samples (Fig. 26C; Fig.33). Collectively, the sequencing data from neurons and the corresponding RT-qPCR experiments validate

the unique presence of Pdx1-Cre and Snca transcripts in KPC DRG neurons, and further analysis of these transcripts in vesicles suggests that they may be selectively packaged and transferred via circulating EVs in vitro and in vivo.

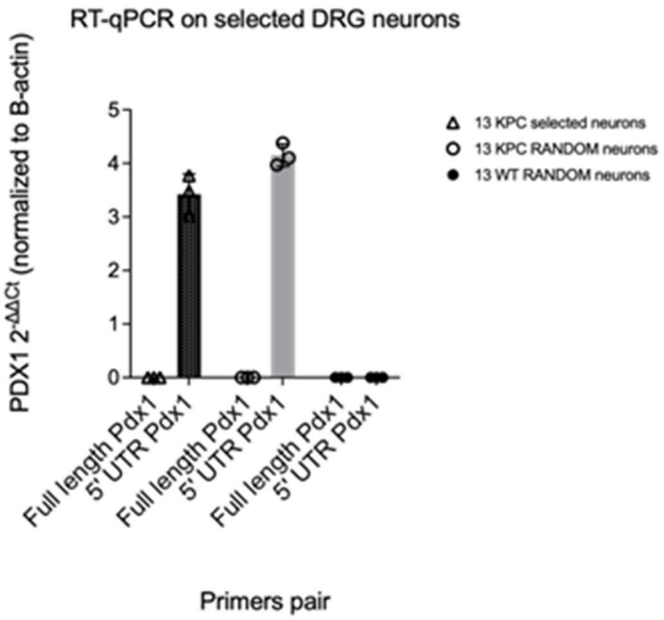


Figure 29. Barplot of RT-qPCR validation of gene of interest (*Pdx1*) across 3 sample types as a pool of selected DRG neurons from the scRNAseq library. (*Pdx1* UMI ≥10; 13 cells from KPC mice 1,2 and 3). Controls were 13 randomly picked DRG neurons from a different animal (mouse KPC4) and from a WT animal (mouse WT 2) as a mock control. We were not able to detect the full length *Pdx1* transcript, while we detected the Pdx1 5'UTR fragment in both the pools from KPC animals. Data are reported as the mean of ΔΔCt in 3 technical replicates, normalized to B-actin.



Fig. 30 2.5% agarose gel in TBE 0.5x for Pdx1 5'UTR transcript in RT-qPCR in pooled DRG neurons from within scRNAseq library. Pdx1 5'UTR amplicon (71bp) is found in pooled KPC DRG neurons only. cDNA negative controls (1,2,3 and 4-) without RetroTranscriptase enzyme; positive control is cDNA from KPC organoids, synthesized with a mix of oligodT and random hexamer.

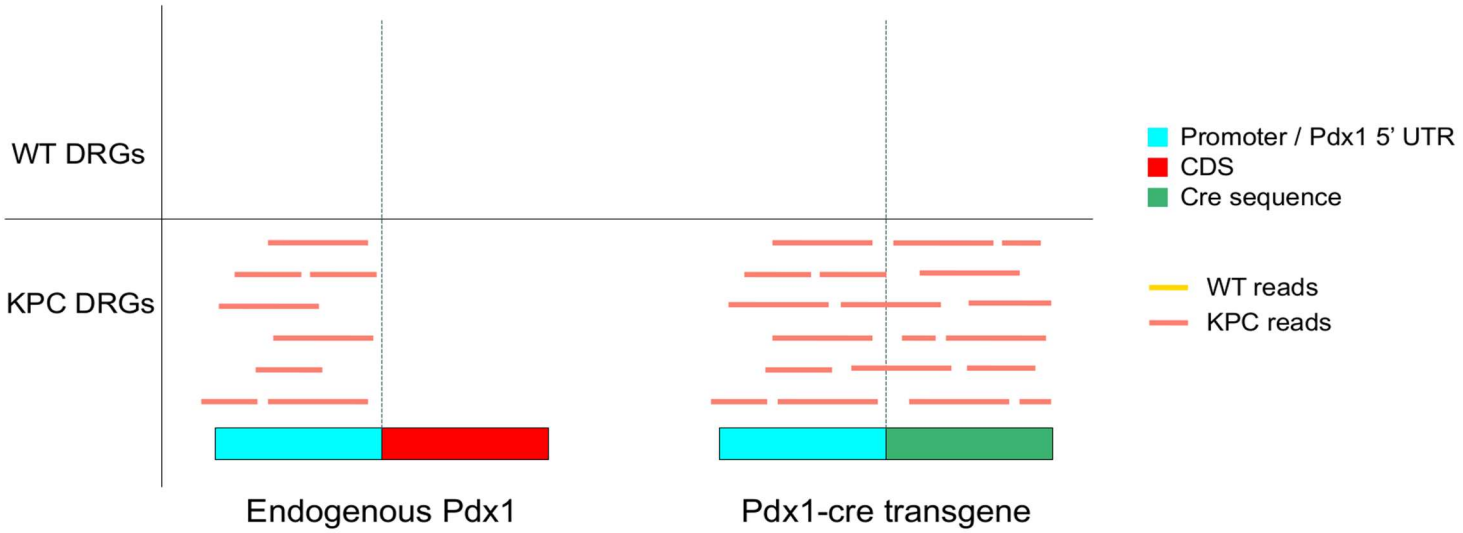


Fig. 31 Schematic cartoon of scRNAseq reads from sequenced KPC and WT DRG neurons innervating the pancreas.

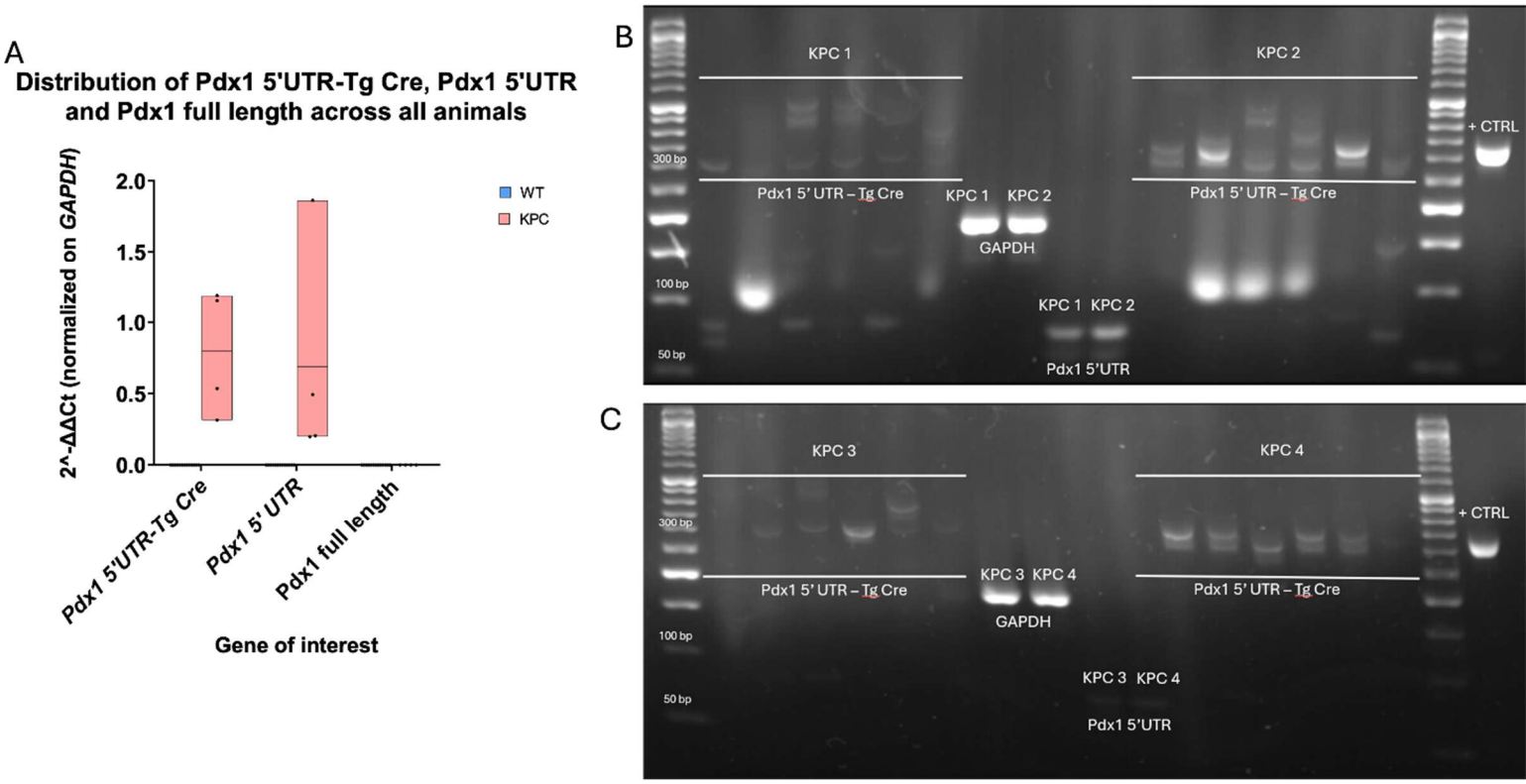


Fig. 32 A: Distribution of Pdx1 5'UTR-Tg CreB, Pdx1 5'UTR and Pdx1 full length fragments in pooled DRG neurons from within scRNAseq library animals tested. B,C: 2.5% agarose gel in TBE 0.5x for Pdx1 5'UTR-Tg Cre transcript in RT-qPCR in pooled DRG neurons from within scRNAseq library. Pdx1 5'UTR-TgCre amplicon (327bp) is found in all pooled KPC DRG neurons across all animals tested (KPC1,2,3, and4). Positive control is total DNA extracted from pancreatic tissue of a KPC animal treated with tamoxifen

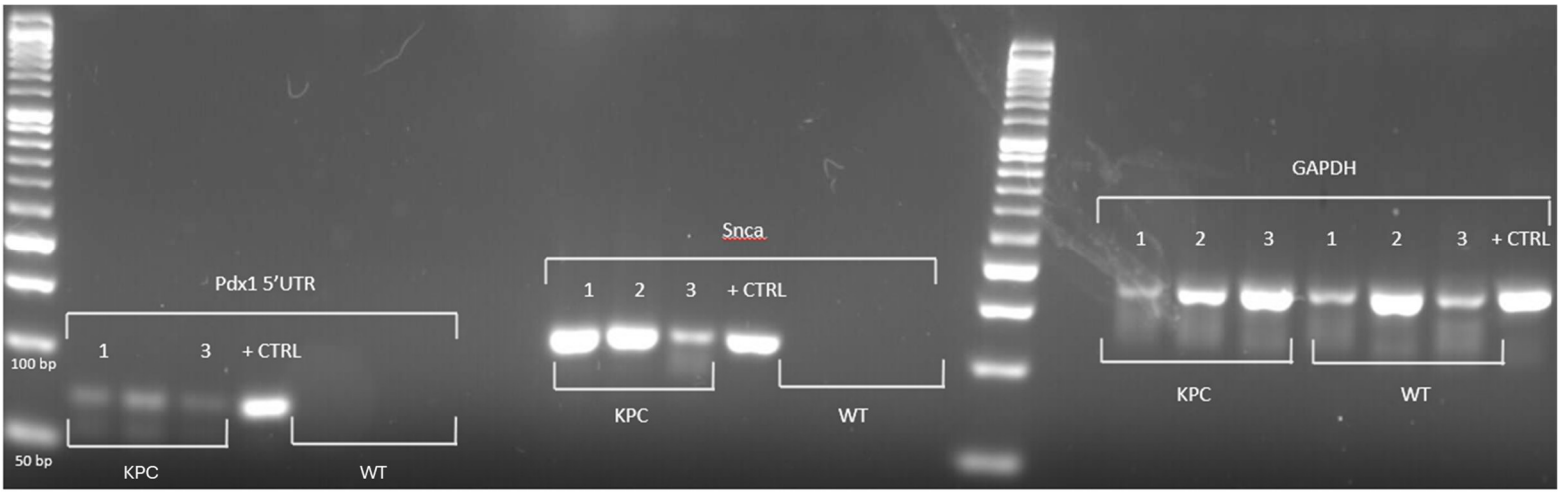


Fig. 33 2.5% agarose gel in TBE 0,5x for *Pdx1 5'UTR* transcript and *Snca* in RT-qPCR in EVs isolated from blood. *Pdx1 5'UTR* amplicon (71 bp) and *Snca* amplicon (112 bp) in EVs isolated from KPC blood only (N=3). *GAPDH* (173 bp) is reported here as a positive control for successful EVs isolation.

6.5 Functional enrichment analysis reveals altered mitochondrial activity in KPC DRGs

To gain insight into the functional pathways disrupted in KPC dorsal root ganglia (DRGs), we performed gene ontology (GO) enrichment analysis on the sets of differentially expressed genes. Notably, upregulated genes were enriched for mitochondrial processes, whereas downregulated genes were linked to immune system processes (Fig. 34A). Motivated by these findings and our earlier observations of EVs transfer, we sought to validate three mitochondrial-related genes—mt-ND3, Cox17, and mt-tQ—previously implicated in cancer and mitochondrial pathways (Suzuki et al., 2003; Jin et al., 2018; Qiu et al., 2021). Using RT-qPCR on EVs isolated from the three models (in vitro organoids, ex vivo acute slices, and in vivo blood), we observed that these genes were largely enriched in KPC EVs (Fig. 34B) (mt-ND3 EVs WT vs KPC, $p < 0.05$; mt-Tq EVs WT vs KPC $p < 0.01$, two-way ANOVA, followed by post hoc pairwise t-tests). In contrast, when we examined pooled DRG neuron samples (Fig.35), these mitochondrial transcripts did not show similar enrichment. We attribute this discrepancy to the random selection of DRGs for pooling in each mouse, which may have masked differences in the expression of these genes due to subtype-specific variations in total mitochondrial content between WT and KPC DRGs. To further explore potential mitochondrial

alterations, we performed mitochondrial staining with MitoRed on Fast Blue–labeled (FB+) DRGs from WT and KPC mice. While no significant differences were evident at the overall population level (Fig.36), subtyping revealed marked variations (Fig. 34C). Specifically, KPC PEP neurons displayed both higher mitochondrial counts and more extensive branching compared with WT PEP neurons (two-way ANOVA, post hoc pairwise t-tests within each DRG type, $p < 0.05$), whereas KPC NP neurons exhibited lower mitochondrial content and fewer branches compared with WT NP neurons (two-way ANOVA, post hoc pairwise t-tests within each DRG type, $p < 0.05$). Representative images of FB+ DRGs (Fig. 37D–G) illustrate these subtype-specific differences, underscoring the heterogeneous mitochondrial responses within distinct DRG populations.

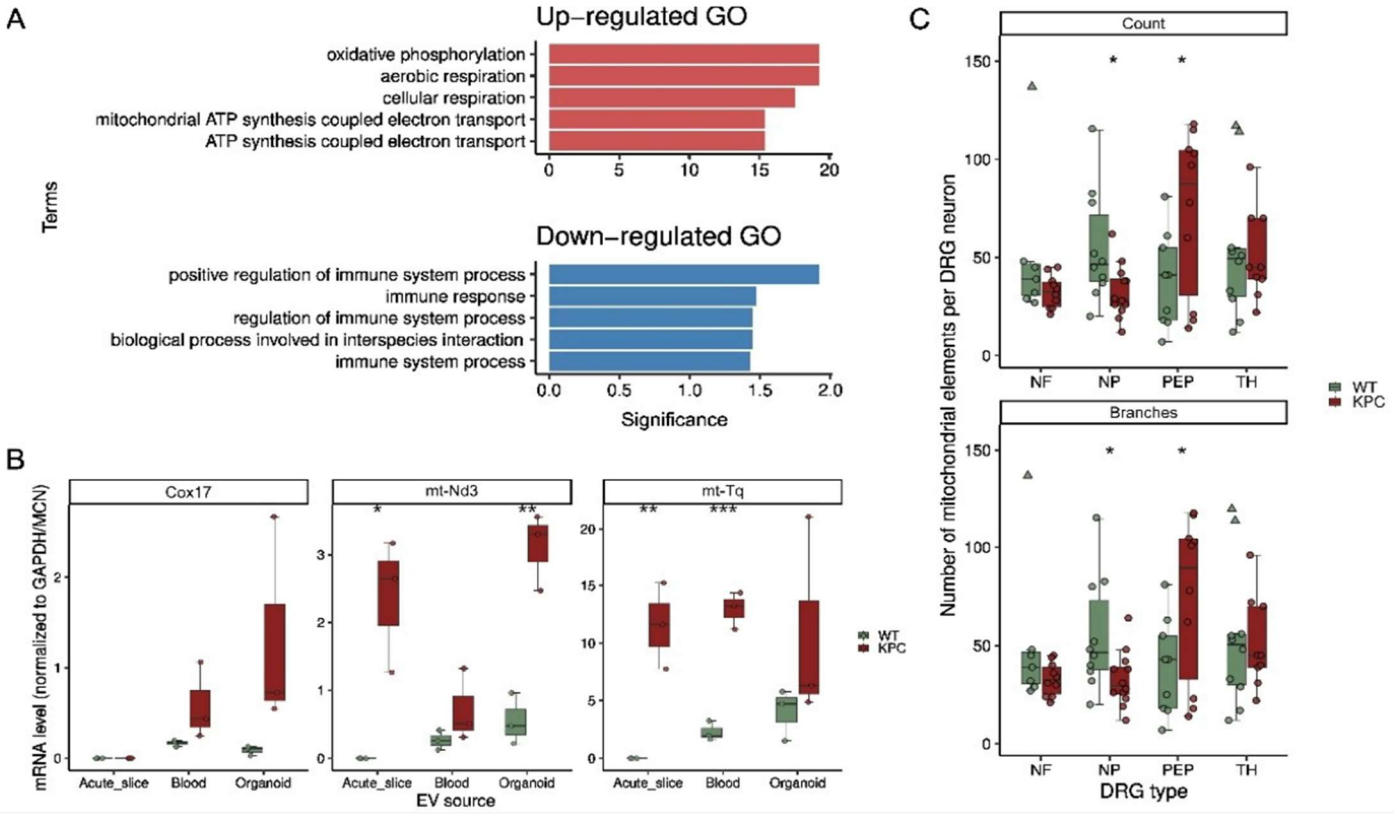


Fig. 34 A: Gene ontology (GO) annotations assigned to WT and KRAS FB+ DRGs. Red bars show the upregulated pathways while blue bars represent the down-regulated pathways. (B) mRNA expression levels of Cox17, mt-ND3, and mt-tQ in extracellular vescicles (EVs) from organoids, acute slices, and blood, comparing WT and KPC (N = 3). Expression levels were analyzed by a two-way ANOVA, followed by post hoc pairwise t-tests (WT vs. KPC) within each EV source. All values were normalized to GAPDH (for Cox17) or MCN (mitochondrial copy number for Mt-Nd3 and Mt-Tq). (C) Mitochondrial count and branch quantification in WT and KPC DRG neurons were analyzed by a two-way ANOVA, followed by post hoc pairwise t-tests within each DRG type.

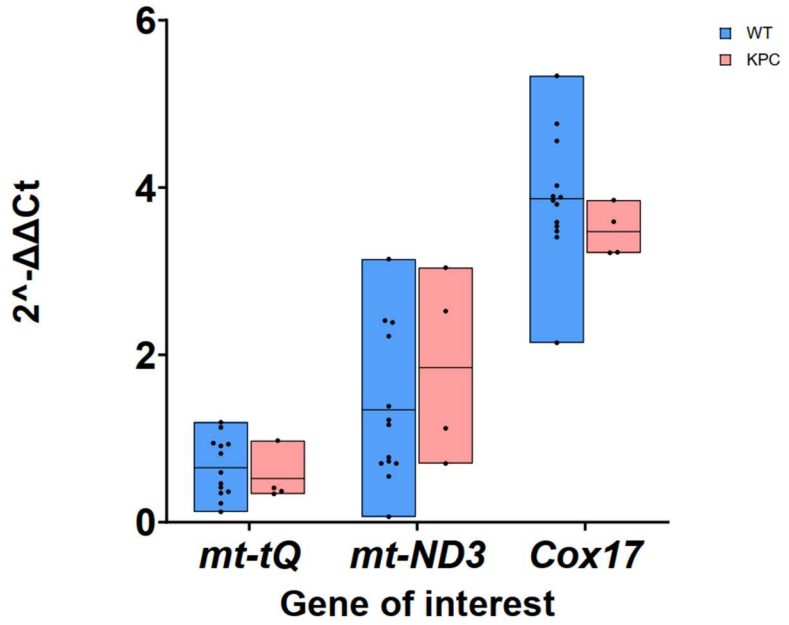


Fig. 35 Boxplot of RT-qPCR validation of genes of interest (*mttQ, Cox17* and *mt-ND3*) showing differential distribution across all animals tested (4 KPC, 13 WT). Samples were treated as technical replicates, as 20 cells were pooled for each animal starting from lysates sent to scRNA seq analysis. *mttQ* and *mt-ND3* normalized on relative mitochondrial copy number, *Cox17* normalized to *GAPDH*.

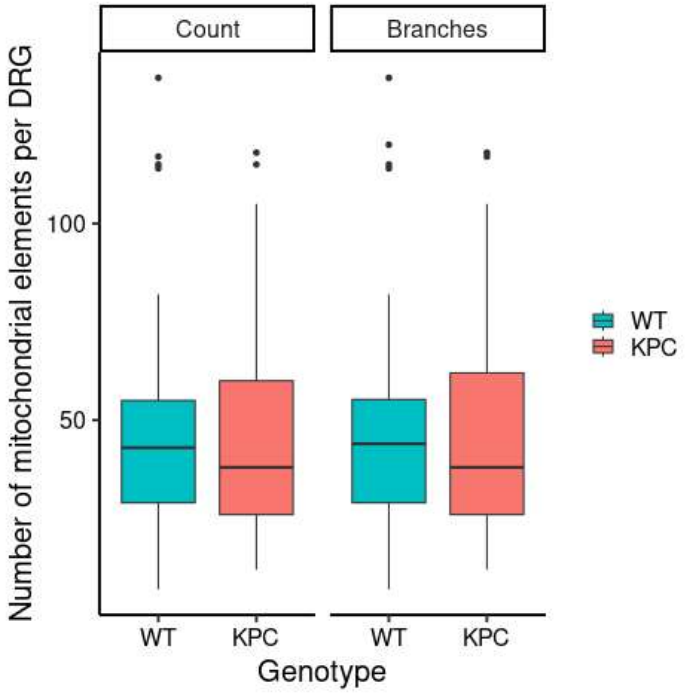


Fig. 36 Mitochondrial count and number of branches comparing FB+ WT and KRAS DRGs at the overall population level. No significant differences were identified.

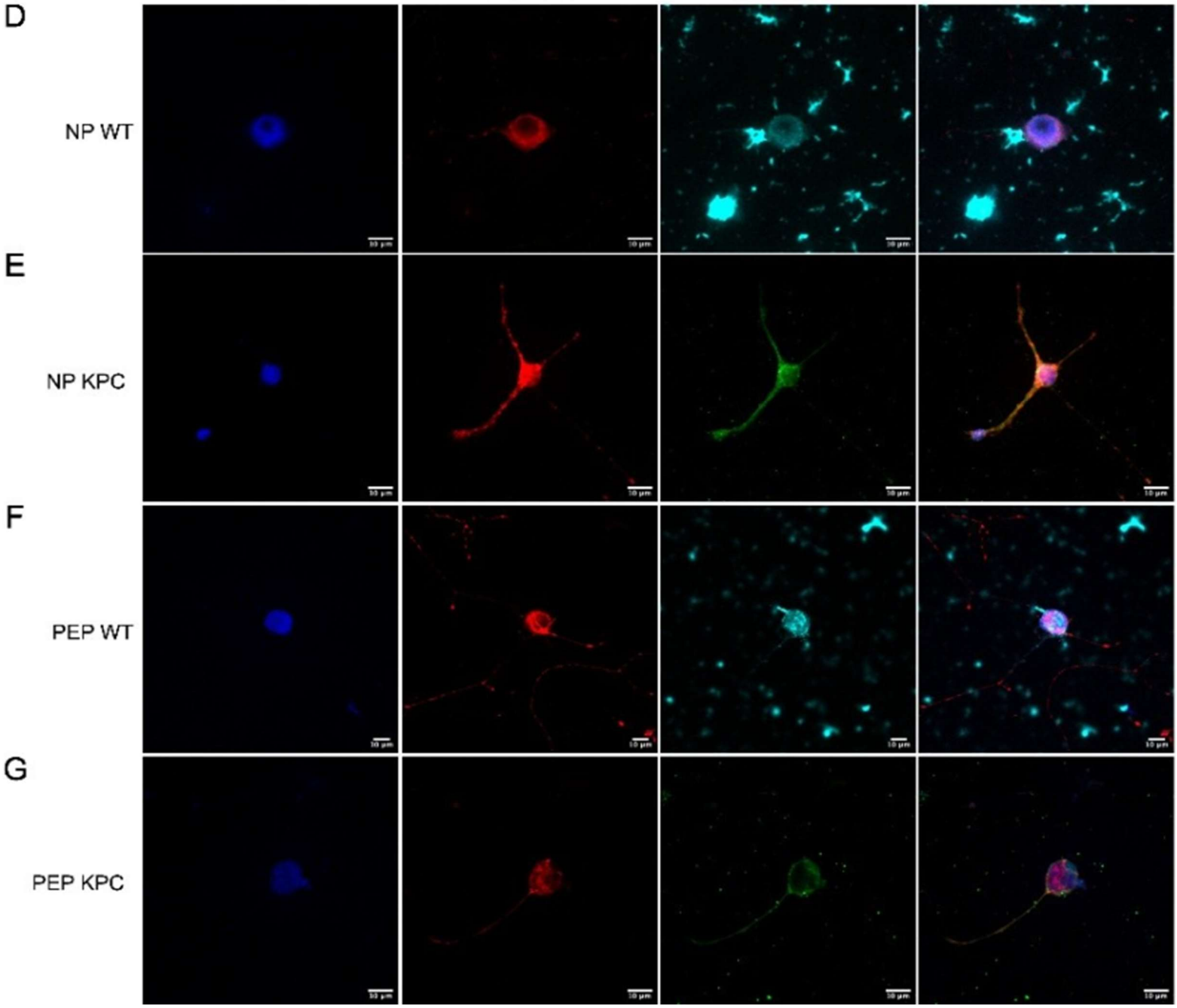


Fig. 37 Mitochondrial count and branch quantification in WT and KPC DRG neurons were analyzed by a two-way ANOVA, followed by post hoc pairwise t-tests within each DRG type. (D-G) Mitored and immunostaining using antibodies against Neurofilament 200 (NF), Isolectin B4 (IB4), Substance P (SP), and Tyrosine Hydroxylase (TH) on WT and KPC FB+ DRGs.

7. DISCUSSION

Here, we applied single-cell RNA sequencing (scRNA-seq) to retrogradely labeled dorsal root ganglia (DRGs) to profile sensory neuron subtypes innervating healthy, PanIN, and early PDAC tissues, and to identify alterations in neuronal gene expression associated with disease progression.

Our initial unsupervised clustering produced broad clusters whose transcriptional signatures did not neatly correspond to distinct DRG subtypes. To address this challenge, we anchored our dataset to the well-characterized DRG dataset generated by Usoskin and colleagues, who utilized comparable methodologies for single-cell profiling (Usoskin et al., 2015). We selected the Usoskin's study as reference dataset over other available resources for several reasons. For example, the study by Zeisel et al. (Zeisel et al., 2018) surveyed the entire mouse nervous system, lacking a dedicated emphasis on sensory neurons. The dataset from Hockley et al. (Hockley et al., 2019) covered only thoracolumbar and lumbosacral DRGs rather than the full range of DRG populations. Meanwhile, the work by Kupari et al. (Kupari et al., 2021) was based on primate rather than mouse DRGs. Notably, both Hockley et al. and Kupari et al. also referenced Usoskin et al.'s classification framework (Usoskin et al., 2015). Guided by this robust reference, we could confidently classify our DRG cells into four canonical sensory neuron subtypes: neurofilament-containing (NF), non-peptidergic (NP), peptidergic (PEP), and tyrosine hydroxylase–expressing (TH) neurons. This reference-based approach not only allowed us to overcome the limitations of nonspecific clustering outcomes but also positioned our findings within a well-established taxonomy of mouse DRG subtypes. Consequently, it serves as a foundation for further exploration of the molecular mechanisms underpinning neuronal involvement in early PDAC progression.

A intriguing outcome from both our transcriptomic and immunofluorescence (IF) analyses was the predominant role of NF neurons in pancreatic innervation, accounting for roughly two-thirds of retrogradely labeled (FB^+) DRGs in our scRNA-seq dataset and approximately 40% by IF. This finding is in line with the recent work by Thiel and colleagues, where sensory neurons innervating

PDAC tissue shift towards a NF subtype (Swain et al., 2023). This observation suggests a potentially significant contribution of large-diameter, myelinated NF neurons to pancreatic physiology and early tumorigenesis (Swain et al., 2023). Although NF neurons are typically associated with proprioception and cutaneous mechanoreception, their marked enrichment in our data suggests they may also sense glandular distension or tissue injury within the pancreas (Demir et al., 2015). Notably, even subtle mechanical perturbations during abdominal surgery can precipitate pancreatitis, and rodent models implicate mechanosensory Piezo ion channels on pancreatic acinar cells as key factors (Demir et al., 2015; Saloman et al., 2018). Furthermore, pancreatic stellate cells and β cells also express Piezo channels linked to fibrosis and insulin secretion, respectively (Saloman et al., 2018). Taken together, these findings support the notion that NF neurons could be uniquely positioned to detect mechanical changes during early PDAC development, thereby influencing disease progression.

In contrast to the stability of NF, PEP, and TH neuron proportions, we observed a significant reduction in NP neurons in KPC mice relative to wild-type (WT) controls. This decrease was consistently detected in both scRNA-seq and IF data, supporting its biological relevance. Reduced NP innervation in early PDAC aligns with a broader literature noting changes in sensory neuronal innervation within tumor regions (Demir et al., 2015; Saloman et al., 2018). The functional significance of NP neurons in modulating local inflammation (Zhang S. et al., 2021) suggests that their loss could deregulate immune cell activity in the pancreatic microenvironment, fuelling unchecked pro-inflammatory signals and possibly accelerating tumour progression. Thus, NP neurons may represent an early target for therapeutic strategies designed to modulate neuroimmune interactions in PDAC.

The coherence between the transcriptomic findings and IF validation underscores the reliability of data interpretation and the robustness of the methods. Both modalities converged on the same result—differential representation of DRG subtypes in the pancreas—laying a foundation for future work exploring how these subpopulations contribute to PDAC pathophysiology and whether they might be harnessed for early detection or therapeutic intervention.

An unexpected finding from our study was the detection of upregulatated DRG transcripts in EVs preparations from multiple sources. We propose that EV-mediated horizontal RNA transfer could be responsible for delivering transcripts from tumor cells to local or distant neurons. This mechanism aligns with broader themes of intercellular communication in oncology (Samandari et al., 2018; Long et al., 2022). Various exosomal cargos, including microRNAs, proteins, and long non-coding RNAs, are implicated in tumor–microenvironment interactions and have been explored as therapeutic targets (Richards et al., 2017; Yin Z. et al., 2019; Yin Z. et al., 2020; Liu Y. et al., 2021). In early PDAC, such EV-driven transfer of transcripts to neurons could contribute to neuropathological remodeling (Hinger et al., 2018).

Circulating EVs have garnered significant attention as potential biomarkers for both prognostic and diagnostic applications (Hsu et al., 2023). Although EV characterization was not our primary goal, our findings that *Snca*, and several mitochondria-related genes (*Cox17*, *mt-ND3*, and *mt-tQ*)—each associated with tumor cell survival or cancer progression (Suzuki et al., 2003; Shekoohi et al., 2021; Bianchini et al., 2023)—are enriched in EVs from KPC mice presents the intriguing possibility of harnessing these molecules as early prognostic biomarkers for pancreatic oncogenesis. Moreover, the detection of *Pdx1-CreERT2* transcripts in EVs and DRG raises important concerns about Cre-dependent mouse models of cancer. If Cre RNA is transferred by EVs between tissues then it may also have the ability to promote recombination and subsequent expression of oncogenic mutations in these tissues, leading to "leakiness" of the model. In the case of the KPC model used here, an inducible Pdx1-CreERT2 line was used, thus recombination will not occur in the absence of tamoxifen. However, such recombination could potentially occur with a constitutive Cre-driver, and it would thus be an interesting line of research to examine horizontal RNA transfer in mouse models based on constitutive Cre.

Gene ontology (GO) analysis of differentially expressed genes revealed that upregulated transcripts were enriched in mitochondrial pathways. This finding aligns with MitoTracker analysis of DRG innervating KPC tissue, which showed increased mitochondrial abundance and branching in

peptidergic neurons (PEP). In contrast, non-peptidergic (NP) neurons exhibited lower mitochondrial counts and reduced branching. Given the reduced proportion of NP neurons in KPC mice, and the potential role of these neurons in shaping local inflammatory responses (Demir et al., 2015), this again highlights the therapeutic potential of targeting this class of neuron, particularly for strategies focused on neuroimmune modulation.

An important question to address in our study is the mechanism underlying PDAC-associated changes in neuronal innervation compared to the normal pancreas. A recent study by Thiel et al. (Thiel et al., 2025) demonstrated that hyperinnervation in PDAC arises primarily from axonal sprouting rather than neurogenesis, and that intrapancreatic cancers may attract NF neurons from nearby organs. Whether extracellular-vesicle transfer of key components contributes to such a process is an intriguing avenue for further research.

In conclusion, our findings identify the specific DRG classes that innervate both the healthy and KPC pancreas. By integrating scRNA-seq data with a comprehensive reference atlas (Usoskin et al. 2015), we classified these neurons and found that NF neurons are the predominant class, while NP neurons are selectively reduced in KPC mice. The scRNA-seq data also uncovered changes in neuronal gene expression during PDAC development, in particular the identification of an upregulated truncated Pdx1 transcript in tumor-innervating DRGs and in EVs from KPC mice and organoids. Whether EV transfer of oncogenic or developmental signals facilitates tumor progression, alters neuronal excitability, or rewires local networks remains an avenue for further inquiry. Collectively, these insights deepen our understanding of sensory neuron function in early PDAC and highlight new possibilities for therapeutic and diagnostic strategies targeting the neuron–tumor axis.

Despite these encouraging findings, I acknowledge one major limiting point of this study, that is the unbalanced cohort of tumor mice (N=4) with respect to the healthy ones (N=13). The reason for this is that we initially tested and optimized the protocol using 6 WT (C57BL/6J) mice. We collected an average of 40 cells per animal, which were then submitted for sequencing. Upon receiving and positively evaluating the results from this first batch, we proceeded to replicate the protocol in 8 KPC

and 8 additional WT mice (C57BL/6J), again collecting an average of 40 cells per animal. In parallel with the single-cell picking from KPC animals, we performed histological analysis of the pancreas to assess tumor stage and/or the presence of pre-neoplastic lesions. Unfortunately, only 4 out of the 8 KPC animals showed histologically confirmed PDAC. Because the single-cell samples had already been submitted for sequencing prior to obtaining the histological results, we subsequently excluded the 4 KPC mice without PDAC from downstream analyses. Of note, 2 of these non-tumor-bearing KPC mice were later used as mock controls for subsequent validation experiments.

In this context, we believe that the validity of our findings is supported by statistically significant results and further corroborated by multiple layers of experimental validation. Importantly, if the dataset were strongly biased due to group imbalance, we would expect to detect significant differences across all measured variables, particularly in the relative abundance of sensory neuronal subtypes innervating the healthy versus tumor-bearing pancreas. This was not the case, suggesting that our conclusions are not an artifact of group size discrepancy

8. BIBLIOGRAPHY

Agerskov RH, Nyeng P. Innervation of the pancreas in development and disease. Development 2024;15;151(2):dev202254.

Albo D, Akay CL, Marshall CL, et al. Neurogenesis in colorectal cancer is a marker of aggressive tumor behavior and poor outcomes. Cancer 2011;1;117(21):4834-45.

Anders S, Pyl PT, Huber W. HTSeq—a Python framework to work with high-throughput sequencing data. bioinformatics 2015;31:166–169

Andrews S. FastQC: A Quality Control Tool for High Throughput Sequence Data. Babraham Bioinformatics - FastQC A Quality Control tool for High Throughput Sequence Data. 2010.

Atkinson MA, Campbell-Thompson M, Kusmartseva I, Kaestner KH. Organisation of the human pancreas in health and in diabetes. Diabetologia. 2020 Oct;63(10):1966-1973.

Ayala GE, Dai H, Powell M, et al. Cancer-related axonogenesis and neurogenesis in prostate cancer. Clin Cancer Res 2008;1;14(23):7593-603.

Ayala GE, Dai H, Powell M, Li R, Ding Y, Wheeler TM, Shine D, Kadmon D, Thompson T, Miles BJ, Ittmann MM, Rowley D. Cancer-related axonogenesis and neurogenesis in prostate cancer. Clin Cancer Res. 2008 Dec 1;14(23):7593-603. doi: 10.1158/1078-0432.CCR-08-1164. PMID: 19047084.

Bai H, Li H, Zhang W, et al. Inhibition of chronic pancreatitis and pancreatic intraepithelial neoplasia (PanIN) by capsaicin in LSL-KrasG12D/Pdx1-Cre mice. Carcinogenesis 2011.

Balak, J. R. A., Juksar, J., Carlotti, F., Lo Nigro, A., & De Koning, E. J. P. (2019). Organoids from the Human Fetal and Adult Pancreas. *Current Diabetes Reports*, *19*(12), 160

Bianchini M, Giambelluca M, Scavuzzo MC, et al. In Pancreatic Adenocarcinoma Alpha-Synuclein Increases and Marks Peri-Neural Infiltration. Int J Mol Sci 2022;29;23(7):3775.

Blighe K, Rana S, Lewis M. EnhancedVolcano: Publication-ready volcano plots with enhanced colouring and labeling. 2024. Available at: https://github.com/kevinblighe/EnhancedVolcano.

Boj SF, Hwang CI, Baker LA, et al. Organoid models of human and mouse ductal pancreatic cancer. Cell 2015;15;160(1-2):324-38.

Capodanno, Y., & Hirth, M. (2023). Targeting the Cancer–Neuronal Crosstalk in the Pancreatic Cancer Microenvironment. *International Journal of Molecular Sciences*, *24*(19), 14989.

Cardona-Alberich, A., Tourbez, M., Pearce, S. F., & Sibley, C. R. (2021). Elucidating the cellular dynamics of the brain with single-cell RNA sequencing. *RNA Biology*, *18*(7), 1063–1084.

Carlson M (2019). GO.db: A set of annotation maps describing the entire Gene Ontology. R package version 3.8.2.

Casamitjana, J., Espinet, E., & Rovira, M. (2022). Pancreatic Organoids for Regenerative Medicine and Cancer Research. *Frontiers in Cell and Developmental Biology*, *10*, 886153.

Catala, M., & Kubis, N. (2013). Gross anatomy and development of the peripheral nervous system. In *Handbook of Clinical Neurology* (Vol. 115, pp. 29–41).

Ceyhan, G.O.; Bergmann, F.; Kadihasanoglu, M.; Altintas, B.; Demir, I.E.; Hinz, U.; Müller, M.W.; Giese, T.; Büchler, M.W.; Giese, N.A.; et al. Pancreatic neuropathy and neuropathic pain—A comprehensive pathomorphological study of 546 cases. Gastroenterology 2009, 136, 177–186.e1.

Ceyhan, G.O.; Demir, I.E.; Rauch, U.; Bergmann, F.; Müller, M.W.; Büchler, M.W.; Friess, H.; Schäfer, K.H. Pancreatic neuropathy results in "neural remodeling" and altered pancreatic innervation in chronic pancreatitis and pancreatic cancer. Am. J. Gastroenterol. 2009, 104, 2555–2565

Chen, G., Ning, B., & Shi, T. (2019). Single-Cell RNA-Seq Technologies and Related Computational Data Analysis. *Frontiers in Genetics*, *10*, 317

Chen, H., Zhuo, Q., Ye, Z., Xu, X., & Ji, S. (2021). Organoid model: A new hope for pancreatic cancer treatment? *Biochimica et Biophysica Acta (BBA) - Reviews on Cancer*, *1875*(1), 188466.

Chen, M.-Y., Zhao, F.-L., Chu, W.-L., Bai, M.-R., & Zhang, D.-M. (2023). A review of tamoxifen administration regimen optimization for Cre/loxp system in mouse bone study. Biomedicine & Pharmacotherapy, 165, 115045

Cheng J, Wang R, Chen Y. Neuroimmune Interactions in Pancreatic Cancer. Biomedicines. 2025 Mar 2;13(3):609

Chien HJ, Chiang TC, Peng SJ, Chung MH, Chou YH, Lee CY, Jeng YM, Tien YW, Tang SC. Human pancreatic afferent and efferent nerves: mapping and 3-D illustration of exocrine, endocrine, and adipose innervation. Am J Physiol Gastrointest Liver Physiol. 2019 Nov 1;317(5):G694-G706.

Chiu YC, Hua TE, Fu YY, Pasricha PJ & Tang SC (2012) 3-D imaging and illustration of the perfusive mouse islet sympathetic innervation and its remodelling in injury. Diabetologia 55: 3252–3261

Corrò, C., Novellasdemunt, L., & Li, V. S. W. (2020). A brief history of organoids. *American Journal of Physiology-Cell Physiology*, *319*(1), C151–C165

Demir IE, Friess H, Ceyhan GO. Neural plasticity in pancreatitis and pancreatic cancer. Nat Rev Gastroenterol Hepatol 2015.

Demir, I.E.; Schorn, S.; Schremmer-Danninger, E.; Wang, K.; Kehl, T.; Giese, N.A.; Algül, H.; Friess, H.; Ceyhan, G.O. Perineural mast cells are specifically enriched in pancreatic neuritis and neuropathic pain in pancreatic cancer and chronic pancreatitis. PLoS ONE2013, 8, e60529

Ding X, Chen J, Zeng W. Neuroimmune regulation in the pancreas. Fundam Res 2022;5;4(2):201-205.

Dobin A, Davis CA, Schlesinger F, et al. STAR: ultrafast universal RNA-seq aligner. Bioinformatics. 2013 Jan 1;29(1):15-21.

Dolenšek J, Rupnik MS & Stožer A (2015) Structural similarities and differences between the human and the mouse pancreas. *Islets* 7

Durinck S, Moreau Y, Kasprzyk A, et al. BioMart and Bioconductor: a powerful link between biological databases and microarray data analysis. Bioinformatics 2005;15;21(16):3439-40.

Esposito, M. F., Malayil, R., Hanes, M., & Deer, T. (2019). Unique Characteristics of the Dorsal Root Ganglion as a Target for Neuromodulation. *Pain Medicine*, *20*(Supplement_1), S23–S30.

Ewels P, Magnusson M, Lundin S, et al. MultiQC: summarize analysis results for multiple tools and samples in a single report. Bioinformatics 2016;1;32(19):3047-8.

Falcon S, Gentleman R. Using GOstats to test gene lists for GO term association. Bioinformatics 2007;15;23(2):257–8.

Fasanella KE, Christianson JA, Chanthaphavong RS, et al. Distribution and neurochemical identification of pancreatic afferents in the mouse. J Comp Neurol 2008;1;509(1):42-52.

Faulkner, S., Jobling, P., March, B., Jiang, C. C., & Hondermarck, H. (2019). Tumor Neurobiology and the War of Nerves in Cancer. *Cancer Discovery*, *9*(6), 702–710

Gasparini G, Pellegatta M, Crippa S, et al. Nerves and Pancreatic Cancer: New Insights into a Dangerous Relationship. 26;11(7):893.

Gopinathan, A., Morton, J. P., Jodrell, D. I., & Sansom, O. J. (2015). GEMMs as preclinical models for testing pancreatic cancer therapies. *Disease Models & Mechanisms*, *8*(10), 1185–1200

Grapin-Botton, A., & Kim, Y. H. (2022). Pancreas organoid models of development and regeneration. *Development*, *149*(20), dev201004.

Gu G, Dubauskaite J, Melton DA. Direct evidence for the pancreatic lineage: NGN3+ cells are islet progenitors and are distinct from duct progenitors. Development. 2002 May;129(10):2447-57.

Guillot J., Dominici C., Lucchesi A., Nguyen H.T.T., Puget A., Hocine M., Rangel-Sosa M.M., Simic M., Nigri J., Guillaumond F., et al. Sympathetic axonal sprouting induces changes in macrophage populations and protects against pancreatic cancer. Nat. Commun. 2022;13:1985.

Guyot M., Simon T., Ceppo F., Panzolini C., Guyon A., Lavergne J., Murris E., Daoudlarian D., Brusini R., Zarif H., et al. Pancreatic nerve electrostimulation inhibits recent-onset autoimmune diabetes. Nat. Biotechnol. 2019;37:1446–1451.

Halbrook, C. J., Lyssiotis, C. A., Pasca Di Magliano, M., & Maitra, A. (2023). Pancreatic cancer: Advances and challenges. *Cell*, *186*(8),

Hao Y, Stuart T, Kowalski MH, et al. Dictionary learning for integrative, multimodal and scalable single-cell analysis. Nat Biotechnol 2024; Feb;42(2):293-304.

Harrison PW, Amode MR, Austine-Orimoloye O, et al. Ensembl 2024. Nucleic acids research 2024;52:891–899.

Hartley SW, Mullikin JC. QoRTs: a comprehensive toolset for quality control and data processing of RNA-Seq experiments. BMC Bioinformatics 2015.

Hennig BP, Velten L, Racke I, et al. Large-Scale Low-Cost NGS Library Preparation Using a Robust Tn5 Purification and Tagmentation Protocol. G3 (Bethesda. 2018;4;8(1):79-89.

Higashiyama H, Sumitomo H, Ozawa A, Igarashi H, Tsunekawa N, Kurohmaru M, Kanai Y. Anatomy of the Murine Hepatobiliary System: A Whole-Organ-Level Analysis Using a Transparency Method. Anat Rec (Hoboken). 2016 Feb;299(2):161-72.

Hinger SA, Cha DJ, Franklin JL, et al. Diverse Long RNAs Are Differentially Sorted into Extracellular Vesicles Secreted by Colorectal Cancer Cells. Cell Rep 2018;725.

Hockley JRF, Taylor TS, Callejo G, et al. Single-cell RNAseq reveals seven classes of colonic sensory neuron. Gut 2019; Apr;68(4):633-644.

Horiguchi SI & Kamisawa T (2010) Major duodenal papilla and its normal anatomy. Dig Surg 27: 90–93

Hruban RH, Adsay NV, Albores-Saavedra J, et al. Pathology of genetically engineered mouse models of pancreatic exocrine cancer: consensus report and recommendations. Cancer Res. 2006 Jan 1;66(1):95-106.

Hsu SK, Jadhao M, Liao WT, et al. The Role of Exosomes in Pancreatic Ductal Adenocarcinoma Progression and Their Potential as Biomarkers. Cancers 2023;15;15(6):1776.

Huan,H.B.; Wen, X.D.; Chen, X.J.; Wu, L.; Wu, L.L.; Zhang, L.; Yang, D.P.; Zhang, X.; Bie, P.; Qian, C.; et al. Sympathetic nervous system promotes hepatocarcinogenesis by modulating inflammation through activation of alpha1-adrenergic receptors of Kupffer cells. Brain Behav. Immun. 2017, 59, 118–134.

Huang D, Su S, Cui X, et al. Nerve fibers in breast cancer tissues indicate aggressive tumor progression. Medicine (Baltimore 2014; Dec;93(27):e172.

Huang FF, Cui WH, Ma LY, et al. Crosstalk of nervous and immune systems in pancreatic cancer. Front Cell Dev Biol 2023;11

Huch M, Bonfanti P, Boj SF, et al. Unlimited in vitro expansion of adult bi-potent pancreas progenitors through the Lgr5/R-spondin axis. EMBO J 2013;16;32(20):2708-21.

Huch, M., Knoblich, J. A., Lutolf, M. P., & Martinez-Arias, A. (2017). The hope and the hype of organoid research. *Development*, *144*(6), 938–941

Iwasaki, T.; Hiraoka, N.; Ino, Y.; Nakajima, K.; Kishi, Y.; Nara, S.; Esaki, M.; Shimada, K.; Katai, H. Reduction of intrapancreatic neural density in cancer tissue predicts poorer outcome in pancreatic ductal carcinoma. Cancer Sci. 2019, 110, 1491–1502.

Jin EH, Sung JK, Lee SI, et al. Mitochondrial NADH Dehydrogenase Subunit 3 (MTND3) Polymorphisms are Associated with Gastric Cancer Susceptibility. Int J Med Sci 2018;10;15(12):1329-1333.

Jones, I., Yelhekar, T. D., Wiberg, R., Kingham, P. J., Johansson, S., Wiberg, M., & Carlsson, L. (2018). Development and validation of an in vitro model system to study peripheral sensory neuron development and injury. Scientific Reports, 8(1), 15961

Jortner BS. Common Structural Lesions of the Peripheral Nervous System. Toxicol Pathol. 2020 Jan;48(1):96-104

Jovic, D., Liang, X., Zeng, H., Lin, L., Xu, F., & Luo, Y. (2022). Single-cell RNA sequencing technologies and applications: A brief overview. *Clinical and Translational Medicine*, *12*(3), e694

Jung M, Dourado M, Maksymetz J, et al. Cross-species transcriptomic atlas of dorsal root ganglia reveals species-specific programs for sensory function. Nat Commun 2023;23;14(1):366.

Keskinov, A. A., Tapias, V., Watkins, S. C., Ma, Y., Shurin, M. R., & Shurin, G. V. (2016). Impact of the Sensory Neurons on Melanoma Growth In Vivo. *PLOS ONE*, *11*(5), e0156095.

Kim, B., Lee, E., & Kim, J. K. (2019). Analysis of Technical and Biological Variability in Single-Cell RNA Sequencing. In G.-C. Yuan (Ed.), *Computational Methods for Single-Cell Data Analysis* (Vol. 1935, pp. 25–43).

Kolbeinsson, H. M., Chandana, S., Wright, G. P., & Chung, M. (2023). Pancreatic Cancer: A Review of Current Treatment and Novel Therapies. *Journal of Investigative Surgery*, *36*(1)

Kolodziejczyk, A. A., Kim, J. K., Svensson, V., Marioni, J. C., & Teichmann, S. A. (2015). The Technology and Biology of Single-Cell RNA Sequencing. *Molecular Cell*, *58*(4), 610–620.

Kretzschmar, K. (2021). Cancer research using organoid technology. *Journal of Molecular Medicine*, *99*(4), 501–515.

Kuksin, M., Morel, D., Aglave, M., Danlos, F.-X., Marabelle, A., Zinovyev, A., Gautheret, D., & Verlingue, L. (2021). Applications of single-cell and bulk RNA sequencing in onco-immunology. *European Journal of Cancer*, *149*, 193–210

Kupari J, Usoskin D, Parisien M, et al. Single cell transcriptomics of primate sensory neurons identifies cell types associated with chronic pain. Nat Commun 2021;8;12(1):1510.

Lan, Y., Zou, S., Wang, W., Chen, Q., & Zhu, Y. (2023). Progress in cancer neuroscience. *MedComm*, *4*(6), e431

Lanigan, L. G., Russell, D. S., Woolard, K. D., Pardo, I. D., Godfrey, V., Jortner, B. S., Butt, M. T., & Bolon, B. (2021). Comparative Pathology of the Peripheral Nervous System. *Veterinary Pathology*, *58*

Li CL, Li KC, Wu D, et al. Somatosensory neuron types identified by high-coverage single-cell RNA-sequencing and functional heterogeneity. Epub 2015 Dec 22 Erratum in: Cell Res 2016; Jan;26(1):83-102.

Li, C., Wang, S., Chen, Y., & Zhang, X. (2018). Somatosensory Neuron Typing with High-Coverage Single-Cell RNA Sequencing and Functional Analysis. Neuroscience Bulletin, 34(1), 200–207

Li, G.; Jiang, Y.; Tong, H.; Liu, J.; Jiang, Z.; Zhao, Y.; Tan, K.; Zhang, Y.; Yin, X.; Yun, H.; et al. Sciatic nerve stimulation enhances NKcell cytotoxicity through dopamine signaling and synergizes immunotherapy in triple-negative breast cancer. Drug Resist Updat 2025, 79, 101212.

Li, J., Kang, R., & Tang, D. (2021). Cellular and molecular mechanisms of perineural invasion of pancreatic ductal adenocarcinoma. *Cancer Communications*, *41*(8), 642–660.

Li, X., & Wang, C.-Y. (2021). From bulk, single-cell to spatial RNA sequencing. *International Journal of Oral Science*, *13*(1), 36

Lindsay TH, Halvorson KG, Peters CM, et al. A quantitative analysis of the sensory and sympathetic innervation of the mouse pancreas. Neuroscience 2006;137:1417–26.

Liu JA, Yu J, Cheung CW. Immune Actions on the Peripheral Nervous System in Pain. Int J Mol Sci. 2021 Feb 1;22(3):1448

Liu Y, Tang T, Yang X, et al. Tumor-derived exosomal long noncoding RNA LINC01133, regulated by Periostin, contributes to pancreatic ductal adenocarcinoma epithelial-mesenchymal transition through the Wnt/β-catenin pathway by silencing AXIN2. Oncogene 2021; Apr 40(17):3164-3179.

Lkhagvasuren B, Mee-Inta O, Zhao ZW, et al. Pancreas-Brain Crosstalk. Front Neuroanat 2021.

Long D, Tian XD, Yang YM. Emerging Role of Exosomal-Derived Long Noncoding RNAs in Human PDAC. Visc Med 2022; Feb;38(1):30-36.

Low, R. R. J., Lim, W. W., Nguyen, P. M., Lee, B., Christie, M., Burgess, A. W., Gibbs, P., Grimmond, S. M., Hollande, F., & Putoczki, T. L. (2021). The Diverse Applications of Pancreatic Ductal Adenocarcinoma Organoids. *Cancers*, *13*(19), 4979

Luecken, M. D., & Theis, F. J. (2019). Current best practices in single-cell RNA-seq analysis: A tutorial. *Molecular Systems Biology*, *15*(6), e8746

Lunde A, Glover JC. A versatile toolbox for semi-automatic cell-by-cell object-based colocalization analysis. Sci Rep 2020;4;10(1):19027.

Lv, G., Zhang, L., Gao, L., Cui, J., Liu, Z., Sun, B., Wang, G., & Tang, Q. (2023). The application of single-cell sequencing in pancreatic neoplasm: Analysis, diagnosis and treatment. *British Journal of Cancer*, *128*(2), 206–218

Makhmutova, M., & Caicedo, A. (2021). Optical Imaging of Pancreatic Innervation. *Frontiers in Endocrinology*, *12*, 663022

Mallya, K., Gautam, S. K., Aithal, A., Batra, S. K., & Jain, M. (2021). Modeling pancreatic cancer in mice for experimental therapeutics. *Biochimica et Biophysica Acta (BBA) - Reviews on Cancer*, *1876*(1)

Mancusi, R., & Monje, M. (2023). The neuroscience of cancer. *Nature*, *618*(7965), 467–479

Mardelle U, Bretaud N, Daher C, et al. From pain to tumor immunity: influence of peripheral sensory neurons in cancer. In: Front Immunol. 2024 Feb 16;15:1335387.

Marstrand-Daucé, L., Lorenzo, D., Chassac, A., Nicole, P., Couvelard, A., & Haumaitre, C. (2023). Acinar-to-Ductal Metaplasia (ADM): On the Road to Pancreatic Intraepithelial Neoplasia (PanIN) and Pancreatic Cancer. *International Journal of Molecular Sciences*, *24*(12), 9946.

Mauffrey P, Tchitchek N, Barroca V, Bemelmans AP, Firlej V, Allory Y, Roméo PH, Magnon C. Progenitors from the central nervous system drive neurogenesis in cancer. Nature. 2019 May;569(7758):672-678. doi: 10.1038/s41586-019-1219-y. Epub 2019 May 15. Erratum in: Nature. 2020 Jan;577(7792):E10. doi: 10.1038/s41586-019-1837-4. PMID: 31092925

McDonald OG. The biology of pancreatic cancer morphology. Pathology. 2022 Mar;54(2):236-247.

Meltzer, S., Santiago, C., Sharma, N., & Ginty, D. D. (2021). The cellular and molecular basis of somatosensory neuron development. *Neuron*, *109*(23), 3736–3757.

Middleton, S. J., Perez-Sanchez, J., & Dawes, J. M. (2022). The structure of sensory afferent compartments in health and disease. *Journal of Anatomy*, *241*(5), 1186–1210

Milojević M, Rožanc J, Vajda J, Činč Ćurić L, Paradiž E, Stožer A, Maver U, Vihar B. In Vitro Disease Models of the Endocrine Pancreas. Biomedicines. 2021 Oct 8;9(10):1415

Monje, M., Borniger, J. C., D'Silva, N. J., Deneen, B., Dirks, P. B., Fattahi, F., Frenette, P. S., Garzia, L., Gutmann, D. H., Hanahan, D., Hervey-Jumper, S. L., Hondermarck, H., Hurov, J. B., Kepecs, A., Knox, S. M., Lloyd, A. C., Magnon, C., Saloman, J. L., Segal, R. A., … Winkler, F. (2020). Roadmap for the Emerging Field of Cancer Neuroscience. *Cell*, *181*(2), 219–222

Ni, B., Yin, Y., Li, Z., Wang, J., Wang, X., & Wang, K. (2023). Crosstalk Between Peripheral Innervation and Pancreatic Ductal Adenocarcinoma. *Neuroscience Bulletin*, *39*(11), 1717–1731

Ordovas-Montanes, J.; Rakoff-Nahoum, S.; Huang, S.; Riol-Blanco, L.; Barreiro, O.; von Andrian, U.H. The Regulation of Immunological Processes by Peripheral Neurons in Homeostasis and Disease. Trends Immunol. 2015, 36, 578–604.

Orkin, R. W., Gehron, P., McGoodwin, E. B., Martin, G. R., Valentine, T., & Swarm, R. (1977). A murine tumor producing a matrix of basement membrane. *The Journal of Experimental Medicine*, *145*(1), 204–220.

Orth M, Metzger P, Gerum S, Mayerle J, Schneider G, Belka C, Schnurr M, Lauber K. Pancreatic ductal adenocarcinoma: biological hallmarks, current status, and future perspectives of combined modality treatment approaches. Radiat Oncol. 2019 Aug 8;14(1):141.

Park, W., Chawla, A., & O'Reilly, E. M. (2021). Pancreatic Cancer: A Review. *JAMA*, *326*(9), 851.

Partecke LI, Käding A, Trung DN, et al. Subdiaphragmatic vagotomy promotes tumor growth and reduces survival via TNFα in a murine pancreatic cancer model. Oncotarget 2017;4;8(14):22501-22512.

Pavlov V.A., Chavan S.S., Tracey K.J. Molecular and Functional Neuroscience in Immunity. Annu. Rev. Immunol. 2018;36:783–812

Picelli S, Faridani OR, Björklund AK, et al. Full-length RNA-seq from single cells using Smart-seq2. Nat Protoc 2014; Jan;9(1):171-81.

Qi, R., Ma, A., Ma, Q., & Zou, Q. (2020). Clustering and classification methods for single-cell RNA-sequencing data. *Briefings in Bioinformatics*, *21*(4), 1196–1208

Qiu Z, Wang Q, Liu L, et al. Riddle of the Sphinx: Emerging Role of Transfer RNAs in Human Cancer. Front Pharmacol 2021;12.

Renthal W, Tochitsky I, Yang L, et al. Transcriptional Reprogramming of Distinct Peripheral Sensory Neuron Subtypes after Axonal Injury. Neuron 2020;144.

Renz BW, Takahashi R, Tanaka T, et al. Wang TC. β2 Adrenergic-Neurotrophin Feedforward Loop Promotes Pancreatic Cancer. Cancer Cell 2018;90.

Renz BW, Tanaka T, Sunagawa M, et al. Cholinergic Signaling via Muscarinic Receptors Directly and Indirectly Suppresses Pancreatic Tumorigenesis and Cancer Stemness. Cancer Discov 2018.

Richards KE, Zeleniak AE, Fishel ML, et al. Cancer-associated fibroblast exosomes regulate survival and proliferation of pancreatic cancer cells. Oncogene 2017;30;36(13):1770-1778.

Rodríguez-Merced NJ, Callaway MK, Provenzano PP. Protocol to culture and image pancreatic ductal adenocarcinoma tumor slices to study T cell migration. STAR Protoc 2023;17;4(1):102135.

Romac JM, Shahid RA, Swain SM, et al. Piezo1 is a mechanically activated ion channel and mediates pressure induced pancreatitis. Nat Commun 2018;30;9(1):1715.

Saiki Y, Horii A. Molecular pathology of pancreatic cancer. Pathol Int. 2014 Jan;64(1):10-9.

Saloman JL, Albers KM, Li D, et al. Ablation of sensory neurons in a genetic model of pancreatic ductal adenocarcinoma slows initiation and progression of cancer. In: Proc Natl Acad Sci U S A. 2016 Mar.Vol 15;113(11):3078-83.

Saloman JL, Singhi AD, Hartman DJ, et al. Systemic Depletion of Nerve Growth Factor Inhibits Disease Progression in a Genetically Engineered Model of Pancreatic Ductal Adenocarcinoma. Pancreas 2018; Aug;47(7):856-863.

Samandari M, Julia MG, Rice A, et al. Liquid biopsies for management of pancreatic cancer. Transl Res 2018.

Saricaoglu ÖC, Teller S, Wang X, Wang S, Stupakov P, Heinrich T, Istvanffy R, Friess H, Ceyhan GO & Demir IE (2020) Localisation analysis of nerves in the mouse pancreas reveals the sites of highest nerve density and nociceptive innervation. Neurogastroenterol Motil 32: 13880

Seow, J. J. W., Wong, R. M. M., Pai, R., & Sharma, A. (2020). Single-Cell RNA Sequencing for Precision Oncology: Current State-of-Art. *Journal of the Indian Institute of Science*, *100*(3), 579–588

Shao JX, Wang B, Yao YN, et al. Autonomic nervous infiltration positively correlates with pathological risk grading and poor prognosis in patients with lung adenocarcinoma. Thorac Cancer 2016; Sep;7(5):588-598.

Shekoohi S, Rajasekaran S, Patel D, et al. Knocking out alpha-synuclein in melanoma cells dysregulates cellular iron metabolism and suppresses tumor growth. Sci Rep 2021;4;11(1):5267.

Sherman, M. H., & Beatty, G. L. (2023). Tumor Microenvironment in Pancreatic Cancer Pathogenesis and Therapeutic Resistance. *Annual Review of Pathology: Mechanisms of Disease*, *18*(1), 123–148

Sinha, S., Fu, Y.-Y., Grimont, A., Ketcham, M., Lafaro, K., Saglimbeni, J. A., Askan, G., Bailey, J. M., Melchor, J. P., Zhong, Y., Joo, M. G., Grbovic-Huezo, O., Yang, I.-H., Basturk, O., Baker, L., Park, Y., Kurtz, R. C., Tuveson, D., Leach, S. D., & Pasricha, P. J. (2017). PanIN Neuroendocrine Cells Promote Tumorigenesis via Neuronal Cross-talk. *Cancer Research*, *77*(8), 1868–1879

Stopczynski, R. E., Normolle, D. P., Hartman, D. J., Ying, H., DeBerry, J. J., Bielefeldt, K., Rhim, A. D., DePinho, R. A., Albers, K. M., & Davis, B. M. (2014). Neuroplastic Changes Occur Early in the Development of Pancreatic Ductal Adenocarcinoma. *Cancer Research*, *74*(6), 1718–1727.

Suzuki C, Daigo Y, Kikuchi T, et al. Identification of COX17 as a therapeutic target for non-small cell lung cancer. Cancer Res 2003.

Swain SM, Liddle RA. Mechanosensing Piezo channels in gastrointestinal disorders. J Clin Invest. 2023 Oct 2;133(19):e171955.

Tang, S.C.; Baeyens, L.; Shen, C.N.; Peng, S.J.; Chien, H.J.; Scheel, D.W.; Chamberlain, C.E.; German, M.S. Human pancreatic neuro-insular network in health and fatty infiltration. Diabetologia 2018, 61, 168–181.

Tavares-Ferreira D, Shiers S, Ray P. Spatial transcriptomics of dorsal root ganglia identifies molecular signatures of human nociceptors. Sci Transl Med 2022;16;14(632):eabj8186.

Thiel V, Renders S, Panten J, et al. Characterization of single neurons reprogrammed by pancreatic cancer. Nature 2025; Feb 17.

Timmins, N. E., & Nielsen, L. K. (2007). Generation of Multicellular Tumor Spheroids by the Hanging-Drop Method. In H. Hauser & M. Fussenegger (Eds.), *Tissue Engineering* (Vol. 140, pp. 141–151). Humana Press

Tiriac, H., Plenker, D., Baker, L. A., & Tuveson, D. A. (2019). Organoid models for translational pancreatic cancer research. *Current Opinion in Genetics & Development*, *54*, 7–11.

Turner, D. A., Baillie-Johnson, P., & Martinez Arias, A. (2016). Organoids and the genetically encoded self-assembly of embryonic stem cells. *BioEssays*, *38*(2), 181–191

Usoskin D, Furlan A, Islam S, et al. Unbiased classification of sensory neuron types by large-scale single-cell RNA sequencing. Nat Neurosci 2015; Jan;18(1):145-53.

Van De Sande, B., Lee, J. S., Mutasa-Gottgens, E., Naughton, B., Bacon, W., Manning, J., Wang, Y., Pollard, J., Mendez, M., Hill, J., Kumar, N., Cao, X., Chen, X., Khaladkar, M., Wen, J., Leach, A., & Ferran, E. (2023). Applications of single-cell RNA sequencing in drug discovery and development. *Nature Reviews Drug Discovery*, *22*(6), 496–520.

Veiga-Fernandes H., Mucida D. Neuro-Immune Interactions at Barrier Surfaces. Cell. 2016;165:801–811. doi: 10.1016/j.cell.2016.04.041

Veiga-Fernandes H., Pachnis V. Neuroimmune regulation during intestinal development and homeostasis. Nat. Immunol. 2017;18:116–122.

Wang L, Wang S, Li W. RSeQC: quality control of RNA-seq experiments. Bioinformatics 2012;15;28(16):2184–5.

Wang, J., Chen, Y., Li, X., & Zou, X. (2021). Perineural Invasion and Associated Pain Transmission in Pancreatic Cancer. *Cancers*, *13*(18), 4594

Wang, W., Li, L., Chen, N., Niu, C., Li, Z., Hu, J., & Cui, J. (2020). Nerves in the Tumor Microenvironment: Origin and Effects. *Frontiers in Cell and Developmental Biology*, *8*, 601738

Wehrwein, E. A., Orer, H. S., & Barman, S. M. (2016). Overview of the Anatomy, Physiology, and Pharmacology of the Autonomic Nervous System. In R. Terjung (Ed.), *Comprehensive Physiology* (1st ed., pp. 1239–1278).

Wickham H. ggplot2. Wiley interdisciplinary reviews: computational statistics 2011;3:180–185.

Winkler, F., Venkatesh, H. S., Amit, M., Batchelor, T., Demir, I. E., Deneen, B., Gutmann, D. H., Hervey-Jumper, S., Kuner, T., Mabbott, D., Platten, M., Rolls, A., Sloan, E. K., Wang, T. C., Wick, W., Venkataramani, V., & Monje, M. (2023). Cancer neuroscience: State of the field, emerging directions. *Cell*, *186*(8), 1689–1707

Wood, L. D., Canto, M. I., Jaffee, E. M., & Simeone, D. M. (2022). Pancreatic Cancer: Pathogenesis, Screening, Diagnosis, and Treatment. *Gastroenterology*, *163*(2), 386-402.e1.

Xie, K., Cheng, X., Zhu, T., & Zhang, D. (2023). Single-cell transcriptomic profiling of dorsal root ganglion: An overview. *Frontiers in Neuroanatomy*, *17*, 1162049

Xu, J., Pham, M.D., Corbo, V. *et al.* Advancing pancreatic cancer research and therapeutics: the transformative role of organoid technology. *Exp Mol Med* **57**, 50–58 (2025).

Yang MW, Tao LY, Jiang YS, Yang JY, Huo YM, Liu DJ, Li J, Fu XL, He R, Lin C, Liu W, Zhang JF, Hua R, Li Q, Jiang SH, Hu LP, Tian GA, Zhang XX, Niu N, Lu P, Shi J, Xiao GG, Wang LW, Xue J, Zhang ZG, Sun YW. Perineural Invasion Reprograms the Immune Microenvironment through Cholinergic Signaling in Pancreatic Ductal Adenocarcinoma. Cancer Res. 2020 May 15;80(10):1991-2003

Yao, J., Yang, M., Atteh, L., Liu, P., Mao, Y., Meng, W., & Li, X. (2021). A pancreas tumor derived organoid study: From drug screen to precision medicine. *Cancer Cell International*, *21*(1), 398

Yin Z, Ma T, Huang B, et al. Macrophage-derived exosomal microRNA-501-3p promotes progression of pancreatic ductal adenocarcinoma through the TGFBR3-mediated TGF-β signaling pathway. J Exp Clin Cancer Res 2019;15;38(1):310.

Yin Z, Zhou Y, Ma T, et al. Down-regulated lncRNA SBF2-AS1 in M2 macrophage-derived exosomes elevates miR-122-5p to restrict XIAP, thereby limiting pancreatic cancer development. J Cell Mol Med 2020; May;24(9):5028-5038.

Yu H, Nagi SS, Usoskin D, et al. Leveraging deep single-soma RNA sequencing to explore the neural basis of human somatosensation. Nat Neurosci 2024; Dec;27(12):2326-2340.

Zeisel A, Hochgerner H, Lönnerberg P, et al. Molecular Architecture of the Mouse Nervous System. Cell 2018;1014.

Zhang L, Guo L, Tao M, Fu W, Xiu D. Parasympathetic neurogenesis is strongly associated with tumor budding and correlates with an adverse prognosis in pancreatic ductal adenocarcinoma. Chin J Cancer Res. 2016 Apr;28(2):180-6.

Zhang S, Edwards TN, Chaudhri VK, et al. Nonpeptidergic neurons suppress mast cells via glutamate to maintain skin homeostasis. Cell 2021;2166.

Zhang, L., Xiu, D., Zhan, J., He, X., Guo, L., Wang, J., Tao, M., Fu, W., & Zhang, H. (2016). High expression of muscarinic acetylcholine receptor 3 predicts poor prognosis in patients with pancreatic ductal adenocarcinoma. *OncoTargets and Therapy*, *Volume 9*, 6719–6726.

Zhang, Y., Wang, D., Peng, M., Tang, L., Ouyang, J., Xiong, F., Guo, C., Tang, Y., Zhou, Y., Liao, Q., Wu, X., Wang, H., Yu, J., Li, Y., Li, X., Li, G., Zeng, Z., Tan, Y., & Xiong, W. (2021). Single-cell RNA sequencing in cancer research. *Journal of Experimental & Clinical Cancer Research*, *40*(1), 81.

Zheng, Q., Dong, X., Green, D. P., & Dong, X. (2022). Peripheral mechanisms of chronic pain. *Medical Review*, *2*(3), 251–270

Chapter II – Engineered Extracellular Vesicles

1. ABRSTRACT

2. LIST OF FIGURES

3. INTRODUCTION

3.1 Extracellular vesicles: general features and their application in gene therapy

3.1.1 An overview of Extracellular Vesicles: Characteristic and Functions

3.1.2 Mechanism of Extracellular vesicles biogenesis

3.1.3 The importance of ESCRT complex in EVs biogenesis and cargo loading

3.1.4 Binding of extracellular vesicles to their target cells

3.1.5 Uptake and fate of extracellular vesicles in recipient cells

3.1.6 Overview of EVs in physiological functions and in cancer-related processes

3.1.7 Therapeutic application of Extracellular vesicles: Current strategies and advantages

3.2 Pseudotyping extracellular vesicles: targeting pancreatic cancer

3.2.1 Lectins: a trojan horse to the cancer cells

3.2.2 Lectins in pancreatic cancer

3.2.3 The SNAP^{TM} Tag reaction: pseudotyping extracellular vesicles

4. AIMS OF THE THESIS

5. MATERIALS AND METHODS

5.1 Plasmids generation and cloning

5.1.1 Cloning IGG4 dimerization signals in pSNAP DISPLAY

5.1.2 Generation of double mutant VSVG

5.1.3 Cloning whole WGA in pSNAP CD8 DISPLAY

5.1.4 Cloning EBNA in pWGA SNAP CD8 DISPLAY

5.1.5 Cloning MCP in pWGA SNAP CD8 DISPLAY

5.1.6 Cloning MCP in pSNAP CD8 DISPLAY

5.1.7 Cloning whole PNA in pSNAP CD8 DISPLAY MCP

5.1.8 Cloning EBNA in pTRANSFERRIN SNAP

5.1.9 Cloning MCP in pTRANSFERRIN SNAP

5.1.10 Cloning WGA in pTRANSFERRIN SNAP

5.1.11 Cloning MCP in pTRANSFERRIN SNAP WGA

5.1.12 Bacterial transformation and amplification, restriction analysis and sequencing

5.2 EVs production

5.3 EVs isolation

5.4 EVs pseudotyping through SNAP reaction

5.5 EVs SDS-PAGE SNAP Tag visualization

5.6 Flow cytometry for Cre recombinase delivery to HEK cells

5.7 Semi-absolute Cre recombinase mRNA RT-qPCR in EVs

5.8 Western Blot characterization

6. RESULTS

6.1 Transmembrane scaffolds domains improve Cre mediated recombination in recipient cells

6.2 Mutant VSV-G–enveloped EVs show significantly impaired targeting activity

6.3 Restoring Target Specificity via Lectin-Mediated Pseudotyping of mutant VSV-G EVs

6.4 Active cargo loading via MS2 mRNA recruitment: scaffolds displaying matter

6.5 Enhancers CIT and NEDD4L synergize with MS2-mediated loading

6.6 Dual-functional EVs reveal uneven contributions of targeting and cargo loading

7. DISCUSSION

8. BIBLIOGRAFHY

1.ABSTRACT

Background & Aims: Extracellular vesicles (EVs) hold promise as therapeutic mRNA delivery tool, yet challenges remain in achieving efficient cargo loading, targeted uptake, and functional delivery. This study aimed to develop a modular EV engineering platform integrating RNA enrichment and cell-specific tropism for improved mRNA-based delivery.

Methods: We employed biotechnology strategies to design EVs with three functional modules: (1) surface display of a fusogen, vesicular stomatitis virus glycoproteins (VSV-G WT and a mutant VSV-G MUT lacking cellular tropism but retaining fusogenicity); (2) active mRNA cargo loading using the MCP system (bacteriophage MS2 Coat Protein, an RNA-binding domain with high affinity and specificity for stem-loop motifs known as MS2 loops); and (3) pseudotyping via SNAP-tag-based conjugation of glycan-binding lectins (e.g., WGA and PNA). EVs were isolated by differential ultracentrifugation and their efficiency assessed via RT-qPCR and FACS reporter assays and characterized by Western blotting.

Results: VSV-G WT enabled sufficient Cre mRNA delivery but lacked specificity, whereas VSV-G MUT allowed modular retargeting. WGA-conjugated VSV-G MUT EVs restored functional delivery, confirming lectin-mediated targeting. SNAP Cd8 Display MCP scaffolds effectively enriched Cre mRNA in small EVs (s-EV), outperforming other scaffolds (i.g., Transferrin SNAP MCP). Both large EVs (L-EV) and s-EV bearing both MCP domains and surface lectins (i.g., WGA) improved reporter cell expression despite significantly lower mRNA content, suggesting enhanced uptake as the primary driver. Western blot analysis revealed that EVs bearing both MCP and surface ligands were less enriched in canonical markers (e.g., Alix, TSG101) compared to their cognate EVs without the MCP, whereas SNAP-tag expression confirmed successful scaffold incorporation across all EV subtypes.

Conclusions: We established a flexible EVs engineering strategy that enables combinatorial control over cargo loading and cell targeting. These findings provide a foundation for programmable EVs tailored for therapeutic mRNA delivery and highlight key parameters governing EVs function and specificity.

Keywords: extracellular vesicles; mRNA delivery; lectins; pseudotyping; MCP; genetically engineering

2. LIST OF FIGURES

Figure 1- General overview of both exosomes and microvesicles content heterogeneity

Figure 2- The highly complex world of EVs and NVEPs, based on their size and origin root

Figure 3- Proposed mechanisms for EVs biogenesis

Figure 4- ESCRT-mediated and ESCRT-independent proposed routes for EVs biogenesis

Figure 5- The influence factors for the EV-cellular interaction

Figure 6- Main mechanisms regulating EVs uptake and cargo fate

Figure 7- Biological role of EVs in homeostasis and pathophysiology

Figure 8- EVs contribution to different aspects of cancer initiation and progression

Figure 9- Unique features of extracellular vesicles

Figure 10- Overview of EVs engineering techniques

Figure 11- Overview of native EVs limitations in clinical applications

Figure 12- Overview of engineered EVs advantages in clinical applications

Figure 13- Current extracellular vesicles based clinical trials for common diseases

Figure 14- Overview of N- and O- glycans found on healthy and cancer cells surface

Figure 15- Overview of important tumor-associated glycans

Figure 16- Sialoglycans enriched in tumor cells and their cognate receptors

Figure 17- Lectins specificity for different pancreatic cell types

Figure 18-The SNAP Tag click chemistry

Figure 19- Transmembrane scaffolds domains improve passive loading of mRNA cargo into EVs

Figure 20- Mutant VSV-G–enveloped EVs show significantly impaired targeting activity

Figure 21- Restoring Target Specificity via Lectin-Mediated Pseudotyping of mutant VSV-G EVs

Figure 22- Comparison of genetically engineering and post modification pseudotyped EVs

Figure 23- Active cargo loading via MS2 mRNA recruitment in engineered EVs

Figure 24- Correlation between Cre mRNA copies in EV and absolute quantification

Figure 25- Evaluation of CIT and NEDD4L enhancers on isolated EVs

Figure 26- Correlation between Cre mRNA copies in EV and absolute quantification when CIT and NEDD4L enhancers are included in the system

Figure 27- Dual-functional EVs reveal uneven contributions of targeting and cargo loading

Figure 28- Characterization of EVs marker via Western Blot

Figure 29- Correlation between Cre mRNA copies in EV and FACS+ reporter cells

3. INTRODUCTION

3.1 Extracellular vesicles: general features and their application in gene therapy

3.1.1 An overview of Extracellular Vesicles: Characteristic and Functions.

Since the discoveries of Christian de Duve, Albert Claude and Georges Palade who shared the 1974 Nobel Prize "for their discoveries concerning the structural and functional organization of the cell", a major objective of cell biology has been to understand the importance of intracellular vesicular compartments for the organization and function of eucaryotic cells. In contrast, the existence of membrane-bound entities in the extracellular space and various body fluids has long been recognized, but the biology of Extracellular Vesicles (EV) has, until recently, been largely ignored (Colombo et al., 2014; Tkach & Théry, 2016; Juan & Fürthauer, 2018). EVs are heterogeneous nano-sized membrane vesicles that are released from various cell types; classically, there are three major subtypes of EVs defined on the basis of their biological pathways: i) exosomes, ii) microvesicles, and iii) apoptotic bodies (Fig.1) Exosomes are vesicles formed by inward invagination of the endosomal membrane and fusion of the multivesicular body (MVB) with the plasma membrane. Microvesicles are formed by direct outward budding from the plasma membrane of healthy cells. Apoptotic bodies are formed during apoptosis by outward blebbing of the plasma membrane of cells (Teng & Fussenegger; 2020).

EVs contain various DNAs, RNAs, proteins, lipids, and metabolites. Some of these components are involved in the biogenesis of EVs, whereas most others are enriched in EVs during biogenesis. DNAs include dsDNA, ssDNA, and mtDNA. RNAs include mRNA, miRNA, lncRNA, tRNA, snoRNA, snRNA, Y-RNA, vRNA, piRNA, mtRNA, and circRNA. Membrane proteins include tetraspanins (e.g., CD63, CD9, and CD81), MHC molecules, integrins, ligands (e.g., Hh, PD-L1), receptors (e.g., EGFR, PDGFR), and flotillins. Lumen proteins include TSG101, ALIX, HSPs, syntenin, and RAB GTPases. Lipids include ceramide, phosphatidylserine, sphingomyelin, and cholesterol. Note that no single EV contains all of these components (Van Niel et al., 2018; Teng & Fussenegger, 2020; Fig.1)

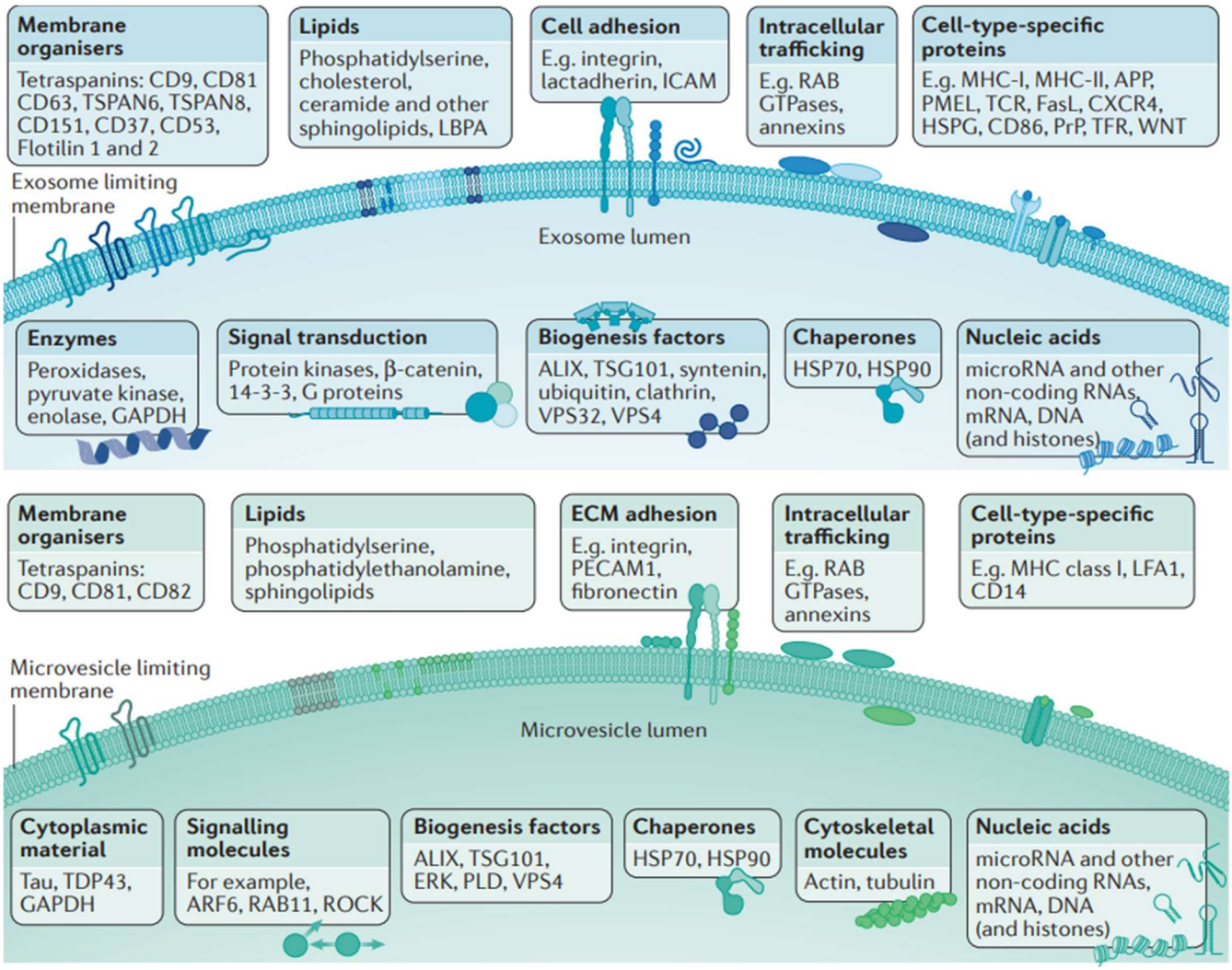


Figure 1. General overview of both exosomes and microvesicles content heterogeneity (from Van Niel et al., 2018).

EVs may adopt the homing pattern of the parental cell of origin, , which suggests that EVs acquire the same repertoire of surface receptors and extracellular matrix-binding proteins as their parent cell (Wiklander et al., 2015); additionally, EVs have their transmembrane proteins in an identical topology to that of the secreting cell, conferring them a degree of cellular identity and possible tropism. This unique feature makes EVs a potential therapeutic tool, emphasizing the importance of choosing the appropriate cell source for derivation of EVs when initiating an in vivo therapeutic project aiming at delivery to a given organ (Sahoo et al., 2011; Wiklander et al., 2015).

With all of the above being said, it is of crucial importance to underline the remaining portion of this Janus's face: It is increasingly appreciated that non-vesicular extracellular NPs (NVEPs), lacking a

lipid bilayer membrane, are present and often plentiful in the extracellular space and bodily fluids (Zhang H. et al., 2018; Zhang Q. et al., 2021). NVEPs include not only well-known entities, such as lipoprotein particles, nucleosomes, and vaults, but also recently discovered exomeres and supermeres (Zhang Q. et al., 2019; Clancy et al., 2022). The expanding world of EVs and NVEPs is largely due to improvements in techniques and methodology, as well as the growing awareness of their complexity and heterogeneity, which has spurred an active search for new particle subsets (Jeppesen et al., 2023; Fig.2).

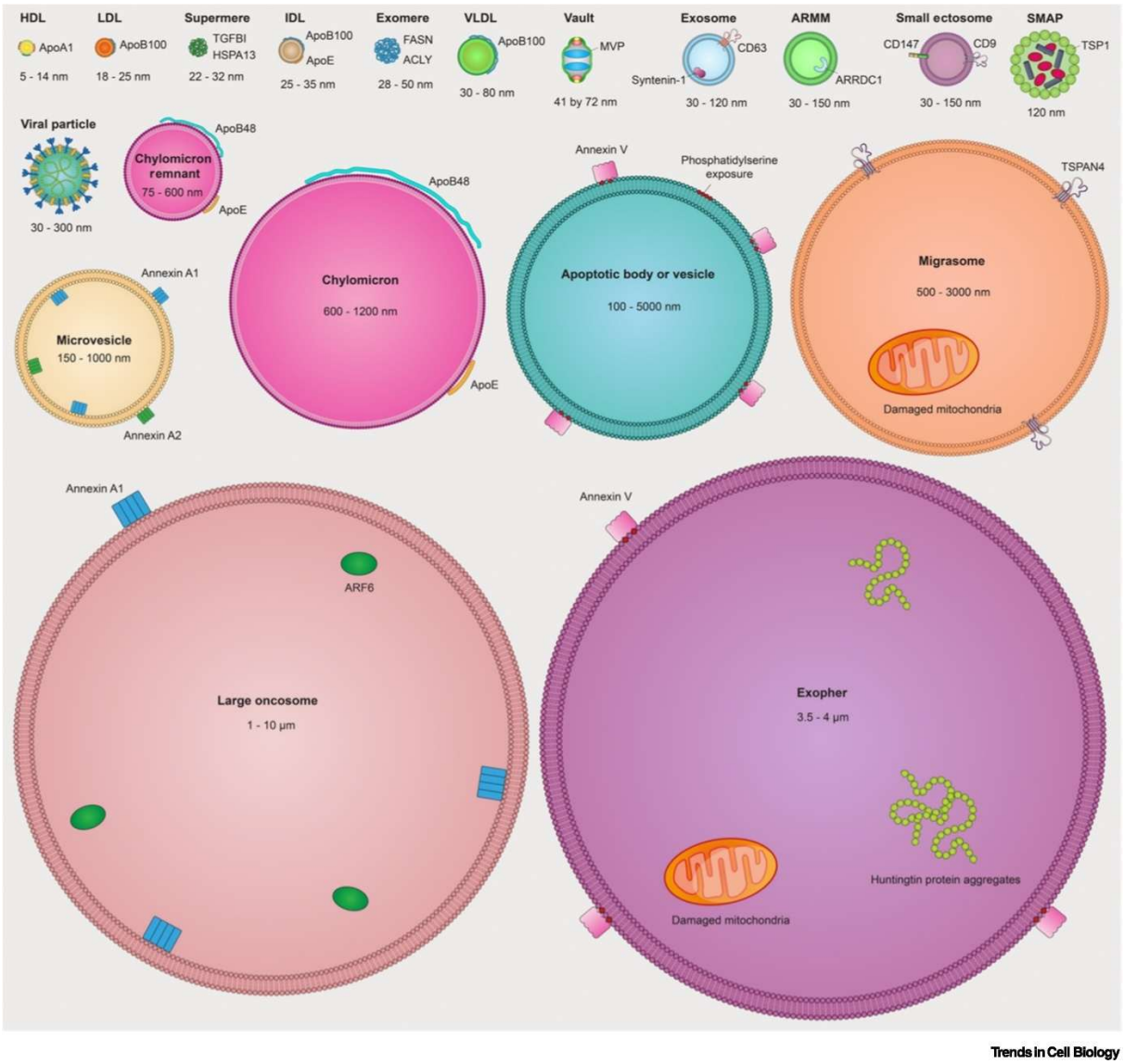


Figure 2. The highly complex world of EVs and NVEPs, based on their size and origin root (from Jeppesen et al., 2023).

3.1.2 Mechanisms of Extracellular vesicles biogenesis.

Briefly, the generation of exosomes consists of three steps: biogenesis, transport and release. Microvesicles (MVs) are derived from the plasma membrane by direct outward budding and fission, which is reminiscent of a reverse version of endocytosis (Meldolesi, 2018; Van Niel et al., 2018).

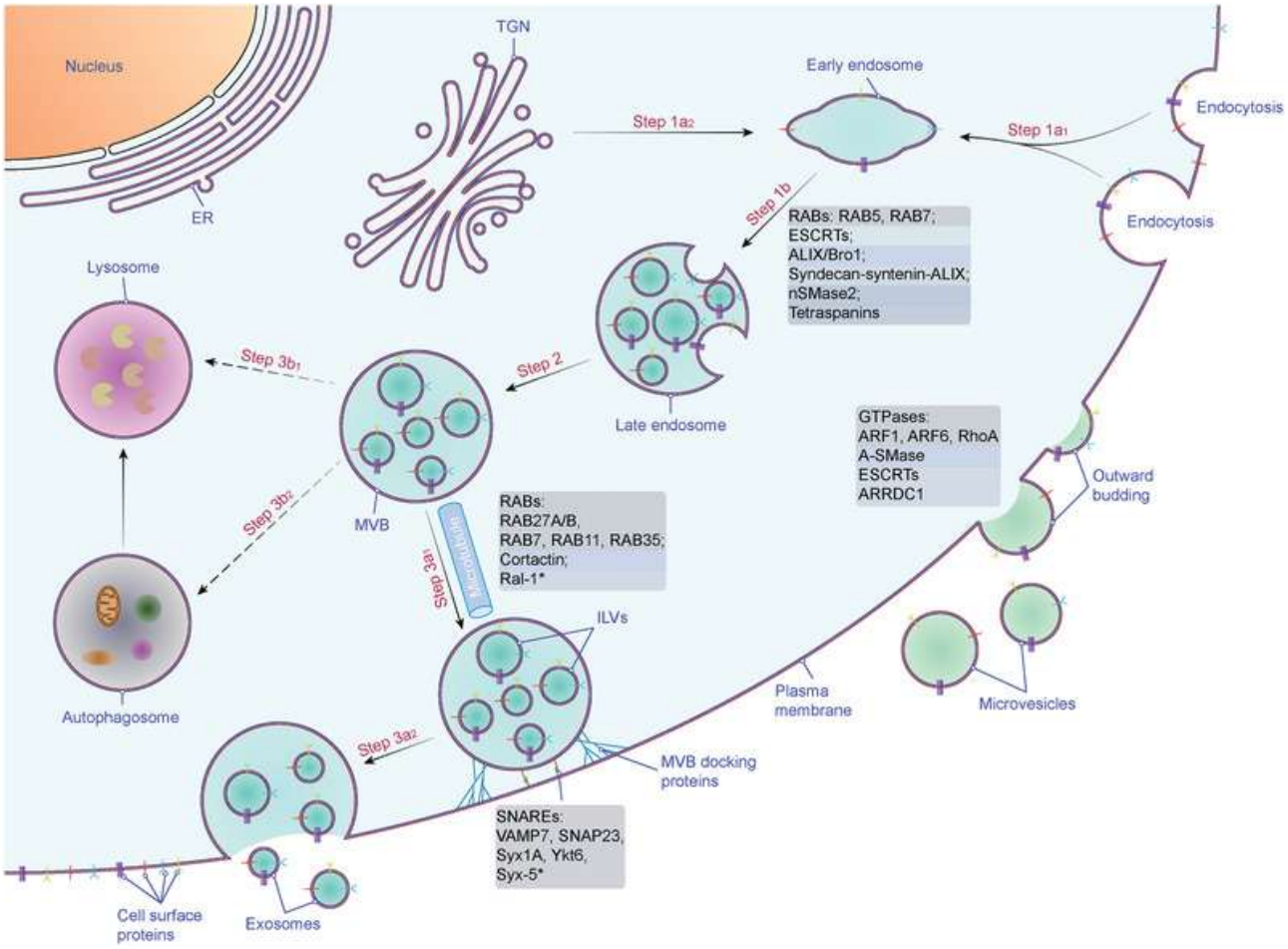


Figure 3. Proposed mechanisms for EVs biogenesis (see text for further details). Classically, exosome biogenesis is initiated from the endosomal pathway, i.e., the formation of early endosomes via invagination of the plasma membrane. In some cases, vesicles derived from the budding of the *trans*-Golgi network (TGN) can fuse with early endosomes. During the following maturation process, early endosomes fuse to form late endosomes, leading to invagination of the endosomal membrane into the lumen and form intraluminal vesicles (ILVs). This in turn leads to the formation of multivesicular endosomes or MVBs with a characteristic multivesicular appearance. MVBs ultimately fuse with the plasma membrane and release the ILVs into the extracellular milieu in the form of exosomes. Alternatively, MVBs can fuse with lysosomes/autophagosomes to be degraded (from Teng & Fussenegger, 2020).

The process of releasing exosomes into the extracellular space contains three distinct steps: exosome biogenesis, intracellular trafficking of MVBs, and fusion of MVBs with the plasma membrane. Early endosomes are formed by the inward budding of the plasma membrane (Fig.3 Step 1a1), or in some

cases from the *trans*-Golgi network (TGN) (Fig.3 Step 1a2). Early endosomes mature into late endosomes (Fig.3 Step 1b) and finally generate MVBs, in which process ILVs are formed by inward invagination of the endosome limiting membrane (Fig.3 Step 2). The fate of MVBs can be fusion with the plasma membrane (Fig.3 Step 3a1), which results in the release of exosomes (Fig.3 Step 3a2). Alternatively, MVBs can fuse with lysosomes/autophagosomes for degradation (Fig.3 Step 3b1 & Step 3b2; Teng & Fussenegger, 2020). Several molecules are involved in the biogenesis (e.g., RABs, ESCRTs, syndecan, ceramide, tetraspanins, etc.), trafficking (e.g., RABs, actin, etc.), and fusion of MVBs with the plasma membrane (e.g., SNAREs). Microvesicles arise from the direct outward budding and fission of the plasma membrane. Several molecules are involved in the biogenesis and release of microvesicles (small GTPases, ESCRTs, ARRDC1, *etc*.).

3.1.3 The importance of ESCRT complex in EVs biogenesis and cargo loading.

The EV field has long contemplated whether cargoes are selectively sorted into EVs, or whether EV cargoes represent nonselective samples of cytoplasm and source membranes. EV cargo "selection" and "sorting" are defined as a process that drives the local increase in cargo concentration within a nascent EV compared to the surrounding concentration. This process is driven through recognition by the biogenesis machinery and by cargo-specific interactions (Tosar et al., 2021; Dixson et al., 2023). Cargoes increase in local concentration because they are captured and clustered by EV biogenesis machineries, with which one of the most well-known being the endosomal sorting complex required for transport (ESCRT; Fig.4; Van Niel et al., 2018). This comprise of five distinct proteins- i.e., ESCRT-0, ESCRT-I, ESCRT-II, ESCRT-III, and Vps4- that function in cargo sorting, membrane remodelling and scission along with disassembly and deubiquitinating enzymes on the endosome membrane. The discovery of the ESCRT machinery as a driver of membrane shaping and scission was the first breakthrough in uncovering the mechanisms involved in the formation of MVEs and ILVs (Hurley, 2008; Van Niel et al., 2018). The ESCRT machinery acts in a stepwise manner wherein ESCRT0 and ESCRTI subunits cluster ubiquitylated transmembrane cargoes on

microdomains of the limiting membrane of MVEs and recruit, via ESCRTII, the ESCRT-III subcomplexes that perform budding and fission of this microdomain (Fig.4). Accordingly, ESCRT0 appears to be required for exosome formation and/or secretion by dendritic cells (Tamai et al., 2010; Van Niel et al., 2018).

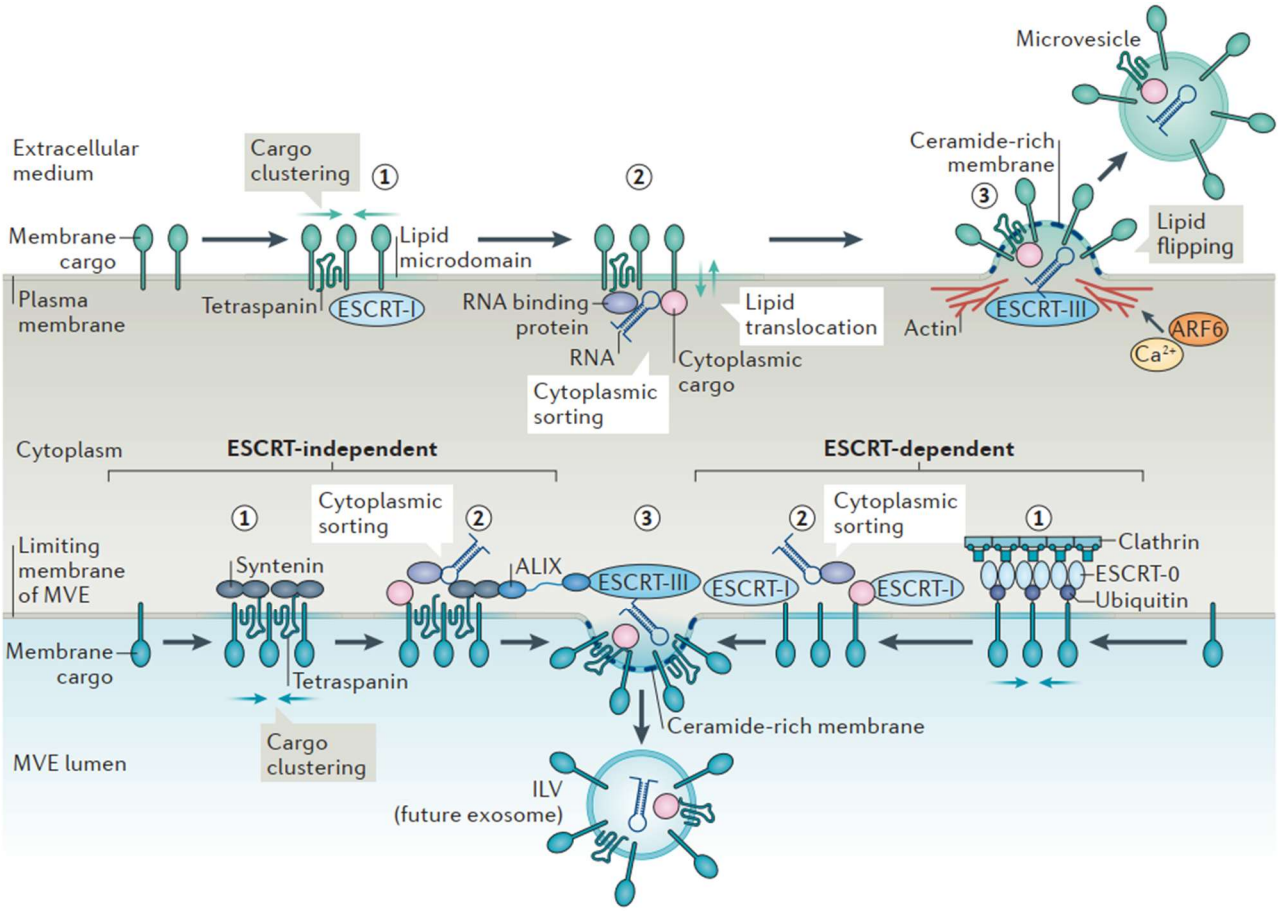


Figure 4. ESCRT-mediated and ESCRT-independent proposed routes for EVs biogenesis (see text for further details; from Van Niel et al., 2018).

Notably, recent evidence targeting multiple components of the ESCRT machinery and associated proteins has clarified various roles for selected members of this family in exosome generation: their inactivation affects either the efficiency of secretion or the composition of the secreted vesicles, indicating that some ESCRT components could act selectively on MVE and ILV subpopulations fated for secretion as exosomes (Colombo et al., 2012; Willms et al., 2016).

Exosomes can also be formed in an ESCRT-independent manner (Fig.4), which was revealed by studies showing that MVEs, featuring ILVs loaded with CD63 (one of the hallmark of exosomes surface proteins), are still formed upon depletion of components of the four ESCRT complexes (Stuffers et al., 2009). The first ESCRT-independent mechanism of exosome biogenesis was shown to require generation of ceramide by neutral type II sphingomyelinase, which hydrolyses sphingomyelin to ceramide. Ceramide may then allow the generation of membrane subdomains, which impose a spontaneous negative curvature on the membranes (Trajkovic et al., 2008; Van Niel et al., 2018; Fig.4). Exosome biogenesis is certainly complex, varies depending on the cargo and on the cell type and can be influenced by other signals and pathological stimuli that the cell can receive. The balance of these pathways leading to changes in the compositional repertoire of exosomes also changes over the course of the differentiation process, as reported for reticulocytes (Carayon et al., 2011); as a consequence of this context, different sorting mechanisms can act on the same endosomal compartment, or different machineries can be used for targeting the same cargo (for example, MHC class II, which can be targeted to MVEs by both ESCRT-dependent and ESCRT-independent mechanisms; Buschow et al., 2009; Van Niel et al., 2011; Van Niel et al., 2018). Exosomal membrane cargoes reach endosomes from the Golgi apparatus or are internalized from the plasma membrane before being sorted to ILVs during endosome maturation (Klumperman et al., 2014). Hence, cargoes that are preferentially recycled to the plasma membrane are not likely to be enriched in exosomes unless their recycling is impaired, as is the case for the transferrin receptor in reticulocytes (Vidal et al., 1997; Van Niel et al., 2018). On the other hand, microvesicle biogenesis requires several molecular rearrangements within the plasma membrane, including changes in lipid components and protein composition, and in Ca2+ levels. Ca2+-dependent enzymatic machineries including flippases and floppases, scramblases and calpain drive rearrangements in the asymmetry of membrane phospholipids (exposition of phosphatidylserine from the inner leaflet to the cell surface), which causes physical bending of the membrane and restructuring of the underlying actin cytoskeleton,

which favour membrane budding and formation of microvesicles (Piccin et al., 2007; Van Niel et al., 2018; Fig.4).

To summarize, actual knowledge of the EV field supports a model whereby the biogenesis of exosomes involves several distinct mechanisms for the preferential recruitment of cargoes probably generating heterogeneous populations of ILVs and exosomes within common or distinct subpopulations of MVEs, with endosomal sorting machineries apparently being the main determinants of both functional properties and the composition of exosomes.

3.1.4 Binding of extracellular vesicles to their target cells

Target cell specificity is likely to be determined by specific interactions between proteins enriched at the surface of extracellular vesicles and receptors at the plasma membrane of the recipient cells, as in neurons for example (Chivet et al., 2014).

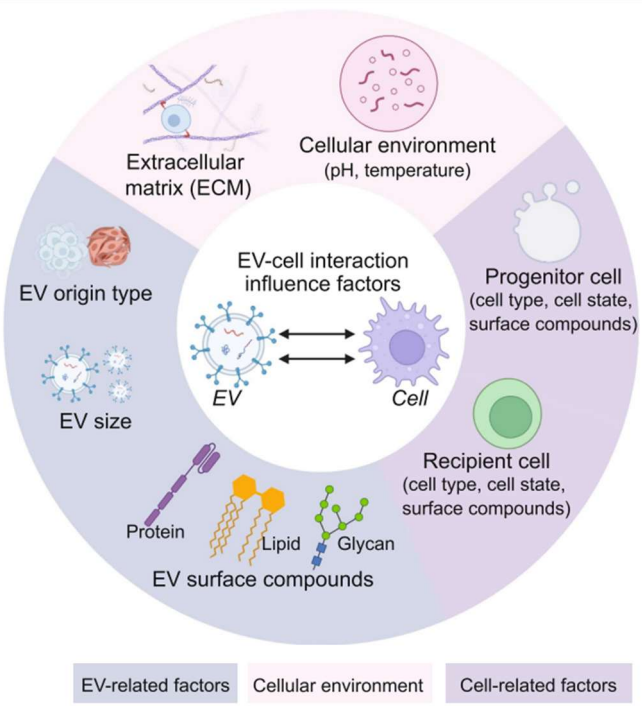


Figure 5. The influence factors for the EV-cellular interaction (from Liu Yj & Wang, 2023).

Several mediators of these interactions are known, including tetraspanins, integrins, lipids, lectins, heparan sulfate proteoglycans and extracellular matrix (ECM) components; despite the number of

studies on such a topic, the cellular and molecular basis for the specific targeting to acceptor cells is still unclear, although many crucial interactions have been elucidated (Van Niel et al., 2018): for example, integrins on extracellular vesicles can interact with adhesion molecules such as intercellular adhesion molecules (ICAMs) at the surface of recipient cells. In addition, the interaction of integrins with extracellular matrix proteins, mostly fibronectin and laminin, has been shown to have important roles in exosome binding to recipient cells (Purushothaman et al., 2016). Exosomal tetraspanins could also regulate cell targeting: they have been shown to interact with integrins and to promote exosome docking and uptake by selected recipient cells (Rana et al., 2011). Other molecules such as heparan sulfate proteoglycans and lectins, both present in extracellular vesicles and at the plasma membrane, contribute to the docking and/or attachment of these vesicles to recipient cells. Additionally, also the lipid composition of extracellular vesicles can also have an impact on recipient-cell targeting: phosphatidylserine can recruit specific lipid-binding proteins such annexin 5 that then induce docking of vesicles to the target cell membrane (Frey & Gaipl, 2011; Van Niel et al., 2018).

Overall, factors that influence and mediate EV-target cell binding include the surfaced characteristic molecules related to EVs themselves, progenitor cell and recipient cell; and the cellular environments of EVs. The characteristic surface molecules include protein, lipid, and glycan, while the cellular environments include temperature, pH and ECM (Van Niel et al., 2018; Liu Yj & Wang, 2023; Fig.5).

3.1.5 Uptake and intracellular fate of extracellular vesicles

The fate of extracellular vesicles is also likely to be related to the presence of specific structures at the plasma membrane of the target cell. As an illustrative example, it has been shown that microvesicles derived from microglia show largely different dynamics of interaction with membranes of microglia and astrocytes (Prada et al., 2016); conversely, The presence of amyloid precursor protein (also known as amyloid-β (A4) protein) on one exosome subtype from neuroblastoma cells specifically targets them to neurons, in contrast to a CD63enriched exosome subtype that binds both neurons and glial cells (Laulagnier et al., 2018). Once released into the extracellular space,

extracellular vesicles can reach recipient cells and deliver their contents to elicit functional responses and promote phenotypic changes that will affect their physiological or pathological status. Extracellular-vesicle-mediated intercellular communication requires docking at the plasma membrane, followed by the activation of surface receptors and signalling, vesicle internalization (endocytosis) or their fusion with target cells (Van Niel et al., 2018; Fig.6).

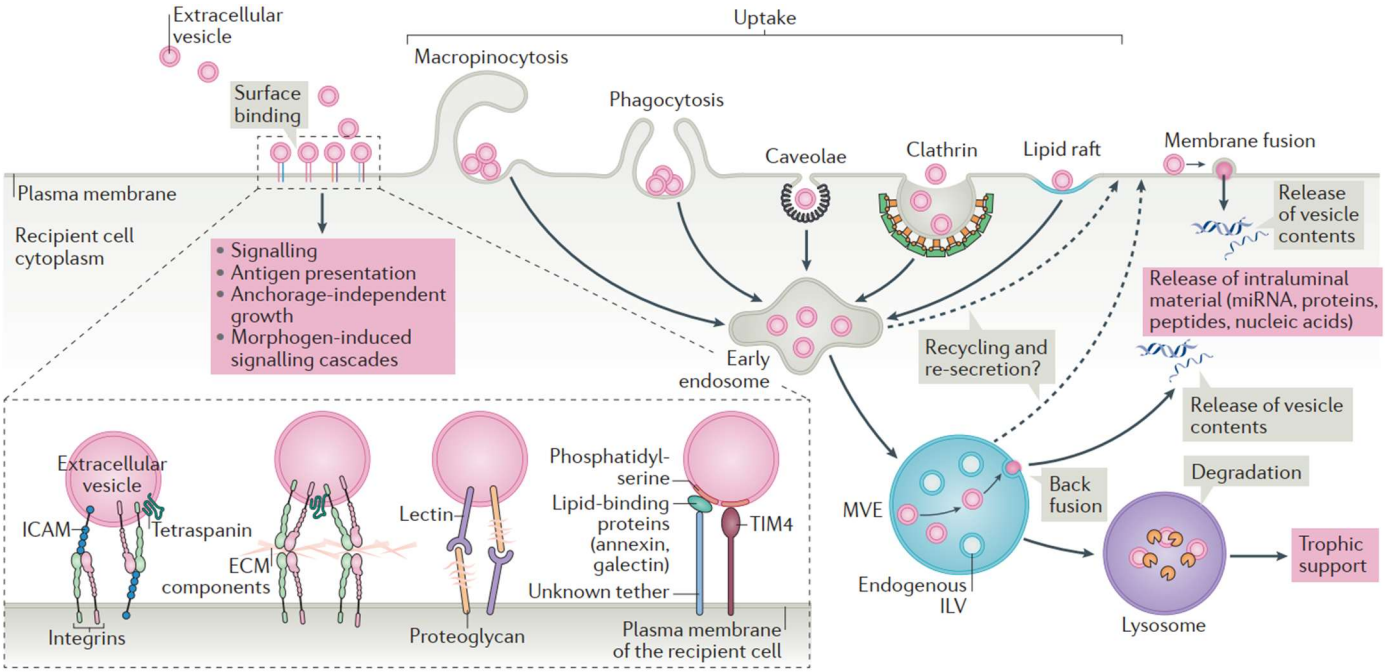


Figure 6. Schematic representation of the main mechanisms that regulate extracellular vesicle uptake and fate at target cells. See text for further details (from Van Niel et al., 2018).

Currently, two models of EV uptake have been proposed and are widely accepted: direct membrane fusion and endocytosis (Morelli et. Al, 2004; Mulcahy et al., 2014; Abels & Breakefield, 2016; Van Niel et al., 2018; Hyenne et al., 2019; Verweij et al, 2019; Teng & Fussenegger; 2020). Indeed, EV uptake via direct fusion with the cell's plasma membrane has been observed directly using fluorescent lipid dequenching (Parolini et al., 2009). Endocytosis is a generic term for cellular internalization, which can be generally subdivided into five categories: receptor-mediated endocytosis (also known as clathrin-mediated endocytosis), caveolin-mediated endocytosis, lipid raft-mediated endocytosis, phagocytosis and micropinocytosis (Van Niel et al., 2018; Fig.6). Surface binding of EVs can initiate intracellular signaling pathways, such as antigen presentation, immune modulation, and morphogen

signaling, with some EVs remaining attached to membrane receptors like integrins to exert their effects. Alternatively, EVs can enter recipient cells—either the original secreting cell or a different target cell—via a range of internalization mechanisms, including membrane fusion, receptor-mediated endocytosis, caveolin-mediated uptake, lipid raft-mediated endocytosis, phagocytosis, and macropinocytosis. Once internalized, EVs are typically routed through the canonical endosomal pathway, where they are trafficked to multivesicular bodies (MVBs), also known as multivesicular endosomes (MVEs). Within MVBs, exogenous EVs may mix with endogenous intraluminal vesicles (ILVs). The fate of these vesicles includes degradation following fusion of MVBs with lysosomes, facilitating metabolic recycling of vesicle components. Alternatively, EVs may undergo back-fusion with the limiting membrane of MVBs or fuse with the plasma membrane, thereby releasing their intraluminal contents—such as microRNAs—directly into the cytoplasm. While the molecular mechanisms underlying these fusion events remain incompletely understood, they are recognized as critical processes for the functional transfer of EV cargos. Furthermore, the potential recycling of internalized vesicles back to the plasma membrane has not been definitively excluded (Van Niel et al., 2018; Teng & Fussenegger; 2020; Fig.6).

3.1.6 Overview of EVs in physiological functions and in cancer-related processes

Both small and large EVs can be released from normal healthy cells under physiological conditions to ensure cell–cell communication to regulate a range of biological processes from cellular maintenance to immune response (). It should be noted that the precise role of EVs under normal physiological conditions remains incompletely understood. This is because of the lack of physiological in vitro and in vivo models to validate the contribution of EVs over other modes of cellular communication and the heterogeneity of EV populations, with subpopulations of EVs lacking precise definition. EVs play a fundamental part in cell–cell communication — whereby they transfer intraluminal EV cargo, including proteins, lipids and regulatory RNA between cells — to maintain normal physiology (Hakulinen et al., 2008; Laghezza Masci et al., 2016; Rackov et al., 2018; Cheng

& Hill, 2022). In the context of cell-cell communication, EVs use a variety of mechanisms to mediate cell–cell communication, such as directly fusing with the plasma membrane of recipient cells to enable the exchange of transmembrane proteins and lipids (Fig.6); EV-uptake mechanisms have also been demonstrated to occur in almost all known endocytosis pathways and membrane-fusion events, mediated by either clathrin-dependent or clathrin-independent mechanisms (Van Niel et al., 2018; Fig.6). Owing to the heterogeneity of the population of EVs circulating in the body, untangling the network of physiological functions mediated by EV cell–cell communication is a challenge. Criticism in the field has challenged the methods used to study the functional transfer of EV cargo (Somiya, 2020; Cheng & Hill, 2022).

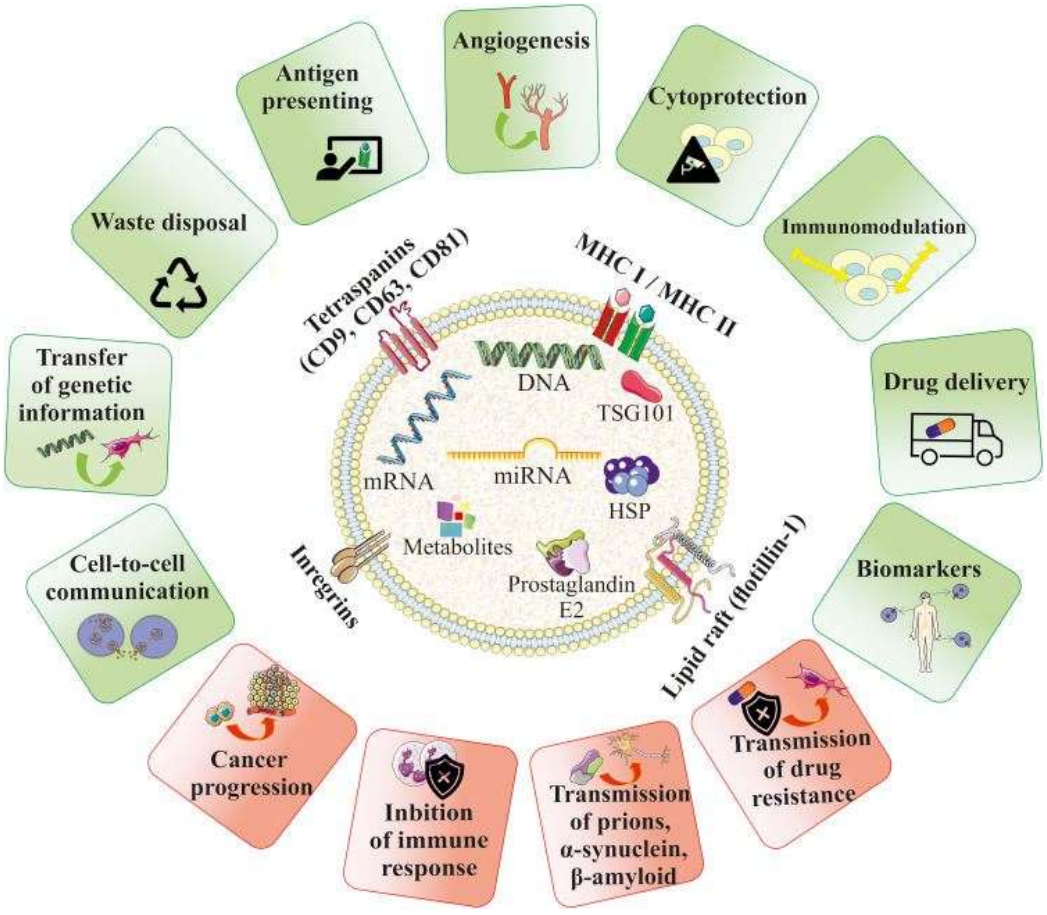


Figure 7 Biological role of EVs in homeostasis and pathophysiology. Green is "GOOD" process", red is "BAD" process (from Karnas et al., 2023).

Concerning tissue development and maintenance, specific interactions allow for the transfer of functional EV cargo that can change the expression of extracellular matrix components to regulate cellular functions such as cellular proliferation, migration and organ morphogenesis (Gebraad et al., 2018; Rackov et al., 2018): for example, certain miRNA cargoes found in EVs derived from bone marrow or stromal stem cells have been shown to regulate osteoblastic differentiation to promote osteoblast activity and bone regeneration (Qin Y et al., 2016). Similarly, endothelial EVs play an important part in optimizing tissue function, ensuring that their cargoes arrive at specific sites in response to physiological cues and stimuli to maintain arterial differentiation. There are a number of endothelial lineage cells that rely on miRNA and protein EV cargo to direct organ development and function (Mathiesen et al., 2021). Finally, EVs secreted by antigen-presenting cells have been found to express the same cell surface proteins such as MHC class 1 and II molecules and can act as 'antigen presenting EVs'. Nevertheless, proteomics studies have revealed that EVs can carry pro-inflammatory and anti-inflammatory receptors and ligands, in addition to cytokines, complement factors, immunoregulatory miRNA, immunosuppressive cargo and other active molecules (Leone et al., 2018; Mardpour et al., 2019; Wang et al., 2020; Cheng & Hill, 2022).

On the other hand, tumour-derived EVs can accelerate tumour growth and promote metastasis, while manipulating supportive tissues to create the optimal tumour microenvironment. The past decade has provided an increasing amount of evidence demonstrating that tumour-derived EVs contain functional oncoproteins and oncogenic RNAs, which are involved in the generation of pre-metastatic niches that mimic the traits of the primary tumour (Skog et al., 2008; Cho et al., 2012; Demory Beckler et al., 2013; Yokoi et al., 2017; Lucotti et al., 2022). Notably, the organotropism of tumour-derived EVs may also be predictable by detecting their integrin expression profile, which can determine their target cells in specific distant organs (Hoshino et al., 2015). The ways in which EVs may selectively package cancer-promoting cargo and how the expression of their content changes in cancer development remain unresolved. It may be that cancer cells are able to dysregulate the ESCRT pathway to increase EV secretion and consequently cause an upregulation of cancer EV-secreted

molecules: an important study from Hikita and colleagues reported for example that EVs can orchestrate cell–cell transfer of oncogenic factors via the ESCRT-mediated pathway to non-tumorigenic neighbouring cells. The proto-oncogene c-src (controlling cell growth, adhesion and migration) can interact with ALIX to recruit ESCRT-mediated ILV formation and be encapsulated into EVs, leading to increased EV release to promote tumour growth (Hikita et al., 2019; Cheng & Hill, 2022).

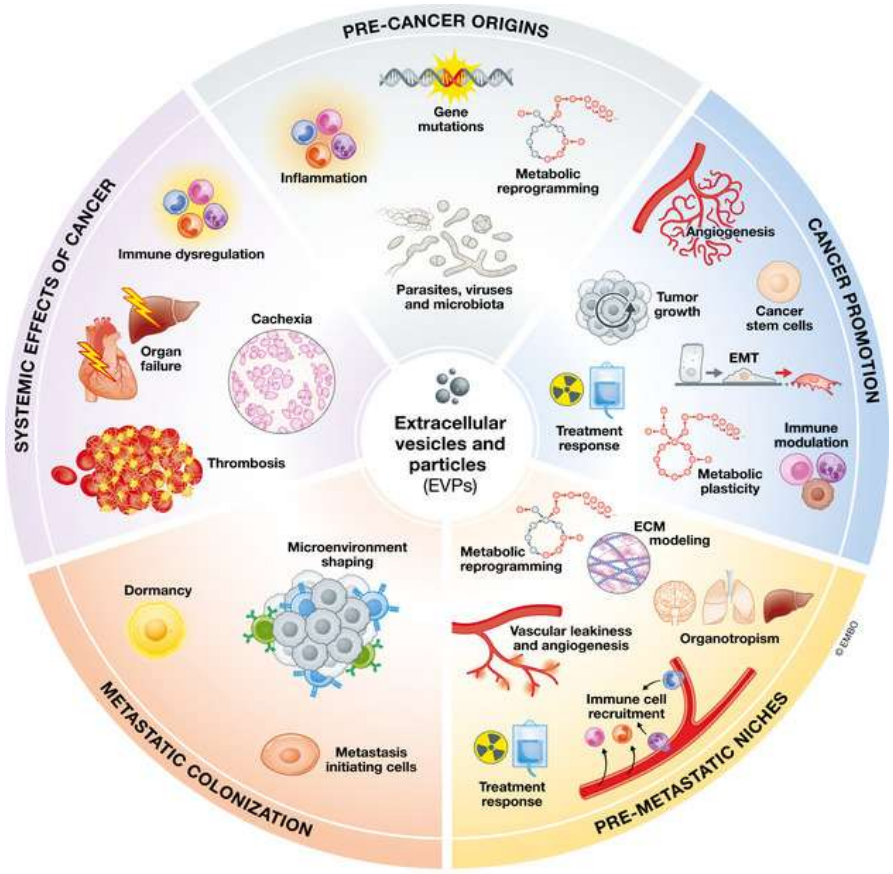


Figure 8 Diagram depicting the contribution of EVs to different aspects of cancer initiation and progression (from Lucotti et al., 2022).

3.1.7 Therapeutic application of Extracellular vesicles: Current strategies and advantages

The biological functions of EVs make them suitable for development as potential therapeutics for several conditions. This is currently a very active area of research, with academic groups and

companies investigating the use of native EV preparations (such as those directly secreted by cells), the potential of loading cargo molecules into EVs, and the use of biomimetic vesicles.

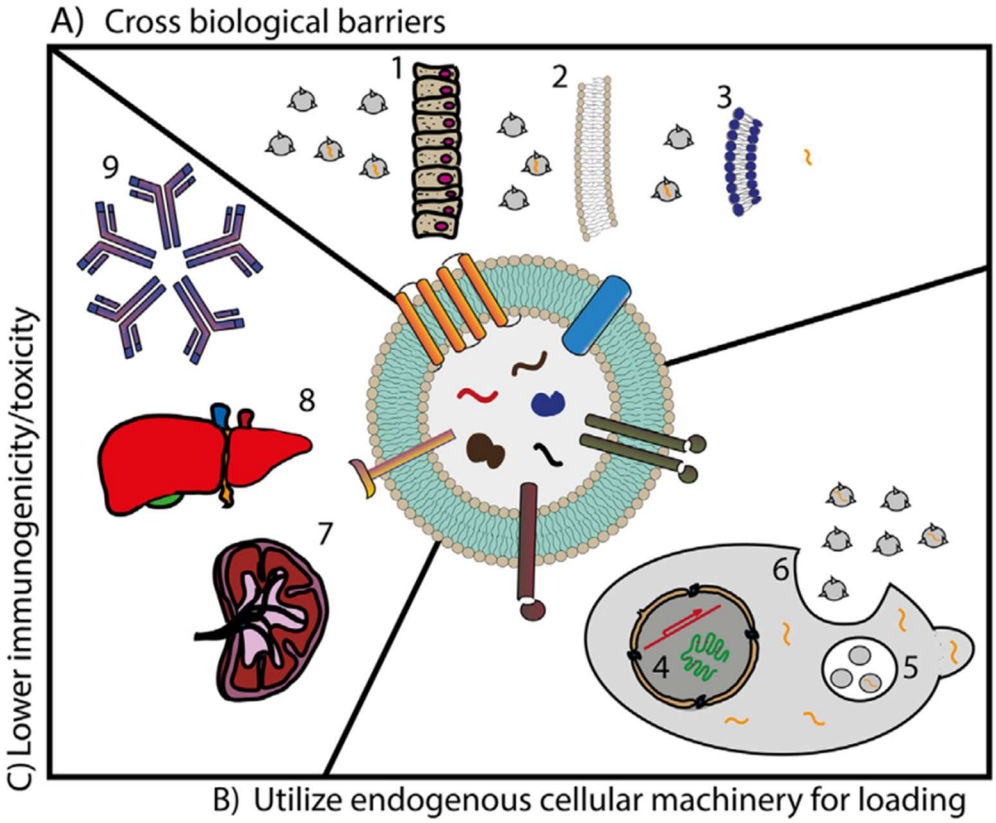


Figure 9 Proposed unique features of extracellular vesicles. EVs are believed to (A) be able to cross various biological barriers including tissue barriers (1), plasma membranes (2), and deliver cargo across endosomal membranes (3), (B) utilize endogenous cellular machinery for manufacture/loading of different cargo through the production inside the nucleus (4), which is then loaded inside MVBs or at the plasma membrane (5), and eventually released in the extracellular space inside EVs (6), and (C) display lower toxicity in spleen (7), and liver (8) as well as reduced immunogenicity (9). From Elsharkasy et al., 2020.

EVs possess features that qualify them as a potential avenue for therapy and as a drug delivery system (Fig.9). More in detail, EVs carry and protect a wide array of nucleic acids and seem intrinsically capable of their functional delivery into recipient cells (Valadi et al., 2007). Another of these features is their intrinsic stability in circulation due to their negatively charged surface and their ability to avoid the mononuclear phagocytic system by exhibiting the surface protein CD47 (De Jong et al., 2019). Moreover, EVs may have the capacity to cross biological barriers, exploit endogenous

intracellular trafficking mechanisms and trigger a response upon uptake by recipient cells (Cooper et al., 2014; Murphy et al., 2019; Fig. 9). As such, these EVs exhibit a promising source of acellular therapy for various conditions, which can be taken advantage of by further engineering these EVs for the delivery of therapeutics. Importantly, EV producer cells can be exploited for the manufacturing of biological therapeutics as well as targeting ligands to be loaded in- or onto EVs. These advantages open the door for a drug delivery vehicle that can potentially compensate for the drawbacks of synthetic delivery systems (Elsharkasy et al., 2020; Fig.10). As a matter of fact, engineering exosomes may provide more ways to create new therapeutic modalities: instead of working with exosomes that capture innately therapeutic molecules from their originating cells, tapping exosomes' capability to carry various payloads to target specific tissues and to go where other types of nanoparticles cannot (Zipkin, 2019; Möller & Lobb, 2020). More in detail, numerous methods of post purification EVs loading with either cytotoxic cargo or antitumour miRNA /siRNA) have been developed and include the use of transfection reagents, sonication, freeze–thaw cycles, saponin and electroporation: however, targeted biodistribution of EVs is the key to their therapeutic potential (Fig.10a). As such, engineering parental cells through the expression of fusion lipid-anchored proteins or fusion to sEV canonical membrane proteins can direct specific biodistribution of EVs, resulting in reduced toxic effects on normal cells and increased therapeutic efficacy with regard to cancer cells (Shen et al., 2011; Hung & Leonard, 2015; Bellavia et al., 2017; Möller & Lobb, 2020; Fig.10b). The intraluminal content of s-EV can be engineered to increase therapeutic efficacy of delivered s-EV. The biogenic mechanisms of sEV loading can be exploited through the fusion of protein cargo with protein tags for sEV packaging or the fusion of the cytoplasmic domain of tetraspanins with inducible binding/release scaffolds for the delivery of soluble proteins, RNA or antibodies to the cytosol of cells. Importantly, post purification loading and engineering of parental cells can be used together, thereby taking advantage of both specific biodistribution and increased antitumour efficacy (Yim et al., 2016; Liang et al., 2020; Möller & Lobb, 2020; Fig.10b).

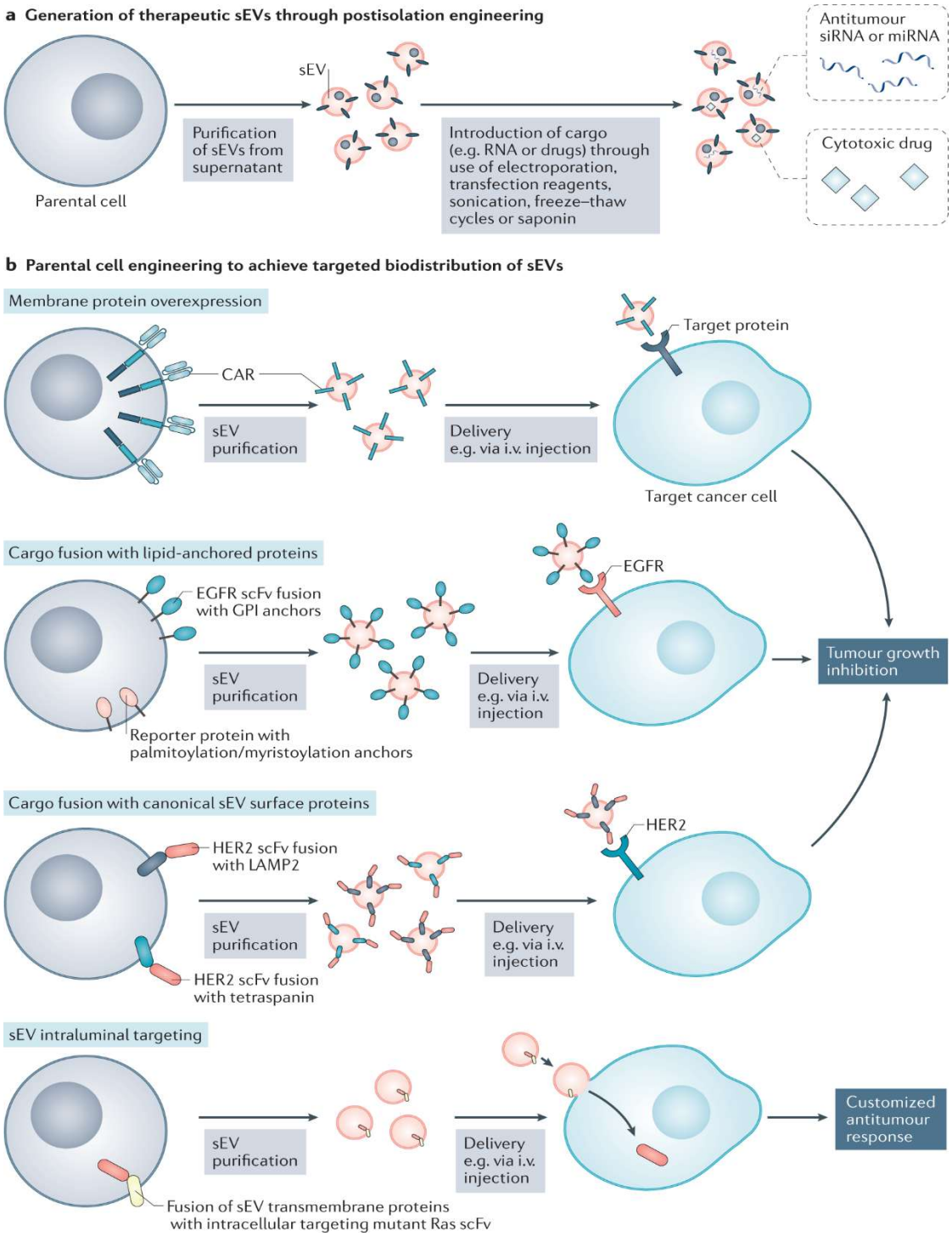


Figure 10 General overview of the main techniques useful to engineering extracellular vesicles. See text for further details (from Möller & Lobb, 2020).

All the above suggests that engineering EVs is the crucial next step toward a sustainable, efficient and tailored clinical application of these potential delivery vectors. More in detail, extensive study so far underlined the main limitations concerning EVs as a clinical tool and how these may have been overcome by molecular engineering. The Holy Grail of using EVs as a clinical drug delivery tool is

to obtain a sufficient degree of efficiency in four main EVs "behaviours" (Fig. 11a,b,c,d LEFT; De Abreu et al., 2020):

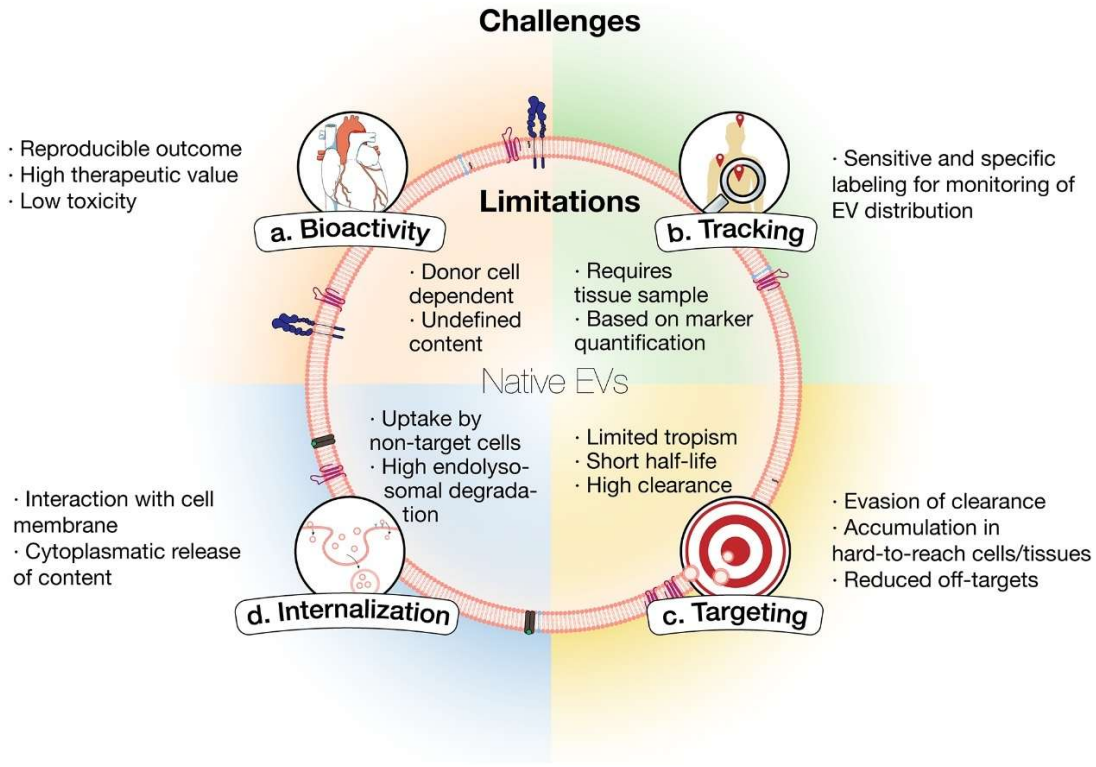


Figure 11 General overview of the main limitations of native ("NOT ENGINEERED") extracellular vesicles application in clinical therapy. (from De Abreu et al., 2023).

that is, ensuring BIOACTIVITY at the target site, eliciting a phenotypical change in a given cell type; ensuring TRACKING of administered EVs, effectively assessing the correct biodistribution; ensuring TARGETING and INTERNALIZATION, by means of cell specific-trophism and efficient cargo release, respectively. It is now generally accepted that via molecular engineering of EVs surface and cargo, scientists would eventually overcome these issues (Fig 12a,b,c,d).

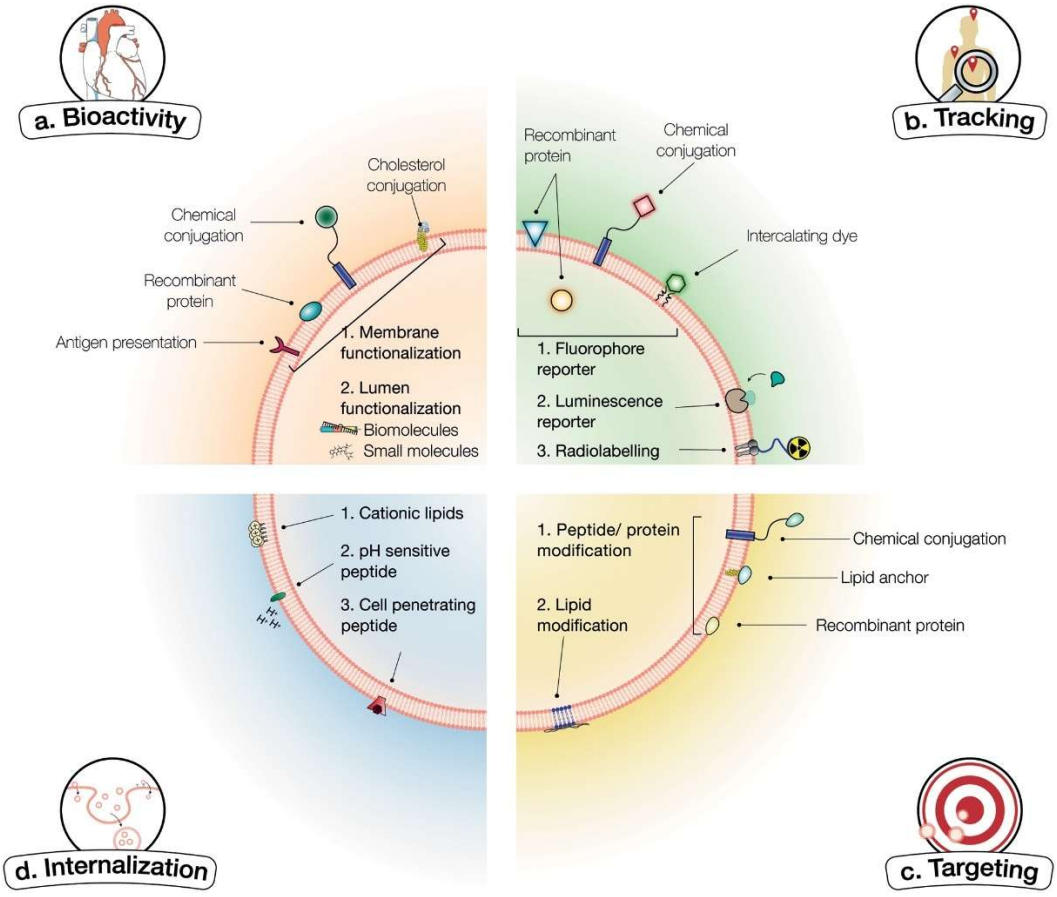


Figure 12 General overview of the main advantages using engineered extracellular vesicles in clinical therapy. (from De Abreu et al., 2023).

Despite the technical issues, still nowadays of great relevance, there are currently 26 ongoing clinical trials employing EVs as therapeutic delivery tools for a wide range of common diseases (Kumar et al., 2024 ;Fig.13), proving that a large and growing attention is every year given to the field of EVs as a potential therapeutical drug delivery tool.

Table 4. Current extracellular vesicles based clinical trials for common diseases

S.No.	Disease	Type	EVs as a therapeutic target	Origin of EVs in clinical Use	Phase, patients	NCT
1	HNSCC	HNSCC		Grapes	$P=1, N=60$	NCT01668849
		OSCC	Blood EVs	Metformin hydrochloride increases EVs	$P=$ NA, $N=30$	NCT02147418
		Oral Mucositis Associated With Chemoradiation Treatment			$P=1$, $N=9$	NCT03109873
2	Gastric Cancer		Circulating Exosomes		$N=80$	NCT01779583
			Hsp70 carrying EVs		$P=$ NA $N=71$	NCT02662621
		Ulcers (wound healing)	Plasma		$P=1$, $N=5$	NCT02565264
3	Breast cancer		Detect EV induced Hypoxia		$N=21$	NCT03262311
			Rosuvastatin reduces TFs		$P=2, N=20$	NCT01299038
4	Lung cancer	Non-small-cell lung cancer lung metastases	Circulating EVs	DC	$P=2$, $N=42$	NCT01159288 NCT03108677
			RNA		$P=$ NA, $N=90$	NCT03108677
	Liver caner	Advanced hepatocellular carcinoma and liver metastasis			$P=1$, $N=9$	NCT05375604
5	Neurodegenerative disorders	Alzheimer's disease		MSC	$P=1/2$,	NCT04388982
		Hypoxia-ischemia		MSC	$N=10$	NCT05490173
		Acute ischemic stroke		MSC	$N=300$	NCT04202770
				MSC	NA	NCT03384433
6	Cardiovascular Diseases	Cerebrovascular disorders		MSC	$P=1$,	NCT05043181
		Acute ischemic stroke		MSC	$P=½$, $N=5$	NCT03384433
7	Diabetes	Insulin resistance		Ginger	NA	NCT03493984
		T1DM		MSCs	$P=2/3$, $N=20$	NCT02138331
		T1DM		Serum	$N=20$	NCT04164966
		T2D		Serum	$N=200$	NCT03264976
8	Renal Disease	Chronic kidney diseases		UC	$P=1$, $N=20$	
9	Autoimmune diseases	Osteoarthritis		MSC	$P=1$	NCT05060107
		Sepsis		DC	$N=50$	NCT02957279
10	Viral Infection	COVID-19		UC	$P=2$, $N=100$	NCT04288102
		COVID-19		MSC	$P=2/3, N=300$	NCT04392778

Fig.13 Current extracellular vesicles based clinical trials for common diseases (from Kumar et al., 2024)

3.2 Pseudotyping extracellular vesicles: targeting pancreatic cancer

4.2.1 Lectins: a trojan horse to the cancer cells

Lectins are a highly diversified group of proteins with carbohydrate binding abilities, ubiquitously found in bacteria, fungi, plants, and animals (Mazalovska & Kouokam, 2020). The term was coined by Boyd and Shapleigh in 1954, to indicate a nonimmunoglobulin protein that binds carbohydrate molecules without modifying them. These proteins are currently considered carbohydrate-binding proteins that reversibly interact with specific saccharides in glycoproteins and glycolipids (Figg. 14 & 15). Given that malignant transformation is closely linked to modified cell surface glycans, these proteins may interact with free and/or cell surface oligosaccharides and may bind cancer cells differently. As a result, lectins may be used as an effective diagnostic tool for cancer and may be developed into anticancer medications (Mazalovska & Kouokam, 2020). The altered glycosylation pattern both with new glycoforms formed or incompletely synthesized glycans (Fig 15), is an important hallmark of malignancy and generates multiple biomarkers for cell malignancy (Pinho & Reis, 2015; Fig.15).

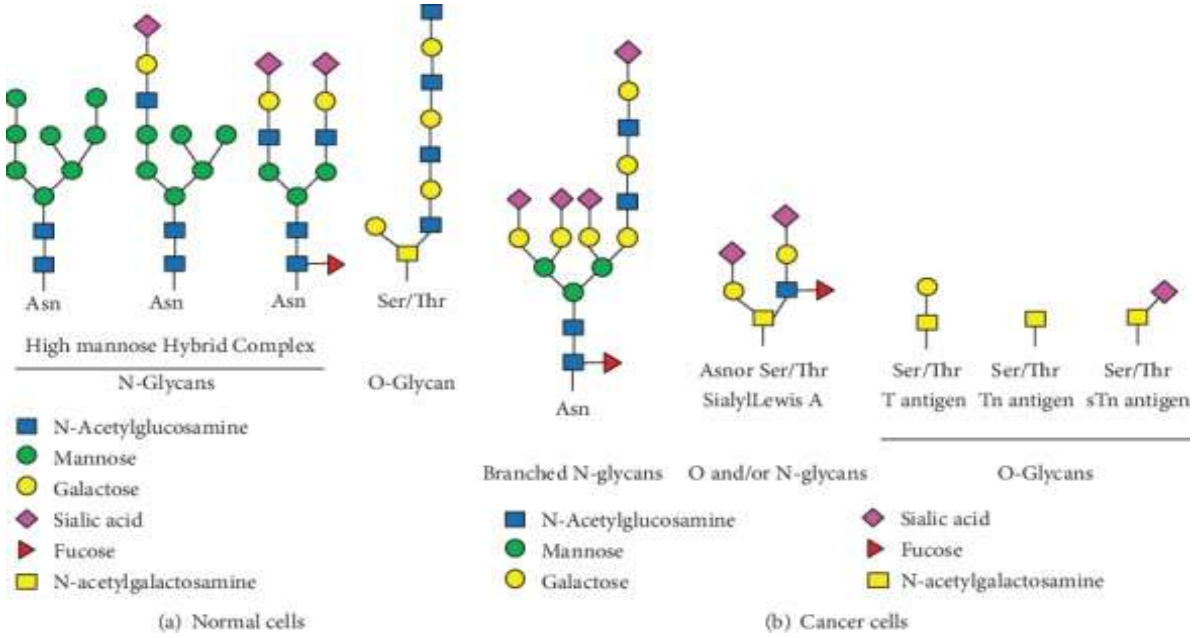


Fig.14 Schematic representation of select N- and O-glycans found in normal and cancer cells. (a) Normal cells have three major types of N-glycans, including high mannose, hybrid, and complex types. (b) Cancer cells have altered glycosylation

patterns, comprising either production of new glycans or incomplete synthesis of original glycans (from Mazalovska & Kouokam, 2020).

The cell surface in eukaryotes encompasses proteins and carbohydrates, which constitute the glycocalyx: glycans are very diverse and complex, with various monosaccharides, glycan attachment sites, and bond and branching types (Varki et al., 2009; Mazalovska & Kouokam, 2020). As summarized in Fig.14, they are mostly linked to the nitrogen of asparagine moieties (N-glycans) or through the oxygen of serine or threonine moieties (O-glycans) on secreted or membrane-bound glycoproteins, with a broad range of structures (Fig.14). Mature glycoproteins vary N-linked oligosaccharides according to cell type, tissue, and species (Goh & Ng, 2017). All eukaryotic cells share the basic mechanisms of glycoprotein synthesis; however, marked differences exist between malignant and noncancerous cells. For example, sialylation is an important modification in cellular glycosylation, as sialylated carbohydrates have an important role in cellular recognition, cell adhesion and cell signaling. An increase in global sialylation has been closely associated with cancer (Cao et al., 2021). Aberrant glycosylation in cancer frequently involves an increase in the expression of sialyl Lewis a ($SLe^{a)}$ and sialyl Lewis x (SLe^{x}), in particular SLe^{x} high expression levels are correlated with poor survival in cancer patients (Tanio et al., 2021; Fig.15).

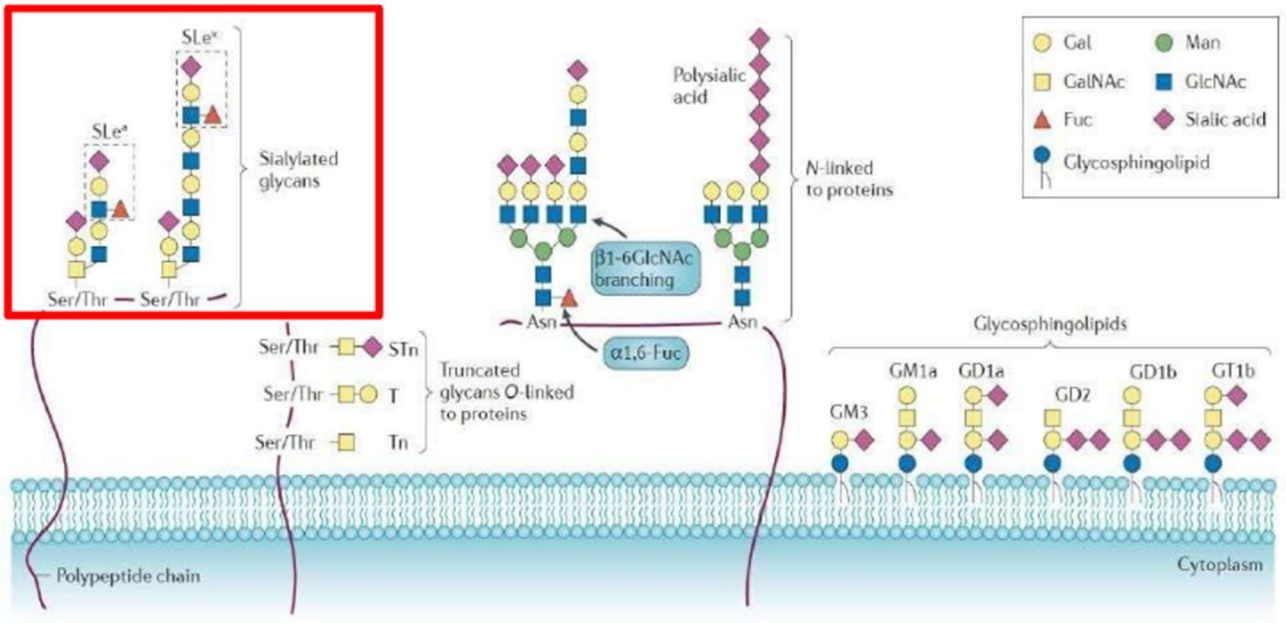


Fig.15 Important tumor-associated glycans (adapted from Pinho & Reis, 2015).

3.2.2 Lectins in pancreatic cancer

Dysregulated sialylation is a hallmark feature of pancreatic and other malignancies. Examples of tumor-associated sialoglycans found on glycoproteins include hypersialylated N-glycans, sialyl Lewis antigens, and sialylated forms of truncated O-glycans (sialyl-Tn and sialyl-T antigens) (Cao et al., 2021; Bellis et al., 2022; Marciel et al., 2023). Sialoglycans play a critical role in regulating tumor cell phenotype by modulating the activity of transmembrane and secreted glycoproteins. Additionally, the hypersialylation of tumor cells can dampen the immune response through sialic acid binding to Siglecs (Sialic acid-binding immunoglobulin-type lectins) on the surface of various immune cells (Fig.16).

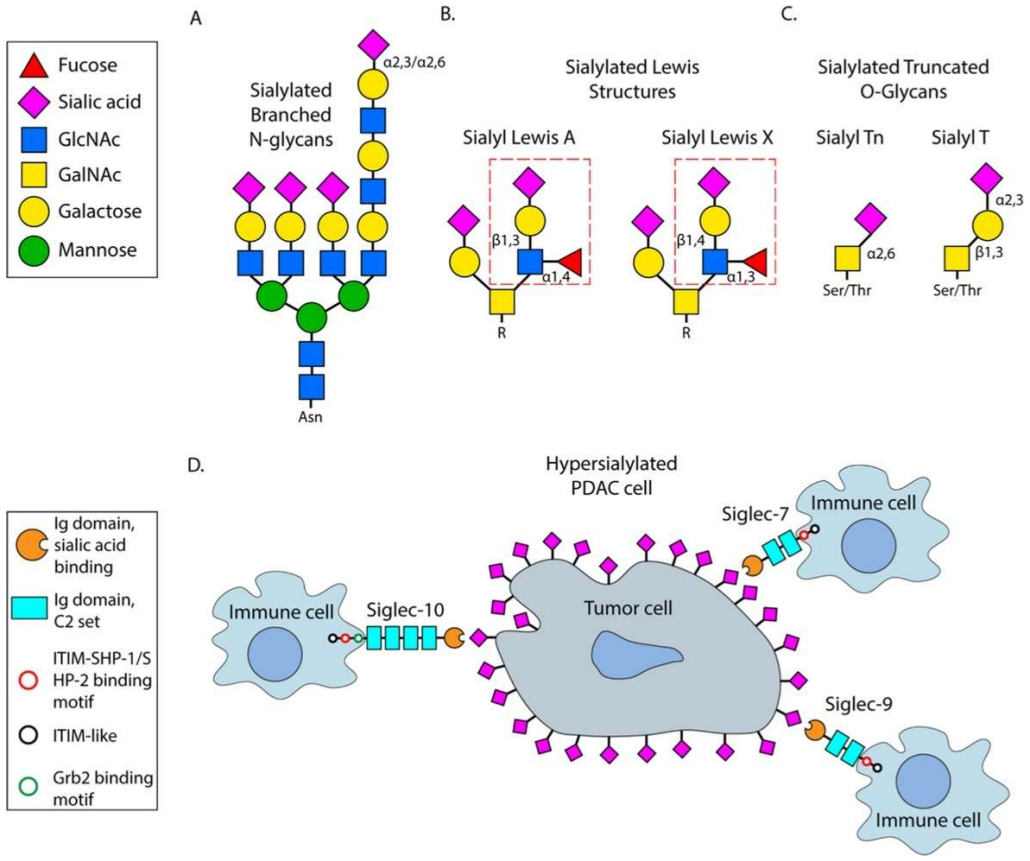


Fig.16 Schematic representation of Sialoglycans enriched in tumor cells and their cognate receptors, Siglecs (from Marciel et al., 2023)

The presence of sialic acids on tumor cells has been associated with a Siglec-mediated reduction in effector T cells, an increase in regulatory T cells (Perdicchio et al., 2016), and differentiation of

monocytes into macrophages with an immunosuppressive phenotype (Rodriguez et al., 2021). Together these effects facilitate tumor escape from immune surveillance. The lack of effective treatments for pancreatic cancer underscores the need for a better understanding of the molecular mechanisms that drive cancer initiation and progression. Elucidating the mechanisms by which sialoglycans promote carcinogenesis may reveal important new targets for therapeutic intervention or biomarkers that can be used to track disease advancement or recurrence. From glycoproteomic analysis, it is reported that various N-linked glycoproteins upregulated in PDAC are mainly modified by sialylated and/or fucosylated glycans, these modifications can be considered potential targets of PDAC (Cao et al., 2021).

Lectin Name	endocrine cell labeling	duct cell labeling	acinar cell labeling	endothelial cell labeling
PNA	NO	NO	Strong	NO
UEA I	NO	NO	Strong	NO
CON A	strong	strong	strong	strong
RCA120	Strong	Strong	Strong	Strong
SBA	NO	Strong	Strong	NO
DBA	NO	strong	NO	NO
WGA	Strong	Strong	Strong	Strong
GSL I	NO	NO	Strong	Weak
LCA	Weak	Strong	No	Strong
PHA-E	Weak	Weak	Weak	Weak
PHA-L	NO	NO	Weak	Weak
PSA	NO	Weak	NO	Strong
Su WGA	NO	NO	Weak	NO
GSL II	NO	NO	NO	Weak
DSL	NO	NO	NO	No
ECL	NO	Weak	Strong	NO
Jacalin	Strong	Weak	NO	NO
LEL	Strong	NO	NO	NO
STL	NO	NO	Strong	Weak
VVA	NO	Strong	NO	No

Fig.17 Lectins specificity for different pancreatic cell types (adapted from Xiao et al., 2016).

The peanut agglutinin from Arachis Hypogaea (PNA) lectin, binds sialyl Lewis X residues (Chandrasekaran et al., 2016; Xiao et al., 2016), therefore it may be considered a useful method to target cancer cells. As a matter of fact, PNA can strongly bind acinar cells (Xiao et al., 2016; Fig.17). Since one of the early processes in the onset of PDAC is the acinar to ductal metaplasia stage, other lectins may represent an efficient strategy to target PDAC cells in the early stages of tumorigenesis. For example, Dolichos biflorus agglutinin (DBA) as well as VVA (Vicia Villosa Lectin), and, wheat germ agglutinin (WGA), all of which capable of binding modified glycans exposed on the surface of ductal cells (; Tao et al., 2008; Xiao et al., 2016; Wu et al., 2022; Fig.17).

3.2.3 The SNAP^{TM} Tag reaction: pseudotyping extracellular vesicles

Given all the stated information about both extracellular vesicles as a potential drug delivery vector and the biological implications of lectin in cancer targeting and therapy, it would be of great benefit to be able to produce and/or purify extracellular vesicles pseudotyped with a given lectin of interest to deliver a therapeutic cargo straight to the cancer cells. Many limitations exist still nowadays (Figg.10,11), as extensively reported in the previous paragraphs of this chapter- with the most important not being able to efficiently engineer source cells with a given protein of interest- yet a novel, feasible, scalable and tuneable way of reaching this may be taking advantage of the so called SNAP^{TM} Tag chemistry.

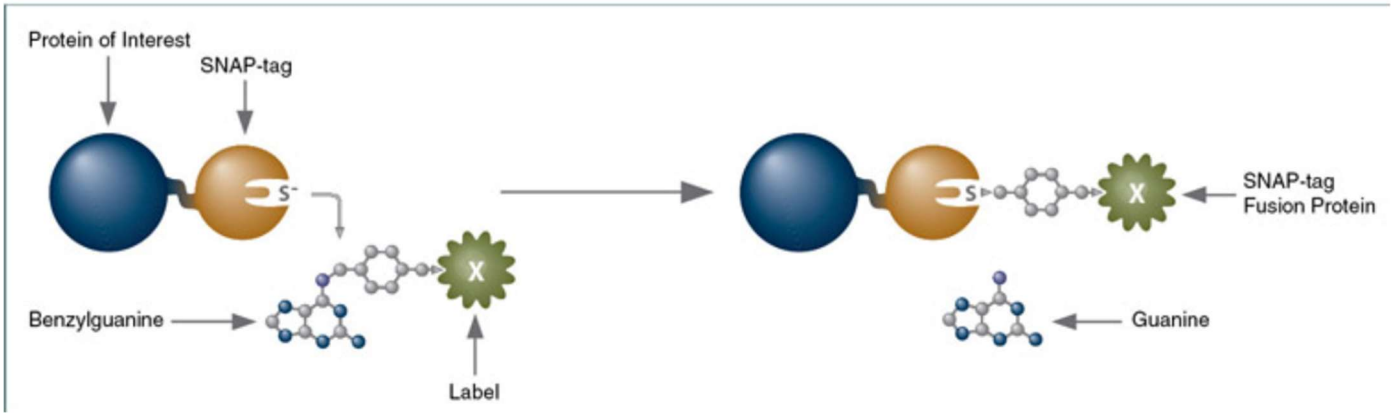


Fig.18 Schematic representation of the SNAP^{TM} Tag chemistry. In this context, "X" may be a given lectin of interest (see text for further details; from NEB website)

SNAP-tag is a 20 kDa mutant of the DNA repair protein O^6-alkylguanine-DNA alkyltransferase that reacts specifically and rapidly with benzylguanine (BG) derivatives (Fig.18), leading to irreversible covalent labelling of the SNAP-tag with a synthetic probe. The rate of the reaction of SNAP-tag with BG derivatives is to a large extent independent of the nature of the synthetic probe attached to BG, permitting the labeling of SNAP fusion proteins with a wide variety of synthetic probes. In such a context, for example, parent cells are first transfected with a construct that enables the exposure of the SNAP tag on their surface (i.e., GPI-anchored proteins fused with SNAP), then extracellular vesicles are isolated from conditioned medium and subjected to the reaction with a BG derivative linked to a lectin of interest (i.e., PNA).

4. AIMS OF THE THESIS

Extracellular vesicles (EVs) are emerging as promising vehicles for the delivery of therapeutic macromolecules, including mRNAs. However, their clinical translation is hindered by key challenges such as poor cargo loading efficiency, lack of targeting specificity, and limited functional delivery. In this study, we aimed to develop a modular and scalable EV engineering platform capable of enhancing mRNA cargo enrichment, controlling cell targeting, and improving functional delivery of therapeutic payloads.

5. MATERIALS AND METHODS

5.1 Plasmids generation and molecular cloning

5.1.1 Cloning IGG4 dimerization signals in pSNAP DISPLAY

To obtain a DNA construct with a IGG4 hinge dimerization signal spanning the SNAP^{TM}-tag and the DISPLAY^{TM} transmembrane domain, pSNAP Display (Addgene #205094**)** was linearized with the restriction enzymes SalI-HF (New England Biolab, NEB R3138S) in NEB Buffer rCutSmart. After that, the restriction product was separated in a 0.8% TAE-agarose gel and visualised at a UV transilluminator through ethidium bromide (Sigma Aldrich, E1510). The band corresponding to the 5832bp was isolated and purified with the kit NucleoSpin PCR and Cleanup (Macherey-Nagel, FC140609N) according to manufacturer's instruction. In order to insert the IGG4 hinge site between SNAP^{TM}-tag and DISPLAY^{TM} domains, the two following synthetic oligos were annealed together and the resulting dsDNA ligated with T4 DNA Ligase (New England Biolab, NEB M0202S) in a 3:1 ratio according to manufacturer's instruction.

pDisplayHingeUp	5' – Tcgacacgcgt**GAGTCCAAGTACGGCCCTCCATGTCCTAGCTGCCCCg** – 3'
pDisplayHingeDown	5'- TcgacGGGGCAGCTAGGACATGGAGGGCCGTACTTGGACTCacgcgtg -3'

5.1.2 Generation of double mutant VSV-G

To being able to mutate VSV-G so that it no longer binds to its cell surface receptors but can still escape endosomes (Nikolic et al., 2018; Dobson et al., 2022) two directed point mutations at K47Q and at R354A were applied. To create this construct, WT sequence of the VSV-G protein was amplified from pMD2.G plasmid (Addgene #12259) following the protocol of the QuickChange XL Site-Directed Mutagenesis Kit (Agilent Technologies, #200516). Primers carrying the codon substitution were designed as follows:

K47Q forward	5'-CCATACAAGTCAAAATGCCCCAGAGTCACAAGGCTATTCAAG -3'
K47Q reverse	5'-CTTGAATAGCCTTGTGACTCTGGGGCATTTTGACTTGTATGG -3
R354A forward	5'-CAGTGGAACTACCACAGAAGCGGAACTGTGGGATGACTGG -3'
R354A reverse	5'-CCAGTCATCCCACAGTTCCGCTTCTGTGGTAGTTCCACTG -3'
SeqR354A_fw	5'-AAGTCTAATTCAGGACGTTG-3'
SeqK47Q_rv	5'-TCAACCAGCACATGGTGAGG-3'

5.1.3 Cloning whole WGA in pSNAP CD8 DISPLAY

To obtain a DNA construct with a lectin ligand (WGA, Agglutinin isolectin 1 from wheat germ *Triticum*, Uniprot ID P10968) the whole WGA sequence was cloned at the N-terminus of the pSNAP CD8 Display upstream the SNAP^{TM}-tag so that it would have been displayed on the surface of the resulting extracellular vesicle. To this aim, pSNAP CD8 Display was enzymatically digested with the restriction enzymes HindIII-HF (New England Biolab, NEB R3104 S) and BstXI (NEB R0113S) in NEB Buffer r2.1 to excise the HA-Tag sequence and create sticky ends. After that, the restriction product was separated in a 0.8% TAE-agarose gel and visualised at a UV transilluminator through ethidium bromide (Sigma Aldrich, E1510). The band corresponding to the 6220bp was isolated and purified with the kit NucleoSpin PCR and Cleanup (Macherey-Nagel, FC140609N) according to manufacturer's instruction. To insert the whole WGA sequence, the latter was amplified through polymerase chain reaction (PCR) with the following Gibson's reaction primers from pWGA-Cre:

WGA FW	5-gagacccaagctggctagcgtttaaacttaAGCTTGCCACCATGCGGAAGATGATGAGCACCATGG_– 3'
WGA RV	5'-catctcgcagtccttGTCCATCGATCCGTCCATAGATCTGGCGTCGCAGCCGCCGGACTGAC -3'

Finally, the vector (pSNAP CD8 Display enzymatically digested with HindIII-HF and BstXI) and whole WGA sequence were assembled in order to obtain pWGA SNAP CD8 DISPLAY through Gibson Assembly® Cloning Kit (NEB, E5510S) at a rato 3:1 WGA:vector.

5.1.4 Cloning EBNA in pWGA SNAP CD8 DISPLAY

To obtain a DNA construct with the EBNA-1 DNA binding protein to enhance the copies of DNA cargo molecule loaded into extracellular vesicles lumen, the EBNA sequence was placed at the C-terminus of the DISPLAY™ domain so that it would have been faced the lumen of the resulting extracellular vesicle. To this aim, previously obtained pWGA SNAP CD8 Display was enzymatically digested with the restriction enzymes EcorI-HF (New England Biolab, NEB R3101S) and XbaI (New England Biolab, NEB R0145S) in NEB Buffer rCutsmart to excise the DISPLAY™ sequence and create sticky ends. After that, the restriction product was separated in a 0.8% TAE-agarose gel and visualised at a UV transilluminator through ethidium bromide (Sigma Aldrich, E1510). The band corresponding to the 6601bp was isolated and purified with the kit NucleoSpin PCR and Cleanup (Macherey-Nagel, FC140609N) according to manufacturer's instruction. To insert the DISPLAY™_EBNA-1 fragment, the latter was isolated similarly as described above (2108bp band) after an enzymatic restriction cut with the same enzymes on a customized fragment (Thermo Fisher, gene synthesis in pMK-RQ, codon optimized) as follows:

5'AVGQDTQEVIVVPHSLPFKVVVISAILALVVLTIISLIILIMLWQKKPRASATMSDEGPGTGPGNGLGE
KGDTSGPEGSGGSGPQRRGGDNHGRGRGRGRGRGGGRPGAPGGSGSGPRHRDGVRRPQKRPSCIGCK
GTHGGTGAGAGAGGAGAGGAGAGGGAGAGGGAGGAGGAGGAGAGGGAGAGGGAGGAGGAGAG
GGAGAGGGAGGAGAGGGAGGAGGAGAGGGAGAGGGAGGAGAGGGAGGAGGAGAGGGAGAGGA
GGAGGAGAGGAGAGGGAGGAGGAGAGGAGAGGAGAGGAGAGGAGGAGAGGAGGAGAGGAGGA
GAGGGAGGAGAGGGAGGAGAGGAGGAGAGGAGGAGAGGAGGAGAGGGAGAGGAGAGGGGRGR
GGSGGRGRGGSGGRGRGGSGGRRGRGRERARGGSRERARGRGRGRGEKRPRSPSSQSSSSGSPPRRPP
PGRRPFFHPVGEADYFEYHQEGGPDGEPDVPPGAIEQGPADDPGEGPSTGPRGQGDGGRRKKGGWFG
KHRGQGGSNPKFENIAEGLRALLARSHVERTTDEGTWVAGVFVYGGSKTSLYNLRRGTALAIPQCRLT
PLSRLPFGMAPGPGPQPGPLRESIVCYFMVFLQTHIFAEVLKDAIKDLVMTKPAPTCNIRVTVCSFDDGV
DLPPWFPPMVEGAAAEGDDGDDGDEGGDGDEGEEGQEISS*SGRL 3'

Finally, the vector (pWGA SNAP CD8 Display enzymatically digested with EcorI-HF and XbaI) and DISPLAY™-EBNA1 gene synthesis fragment sequence were assembled in order to obtain pWGA

SNAP CD8 DISPLAY EBNA through Gibson Assembly® Cloning Kit (NEB, E5510S) at a rato 5:1 DIPALY^{TM}-EBNA1:vector.

5.1.5 Cloning MCP in pWGA SNAP CD8 DISPLAY

To obtain a DNA construct with the MCP (here after: "MS2") bacterial RNA binding protein to enhance the copies of mRNA cargo molecule loaded into extracellular vesicles lumen (Horns et al., 2023), the MS2 sequence was placed at the C-terminus of the DISPLAY^{TM} domain so that it would have been faced the lumen of the resulting extracellular vesicle. To this aim, previously obtained pWGA SNAP CD8 Display EBNA was enzymatically digested with the restriction enzymes NheI-HF (New England Biolab, NEB R3131S) and XbaI (New England Biolab, NEB R0145S) in NEB Buffer rCutsmart to excise the EBNA sequence and create sticky ends. After that, the restriction product was separated in a 0.8% TAE-agarose gel and visualised at a UV transilluminator through ethidium bromide (Sigma Aldrich, E1510). The band corresponding to the 6754bp was isolated and purified with the kit NucleoSpin PCR and Cleanup (Macherey-Nagel, FC140609N) according to manufacturer's instruction. To insert the MS2-N55K fragment, the latter was amplified through polymerase chain reaction (PCR) with the following Gibson's reaction primers from PCR from PB-EPN24-MCP_I-T2A-eGFP-PGK-Blast (Addgene # pFH2.106), and the resulting amplicon of 387bp isolated from 0.8% TAE-agarose gel:

MS2 FW	5- TGATTATGCTGTGGCAGAAGAAGCCCAGAGCTAGCgcttcaaactttactcagttcgtgc– 3'
MS2 RV	5'- cgaggctgatcagcgggtttaaacgggccctctagaTCAgtagatacctgagttagcggcga-3'

Finally, the vector (pWGA SNAP CD8 Display EBNA enzymatically digested with NheI-HF and XbaI) and MS2-N55K fragment sequence were assembled in order to obtain pWGA SNAP CD8 DISPLAY MS2 through Gibson Assembly® Cloning Kit (NEB, E5510S) at a rato 5:1 MS2:vector.

5.1.6 Cloning MCP in pSNAP CD8 DISPLAY

To obtain a DNA construct with the MCP (here after: "MS2") bacterial RNA binding protein without the lectin ligand WGA as a control plasmid, the whole sequence of WGA was excise. To this aim, previously obtained pWGA SNAP CD8 Display MS2 was enzymatically digested with the restriction enzymes BamHI (New England Biolab, NEB R0136S) and NdeI (New England Biolab, NEB R0111S) in NEB Buffer r3.1 to excise the fragment including portion of the CMV promoter, the WGA and the SNAP tag sequences, creating sticky ends. After that, the restriction product was separated in a 0.8% TAE-agarose gel and visualised at a UV transilluminator through ethidium bromide (Sigma Aldrich, E1510). The band corresponding to the 5262bp was isolated and purified with the kit NucleoSpin PCR and Cleanup (Macherey-Nagel, FC140609N) according to manufacturer's instruction. To insert back the rest of the CMV promoter and the SNAP tag fragment, pSNAP CD8 DISPLAY was enzymatically digested with the same enzymes as before and the 1096 product isolated accordingly. Finally, the vector (pWGA SNAP CD8 Display MS2 enzymatically digested with BamHI and NdeI) and partial CMV promoter-SNAP tag fragment were assembled in order to obtain pSNAP CD8 DISPLAY MS2 through T4 Ligase ligation (New England Biolab, NEB M0202S) at a rato 3:1 fragment:vector.

5.1.7 Cloning whole PNA in pSNAP CD8 DISPLAY MCP

To obtain a DNA construct with a lectin ligand (PNA, Peanut Agglutinin from *Arachis hypogaea*, Uniprot ID P02872) the whole PNA sequence was cloned at the N-terminus of the previously obtained pSNAP CD8 Display MS2 upstream the SNAP^{TM}-tag so that it would have been displayed on the surface of the resulting extracellular vesicle. To this aim, pSNAP CD8 Display MS2 was enzymatically digested with the restriction enzymes HindIII-HF (New England Biolab, NEB R3104 S) and EcorI-HF (New England Biolab, NEB R3101S) in NEB Buffer rCutsmart to excise the WGA-SNAP tag sequence and create sticky ends. After that, the restriction product was separated in a 0.8% TAE-agarose gel and visualised at a UV transilluminator through ethidium bromide (Sigma Aldrich, E1510). The band corresponding to the 5827bp was isolated and purified with the kit NucleoSpin

PCR and Cleanup (Macherey-Nagel, FC140609N) according to manufacturer's instruction. To insert the whole PNA-SNAP tag-CD8 sequence, the latter was obtained from the enzymatic digestion of pPNA SNAP CD8 Display (custom gene synthesis below, Thermo Fisher, codon optimised) with the same enzymes as before and the resulting product isolated as previously described (1599bp):

5'MKPFCVFLTFFLLLAASSKKVDSAETVSFNFNSFSEGNPAINFQGDVTVLSNGNIQLTNLNKVNSVGR
VLYAMPVRIWSSATGNVASFLTSFSFEMKDIKDYDPADGIIFFIAPEDTQIPAGSIGGGTLGVSDTKGAG
HFVGVEFDTYSNSEYNDPPTDHVGIDVNSVDSVKTVPWNSVSGAVVKVTVIYDSSTKTLSVAVTNDN
GDITTIAQVVDLKAKLPERVKFGFSASGSLGGRQIHLIRSWSFTSTLITTTRRSIDNNEKKIMNMASAGG
GLNDIFEAQKIEWHEGSELGTMDKDCEMKRTTLDSPLGKLELSGCEQGLHEIIFLGKGTSAADAVEVPA
PAAVLGGPEPLMQATAWLNAYFHQPEAIEEFPVPALHHPVFQQESFTRQVLWKLLKVVKFGEVISYSH
LAALAGNPAATAAVKTALSGNPVPILIPCHRVVQGDLDVGGYEGGLAVKEWLLAHEGHRLGKPGLGG
SPAKPTTTPAPRPPTPAPTIASQPLSLRPEACRPAAGGAVHTRGLDFACDEFAVGQDTQEVIVVPHSLPF
KVVVISAILALVVLTIISLIILIMLWQKKPR*AA 3'

Finally, the vector (pWGA SNAP CD8 Display MS2 enzymatically digested with EcorI-HF and HindIII-HF) and PNA-SNAP tag-CD8 fragment sequence were assembled in order to obtain pPNA SNAP CD8 DISPLAY MS2 through T4 Ligase ligation (New England Biolab, NEB M0202S) at a rato 3:1 fragment:vector

5.1.8 Cloning EBNA in pTRANSFERRIN SNAP

Similarly to what has been done in 6.3.4 for pWGA SNAP CD8 DISPLAY, we aimed at cloning the EBNA-1 sequence at the N-terminus of the transferrin receptor, so that this protein it would have been faced the lumen of the resulting extracellular vesicle. To this aim, pCDH-EF1-TfR20-SNAP-IRES-Puro (Addgene #171018) was enzymatically digested with the restriction enzymes NheI-HF (New England Biolab, NEB R3131S) and XhoI (New England Biolab, NEB R0146S) in NEB Buffer rCutsmart to excise a 22bp fragment upstrea the Transferrin receptor. and create sticky ends. After

that, the restriction product corresponding to the 11078bp was isolated and purified with the kit NucleoSpin PCR and Cleanup (Macherey-Nagel, FC140609N) according to manufacturer's instruction. To insert the EBNA-1 fragment, the latter was isolated similarly as described above (1937bp band) after an enzymatic restriction cut with the same enzymes on a customized fragment (Thermo Fisher, gene synthesis in pMK-RQ, codon optimized) as in section 6.3.4. Finally, the vector (pCDH-EF1-TfR20-SNAP-IRES-Puro enzymatically digested with NheI-HF and XhoI) and EBNA-1 fragment sequence were assembled to obtain pEBNA Transferrin SNAP through T4 Ligase ligation (New England Biolab, NEB M0202S) at a rato 7:1 fragment:vector.

5.1.9 Cloning MCP in pTRANSFERRIN SNAP

Similarly to what has been done in 6.3.5 for pWGA SNAP CD8 DISPLAY, we aimed at cloning the MS2 sequence at the N-terminus of the transferrin receptor, so that this protein would have been faced the lumen of the resulting extracellular vesicle, this time without including a ligand on the surface. To this aim, previously obtained pEBNA Transferrin SNAP was enzymatically digested with the restriction enzymes NheI-HF (New England Biolab, NEB R3131S) and XhoI (New England Biolab, NEB R0146S) in NEB Buffer rCutsmart to excise the EBNA sequence and create sticky ends. After that, the restriction product was separated in a 0.8% TAE-agarose gel and visualised at a UV transilluminator through ethidium bromide (Sigma Aldrich, E1510). The band corresponding to 10523bp was isolated and purified with the kit NucleoSpin PCR and Cleanup (Macherey-Nagel, FC140609N) according to manufacturer's instruction. To insert the MS2-N55K fragment, the latter was amplified through polymerase chain reaction (PCR) with the following Gibson's reaction primers from PCR from PB-EPN24-MCP_I-T2A-eGFP-PGK-Blast (Addgene # pFH2.106) and the resulting amplicon of 387bp isolated from 0.8% TAE-agarose gel:

MS2 FW	5'TCCAAGCTGTGACCGGCGCCTACTCTAGAGCTAGCGCCACCATGgcttcaaactttactcagttcgtgc–3'
MS2 RV	5'- CTGATCTAGCTTGATCCATCATGGTGGCGCTCGAGctgtagatacctgagttagcggcga -3'

Finally, the vector (pEBNA Transferrin SNAP enzymatically digested with NheI-HF and XhoI) and MS2-N55K fragment sequence were assembled in order to obtain pMS2 Transferrin SNAP through Gibson Assembly® Cloning Kit (NEB, E5510S) at a ratio 7:1 MS2:vector.

5.1.10 Cloning WGA in pTRANSFERRIN SNAP

Similarly to what has been done in 6.3.4 for pSNAP CD8 DISPLAY, the WGA sequence, depleted of its first 20 AA was fused at the C-terminus of the p-human TRANSFERRIN receptor-1 (hereafter: "pTRANSFERRIN SNAP"). To this aim, pCDH-EF1-TfR20-SNAP-IRES-Puro (Addgene #171018) was enzymatically digested with the restriction enzymes BamhI-HF (New England Biolab, NEB R3136S) and NotI-HF (NEB R3189S) in NEB Buffer rCutSmart to excise the SNAP-Tag sequence and create sticky ends. After that, the restriction product was separated in a 0.8% TAE-agarose gel and visualised at a UV transilluminator through ethidium bromide (Sigma Aldrich, E1510). The band corresponding to the 9976bp was isolated and purified with the kit NucleoSpin PCR and Cleanup (Macherey-Nagel, FC140609N) according to manufacturer's instruction. To insert the WGA sequence of interest, the latter was obtained from the enzymatic digestion of SNAPtag-WGA fragment (custom gene synthesis below, Thermo Fisher, codon optimised) with the same enzymes as before and the resulting product isolated as previously described (1124bp):

5'MDKDCEMKRTTLDSPLGKLELSGCEQGLHRIIFLGKGTSAADAVEVPAPAAVLGGPEPLMQATAWL
NAYFHQPEAIEEFPVPALHHPVFQQESFTRQVLWKLLKVVKFGEVISYSHLAALAGNPAATAAVKTAL
SGNPVPILIPCHRVVQGDLDVGGYEGGLAVKEWLLAHEGHRLGKPGLGGGGSGGGGSGGGGSTGQ
RCGEQGSNMECPNNLCCSQYGYCGMGGDYCGKGCQNGACWTSKRCGSQAGGATCPNNHCCSQYGH

CGFGAEYCGAGCQGGPCRADIKCGSQSGGKLCPNNLCCSQWGFCGLGSEFCGGGCQSGACSTDKPCG
KDAGGRVCTNNYCCSKWGSCGIGPGYCGAGCQSGGCD*CTAA3'

Finally, the vector (pCDH-EF1-TfR20-SNAP-IRES-Puro enzymatically digested with BamHI-HF and NotI-HF) and SNAPtag-WGA fragment sequence were assembled to obtain pTransferrin SNAP WGA through T4 Ligase ligation (New England Biolab, NEB M0202S) at a rato 5:1 fragment:vector.

5.1.11 Cloning MCP in pTRANSFERRIN SNAP WGA

Similarly to what has been done in 6.3.5 for pWGA SNAP CD8 DISPLAY, we aimed at cloning the MS2 protein at the N-terminus of the Transferrin receptor and the ligand at its C-terminus. To this aim, previously obtained pMS2 Transferrin SNAP was enzymatically digested with the restriction enzymes BamhI-HF (New England Biolab, NEB R3136S) and NotI-HF (NEB R3189S) in NEB Buffer rCutSmart to excise the SNAP-Tag sequence and create sticky ends. After that, the restriction product was separated in a 0.8% TAE-agarose gel and visualised at a UV transilluminator through ethidium bromide (Sigma Aldrich, E1510). The band corresponding to the 10358bp was isolated and purified with the kit NucleoSpin PCR and Cleanup (Macherey-Nagel, FC140609N) according to manufacturer's instruction. To insert the SNAPtag-WGA sequence of interest, the latter was obtained from the enzymatic digestion of SNAPtag-WGA fragment (custom gene synthesis, Thermo Fisher, codon optimised) with the same enzymes as before and the resulting product isolated as previously described in section 6.3.10 (1124bp). Finally, the vector (MS2 Transferrin SNAP enzymatically digested with BamHI-HF and NotI-HF) and SNAPtag-WGA fragment sequence were assembled to obtain pMS2Transferrin SNAP WGA through T4 Ligase ligation (New England Biolab, NEB M0202S) at a rato 7:1 fragment:vector.

5.1.12 Bacterial transformation and amplification, restriction analysis and sequencing

After the desired constructs were designed and the reactions concluded, the recombinant DNA was transformed into competent bacteria strains, listed in the following table according to the single experiment.

Chemically competent Stbl3E.Coli (Invitrogen LSC737303)	PCR amplificauon, T4 ligation
NEB 5-alpha Competent E.Coli (NEB C2987H)	Gibson reaction
XL10-Gold Ultracompetent cells (Agilent Technologies, 200314)	QuickChange Mutagenesis protocol

Single colonies were then picked for mini-prep inoculation and DNA purification with the kit QIAprep Spin Miniprep Kit (Qiagen #27104). The purified DNA was analysed through restriction analysis and sequenced by Eurofins Genomics at the sequence downstream the promoter in the construct, thereby using one of the following primers:

T7 forward	5'- -3'
CAG forward	5'- GCAACGTGCTGGTTATTGTG -3'

Finally, the constructs were amplified and isolated through MaxiPrep (Macherey-Nagel, FC140414M) according to manufacturer's instruction.

5.2 EV production

HEK293T cells (passage 6-15) were plated on 60 cm dishes (BD falcon, #353004) with 2,500,000 cells per dish and co-transfected the following day with 13.4 µg of plasmid mix using linear PEI 0.3mg/mL (Merck, #765090) 11uL/ µg of plasmid DNA. Plasmids for all the experiments included the fusogen (VSV-G (either WT or mutant; 0.7 µg), the scaffold construct of interest (6.4 µg) and the cargo (Cre; 6.4 µg): the final transfection ratio fusogen:scaffold:cargo was therefore 1:20:20. Control conditions employed inert plasmidic DNA pCDNA 3.1(-). Media was harvested 48 hours after transfection.

5.3 EV isolation

48h after transfection the medium was collected and centrifuged at 500×g for 10 minutes at 4°C to remove cell debris. The supernatant was subsequently centrifuged at 2,000×g for 20 minutes at 4°C to eliminate apoptotic bodies and microvesicles. An additional, final round of centrifugation at 10,000×g for 40 minutes resulted in a pellet consisting of the large extracellular vesicles fraction (L-EV). The supernatant was not discarded, rather it was concentrated through an Amicon 100K filter (Millipore, UFC8100) to clear off any L-EV remains from the subsequent fraction to be isolated. Finally, concentrated supernatant underwent ultracentrifugation at 167,000×g for 4h at 4°C using a swinging rotor (Optima XE-90, Swinging Rotor SW41 Ti, Beckman & Coulter). This resulted in a pellet consisting of the small extracellular vesicles fraction (s-EV). Depending on downstream applications, both fractions pellets were resuspended as below: for FACS experiments, Cre delivery to LSL Td Tom HEK cells and RT-qPCR, 100uL of ice cold-PBS; for SDS PAGE and WB experiments, 40µL of RIPA buffer supplemented with protease inhibitor (COEDTAF-RO, Roche).

5.4 Labeling EV surface SNAP-tag Fusion Proteins with BG-substrates

Prior to the SNAP tag conjugation, the ligand of interest was coupled to BG-GLA-NHS (New England Biolabs, NEB S9151S). Briefly, 2mg of BG-GLA-NHS were resuspended in 208µL of deuterated DMSO (Merck, #175943) according to manufacturer's instruction. Subsequently, 2.8µL of this solution were added to 100µL of 27µM of the ligand of interest (1mg/mL WGA; Sigma Aldrich, L9640) and left at room temperature for 3h on a gently shaking. The reaction mix was then cleaned up several times through an Amicon 10K filter (Merck, UFC5010) to remove the WGA excess. The final product (BG-WGA) was collected in a low protein binding tube (Thermo, 90411), brought back to a final volume of 100uL in PBS and quantified at Nanodrop λ_{280} and kept at -20°C until needed. For the SNAP-tag labelling reaction, 100µL of PBS either isolated L-EV or s-EV were labelled with 3µM of BG-WGA in a low protein binding tube for 1h at room temperature, still. Finally, according to the fraction being used, EVs were washed again through either 10,000x*g* centrifugation (L-EV) or 167,000x*g* ultracentrifugation (s-EV) to remove excess WGA, resuspended in PBS and readily applied to reporter cells.

5.5 EV SDS-PAGE SNAP Tag visualization

To visualize the SNAP-tag exposition on EV surface, a similar approach to the SNAP-tag labelling with protein was employed, using SNAP-Surface® 594 (New England Biolabs, NEB S9134S) which after coupling to the SNAP-tag allows simple visualization via UV-transilluminator. Briefly, 5 mL of conditioned medium were collected 48h after transfection and cleared from cells debris and apoptotic body through 2000x*g* for 20 minutes. The supernatant was then concentrated through an Amicon 50K filter (Merck, UFC8050) to a final volume of 500µL, collected in a low protein binding tube and reacted with SNAP-Surface® 594 according to manufacturer's instruction for 1h at 37°C protected from light. After this step each of the L-EV and s-EV fractions were isolated as described earlier in this section. Briefly, the total reaction volume was diluted in 5 mL of PBS and L-EV fraction pelleted at 10000x*g* for 40 minutes at 4°C. The supernatant was not discarded; it underwent ultracentrifugation

step at 167000x*g* for 4h at 4°C to isolate s-EV fraction. Both pellets were resuspended in 40uL RIPA buffer and readily treated with 10µL of Laemli's solution supplemented with 100mM DTT, left 5 minutes at 95°C shaking and loaded onto 4–20% Mini-PROTEAN® TGX™ Precast Protein Gels (biorad, #4561094) for 1h at 120V. Finally, the gel was removed from its support and SNAP-tag 594 signals visualized at UV-transilluminator.

5.6 Flow cytometry for Cre recombinase delivery to HEK cells

To test delivery of Cre-encoding mRNA by EVs, and how different scaffold domain may enhance cargo loading, either L-EV or s-EV fractions were isolated from conditioned medium as described earlier in this section and applied to receiver cells which activate RFP expression upon Cre recombination (HEK293T-LSL TdTomato, herafter: "Cre reporter"). Briefly, 1 day prior to treatment Cre reporter cells were plated on 12-wells plate (BD Falcon, #353043) with 100,000 cells/well; the following day, medium was replaced with 600µL of treatment mix consisting in 500µL of fresh HEK complete medium and 100µL of isolated, PBS resuspended-EVs and then maintained at 37 °C and 5% CO_2 in a humidified incubator for 72h. After 3 days, cells were detached, resuspended in FACS buffer (1× PBS; 5% FBS), filtered through 75µm filter and counted via flow cytometry at an S3e Cell Sorter (Bio-Rad). The results were analysed with FlowJo_v10.10.0.

5.7 Cre recombinase mRNA RT-qPCR in EVs

RNA was extracted from freshly isolated EVs resuspended in 100uL of fresh cold PBS via Trizol reagent (ThermoFisher, AM9738). 500ng of total RNA was used as input for subsequently cDNA conversion performed using the Takara kit (Takara, RR047A) following the manufacturer's instructions with slight modification. First, genomic DNA (gDNA) was digested by incubating the sample with gDNA Eraser at 42°C for 6 minutes. cDNA synthesis was then carried out using oligo(dT) primers and random hexamers supplied with the kit. The reaction mix contained 5 µL of this solution, 2.5 µL of reverse transcriptase enzyme, and was supplemented with 1 M betaine, and 6

mM MgCl2. The cDNA conversion was performed at 37°C for 15 mins followed by 50°C for 2 mins, and 37°C for 2 mins, for 15 cycles (Picelli et al., 2014). The reaction was then inactivated by heating at 85°C for 10 seconds. Subsequently, 1 µL of the synthesized cDNA was added directly to 9 µL of a qPCR mastermix solution (SsoAdvanced, 1725270, Bio-Rad) containing 250nM of primers. qPCR was performed for 40 cycles with the following conditions: 95°C for 30 seconds, followed by 95°C for 10 seconds and 60°C for 10 seconds per cycle. The run concluded with a melting curve analysis, conducted at a temperature increment of 0.5°C per cycle, with each step lasting 15 seconds. Semi-absolute quantification of total copies/uL of Cre mRNA in EVs was obtained projecting the respective C_t to those from an in-house Cre standard curve prepared with a full-length plasmid harbouring the Cre gene as reported in "Creating Standard Curves with Genomic DNA or Plasmid Templates for use in Quantitative PCR" (thermofisher.com). similarly, semi absolute quantification of total copies/uL of reference gene *OST4* (Pinheiro et al., 2024) was obtained in the same way but the standard curve was based on the resulting amplicon isolated from cDNA from 10^6 HEK293T cells. Results were normalized on *OST4* and relative expressions calculated according to the ΔΔ Ct equation (Vandersompele, J. et al, 2002). The primers used were as follows:

Target	FW (5'->3')	RV (5'->3')
Cre	agatgccaggacatcaggaacctg	atcagccacaccagacacagagatc
hOST4	ACGTGCAGCTCGCCATCT	TGTTGACGGCCACGTAGTGA

5.8 Western Blot

The expression of EVs markers was evaluated by Western Blot. Freshly isolated EVs fractions from conditioned medium were resuspended in 40µL of RIPA buffer supplemented with protease inhibitor (COEDTAF-RO, Roche), sonicated twice for 5 seconds at 25% amplitude, then added with 4X Laemmli buffer with 100mM DTT and denaturated at 95 °C for 5 minutes on shaking. 40uL of sample was loaded on onto 4–20% Mini-PROTEAN® TGX™ Precast Protein Gels (Biorad, #4561094) and thus separated for 1h at 120V. Proteins were transferred onto nitrocellulose membranes (Biorad, # 1620112) by the semi-dry system Trans-Blot® Turbo™ Transfer System

(Biorad, cat. no. 1704150) at 0.72 A and 25 V for 1 h. After blocking in 5% NFDM in TBS with 0.1%Tween 20 (TBST1x) for 1 h at RT, membranes were incubated with the primary antibodies overnight at 4 °C with gentle shaking in block solution: rabbit polyclonal anti-SNAP tag (Thermo, #CAB4255; 1:500) rabbit monoclonal anti-TSG101 (Abcam, #EPR7131; 1:500), and mouse monoclonal anti-Alix (SantaCruz, # sc-53540; 1:250). After three 5 min washes in TBST1x, membranes were incubated with goat anti-rabbit and anti-mouse HRP-conjugated secondary antibodies (Dako, #P0447 and #P0449; 1:1000) for 1 h at RT in blocking solution, washed three times for 10 minutes in TBS1x and then incubated for 5 min. in Clarity Western ECL Subs Substrate (Biorad, #1705060) and finally analysed with the transilluminator NineAlliance^{TM} (Uvitec, Cambridge, UK) with super sensitivity settings.

6. Results

6.1 Transmembrane scaffolds domains improve Cre mediated recombination in recipient cells

To explore whether different transmembrane scaffold domains may influence Cre cargo delivery via VSV-G–enveloped extracellular vesicles (EVs), we systematically screened a panel of surface displaying constructs fused to the SNAP protein. Each construct was designed to localize the SNAP protein to the EV membrane surface via distinct anchoring mechanisms: IgG4-based transmembrane domain (SNAP Display IgG4), Cd8α domain (SNAP Display Cd8), a GPI-anchor (SNAP Gpi), and the whole human transferrin receptor (Transferrin SNAP). HEK293T cells were transiently transfected with these constructs alongside Cre-encoding cargo and VSV-G plasmids and cultured for 48 hours prior to EV isolation. large EV (L-EV) and small EV (s-EV) fractions were isolated from 5 mL of conditioned medium, purified, and resuspended in 100 μL PBS. EVs were subsequently incubated with HEK293T LSL-tdTomato Cre-reporter cells, and delivery efficacy was quantified by measuring the number of TdTomato+ cells via FACS analysis after 72h treatment (Fig.19 A,B).

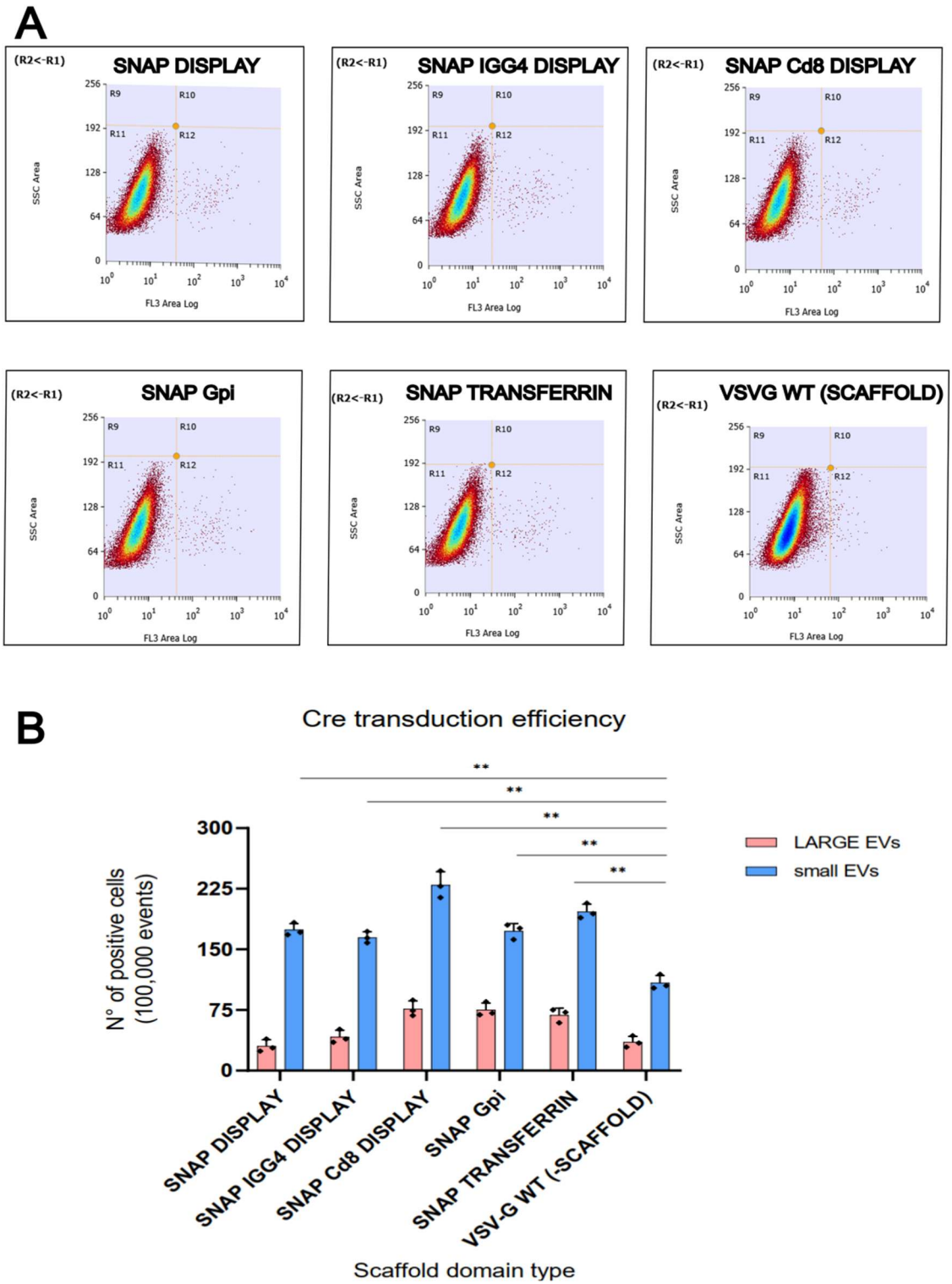


Fig.19 A: Representative FACS plots for HEK293T LSL-TdTomato reporter cells treated with VSV-G–enveloped s-EV. Control is s-EV isolated from cells transfected with just Cre and VSV-G plasmids; total N° of events was set at 100,000. B: Barplot depicting different Cre transduction efficiency for both L-EV and s-EV on reporter cells analyzed by FACS. All the independent values with error bars from three replicates are shown; two-tailed ratio paired t test, $p < 0.05$; N=3.

To quantify the contribution of each scaffold to Cre delivery, we compared reporter cells activation across each engineered condition relative to a negative control transfected with just Cre-encoding and VSV-G plasmids (VSV-G WT CTRL). We observed that s-EV but not L-EV from cells transfected with scaffold constructs promoted a significantly cre mediated recombination in recipient cells. compared to s-EV from the control (Fig.19 B; two-tailed ratio paired t test, $p < 0.05$; N=3). These results suggest that the presence and identity of a given transmembrane anchor may influence both quality and efficiency of Cre loading into EVs, or either more vesicles are produced and/or purified, or somehow the SNAP interacts with the surface of the recipient cell.

6.2 Mutant VSV-G–enveloped EVs show significantly impaired targeting activity

To explore strategies for disrupting the broad tropism of enveloped EVs and lay the groundwork for engineering these with selective targeting capabilities, we generated EVs displaying either wild-type (WT) or mutant (MUT) forms of the vesicular stomatitis virus glycoprotein (VSV-G). VSV-G WT is known to facilitate membrane fusion and endosomal escape, contributing to enhanced cargo release into recipient cells. In contrast, the VSV-G MUT variant was designed to retain endosomal escape functionality while being impaired in surface receptor binding and subsequent cellular uptake (Dobson et al., 2022). EVs were generated by transient transfection of HEK293T cells with plasmids encoding either VSV-G WT or VSV-G MUT, together with a Cre cargo and surface display constructs (SNAP Display Cd8 and Transferrin–SNAP). After 48 hours, both L-EV and s-EV fractions were isolated and then applied to HEK293T LSL-tdTomato Cre-reporter cells. Cargo delivery was quantified by measuring the number of tdTomato+ cells via FACS (Fig.20 B,D).

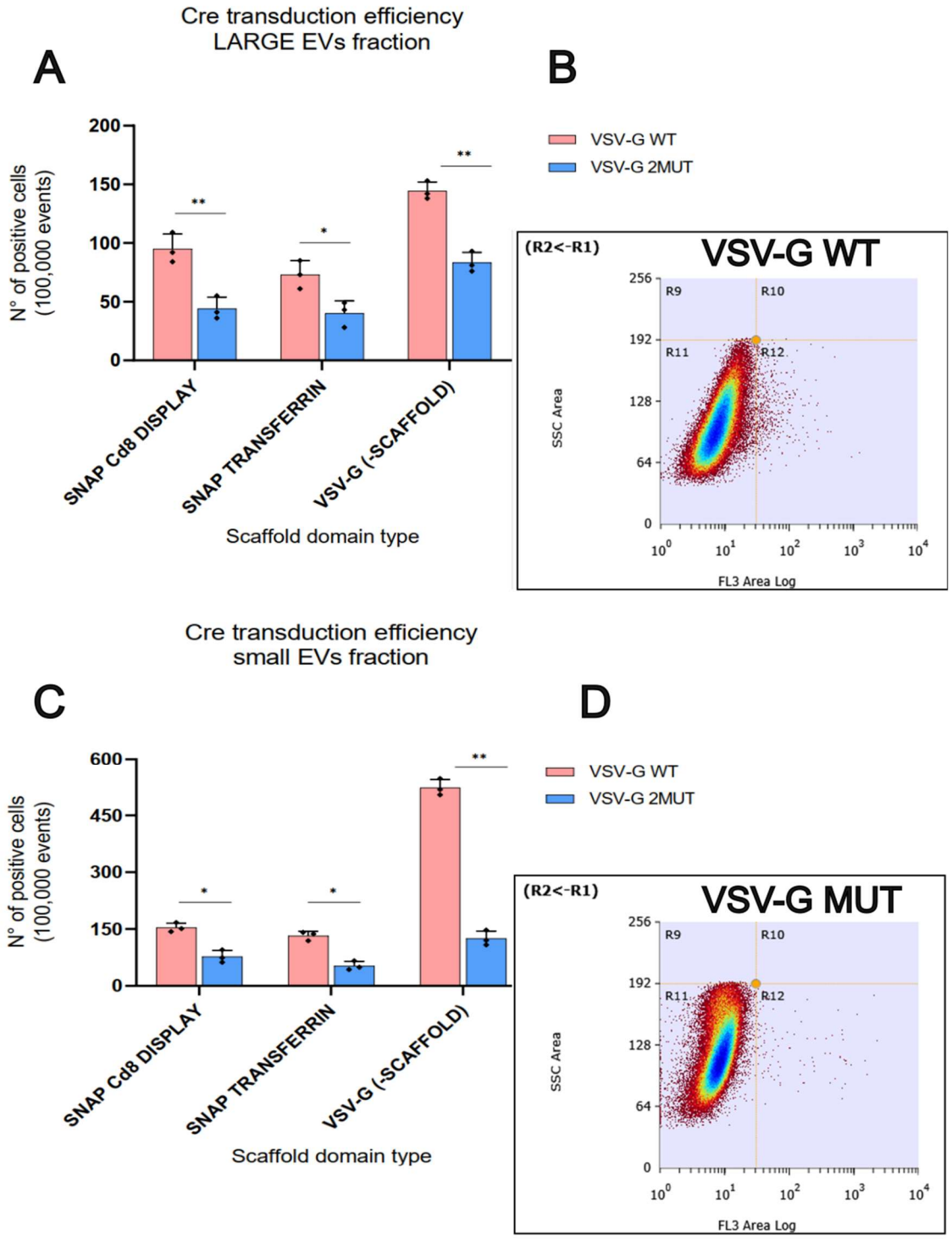


Fig.20 B,D: Representative FACS plots for HEK293T LSL-TdTomato reporter cells treated with either VSV-G WT–enveloped s-EV or VSV-G MUT–enveloped s-EV, respectively. Total N° of events was set at 100,000. A,C: Barplots depicting different Cre transduction efficiency for both L-EV and s-EV enveloped with either VSV-G WT or VSV-G MUT on reporter cells analyzed by FACS. Controls are either L-EV or s-EV isolated from cells transfected with just Cre and VSV-G plasmids, without the displaying scaffold domain (VSV-G,-SCAFFOLD). All the independent values with error bars from three replicates are shown; two-tailed ratio paired t test, $p < 0.05$; N=3.

Across all conditions, EVs enveloped with VSV-G MUT induced significantly fewer FACS+ reporter cells than their VSV-G WT counterparts, despite being otherwise equivalent in input volume (100uL PBS-resuspended EVs pellet). This reduction was observed for both L-EV and s-EV and was consistent regardless of the membrane scaffold used (SNAP–CD8 or Transferrin–SNAP). Statistical evaluation using a two-tailed ratio paired t test confirmed that the difference in transduction efficiency between VSV-G WT and VSV-G MUT-enveloped EVs was highly significant (Fig. 20 A,C; $p < 0.05$, $N = 3$ biological replicates). These findings suggest that the VSV-G MUT envelope selectively impairs EV uptake while still preserving transduction in recipient, thus providing a tool for dissecting entry versus release mechanisms in EV-mediated delivery systems.

6.3 Restoring Target Specificity via Lectin-Mediated Pseudotyping of mutant VSV-G EVs

To further assess the potential for restoring selective cellular uptake and cargo delivery in engineered EVs with impaired targeting capacity, we examined whether pseudotyping VSV-G–enveloped EVs with the lectin wheat germ agglutinin (WGA) could compensate for the loss of function caused by VSV-G mutation. WGA is a carbohydrate-binding lectin that recognizes N-acetylglucosamine and sialic acid moieties on mammalian cell surfaces, and it has been widely used to enhance cellular binding and endocytosis. Based on these properties, WGA was considered a suitable candidate for promoting EV–cell interactions. To test this, we engineered the SNAP protein onto selected scaffold domains—Display Cd8 SNAP and Transferrin SNAP—by fusing the WGA lectin either to the N-terminus or the C-terminus of SNAP, respectively. In this way, WGA was displayed on the surface of the resulting EVs. Both L-EV and s-EV fractions were isolated from the conditioned medium of HEK293T cells transfected with a Cre cargo expression plasmid, VSV-G (WT or MUT) envelope plasmid, and WGA-SNAP-scaffold plasmid. After 48 h of transient expression, EVs were applied to HEK293T LSL-tdTomato Cre-reporter cells and analyzed by FACS (Fig. 21A,B).

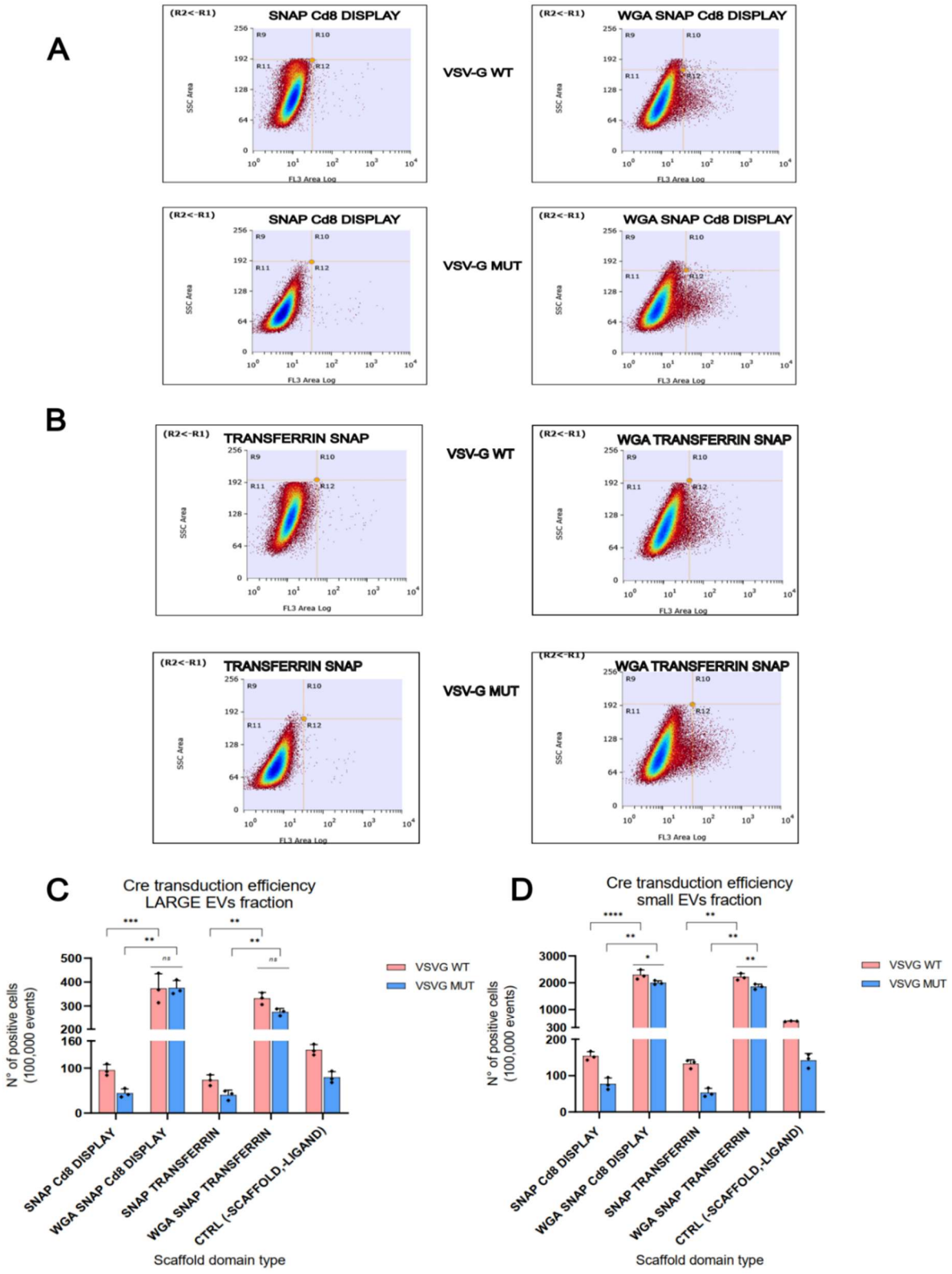


Fig.21 A,B: Representative FACS plots for HEK293T LSL-TdTomato reporter cells treated with either WGA-SNAP Display Cd8 and WGA-Transferrin SNAP, respectively. The plots show an increase in FACS+ reporting cells when EVs were pseudotyped with WGA, independently of their envelope (VSV-G WT or MUT), suggesting lectin pseudotyping of EVs surface may positively modulate their tropism; total N° of events was set at 100,000. C,D: Barplots depicting different Cre transduction efficiency for both L-EV and s-EV enveloped with either VSV-G WT or VSV-G MUT and pseudotyped with WGA on reporter cells analyzed by FACS, respectively. Controls are either L-EV or s-EV isolated from cells

transfected with just Cre and VSV-G plasmids, without the displaying scaffold domain (VSV-G,-SCAFFOLD,-LIGAND). WGA-pseudotyped s-EV enveloped with mutant VSV-G appear to be significantly less efficient in cargo Cre mRNA delivery with respect to their VSV-G WT enveloped counterparts, indicating that envelope coupled to pseudotyping would be a feasible strategy to produce engineered EVs with a specific targeting activity and a retained delivery efficiency. All the independent values with error bars from three replicates are shown; two-tailed ratio paired t test, $p < 0.05$; *ns*=non-significant; N=3.

WGA pseudotyping significantly increased the number of FACS+ reporter cells across both large and small EV fractions compared to their non-pseudotyped counterparts (Fig. 21C,D; two-tailed ratio paired t-test, $p < 0.05$, N = 3 biological replicates). This enhancement was consistent for both VSV-G WT–enveloped and VSV-G MUT–enveloped EVs, demonstrating the efficacy of lectin-based surface functionalization in improving cellular interaction and uptake. Remarkably, VSV-G MUT–enveloped EVs pseudotyped with WGA restored reporter cell activation to levels close to those achieved by WGA-pseudotyped VSV-G WT EVs. These results indicate that lectin-driven pseudotyping can overcome the impaired targeting phenotype of VSV-G MUT. Overall, this supports the potential of lectins such as WGA in modulating EV tropism independently of viral glycoprotein function.

We next evaluated whether comparable targeting and delivery efficiency could be achieved using a post-production modification strategy, exploiting the surface-exposed SNAP tag on EVs. This approach has translational relevance, since surface functionalization after EV production is generally preferable for clinical applications due to advantages in scalability, regulatory compliance, and manufacturing flexibility. For these experiments, we focused on VSV-G MUT–enveloped EVs, which in previous assays demonstrated delivery efficiency comparable to VSV-G WT EVs when pseudotyped. Their surface was functionalized via BG-SNAP chemistry by conjugating benzylguanine-modified WGA (BG-WGA) directly to the SNAP tag on EVs produced from cells transfected with either SNAP Display Cd8 or Transferrin SNAP.

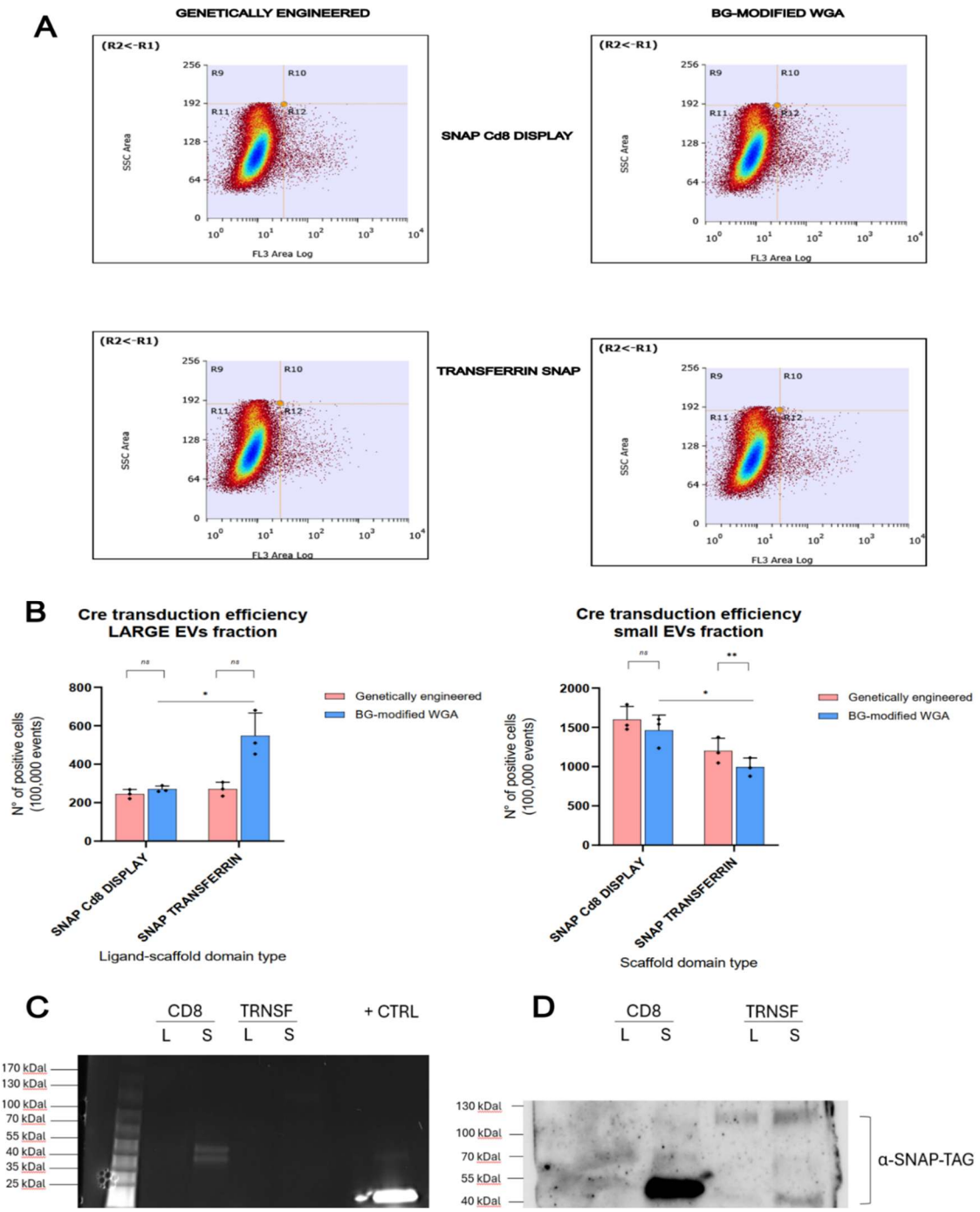


Fig.22 A: Representative FACS plots for HEK293T LSL-TdTomato reporter cells treated with either genetically engineered WGA-SNAP Display Cd8 and WGA-Transferrin SNAP pseudotyped s-EV (left) and postproduction-modified s-EV via BG-SNAP reaction (right), respectively. The plots show a similar number of FACS+ reporting cells across the two kinds of s-EV tested. Total N° of events was set at 100,000. B: Barplots depicting different Cre transduction efficiency on reporter cells analyzed by FACS for both L-EV (left) and s-EV (right) enveloped with VSV-G MUT and pseudotyped with WGA in both settings (genetically engineered or postproduction-modified through BG-SNAP reaction). Results show that cargo delivery efficiency of genetically engineered EVs with ligand is comparable to that of post-production modification for both the SNAP displaying scaffolds in L-EV fraction but not in s-EV fraction (SNAP TRANSFERRIN). All the independent values with error bars from three replicates are shown; two-tailed ratio paired t

test, $p < 0.05$; *ns*=non-significant; N=3. C: SDS-PAGE of genetically engineered L-EV and s-EV bearing SNAP-Tag labelled with BG-Surface Alexa Fluo594 and visualized at UV transilluminator, showing SNAP protein is successfully displayed onto EVs surface. Despite the FACS+ data from L-EV fraction on reporter cells, no signal was detected in L-EV fraction, likely due to both limit of detection of the assay and a higher enrichment of SNAP-EVs in the small fractions. Positive control is 5µg purified SNAP protein. D: WB of genetically engineered L-EV and s-EV bearing SNAP-Tag using αSNAP-Tag antibody. Similar to what is depicted in B, an enrichment of the SNAP-tag is observed in the s-EV over the L-EV.

Following EV isolation, both genetically engineered and BG-WGA–modified EVs were applied to HEK293T LSL-tdTomato reporter cells at equal volumes of large and small fractions, and reporter activation was measured by FACS.

The results showed no statistically significant difference (two-tailed ratio paired t-test, N = 3) in the number of FACS+ reporter cells between EVs pseudotyped with WGA via genetic engineering and those modified post-production with BG-SNAP chemistry, for both L-EV and s-EV fractions. The only exception was BG-WGA–modified Transferrin SNAP s-EVs, which exhibited a significant reduction in delivery efficiency for reasons that remain unclear (Fig. 22B, right panel). Similarly, when reporter cells were treated with Transferrin SNAP L-EV BG-WGA modified, we observed a marked increase in Cre transduction (Fig.22B, left panel), suggesting an enrichment towards distinct EV fractions potentially depending on the SNAP displaying scaffolds and their membrane interactions. These data indicate that post-production modification of VSV-G MUT–enveloped EVs can reproduce the targeting and delivery functions obtained with genetically encoded pseudotyping, underscoring the translational promise of SNAP-mediated lectin display.

To validate the actual localization and accessibility of SNAP on EV membranes, we performed SDS-PAGE followed by BG–Alexa Fluor labeling. This analysis confirmed covalent attachment of fluorophore-conjugated ligands to SNAP-tagged s-EVs, but not L-EVs, for both SNAP Display Cd8 and Transferrin SNAP scaffolds (Fig. 22C). The absence of detectable signal in L-EVs was likely due to the detection limit of the assay combined with a higher enrichment of SNAP-EVs in the small

fraction. Western blot analysis using an anti-SNAP antibody further confirmed the presence of SNAP-fused constructs on the EV surface (Fig. 22D). In this case, SNAP was detected in both L-EV and s-EV fractions for both SNAP Display Cd8 and Transferrin SNAP scaffolds, although at lower levels in L-EVs, consistent with the relative enrichment of SNAP-EVs in s-EVs.

Taken together, these findings establish BG-SNAP chemistry as a reliable and modular method for EV surface engineering. This approach recapitulates the functional outcomes of genetic pseudotyping while offering greater flexibility and compatibility with clinical translation, where cell-free, post-production strategies are often required.

6.4 Active cargo loading via MS2 mRNA recruitment: scaffolds displaying matter

To investigate strategies for enhancing the selective incorporation of RNA into extracellular vesicles, we employed the bacteriophage MS2 coat protein (MCP), an RNA-binding domain with high affinity and specificity for stem-loop motifs known as MS2 loops. The stability and programmability of this interaction render the MCP–MS2 system a versatile tool for engineering vesicles capable of carrying selected RNA cargos. To adapt this mechanism to our scaffolds, we fused the MCP domain to either the C-terminus of the SNAP protein in the SNAP Cd8 Display scaffold or the N-terminus of the Transferrin SNAP scaffold, orienting the MCP toward the vesicle lumen where it could interact with cargo RNA enriched in MS2 loops. We evaluated RNA enrichment by calculating the "fold enrichment of cargo RNA ±MS2," defined as the ratio of Cre mRNA to OST4 mRNA in vesicles derived from cells expressing MS2 fusion scaffolds compared to those expressing the corresponding scaffold without MS2. Both large and small vesicles were purified from transfected HEK293T cell cultures after 48 hours, and RNA was extracted, reverse-transcribed, and quantified by RT-qPCR using *OST4* as a reference gene.

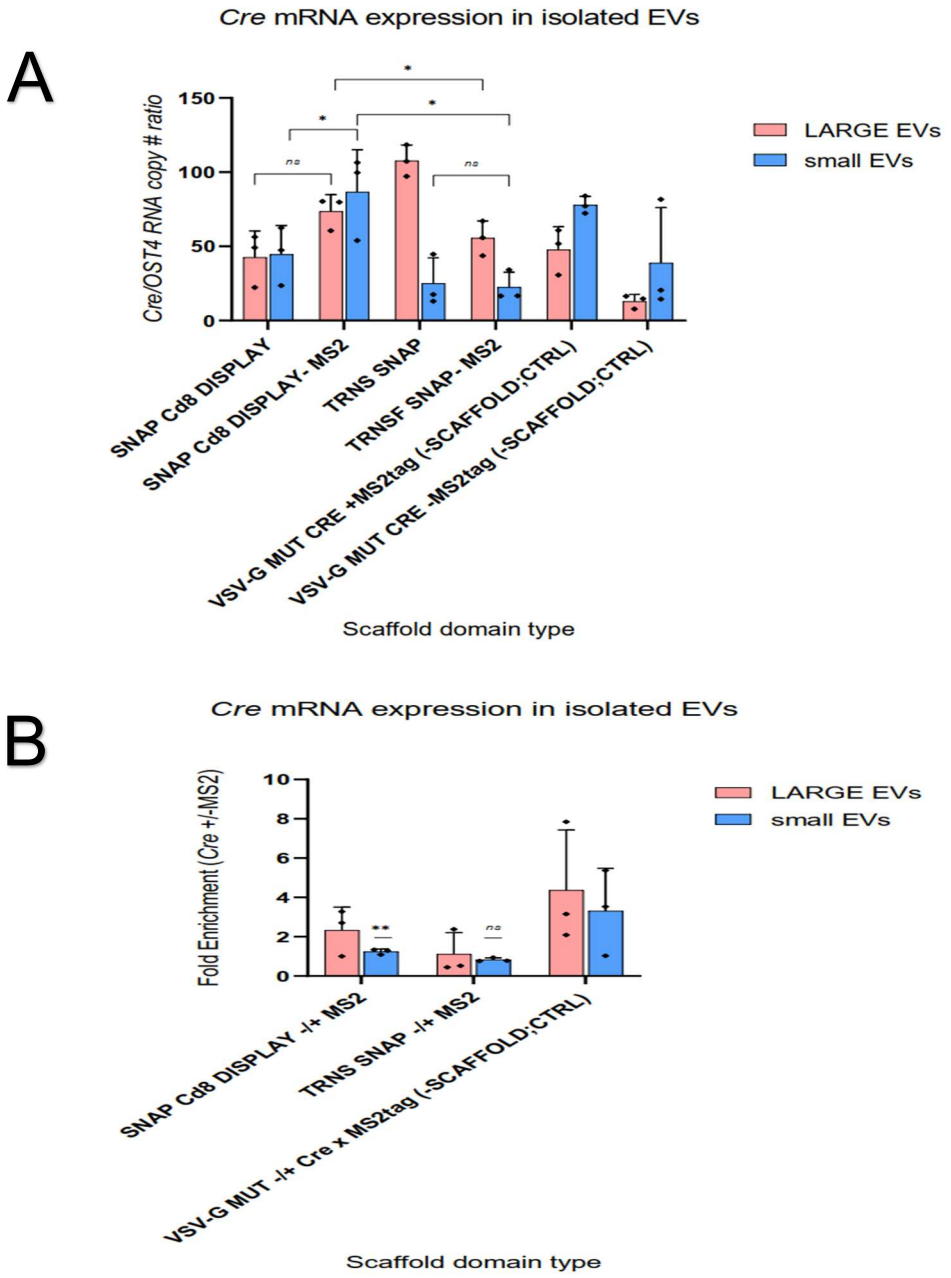


Fig.23 A: mRNA *Cre* quantification via RT-qPCR in isolated L-EV and s-EV engineered with different scaffold displaying domains, normalized on reference gene *OST4*. Biological results are expressed as fold enrichment of cargo RNA +/−MS2, defined as the ratio of *Cre* mRNA/*OST4* mRNA in EVs derived from cells expressing –MS2 fusion constructs, divided by the same RNA ratio in EVs derived from cells expressing the corresponding scaffold without MS2. All the independent values with error bars from three replicates are shown; two-tailed ratio paired t test, $p < 0.05$; *ns*=non-significant; N=3; B: mRNA *Cre* quantification via RT-qPCR in isolated L-EV and s-EV, normalized on reference gene *OST4.* Biological results are expressed as absolute quantification. The MS2 binding motif appears to be more efficient into loading target mRNA cargo when fused to the Display domain instead of Transferrin, regardless of the EV fraction. All the independent values with error bars from three replicates are shown; two-tailed ratio paired t test, $p < 0.05$; *ns*=non-

significant; N=3. Controls are either L-EV or s-EV isolated from cells transfected with either just Cre-encoding with or without the MS2 loops (+/- MS2Tag) and VSV-G MUT plasmid.

The results revealed a significant increase in fold enrichment of Cre mRNA in vesicles-EV derived from SNAP Cd8 Display–MS2 compared to the SNAP Cd8 Display control, while no enhancement was observed in large vesicles from the same condition (Fig. 23A; two-tailed ratio paired t-test, N=3). Conversely, Transferrin SNAP–MS2 did not display significant differences relative to its control counterpart. A consistent trend was observed when results were expressed as absolute copy number ratios of *Cre*/*OST4* per vesicle fraction (Fig. 23B; two-tailed ratio paired t-test, N=3), indicating scaffold-specific variability in MS2-mediated cargo loading and suggesting that RNA targeting may preferentially occur in small extracellular vesicles. This interpretation was reinforced by the positive correlation between relative *Cre* mRNA levels ($2^{-\Delta\Delta Ct}$) and absolute quantification (*Cre*/*OST4* copy ratio) in both vesicle fractions for SNAP Cd8 Display and SNAP Cd8 Display–MS2 (Fig. 24; two tailed Pearson correlation, $\alpha = 0.01$, 99% confidence, N = 3).

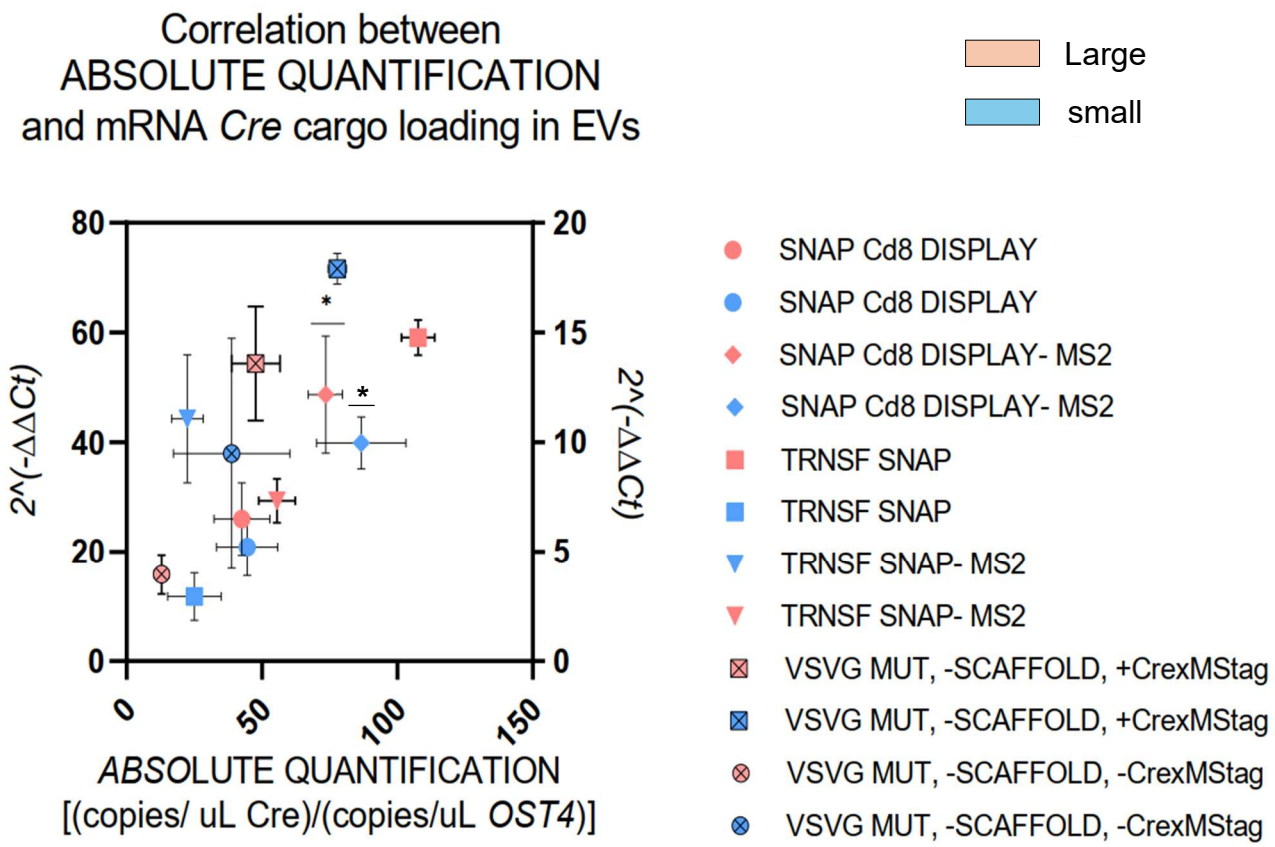


Fig.24 Correlation between *Cre* mRNA expression levels expressed as $2^{-\Delta\Delta Ct}$ and absolute quantification (*Cre*/*OST4* copy ratio) in both L-EV and s-EV engineered with different scaffold displaying domains. Controls are either L-EV or s-EV isolated from cells transfected with either just Cre-encoding with or without the MS2 loops (+/- MS2Tag) and VSV-G MUT plasmid. Please note that following values are plotted on the right Y axis: s-EV Transferrin SNAP MS2. All the independent values with error bars from three replicates are shown: Two tailed Pearson correlation, $\alpha = 0.01$, 99% confidence, N = 3.

Collectively, these data demonstrate the feasibility of MCP fusion domains to mediate active and specific mRNA loading into vesicles, with construct-dependent differences that highlight the relevance of scaffold choice in optimizing RNA packaging.

6.5 Enhancers CIT and NEDD4L synergize with MS2-mediated loading

To assess whether active RNA recruitment through the MS2 system could be further potentiated by mechanisms that enhance vesicle biogenesis and release, we co-expressed the constructs with the proteins CIT (citron rho-interacting serine/threonine kinase) and NEDD4L (neural precursor cell expressed developmentally downregulated gene 4- like). These enhancers have previously been implicated in the stimulation of viral particle budding through the recruitment of ESCRT-I components, suggesting that their action could generalize to extracellular vesicle secretion (Horns et al., 2023; ding et al., 2016; Chung et al., 2008). When HEK293T producer cells were co-transfected with CIT and NEDD4L alongside SNAP Cd8 Display or SNAP Cd8 Display–MS2, we observed a marked amplification of the MS2-dependent enrichment effect, although no such effect was observed in Transferrin SNAP/Transferrin SNAP MS2 constructs (Fig.25 A,B; two-tailed ratio paired t-test, N=3 .

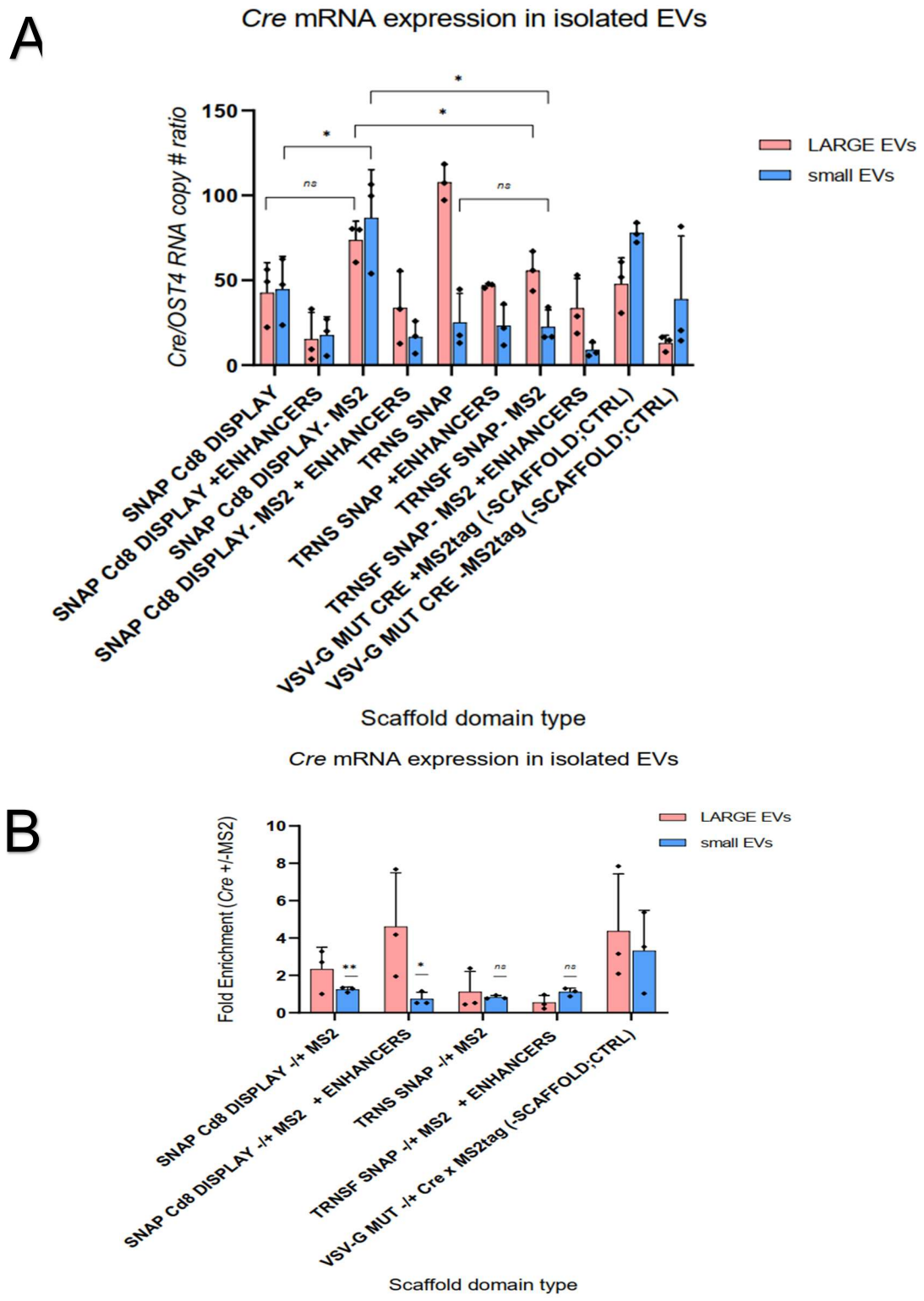


Fig.25 Evaluation of CIT and NEDD4L enhancers on isolated EVs. A: mRNA *Cre* quantification via RT-qPCR in isolated L-EVs and s-EVs engineered with different scaffold displaying domains, produced in cells co-transfected with CIT and NEDD4L enhancers plasmids., normalized on reference gene *OST4*. Biological results are expressed as fold enrichment of cargo RNA +/−MS2, defined as the ratio of *Cre* mRNA/*OST4* mRNA in EVs derived from cells expressing –MS2 fusion constructs, divided by the same RNA ratio in EVs derived from cells expressing the corresponding scaffold without MS2. Coupled activity of the MS2 binding motif and enhancers significantly increased target mRNA cargo

loading in SNAP Cd8 Display MS2 construct but not in Transferrin SNAP MS2, regardless of the EV fraction All the independent values with error bars from three replicates are shown; two-tailed ratio paired t test, $p < 0.05$; *ns*=non-significant; N=3; B: mRNA *Cre* quantification via RT-qPCR in isolated L-EVs and s-EVs engineered with different scaffold displaying domains, produced in cells co-transfected with CIT and NEDD4L enhancers plasmids., normalized on reference gene *OST4.* Biological results are expressed as absolute quantification. All the independent values with error bars from three replicates are shown; two-tailed ratio paired t test, $p < 0.05$; *ns*=non-significant; N=3. Controls are either L-EVs or s-EVs isolated from cells transfected with either just Cre-encoding with or without the MS2 loops (+/- MS2Tag) and VSV-G MUT plasmid

Specifically, the presence of enhancers strengthened the positive correlation between relative Cre mRNA expression ($2^{-\Delta\Delta Ct}$) and absolute *Cre*/*OST4* copy ratios in both L-EV and s-EV (Fig. 26A and B, respectively; two tailed Pearson correlation, $\alpha = 0.01$, 99% confidence, $N = 3$), supporting the notion that elevated vesicle output can magnify the functional consequences of active cargo loading. These findings indicate that combining programmable RNA-binding domains with modulators of vesicle secretion represents a synergistic strategy to improve both the efficiency and robustness of RNA cargo incorporation. By leveraging CIT- and NEDD4L-driven pathways, it may be possible to overcome intrinsic limitations in scaffold-specific loading capacity and thus achieve more consistent delivery outcomes across different vesicle fractions.

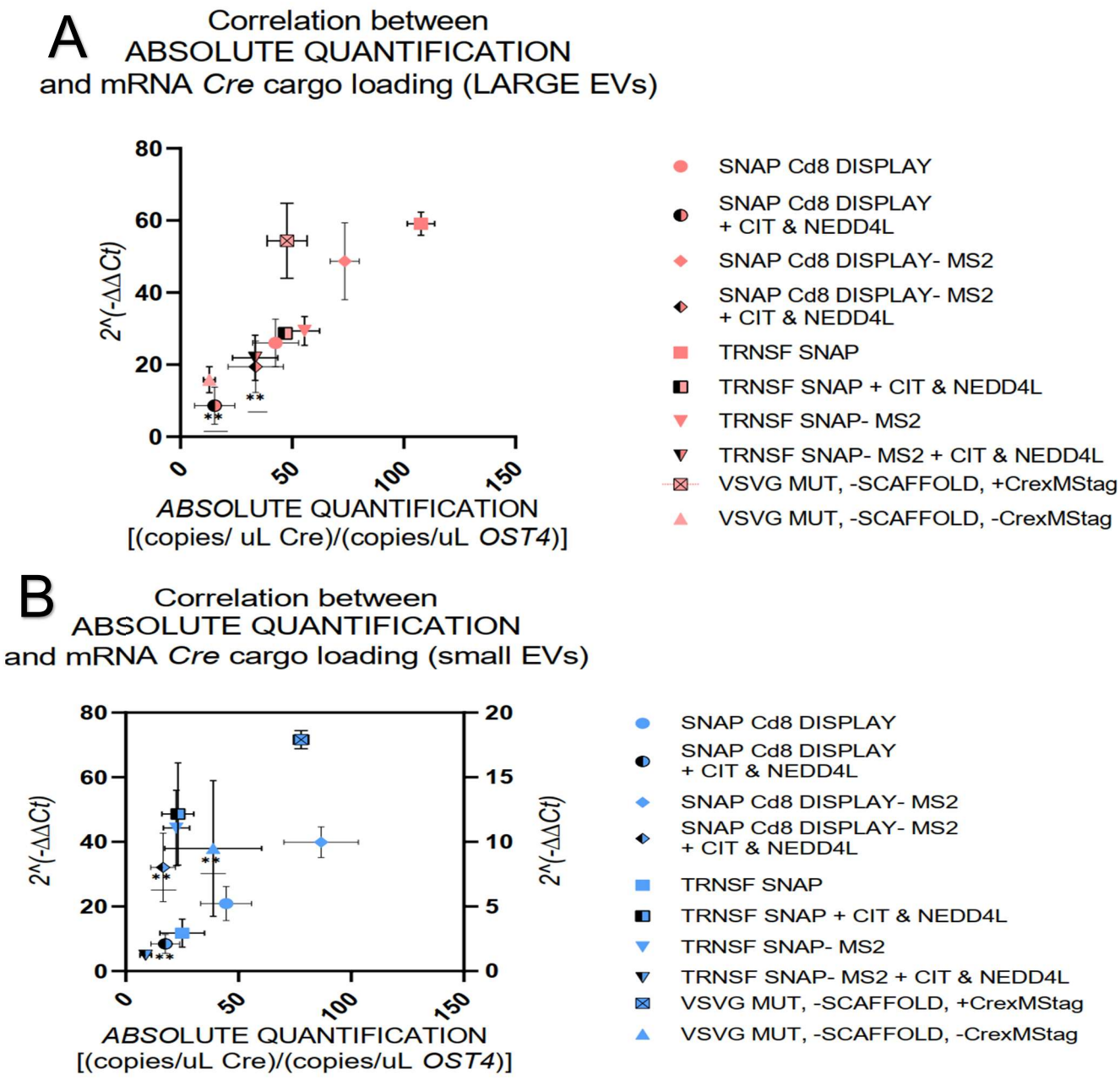


Fig.26 Correlation between *Cre* mRNA expression levels expressed as $2^{-\Delta\Delta Ct}$ and absolute quantification (*Cre*/*OST4* copy ratio) in both L-EVs (A) and s-EVs (B) engineered with different scaffold displaying domains produced in cells co-transfected with CIT and NEDD4L enhancers plasmids. Coupled activity of the MS2 binding motif and enhancers significantly increased target mRNA cargo loading in SNAP Cd8 Display MS2 construct but not in Transferrin SNAP MS2, regardless of the EV fraction Controls are either L-EVs or s-EVs isolated from cells transfected with either just Cre-encoding with or without the MS2 loops (+/- MS2Tag) and VSV-G MUT plasmid. Please note that in B the following values are plotted on the right Y axis: SNAP Cd8 Display MS2 + CIT & NEDD4L, Transferrin SNAP + CIT & NEDD4L and Transferrin SNAP MS2. All the independent values with error bars from three replicates are shown: Two tailed Pearson correlation, $\alpha = 0.01$, 99% confidence, N = 3.

6.6 Dual-functional EVs reveal uneven contributions of targeting and cargo loading

Building upon these results demonstrating active mRNA loading via MS2-mediated recruitment in SNAP Cd8 Display constructs, we next engineered EVs that combined both targeted surface pseudotyping and RNA cargo enrichment. Specifically, we designed constructs in which wheat germ agglutinin (WGA) was fused to the N-terminus of the SNAP tag in the SNAP Cd8 Display MS2 scaffold, yielding WGA SNAP Cd8 Display MS2. To assess the functional delivery of EV-encapsulated Cre mRNA, reporter cells were treated with either L-EV or s-EV derived from cells transfected with the following constructs: SNAP Cd8 Display, SNAP Cd8 Display MS2, WGA SNAP Cd8 Display, and WGA SNAP Cd8 Display MS2 (Fig.27 A). A statistically significant increase in the number of FACS+ reporter cells was observed upon treatment with both WGA SNAP Cd8 Display and WGA SNAP Cd8 Display MS2 EVs, consistent with enhanced uptake due to WGA-mediated targeting (Fig.27 B; two-tailed ratio paired t-test, N = 3). Notably, the addition of the MS2 RNA carrier to the WGA SNAP Cd8 Display construct resulted in an even greater number of FACS+ cells, suggesting the synergistic contribution of targeted entry and increased RNA loading.

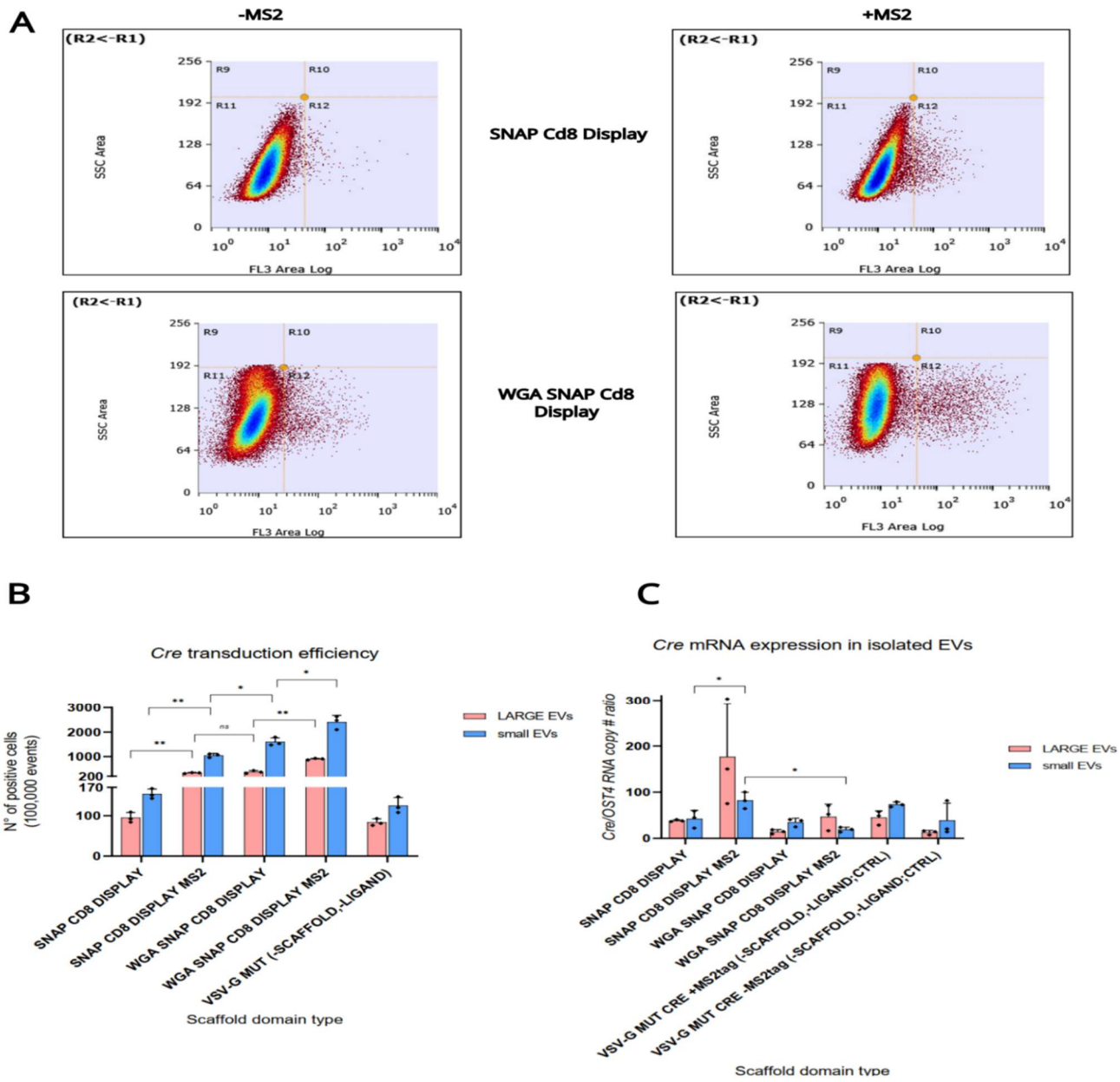


Fig.27 A: Representative FACS plots for HEK293T LSL-TdTomato reporter cells treated with either pseudotyped or non-pseudotyped s-EV. Plots on the left depict constructs without MS2 (-MS2) and likewise plots on the right depict constructs with MS2 (+MS2). Total N° of events was set at 100,000. B: Barplots depicting different Cre mRNA transduction efficiency on reporter cells analyzed by FACS for both L-EV and s-EV pseudotyped or non-pseudotyped with WGA and harboring or not the MS2 RNA binding motif. Controls are EVs without both WGA and MS2. All the independent values with error bars from three replicates are shown; two-tailed ratio paired t test, $p < 0.05$; *ns*=non-significant; N=3. C: mRNA *Cre* quantification via RT-qPCR in isolated L-EV and s-EV, normalized on reference gene *OST4*. Biological results are expressed as absolute quantification. All the independent values with error bars from three replicates are shown; two-tailed ratio paired t test, $p < 0.05$; N=3. Controls are either L-EV or s-EV isolated from cells

transfected with either just Cre-encoding with or without the MS2 loops (+/- MS2Tag) and VSV-G MUT plasmid, without both WGA and MS2.

However, this hypothesis was challenged by RT-qPCR analysis of Cre mRNA content in the same EV preparations (Fig.27 C, Fig.28 A). Surprisingly, s-EV from WGA SNAP Cd8 Display MS2 contained significantly fewer Cre mRNA copies than those from SNAP Cd8 Display MS2, indicating that the enhanced reporter activation may stem primarily from improved cellular entry conferred by WGA, rather than from increased RNA cargo. This interpretation was further supported by correlation analyses: Pearson two-tailed tests ($\alpha = 0.01$, 99% confidence) revealed no statistically significant correlation between fold enrichment and ΔFACS+ cells across all tested conditions (Fig.28 B), neither for SNAP Cd8 Display MS2 nor for WGA SNAP Cd8 Display MS2. Similarly, no significant correlation was found when comparing absolute RNA quantification with FACS+ cells (Fig.29 A). In contrast, a positive and statistically significant correlation was observed between absolute RNA quantification and 2^-ΔΔCt values for SNAP Cd8 Display MS2 EVs only (Fig.29 B), highlighting the internal consistency of the qPCR-based measurements for RNA loading in the absence of targeting ligands.

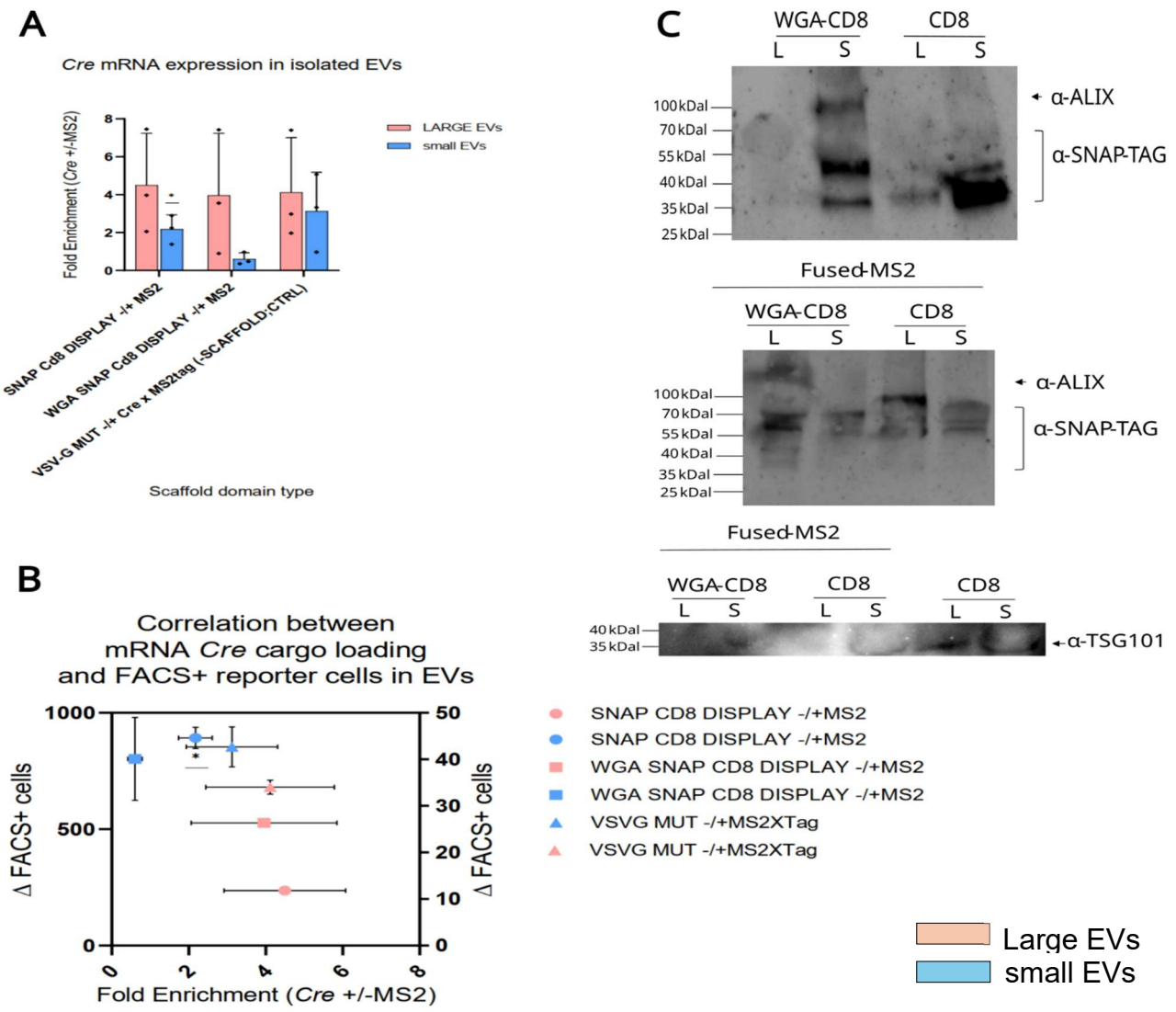


Fig.28 A: mRNA *Cre* quantification via RT-qPCR in isolated L-EV and s-EV engineered with both WGA and MS2 RNA binding motif, normalized on reference gene *OST4*. Biological results are expressed as fold enrichment of cargo RNA +/−MS2, defined as the ratio of *Cre* mRNA/*OST4* mRNA in EVs derived from cells expressing –MS2 fusion constructs, divided by the same RNA ratio in EVs derived from cells expressing the corresponding scaffold without MS2. All the independent values with error bars from three replicates are shown; two-tailed ratio paired t test, $p < 0.05$; N=3. B: Westernblot marker characterization of isolated L-EV and s-EV engineered with both ligand and MS2 RNA binding motif (middle panel; "Fused -MS2") or with just the ligand (top panel). TSG101 exosomal marker is less expressed in s-EV presenting both the ligand and the MS2. SNAP tag is found in both fractions, suggesting a preferential enrichment of pseudotyped-MS2 EVs. Please note that constructs name have been truncated for simplicity: PNA-CD8, WGA-Cd8 and CD8 refer to PNA SNAP CD8 Display, WGA SNAP Cd8 Display and to SNAP Cd8 Display, respectively. C: Correlation between *Cre* mRNA expression levels expressed as Fold enrichment and ΔFACS+ reporter cells in both L-EV and s-EV engineered with both WGA and MS2. . Please note that the following values are plotted on the right Y axis: L-EV VSV-

G MUT -/+ MS2XTag AND s-EV VSV-G MUT -/+ MS2XTag Controls are either L-EV or s-EV isolated from cells transfected with either just Cre-encoding with or without the MS2 loops (+/- MS2Tag) and VSV-G MUT plasmid, without WGA and MS2 RNA binding motif. All the independent values with error bars from three replicates are shown: Two tailed Pearson correlation, $\alpha = 0.01$, 99% confidence, N = 3.

Despite these nuanced findings, our results support the feasibility of combining lectin-based pseudotyping and MS2-driven RNA loading as a promising strategy for engineering EVs with enhanced delivery capabilities. To further characterize the molecular composition of our EV preparations, we performed Western blot analyses using canonical EV markers (Alix, TSG101) and anti-SNAP antibodies. These analyses confirmed that the majority of EV-specific markers were enriched in the small EV fraction (Fig.28 C). Interestingly, pseudotyped EVs engineered with MS2 RNA carriers (WGA SNAP Cd8 Display MS2 and PNA SNAP Cd8 Display MS2) exhibited reduced expression of TSG101 compared to EVs lacking lectin ligands (SNAP Cd8 Display MS2). Given that SNAP-tag expression was clearly detected in both large and small EVs, this pattern suggests that dual-engineered EVs bearing both targeting ligands and RNA-binding domains are preferentially produced and enriched in the small EV population

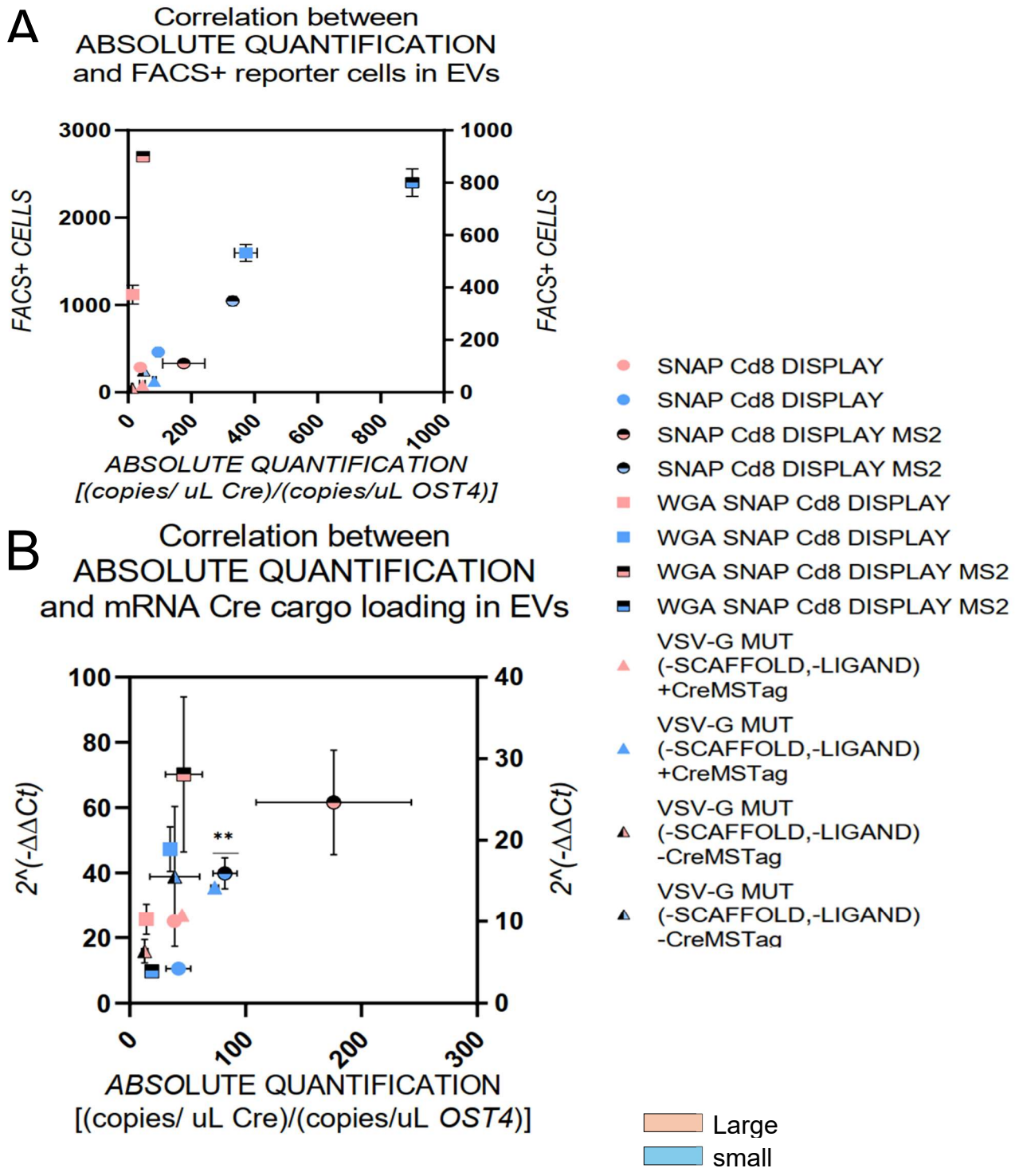


Fig.29 A: Correlation between *Cre* mRNA expression levels expressed as absolute quantification (*Cre*/*OST4* copy ratio) and FACS+ cells in both L-EV and s-EV engineered with both WGA and MS2. Controls are either L-EV or s-EV isolated from cells transfected with either just Cre-encoding with or without the MS2 loops (+/- MS2Tag) and VSV-G MUT plasmid, without WGA and MS2 RNA binding motif. Please note that the following values are plotted on the right Y axis: L-EV SNAP Cd8 Display, s-EV SNAP Cd8 Display, L-EV WGA SNAP Cd8 Display, L-EV WGA SNAP Cd8 Display MS2, L-EV VSV-G MUT (-SCAFFOLD,-LIGAND) -CreMSTag, and s-EV VSV-G MUT (-SCAFFOLD,-

LIGAND) -CreMSTag. All the independent values with error bars from three replicates are shown: Two tailed Pearson correlation, α = 0.01, 99% confidence, N=3. B: Correlation between *Cre* mRNA expression levels expressed as 2^-ΔΔCt and absolute quantification (*Cre*/*OST4* copy ratio) in both L-EV and s-EV engineered with both WGA and MS2. Controls are either L-EV or s-EV isolated from cells transfected with either just Cre-encoding with or without the MS2 loops (+/- MS2Tag) and VSV-G MUT plasmid, without WGA and MS2 RNA binding motif. Please note that the following values are plotted on the right Y axis: L-EV WGA SNAP Cd8 Display, s-EV WGA SNAP Cd8 Display, L-EV WGA SNAP Cd8 Display MS2. All the independent values with error bars from three replicates are shown: Two tailed Pearson correlation, α = 0.01, 99% confidence, N = 3.

7. Discussion

In this study, we sought to systematically investigate and optimize extracellular vesicle (EV) engineering for enhanced mRNA cargo delivery and target cell specificity. By employing several different biotechnology tools including viral envelope glycoprotein engineering, RNA binding domain-mediated active RNA loading, and either post-production pseudotyping with lectins via SNAP-tag chemistry or genetic engineering of producer cells, we present a modular framework for advancing EV-mediated communication. Our findings delineate distinct yet complementary strategies for manipulating EV surface and luminal components, offering mechanistic insight into their influence on targeting, cargo loading, and functional delivery.

Within the different goals of our investigation, the role of the vesicular stomatitis virus glycoprotein (VSV-G), a well-characterized fusogenic envelope protein widely used in lentiviral vector systems (Cronin et al., 2005), was of crucial importance. VSV-G enables pH-dependent membrane fusion and endosomal escape, facilitating cargo release into target cells. However, its broad tropism presents a limitation for cell-type-specific EV targeting (Yang Y. et al., 2017; Yang Y. et al., 2018). We therefore explored whether a mutant form of VSV-G (VSV-G MUT), predicted to retain fusogenic capacity while exhibiting impaired cell binding, could decouple these functionalities (Dobson et al., 2022). Our results demonstrate that EVs enveloped with VSV-G MUT maintain their ability to mediate mRNA Cre delivery into reporter cells, albeit with significantly reduced efficiency compared to wild-type VSV-G EVs. This observation was consistent across both large and small EV fractions, indicating that the targeting deficit of VSV-G MUT affects a general mechanism of EV-cell interaction rather than a size-dependent property of EV subtypes. Importantly, this separation of function opens up new possibilities for targeted EV engineering: by preserving the fusion competency of VSV-G while removing its pan-cellular affinity, we gain a versatile platform for reconstituting targeting specificity through modular pseudotyping (Banskota et al., 2022; Dobson et al., 2022; Yu B et al., 2022).

This hypothesis was next tested through EV surface display of wheat germ agglutinin (WGA), a plant lectin that binds sialic acid and N-acetylglucosamine moieties on glycoproteins and glycolipids commonly enriched on mammalian cells. When VSV-G MUT-enveloped EVs were enriched with WGA ligand, we observed a significant rescue of functional mRNA delivery, as evidenced by increased numbers of FACS+ reporter cells. Notably, WGA-pseudotyped VSV-G MUT EVs achieved levels of delivery comparable to those obtained with WGA-pseudotyped VSV-G WT EVs, indicating that WGA can compensate for the loss of intrinsic targeting in the MUT variant. This strategy pinpoints the capacity of lectins in particular- as well as any other cell type targeting-ligand- to reintroduce specificity in a controllable and modular fashion. Given the increasing interest in targeted therapies, lectin-mediated pseudotyping may offer a generalizable mechanism for directing EV tropism to selected cell types (Banskota et al., 2022; Bui S. et al., 2025).

Recognizing the limitations and complexities associated with the genetic engineering of producer cells (Xia Y et al., 2024; Maryam Sanaee et al., 2023; Claridge et al., 2021), we extended our approach to evaluate post-production modification of EVs as a flexible alternative. Using SNAP-tag-based surface display, we conjugated BG (benzylguanine)-functionalized WGA to pseudotype EVs after isolation. This allowed us to bypass the need for lectin expression during EV biogenesis. We observed that post-modified VSV-G MUT enveloped EVs with BG-WGA displayed equivalent efficacy in delivering Cre mRNA to reporter cells as genetically encoded WGA-bearing EVs. This was validated across both large and small EVs subpopulations, with only one exception (e.g., Transferrin SNAP small EVs), possibly reflecting construct-specific packaging or surface expression issues (Zhang J et al., 2022).

To corroborate these results, we verified the presence and integrity of SNAP-tagged surface proteins on EVs via SDS-PAGE with BG-Alexa Fluor labeling and Western blotting against the SNAP epitope. These findings confirm the accessibility and functional competence of SNAP domains for conjugation, thereby validating post-production pseudotyping as an efficient and scalable method to modulate EV tropism and highlighting its promise for translational applications.

Concurrently, we sought to investigate strategies for actively loading mRNA cargo into the EV lumen, focusing on the RNA-binding domain of bacteriophage MS2 coat protein (aka: MCP). MS2 binds with high affinity to MS2 stem-loop RNA motifs, and its use in tethering specific RNAs to subcellular locations or fusion partners has been well-characterized (Horns et al., 2023; Peabody DS, 1993). By fusing MCP to either the C-terminus or N-terminus of a selected displaying scaffold (SNAP-CD8 Display and Transferrin-SNAP, respectively), we positioned MS2 within the EV interior. Reporter Cre mRNA was engineered to contain MS2 cognate RNA hairpin aptamer in its 3' UTRs to facilitate specific capture and retention during EV biogenesis (Hung & Leonard, 2016; Horns et al., 2023).

Quantification of Cre mRNA levels in EVs using both relative and absolute methods revealed a statistically significant increase in s-EV derived from cells expressing SNAP Cd8 Display MS2 compared to their cognate controls expressing SNAP Cd8 Display alone. This enrichment was not observed in the Transferrin SNAP MS2 condition, likely due to scaffold-specific effects on loading efficiency. To assess the functional relevance of mRNA loading, we correlated cargo mRNA abundance with reporter cell activation. Pearson correlation analysis revealed a significant relationship between relative expression and absolute quantification of Cre mRNA in s-EV from SNAP Cd8 Display MS2 samples. This suggests that the observed biological activity in recipient cells is driven, at least in part, by actual differences in mRNA copy number delivered.

These data underscore the complexity of EV-mediated communication, where factors beyond cargo abundance (e.g., surface presentation, uptake kinetics, intracellular trafficking) play critical roles (Zheng W. et al., 2023; Zhang J. et al., 2022). To further explore the synergy between targeting and cargo delivery, we generated a dual-functional EV type by engineering scaffold proteins to include both MS2 and surface-displayed ligands (WGA. These dual-functional EVs thus possess both cell-specific targeting and mRNA loading capabilities. When tested for functional Cre delivery, both WGA SNAP Cd8 Display MS2 large and small EVs fractions elicited a significantly greater number of FACS+ reporter cells compared to controls, consistent with additive or synergistic effects from targeting and cargo loading. However, RT-qPCR analysis revealed the very opposite: WGA SNAP

Cd8 Display MS2 s-EV actually contained significantly less Cre mRNA copies than SNAP Cd8 Display MS2 s-EV, suggesting that the increase in FACS+ cells was likely due to enhanced uptake rather than increased RNA payload.

This interpretation was further supported by lack of correlation between mRNA abundance and FACS activation in WGA ligand pseudotyped EVs. Additionally, Western blot analyses showed that expression of canonical EV markers (Alix, TSG101) was skewed toward the sEV fraction. EVs displaying ligands and MCP exhibited reduced TSG101 levels relative to MCP-only EVs, possibly reflecting differences in biogenesis pathways (e.g., microvesicle versus exosome origin) or altered recruitment of ESCRT machinery. Nonetheless, SNAP protein was readily detectable in both large and small EV fractions across all conditions, affirming the presence and structural integrity of engineered scaffold proteins. These data underscore the complexity of EV-mediated communication, where factors beyond cargo abundance (e.g., surface presentation, uptake kinetics, intracellular trafficking) play critical roles.

Despite these promising results, several limitations must be considered when interpreting our findings. First, we were unable to quantify the absolute number of EVs applied to recipient reporter cells in most experiments. Variability in EVs production and recovery during isolation (e.g., ultracentrifugation efficiency, vesicle integrity) could thus have confounded delivery outcomes. However, to mitigate this issue in RT-qPCR experiments, we normalized cDNA input and consistently used 500 ng of total RNA per reaction to allow comparisons across conditions (MISEV 2023; Dong L et al., 2020; Gudbergsson et al., 2016).

Second, although statistically significant differences in reporter cell activation were observed by FACS, the proportion of activated cells remained low, typically ranging between 2–3%. This indicates that, despite engineering advances, several operational and technical bottlenecks remain unresolved. These findings are consistent with previous reports in the field (Segel et al., 2021; Somiya M., 2020; Sterzenbach et al., 2017) and highlight the need for further optimization of uptake, endosomal escape, and functional release of EV contents. In the context of delivered mRNA Segel and colleagues

reached a range of 5 to 20% of Cre reporter cells activated, whereas Sterzenbach reached about 1.5% in the context of delivering full length proteins. Other studies reported that EVs can fuse with the recipient cell plasma membrane and directly deliver cargo into the cytosol through different kind of fusogens, however endocytosis is still the major pathway of EV uptake and over 70% of endocytosed EVs are re-localized into lysosomes (Wang L. et al., 2023; Van Niel et al., 2018; Prada & Meldolesi; 2016).

Third, while VSV-G MUT offered an effective approach to decouple targeting from fusion, it remains an immunogenic and potentially cytotoxic component (Temchura et al., 2008; Ory et al., 1997; Burns et al., 1993). Future research should focus on alternative fusogens or membrane fusion strategies with improved safety profiles suitable for therapeutic development, like for example syncytin, actin, epithelial fusion failure-1, anchor cell fusion failure-1, and other exoplasmic fusogens (Wang L. et al., 2023; Vance & Lee, 2020).

Fourth, both the large and small EV fractions analyzed in this study were derived using standard ultracentrifugation protocols without the application of sucrose cushions or iodixanol gradients. As such, these isolates should be considered "crude" and likely contain a heterogeneous mix of vesicle types, including small, medium, and large EVs. Importantly, these EV populations were not characterized via nanoparticle tracking analysis (NTA), atomic force microscopy (AFM), or other sizing technologies. Comprehensive biophysical characterization will be essential to delineate the vesicle subtypes contributing to delivery efficacy.

Finally, while we assessed EV protein content using markers such as Alix and TSG101, future studies should incorporate a broader panel of EV-specific markers, including tetraspanins such as CD63 and CD9. These markers would facilitate more precise classification of vesicle subtypes (e.g., exosomes) and help guide mechanistic insights into their biogenesis, targeting, and functional output.

In conclusion, our work provides a comprehensive framework for engineering EVs with tunable targeting and cargo properties. By integrating orthogonal strategies—surface pseudotyping via lectins, active loading via RNA-binding motifs, and post-production surface modification via SNAP

chemistry—we demonstrate the feasibility of constructing multifunctional EVs tailored for specific therapeutic applications. Future work should further explore the dynamics of EV uptake, trafficking, and endosomal escape in vivo, as well as the impact of cargo secondary structure, stoichiometry, and translational competency. Ultimately, such advances will be instrumental in advancing EV-based platforms from experimental tools to clinical-grade delivery vehicles.

9. BIBLIOGRAPHY

Abels ER, Breakefield XO. Introduction to Extracellular Vesicles: Biogenesis, RNA Cargo Selection,

Content, Release, and Uptake. Cell Mol Neurobiol. 2016 Apr;36(3):301-12.

Banskota S, Raguram A, Suh S, Du SW, Davis JR, Choi EH, Wang X, Nielsen SC, Newby GA, Randolph PB, Osborn MJ, Musunuru K, Palczewski K, Liu DR. Engineered virus-like particles for efficient in vivo delivery of therapeutic proteins. Cell. 2022 Jan 20;185(2):250-265.e16.

Bellavia D, Raimondo S, Calabrese G, Forte S, Cristaldi M, Patinella A, Memeo L, Manno M, Raccosta S, Diana P, Cirrincione G, Giavaresi G, Monteleone F, Fontana S, De Leo G, Alessandro R. Interleukin 3- receptor targeted exosomes inhibit *in vitro* and *in vivo* Chronic Myelogenous Leukemia cell growth. Theranostics. 2017 Mar 16;7(5):1333-1345

Bellis SL, Reis CA, Varki A, Kannagi R, Stanley P. Glycosylation Changes in Cancer. In: Varki A, Cummings RD, Esko JD, Stanley P, Hart GW, Aebi M, Mohnen D, Kinoshita T, Packer NH, Prestegard JH, Schnaar RL, Seeberger PH, editors. Essentials of Glycobiology [Internet]. 4th ed. Cold Spring Harbor (NY): Cold Spring Harbor Laboratory Press; 2022. Chapter 47.

Bui S, Lainé J, Chevé M, Vassilopoulos S, Lavieu G. Versatile tethering system to control cell-specific targeting of bioengineered extracellular vesicles. Sci Rep. 2025 Jun 3;15(1):19454

Burns JC, Friedmann T, Driever W, Burrascano M, Yee JK. Vesicular stomatitis virus G glycoprotein pseudotyped retroviral vectors: concentration to very high titer and efficient gene transfer into mammalian and nonmammalian cells. Proc Natl Acad Sci U S A. 1993 Sep 1;90(17):8033-7

Buschow SI, Nolte-'t Hoen EN, van Niel G, Pols MS, ten Broeke T, Lauwen M, Ossendorp F, Melief CJ, Raposo G, Wubbolts R, Wauben MH, Stoorvogel W. MHC II in dendritic cells is targeted to lysosomes or T cell-induced exosomes via distinct multivesicular body pathways. Traffic. 2009 Oct;10(10):1528-42

Cao L, Huang C, Cui Zhou D, Hu Y, Lih TM, Savage SR, Krug K, Clark DJ, Schnaubelt M, Chen L, da Veiga Leprevost F, Eguez RV, Yang W, Pan J, Wen B, Dou Y, Jiang W, Liao Y, Shi Z, Terekhanova NV, Cao S, Lu RJ, Li Y, Liu R, Zhu H, Ronning P, Wu Y, Wyczalkowski MA, Easwaran H, Danilova L, Mer AS, Yoo S, Wang JM, Liu W, Haibe-Kains B, Thiagarajan M, Jewell SD, Hostetter G, Newton CJ, Li QK, Roehrl MH, Fenyö D, Wang P, Nesvizhskii AI, Mani DR, Omenn GS, Boja ES, Mesri M, Robles AI, Rodriguez H, Bathe OF, Chan DW, Hruban RH, Ding L, Zhang B, Zhang H; Clinical Proteomic Tumor Analysis Consortium. Proteogenomic characterization of pancreatic ductal adenocarcinoma. Cell. 2021 Sep 16;184(19):5031-5052.e26.

Carayon K, Chaoui K, Ronzier E, Lazar I, Bertrand-Michel J, Roques V, Balor S, Terce F, Lopez A, Salomé L, Joly E. Proteolipidic composition of exosomes changes during reticulocyte maturation. J Biol Chem. 2011 Sep 30;286(39):34426-39.

Cheng L, Hill AF. Therapeutically harnessing extracellular vesicles. Nat Rev Drug Discov. 2022 May;21(5):379-399

Chivet M, Javalet C, Laulagnier K, Blot B, Hemming FJ, Sadoul R. Exosomes secreted by cortical neurons upon glutamatergic synapse activation specifically interact with neurons. J Extracell Vesicles. 2014 Nov 13;3:24722.

Cho, J. A., Park, H., Lim, E. H. & Lee, K. W. Exosomes from breast cancer cells can convert adipose tissue-derived mesenchymal stem cells into myofibroblast-like cells. *Int. J. Oncol.* **40**, 130–138 (2012).

Chung HY, Morita E, von Schwedler U, Müller B, Kräusslich HG, Sundquist WI. NEDD4L overexpression rescues the release and infectivity of human immunodeficiency virus type 1 constructs lacking PTAP and YPXL late domains. J Virol. 2008 May;82(10):4884-97

Clancy JW, Boomgarden AC, D'Souza-Schorey C. Profiling and promise of supermeres. Nat Cell Biol. 2021 Dec;23(12):1217-1219. doi: 10.1038/s41556-021-00808-5. Erratum in: Nat Cell Biol. 2022 Feb;24(2):279.

Claridge B, Lozano J, Poh QH, Greening DW. Development of Extracellular Vesicle Therapeutics: Challenges, Considerations, and Opportunities. Front Cell Dev Biol. 2021 Sep 20;9:734720.

Colombo M, Moita C, van Niel G, Kowal J, Vigneron J, Benaroch P, Manel N, Moita LF, Théry C, Raposo G. Analysis of ESCRT functions in exosome biogenesis, composition and secretion highlights the heterogeneity of extracellular vesicles. J Cell Sci. 2013 Dec 15;126(Pt 24):5553-65

Colombo M, Raposo G, Théry C. Biogenesis, secretion, and intercellular interactions of exosomes and other extracellular vesicles. Annu Rev Cell Dev Biol. 2014

Cooper JM , P.B.O. Wiklander, J.Z. Nordin, R. Al-Shawi, M.J. Wood, M. Vithlani, A.H.V. Schapira, J.P. Simons, S. El-Andaloussi, L. Alvarez-Erviti, Systemic exosomal siRNA delivery reduced alpha-synuclein aggregates in brains of transgenic mice, Mov. Disord. (2014)

Cronin J, Zhang XY, Reiser J. Altering the tropism of lentiviral vectors through pseudotyping. Curr Gene Ther. 2005 Oct;5(5):531

De Abreu RC, Fernandes H, da Costa Martins PA, Sahoo S, Emanueli C, Ferreira L. Native and bioengineered extracellular vesicles for cardiovascular therapeutics. Nat Rev Cardiol. 2020 Nov;17(11):685-697.

De Jong OG, S.A.A. Kooijmans, D.E. Murphy, L. Jiang, M.J.W. Evers, J.P.G. Sluijter, P. Vader, R.M. Schiffelers, Drug delivery with extracellular vesicles: from imagination to innovation, Acc. Chem. Res. (2019)

Demory Beckler M, Higginbotham JN, Franklin JL, Ham AJ, Halvey PJ, Imasuen IE, Whitwell C, Li M, Liebler DC, Coffey RJ. Proteomic analysis of exosomes from mutant KRAS colon cancer cells identifies intercellular transfer of mutant KRAS. Mol Cell Proteomics. 2013 Feb;12(2):343-55.

Ding J, Zhao J, Sun L, Mi Z, Cen S. Citron kinase enhances ubiquitination of HIV-1 Gag protein and intracellular HIV-1 budding. Arch Virol. 2016 Sep;161(9):2441-8.

Dixson AC, Dawson TR, Di Vizio D, Weaver AM. Context-specific regulation of extracellular vesicle biogenesis and cargo selection. Nat Rev Mol Cell Biol. 2023 Jul;24(7):454-476.

Dobson CS, Reich AN, Gaglione S, Smith BE, Kim EJ, Dong J, Ronsard L, Okonkwo V, Lingwood D, Dougan M, Dougan SK, Birnbaum ME. Antigen identification and high-throughput interaction mapping by reprogramming viral entry. Nat Methods. 2022 Apr;19(4):449-460.

Dong L, Zieren RC, Horie K, Kim CJ, Mallick E, Jing Y, Feng M, Kuczler MD, Green J, Amend SR, Witwer KW, de Reijke TM, Cho YK, Pienta KJ, Xue W. Comprehensive evaluation of methods for small extracellular vesicles separation from human plasma, urine and cell culture medium. J Extracell Vesicles. 2020 Dec;10(2):e12044.

Elsharkasy OM, Nordin JZ, Hagey DW, de Jong OG, Schiffelers RM, Andaloussi SE, Vader P. Extracellular vesicles as drug delivery systems: Why and how? Adv Drug Deliv Rev. 2020;159:332-343.

Frey B, Gaipl US. The immune functions of phosphatidylserine in membranes of dying cells and microvesicles. Semin Immunopathol. 2011 Sep;33(5):497-516

Gebraad A, Kornilov R, Kaur S, Miettinen S, Haimi S, Peltoniemi H, Mannerström B, Seppänen-Kaijansinkko R. Monocyte-derived extracellular vesicles stimulate cytokine secretion and gene expression of matrix metalloproteinases by mesenchymal stem/stromal cells. FEBS J. 2018 Jun;285(12):2337-2359

Goh J. B., Ng S. K. Impact of host cell line choice on glycan profile. Critical Reviews in Biotechnology. 2017;38(6):851–867.

Gudbergsson JM, Johnsen KB, Skov MN, Duroux M. Systematic review of factors influencing extracellular vesicle yield from cell cultures. Cytotechnology. 2016 Aug;68(4):579-92.

H. Valadi, K. Ekström, A. Bossios, M. Sjöstrand, J.J. Lee, J.O. Lötvall, Exosomemediated transfer of mRNAs and microRNAs is a novel mechanism of genetic exchange between cells, Nat. Cell Biol. (2007)

Hakulinen, J., Sankkila, L., Sugiyama, N., Lehti, K. & Keski-Oja, J. Secretion of active membrane type 1 matrix metalloproteinase (MMP-14) into extracellular space in microvesicular exosomes. *J. Cell. Biochem.* 105, 1211–1218 (2008).

Hikita, T., Kuwahara, A., Watanabe, R., Miyata, M. & Oneyama, C. Src in endosomal membranes promotes exosome secretion and tumor progression. *Sci. Rep.* **9**, 3265 (2019).

Horns F, Martinez JA, Fan C, Haque M, Linton JM, Tobin V, Santat L, Maggiolo AO, Bjorkman PJ, Lois C, Elowitz MB. Engineering RNA export for measurement and manipulation of living cells. Cell. 2023 Aug 17;186(17):3642-3658.e32.

Hoshino A, Costa-Silva B, Shen TL, Rodrigues G, Hashimoto A, Tesic Mark M, Molina H, Kohsaka S, Di Giannatale A, Ceder S, Singh S, Williams C, Soplop N, Uryu K, Pharmer L, King T, Bojmar L, Davies AE, Ararso Y, Zhang T, Zhang H, Hernandez J, Weiss JM, Dumont-Cole VD, Kramer K, Wexler LH, Narendran A, Schwartz GK, Healey JH, Sandstrom P, Labori KJ, Kure EH, Grandgenett PM, Hollingsworth MA, de Sousa M, Kaur S, Jain M, Mallya K, Batra SK, Jarnagin WR, Brady MS, Fodstad O, Muller V, Pantel K, Minn AJ, Bissell MJ, Garcia BA, Kang Y, Rajasekhar VK, Ghajar CM, Matei I, Peinado H, Bromberg J, Lyden D. Tumour exosome integrins determine organotropic metastasis. Nature. 2015 Nov 19;527(7578):329-35.

Hung M.E., Leonard JN. A platform for actively loading cargo RNA to elucidate limiting steps in EV-mediated delivery. J Extracell Vesicles. 2016 May 13;5:31027.

Hung, M. E. & Leonard, J. N. Stabilization of exosome-targeting peptides via engineered glycosylation. *J. Biol. Chem.* 290, 8166–8172 (2015)

Hurley JH. ESCRT complexes and the biogenesis of multivesicular bodies. Curr Opin Cell Biol. 2008 Feb;20(1):4-11

Hyenne V, Ghoroghi S, Collot M, Bons J, Follain G, Harlepp S, Mary B, Bauer J, Mercier L, Busnelli I, Lefebvre O, Fekonja N, Garcia-Leon MJ, Machado P, Delalande F, López AA, Silva SG, Verweij FJ, van Niel G, Djouad F, Peinado H, Carapito C, Klymchenko AS, Goetz JG. Studying the Fate of Tumor Extracellular Vesicles at High Spatiotemporal Resolution Using the Zebrafish Embryo. Dev Cell. 2019 Feb 25;48(4):554-572

Jeppesen DK, Zhang Q, Franklin JL, Coffey RJ. Extracellular vesicles and nanoparticles: emerging complexities. Trends Cell Biol. 2023 Aug;33(8):667-681.

Juan T, Fürthauer M. Biogenesis and function of ESCRT-dependent extracellular vesicles. Semin Cell Dev Biol. 2018 Feb;74:66-77. Tkach M, Théry C. Communication by Extracellular Vesicles: Where We Are and Where We Need to Go. Cell. 2016 Mar 10;164(6):1226-1232.

Karnas E, Dudek P, Zuba-Surma EK. Stem cell- derived extracellular vesicles as new tools in regenerative medicine - Immunomodulatory role and future perspectives. Front Immunol. 2023 Jan 24;14:1120175.

Klumperman J, Raposo G. The complex ultrastructure of the endolysosomal system. Cold Spring Harb Perspect Biol. 2014 May 22;6(10):a016857.

Kumar MA, Baba SK, Sadida HQ, Marzooqi SA, Jerobin J, Altemani FH, Algehainy N, Alanazi MA, Abou-Samra AB, Kumar R, Al-Shabeeb Akil AS, Macha MA, Mir R, Bhat AA. Extracellular vesicles as tools and targets in therapy for diseases. Signal Transduct Target Ther. 2024 Feb 5;9(1):27.

Laghezza Masci, V., Taddei, A. R., Gambellini, G., Giorgi, F. & Fausto, A. M. Microvesicles shed from fibroblasts act as metalloproteinase carriers in a 3-D collagen matrix. *J. Circ. Biomark.* **5**, 1849454416663660 (2016).

Laulagnier K, Javalet C, Hemming FJ, Chivet M, Lachenal G, Blot B, Chatellard C, Sadoul R. Amyloid precursor protein products concentrate in a subset of exosomes specifically endocytosed by neurons. Cell Mol Life Sci. 2018 Feb;75(4):757-773.

Leone, D. A., Rees, A. J. & Kain, R. Dendritic cells and routing cargo into exosomes. *Immunol. Cell Biol.* **96**, 683–693 (2018).

Liang G, Zhu Y, Ali DJ, Tian T, Xu H, Si K, Sun B, Chen B, Xiao Z. Engineered exosomes for targeted co-delivery of miR-21 inhibitor and chemotherapeutics to reverse drug resistance in colon cancer. J Nanobiotechnology. 2020 Jan 9;18(1):10.

Liu YJ, Wang C. A review of the regulatory mechanisms of extracellular vesicles-mediated intercellular communication. Cell Commun Signal. 2023 Apr 13;21(1):77

Lucotti S, Kenific CM, Zhang H, Lyden D. Extracellular vesicles and particles impact the systemic landscape of cancer. EMBO J. 2022 Sep 15;41(18):e109288

Marciel MP, Haldar B, Hwang J, Bhalerao N, Bellis SL. Role of tumor cell sialylation in pancreatic cancer progression. Adv Cancer Res. 2023;157:123-155

Marciniak A, Cohrs CM, Tsata V, Chouinard JA, Selck C, Stertmann J, Reichelt S, Rose T, Ehehalt F, Weitz J, Solimena M, Slak Rupnik M, Speier S. Using pancreas tissue slices for in situ studies of islet of Langerhans and acinar cell biology. Nat Protoc. 2014 Dec;9(12):2809-22.

Mardpour S, Hamidieh AA, Taleahmad S, Sharifzad F, Taghikhani A, Baharvand H. Interaction between mesenchymal stromal cell-derived extracellular vesicles and immune cells by distinct protein content. J Cell Physiol. 2019 Jun;234(6):8249-8258.

Maryam Sanaee, K. Göran Ronquist, Jane M. Morrell, Muhammet S. Toprak, Katia Gallo. Size stability and self-agglomeration of erythrocyte-derived membrane nanovesicles versus physiological extracellular vesicles, arXiv:2312.03554v1 2023

Mathiesen A, Hamilton T, Carter N, Brown M, McPheat W, Dobrian A. Endothelial Extracellular Vesicles: From Keepers of Health to Messengers of Disease. Int J Mol Sci. 2021 Apr 28;22(9):4640.

Mazalovska M, Kouokam JC. Plant-Derived Lectins as Potential Cancer Therapeutics and Diagnostic Tools. Biomed Res Int. 2020 May 15;2020:1631394

Meldolesi J. Exosomes and Ectosomes in Intercellular Communication. Curr Biol. 2018 Apr 23;28(8):R435-R444.

MISEV (2023): Welsh JA, Goberdhan DCI, O'Driscoll L, Buzas EI, Blenkiron C, Bussolati B, Cai H, Di Vizio D, Driedonks TAP, Erdbrügger U, Falcon-Perez JM, Fu QL, Hill AF, Lenassi M, Lim SK, Mahoney MG, Mohanty S, Möller A, Nieuwland R, Ochiya T, Sahoo S, Torrecilhas AC, Zheng L, Zijlstra A, Abuelreich S, Bagabas R, Bergese P, Bridges EM, Brucale M, Burger D, Carney RP, Cocucci E, Crescitelli R, Hanser E, Harris AL, Haughey NJ, Hendrix A, Ivanov AR, Jovanovic-Talisman T, Kruh-Garcia NA, Ku'ulei-Lyn Faustino V, Kyburz D, Lässer C, Lennon KM, Lötvall J, Maddox AL, Martens-Uzunova ES, Mizenko RR, Newman LA, Ridolfi A, Rohde E, Rojalin T, Rowland A, Saftics A, Sandau US, Saugstad JA, Shekari F, Swift S, Ter-Ovanesyan D, Tosar JP, Useckaite Z, Valle F, Varga Z, van der Pol E, van Herwijnen MJC, Wauben MHM, Wehman AM, Williams S, Zendrini A, Zimmerman AJ; MISEV Consortium; Théry C, Witwer KW. Minimal information for studies of extracellular vesicles (MISEV2023): From basic to advanced approaches. J Extracell Vesicles. 2024 Feb;13(2):e12404. doi: 10.1002/jev2.12404. Erratum in: J Extracell Vesicles. 2024 May;13(5):e12451

Möller A, Lobb RJ. The evolving translational potential of small extracellular vesicles in cancer. Nat Rev Cancer. 2020 Dec;20(12):697-709

Morelli AE, Larregina AT, Shufesky WJ, Sullivan ML, Stolz DB, Papworth GD, Zahorchak AF, Logar AJ, Wang Z, Watkins SC, Falo LD Jr, Thomson AW. Endocytosis, intracellular sorting, and processing of exosomes by dendritic cells. Blood. 2004

Mulcahy LA, Pink RC, Carter DR. Routes and mechanisms of extracellular vesicle uptake. J Extracell Vesicles. 2014 Aug 4;3

Murphy DE, O.G. de Jong, M. Brouwer, M.J. Wood, G. Lavieu, R.M. Schiffelers, P. Vader, Extracellular vesicle-based therapeutics: natural versus engineered targeting and trafficking, Exp. Mol. Med. (2019)

Nikolic J, Belot L, Raux H, Legrand P, Gaudin Y, A Albertini A. Structural basis for the recognition of LDL-receptor family members by VSV glycoprotein. Nat Commun. 2018 Mar 12;9(1):1029.

Ory DS, Neugeboren BA, Mulligan RC. A stable human-derived packaging cell line for production of high titer retrovirus/vesicular stomatitis virus G pseudotypes. Proc Natl Acad Sci U S A. 1996 Oct 15;93(21):11400-6

Parolini I, Federici C, Raggi C, Lugini L, Palleschi S, De Milito A, Coscia C, Iessi E, Logozzi M, Molinari A, Colone M, Tatti M, Sargiacomo M, Fais S. Microenvironmental pH is a key factor for exosome traffic in tumor cells. J Biol Chem. 2009 Dec 4;284(49):34211-22.

Peabody DS. The RNA binding site of bacteriophage MS2 coat protein. EMBO J. 1993 Feb;12(2):595-600.

Perdicchio M, Cornelissen LA, Streng-Ouwehand I, Engels S, Verstege MI, Boon L, Geerts D, van Kooyk Y, Unger WW. Tumor sialylation impedes T cell mediated anti-tumor responses while promoting tumor associated-regulatory T cells. Oncotarget. 2016 Feb 23;7(8):8771-82

Piccin A, Murphy WG, Smith OP. Circulating microparticles: pathophysiology and clinical implications. Blood Rev. 2007 May;21(3):157-71.

Pinheiro C, Guilbert N, Lippens L, Roux Q, Boiy R, Fischer S, Van Dorpe S, De Craene B, Berx G, Boterberg T, Sys G, Denys H, Miinalainen I, Mestdagh P, Vandesompele J, De Wever O, Hendrix A. Identification and validation of extracellular vesicle reference genes for the normalization of RT-qPCR data. J Extracell Vesicles. 2024 Apr;13(4):e12421

Pinho SS, Reis CA. Glycosylation in cancer: mechanisms and clinical implications. Nat Rev Cancer. 2015 Sep;15(9):540-55.

Prada I, Amin L, Furlan R, Legname G, Verderio C, Cojoc D. A new approach to follow a single extracellular vesicle-cell interaction using optical tweezers. Biotechniques. 2016 Jan 1;60(1):35-41.

Prada I, Meldolesi J. Binding and Fusion of Extracellular Vesicles to the Plasma Membrane of Their Cell Targets. Int J Mol Sci. 2016 Aug 9;17(8):1296.

Purushothaman A, Bandari SK, Liu J, Mobley JA, Brown EE, Sanderson RD. Fibronectin on the Surface of Myeloma Cell-derived Exosomes Mediates Exosome-Cell Interactions. J Biol Chem. 2016 Jan 22;291(4):1652-1663.

Qin Y, Wang L, Gao Z, Chen G, Zhang C. Bone marrow stromal/stem cell-derived extracellular vesicles regulate osteoblast activity and differentiation in vitro and promote bone regeneration in vivo. Sci Rep. 2016 Feb 25;6:21961.

Rackov G, Garcia-Romero N, Esteban-Rubio S, Carrión-Navarro J, Belda-Iniesta C, Ayuso-Sacido A. Vesicle-Mediated Control of Cell Function: The Role of Extracellular Matrix and Microenvironment. Front Physiol. 2018 Jun 5;9:651.

Rana S, Claas C, Kretz CC, Nazarenko I, Zoeller M. Activation-induced internalization differs for the tetraspanins CD9 and Tspan8: Impact on tumor cell motility. Int J Biochem Cell Biol. 2011 Jan;43(1):106-19.

Rodriguez E, Boelaars K, Brown K, Eveline Li RJ, Kruijssen L, Bruijns SCM, van Ee T, Schetters STT, Crommentuijn MHW, van der Horst JC, van Grieken NCT, van Vliet SJ, Kazemier G, Giovannetti E, Garcia-Vallejo JJ, van Kooyk Y. Sialic acids in pancreatic cancer cells drive tumour-

associated macrophage differentiation via the Siglec receptors Siglec-7 and Siglec-9. Nat Commun. 2021 Feb 24;12(1):1270.

Sahoo S, Klychko E, Thorne T, Misener S, Schultz KM, Millay M, Ito A, Liu T, Kamide C, Agrawal H, Perlman H, Qin G, Kishore R, Losordo DW. Exosomes from human CD34(+) stem cells mediate their proangiogenic paracrine activity. Circ Res. 2011 Sep 16;109(7):724-8

Segel M, Lash B, Song J, Ladha A, Liu CC, Jin X, Mekhedov SL, Macrae RK, Koonin EV, Zhang F. Mammalian retrovirus-like protein PEG10 packages its own mRNA and can be pseudotyped for mRNA delivery. Science. 2021 Aug 20;373(6557):882-889.

Shen, B., Wu, N., Yang, J. M. & Gould, S. J. Protein targeting to exosomes/microvesicles by plasma membrane anchors. *J. Biol. Chem.* 286, 14383–14395 (2011).

Skog J, Würdinger T, van Rijn S, Meijer DH, Gainche L, Sena-Esteves M, Curry WT Jr, Carter BS, Krichevsky AM, Breakefield XO. Glioblastoma microvesicles transport RNA and proteins that promote tumour growth and provide diagnostic biomarkers. Nat Cell Biol. 2008 Dec;10(12):1470-6.

Somiya M. Where does the cargo go?: Solutions to provide experimental support for the "extracellular vesicle cargo transfer hypothesis". J Cell Commun Signal. 2020 Jun;14(2):135-146.

Sterzenbach U, Putz U, Low LH, Silke J, Tan SS, Howitt J. Engineered Exosomes as Vehicles for Biologically Active Proteins. Mol Ther. 2017 Jun 7;25(6):1269-1278

Stuffers S, Sem Wegner C, Stenmark H, Brech A. Multivesicular endosome biogenesis in the absence of ESCRTs. Traffic. 2009 Jul;10(7):925-37

Tamai K, Tanaka N, Nakano T, Kakazu E, Kondo Y, Inoue J, Shiina M, Fukushima K, Hoshino T, Sano K, Ueno Y, Shimosegawa T, Sugamura K. Exosome secretion of dendritic cells is regulated by Hrs, an ESCRT-0 protein. Biochem Biophys Res Commun. 2010 Aug 27;399(3):384-90

Tanio M, Muramoto A, Hoshino H, Murahashi M, Imamura Y, Yokoyama O, Kobayashi M. Expression of functional E-selectin ligands on the plasma membrane of carcinoma cells correlates with poor prognosis in clear cell renal cell carcinoma. Urol Oncol. 2021 May;39(5):302.e9-302.e18.

Temchura VV, Tenbusch M, Nchinda G, Nabi G, Tippler B, Zelenyuk M, Wildner O, Uberla K, Kuate S. Enhancement of immunostimulatory properties of exosomal vaccines by incorporation of fusion-competent G protein of vesicular stomatitis virus. Vaccine. 2008 Jul 4;26(29-30):3662-72.

Teng F, Fussenegger M. Shedding Light on Extracellular Vesicle Biogenesis and Bioengineering. Adv Sci (Weinh). 2020 Nov 27;8(1):2003505.

Tosar JP, Witwer K & Cayota A Revisiting Extracellular RNA Release, Processing, and Function. Trends Biochem Sci 46, 438–445, 2021

Trajkovic K, Hsu C, Chiantia S, Rajendran L, Wenzel D, Wieland F, Schwille P, Brügger B, Simons M. Ceramide triggers budding of exosome vesicles into multivesicular endosomes. Science. 2008 Feb 29;319(5867):1244-7.

Van Niel G, Charrin S, Simoes S, Romao M, Rochin L, Saftig P, Marks MS, Rubinstein E, Raposo G. The tetraspanin CD63 regulates ESCRT-independent and -dependent endosomal sorting during melanogenesis. Dev Cell. 2011 Oct 18;21(4):708-21.

Van Niel G, D'Angelo G, Raposo G. Shedding light on the cell biology of extracellular vesicles. Nat Rev Mol Cell Biol. 2018 Apr;19(4):213-228.

Vance TDR, Lee JE. Virus and eukaryote fusogen superfamilies. Curr Biol. 2020 Jul 6;30(13):R750-R754.

Varki A, Cummings RD, Esko JD, Freeze HH, Stanley P, Bertozzi CR, Hart GW, Etzler ME, editors. Essentials of Glycobiology. 2nd ed. Cold Spring Harbor (NY): Cold Spring Harbor Laboratory Press; 2009.

Verweij FJ, Revenu C, Arras G, Dingli F, Loew D, Pegtel DM, Follain G, Allio G, Goetz JG, Zimmermann P, Herbomel P, Del Bene F, Raposo G, van Niel G. Live Tracking of Inter-organ Communication by Endogenous Exosomes In Vivo. Dev Cell. 2019 Feb 25;48(4):573-589

Vidal M, Mangeat P, Hoekstra D. Aggregation reroutes molecules from a recycling to a vesicle-mediated secretion pathway during reticulocyte maturation. J Cell Sci. 1997 Aug;110 (Pt 16):1867-77.

Wang L, Wang G, Mao W, Chen Y, Rahman MM, Zhu C, Prisinzano PM, Kong B, Wang J, Lee LP, Wan Y. Bioinspired engineering of fusogen and targeting moiety equipped nanovesicles. Nat Commun. 2023 Jun 8;14(1):3366.

Wang R, Ji Q, Meng C, Liu H, Fan C, Lipkind S, Wang Z, Xu Q. Role of gingival mesenchymal stem cell exosomes in macrophage polarization under inflammatory conditions. Int Immunopharmacol. 2020 Apr;81:106030

Wiklander OP, Nordin JZ, O'Loughlin A, Gustafsson Y, Corso G, Mäger I, Vader P, Lee Y, Sork H, Seow Y, Heldring N, Alvarez-Erviti L, Smith CI, Le Blanc K, Macchiarini P, Jungebluth P, Wood MJ, Andaloussi SE. Extracellular vesicle in vivo biodistribution is determined by cell source, route of administration and targeting. J Extracell Vesicles. 2015 Apr 20;4:26316.

Willms E, Johansson HJ, Mäger I, Lee Y, Blomberg KE, Sadik M, Alaarg A, Smith CI, Lehtiö J, El Andaloussi S, Wood MJ, Vader P. Cells release subpopulations of exosomes with distinct molecular and biological properties. Sci Rep. 2016 Mar 2;6:22519

Xia Y, Zhang J, Liu G, Wolfram J. Immunogenicity of Extracellular Vesicles. Adv Mater. 2024 Aug;36(33):e2403199.

Xiao X, Fischbach S, Fusco J, Zimmerman R, Song Z, Nebres P, Ricks DM, Prasadan K, Shiota C, Husain SZ, Gittes GK. PNA lectin for purifying mouse acinar cells from the inflamed pancreas. Sci Rep. 2016 Feb 17;6:21127

Yang Y, Hong Y, Cho E, Kim GB, Kim IS. Extracellular vesicles as a platform for membrane-associated therapeutic protein delivery. J Extracell Vesicles. 2018 Mar 1;7(1):1440131.

Yang Y, Hong Y, Nam GH, Chung JH, Koh E, Kim IS. Virus-Mimetic Fusogenic Exosomes for Direct Delivery of Integral Membrane Proteins to Target Cell Membranes. Adv Mater. 2017 Apr;29(13).

Yim N, Ryu SW, Choi K, Lee KR, Lee S, Choi H, Kim J, Shaker MR, Sun W, Park JH, Kim D, Heo WD, Choi C. Exosome engineering for efficient intracellular delivery of soluble proteins using optically reversible protein-protein interaction module. Nat Commun. 2016 Jul 22;7:12277

Yokoi A, Yoshioka Y, Yamamoto Y, Ishikawa M, Ikeda SI, Kato T, Kiyono T, Takeshita F, Kajiyama H, Kikkawa F, Ochiya T. Malignant extracellular vesicles carrying MMP1 mRNA facilitate peritoneal dissemination in ovarian cancer. Nat Commun. 2017 Mar 6;8:14470.

Yu B, Shi Q, Belk JA, Yost KE, Parker KR, Li R, Liu BB, Huang H, Lingwood D, Greenleaf WJ, Davis MM, Satpathy AT, Chang HY. Engineered cell entry links receptor biology with single-cell genomics. Cell. 2022 Dec 22;185(26):4904-4920.e22.

Zhang H, Freitas D, Kim HS, Fabijanic K, Li Z, Chen H, Mark MT, Molina H, Martin AB, Bojmar L, Fang J, Rampersaud S, Hoshino A, Matei I, Kenific CM, Nakajima M, Mutvei AP, Sansone P, Buehring W, Wang H, Jimenez JP, Cohen-Gould L, Paknejad N, Brendel M, Manova-Todorova K, Magalhães A, Ferreira JA, Osório H, Silva AM, Massey A, Cubillos-Ruiz JR, Galletti G, Giannakakou P, Cuervo AM, Blenis J, Schwartz R, Brady MS, Peinado H, Bromberg J, Matsui H, Reis CA, Lyden D. Identification of distinct nanoparticles and subsets of extracellular vesicles by asymmetric flow field-flow fractionation. Nat Cell Biol. 2018 Mar;20(3):332-343.

Zhang J, Brown A, Johnson B, Diebold D, Asano K, Marriott G, Lu B. Genetically Engineered Extracellular Vesicles Harboring Transmembrane Scaffolds Exhibit Differences in Their Size, Expression Levels of Specific Surface Markers and Cell-Uptake. Pharmaceutics. 2022 Nov 23;14(12):2564

Zhang Q, Higginbotham JN, Jeppesen DK, Yang YP, Li W, McKinley ET, Graves-Deal R, Ping J, Britain CM, Dorsett KA, Hartman CL, Ford DA, Allen RM, Vickers KC, Liu Q, Franklin JL, Bellis SL, Coffey RJ. Transfer of Functional Cargo in Exomeres. Cell Rep. 2019 Apr 16;27(3):940-954.e6.

Zhang Q, Jeppesen DK, Higginbotham JN, Graves-Deal R, Trinh VQ, Ramirez MA, Sohn Y, Neininger AC, Taneja N, McKinley ET, Niitsu H, Cao Z, Evans R, Glass SE, Ray KC, Fissell WH, Hill S, Rose KL, Huh WJ, Washington MK, Ayers GD, Burnette DT, Sharma S, Rome LH, Franklin JL, Lee YA, Liu Q, Coffey RJ. Supermeres are functional extracellular nanoparticles replete with disease biomarkers and therapeutic targets. Nat Cell Biol. 2021 Dec;23(12):1240-1254.

Zheng W, Rädler J, Sork H, Niu Z, Roudi S, Bost JP, Görgens A, Zhao Y, Mamand DR, Liang X, Wiklander OPB, Lehto T, Gupta D, Nordin JZ, El Andaloussi S. Identification of scaffold proteins for improved endogenous engineering of extracellular vesicles. Nat Commun. 2023 Aug 7;14(1):4734.

Zipkin M. Exosome redux. Nat Biotechnol. 2019 Dec;37(12):1395-1400